Electrical Transport in Graphene Heterostructures and Other 2D Crystals

A thesis submitted to the University of Manchester for the degree of Doctor of Philosophy

in the Faculty of Sciences and Engineering

2020

Zihao Wang

Department of Physics and Astronomy

Abstract

This PhD thesis, submitted to The University of Manchester, mainly refers to any fundamental knowledge of transport measurement, the description of different measurement instruments and my research based on transport measurement ranging from the single alignment between graphene and one side hBN to double alignment where graphene is intentionally aligned to hBN on both sides, and extended from graphene - hBN superlattice to other twisted heterostructures. Twisted superconductors $NbSe_2$ has been discussed. Furthermore, the high-quality CVD graphene and exploration of twisted CVD graphene are also referred.

July 2020

Zihao Wang

Declaration

No portion of the work referred to in this thesis has been submitted in support of an application for another degree or qualification of this or any other university or other institutes.

Copyright statement

The author of this thesis (including any appendices and/or schedules to this thesis) owns certain copyright or related rights in it (the "Copyright") and s/he has given The University of Manchester certain rights to use such Copyright, including for administrative purposes.

Copies of this thesis, either in full or in extracts and whether in hard or electronic copy, may be made only in accordance with the Copyright, Designs and Patents Act 1988 (as amended) and regulations issued under it or, where appropriate, in accordance with licensing agreements which the University has from time to time. This page must form part of any such copies made.

The ownership of certain Copyright, patents, designs, trademarks and other intellectual property (the "Intellectual Property") and any reproductions of copyright works in the thesis, for example, graphs and tables ("Reproductions"), which may be described in this thesis, may not be owned by the author and may be owned by third parties. Such Intellectual Property and Reproductions cannot and must not be made available for use without the prior written permission of the owner(s) of the relevant Intellectual Property and/or Reproductions.

Further information on the conditions under which disclosure, publication and commercialisation of this thesis, the Copyright and any Intellectual Property and/or Reproductions described in it may take place is available in the University IP Policy (see http://documents.manchester.ac.uk/DocuInfo.aspx?DocID=487), in any relevant Thesis restriction declarations deposited in the University Library, The University Library's regulations (see http://www.manchester.ac.uk/library/aboutus/regulations) and in The University's policy on Presentation of Theses.

Acknowledgements

During my childhood, I have a dream to become a person like Jobs, Bill Gates and Ren Zhengfei. Their technology advancement really changes everyone's lifestyle, entering every family's daily life. As the years went by, my increase of experience reminded me that this is extremely difficult and just diligence and persistence cannot promise success. Talent, good luck, social demands and every possible random factor can influence the final result. Luckily, I have realized that I don't need to have such a high requirement for myself. Owning a colourful career, contributing really to my field, giving my family a good life and achieving my dream partly have been beautiful enough. Regarding the final result, let me just do what I can do. Currently, I am working in a world-leading lab supervised by a top scientist, doing cutting-edge technology and enjoying the best research resources in this world. I am still on the road towards my initial dream. I am lucky enough. I am sincerely thankful for everyone around me - the ones bringing me up, accompanying me, inspiring me, helping me and even competing with me. I hope after this milestone, in my future life, I could always own the heart of thanksgiving, work hard and make more contributions to my direction. (勿忘初心)

As for my PhD life, Prof Kostya Novoselov is the most important person. When I was studying as an undergraduate in the Department of Physics in Manchester, I went to his offices directly and expressed my hope to apply for PhD under his supervision. At that time, I have nothing except good exam grades and aspiration of a teenager. He accepted me after my self-introduction in haste. Up to now, it still seems a dream to me. Super grateful for his acceptance and trust which gave me a chance to lead a meaningful life in the following 4 years. After I entered the group, Kostya helped me enter the field of 2D crystals transport quickly in all kinds of ways. I can use cryostat Hulk alone for 4 years and measured many important samples even in the first learning stage as a freshman. During my 4-year measurement, he often instructed me face to face or online even very busy. Dear Kostya, Many thanks for your trust and help. Moreover, Kostya's working attitude and diligence influenced me indirectly, imperceptibly, gradually but deeply and profoundly. I still remember the Manchester's every morning, usually, he is the first researcher to arrive on the second floor, maybe the first in the whole Schuster Building. I am ashamed to admit that I did not develop a good habit to come to work as early as possible every day. In the aspect of work attitude, his mode of thinking taught me to focus on any problem perseverely by attempting any possible approaches until no

better solutions come up finally, not giving up, not complaining, not satisfied with an 'OK' solution. All these wonderful spirits along with the knowledge picked up from him is so beneficial to me. I hope in Singapore, with my identity upgraded, I can learn more from Kostya, improve myself more quickly and have the ability to contribute to our group more in my next career stage.

Besides Kostya, other members of our group are all nice and friendly to me. When I just entered the group, Jack (Mengjian Zhu) mentored me, training me how to operate the cryostat low-temperature system. He is so warm-hearted, helpful and knowledgeable. Since I never had any experience in scientific research before I entered the group, I made many naïve mistakes and sometimes I think I caused too many troubles to him. But he always kept patient to teach me, inspire me and guide me repeatedly how to do experiments. (在我刚进入实验室的时候，朱梦剑作为我的mentor，培训我如何使用cryostat低温设备，他是如此的热心，乐于助人，知识丰富。因为我以前没有任何的科研经验，我犯过很多幼稚的错误，一些时候我自己都觉得自己给他带来了很多麻烦，但他总是非常耐心的帮助我，激励我，不断地给讲解实验步骤。)

Jun Yin has done the transport measurement for 3 years in our group. This period right overlapped with me. His experience in all kinds of experiments, plus his senior-style warm hearts made the time together with him very meaningful and amusing. Most of my elementary knowledge of lab working has been acquired from him and I still cherished the time I chattered away happily with him after one day working. （殷俊在我们组做了三年的测试，这段时间正好和我共事，他的实验经验非常全面，师兄般的暖心让我们的相处非常开心，我大部分非常基础的实验室经验都来自殷俊师兄的教导，我依旧很怀念每天辛苦的工作，，我依旧很怀念每天辛苦的工作到达尾声时，临走前和他开心的肆意闲聊）

Colin and LiLin fabricated many samples for our group. Without them, I cannot learn a lot from their sample measurement and their experience as a senior taught me a lot of things from paper writing to submission, from CVD growing to AFM image. With their education, my scope of knowledge covered many different aspects of 2D materials.

LiLin came to our group during my third year of PhD. But his cooperation with me largely increases the efficiency of our projects. Furthermore, his life experience also helped me really a lot. When I felt depressed, my senior and good friend LiLin listened to my phone for 2 hours. Thanks for your patience and sincere help.（林立在我博士第三年来到我们组，但他和我的合作极大地提高了

我们项目推进的效率，不仅如此，他的生活经验真的帮助我很多，在我焦虑失望的时候，我的师兄也是好友跟我电话两小时，这件事我始终记得，感谢他的耐心和真诚的帮助。）

Besides, Artem, Roshan, Minsoo, Alexey, Davit, Denis, Servet, Julien, Carian and Serge all discussed with me and gave many useful ideas on transport measurement. Shuigang, Matt, Yibo, Cao Yang, Abhishek and Yaping provided me with a lot of high-quality samples. Thanks a lot for you all.

Thanks to my seniors, Geliang, Kaige, Yang Su, Guangping, Qian Yang, Pengzhan, Yuanxun, and Sheng Zhang and my friends, Ziwei, Wenjun, Junhao, Tongcheng. It is a pleasure to meet you all in Manchester.

I am also grateful to other group leaders, Sir Prof Andre Geim and Prof Volodya Falko. Thanks for their much helpful discussion and theory support for our projects. It does not make any sense to list their regalia. I appreciate the chance to work in the same lab and learn from you.

Finally, in the final part of acknowledgement, I want to express my most sincere gratitude to my parents and my wife. Every weekend in Manchester, I would video with my parents about what happened in the weekdays. I can feel their sentiment of missing across the screen. In the future, I will take care of myself better, keeping healthy, enjoying life and maintaining a good mood no matter what obstacles. I met my true love in Manchester. She chose to stay in Manchester accompanying me but we will separate in a short term. I will be in Singapore. You will be in Manchester. Please take care of yourself, don't worry about me. When our study is completed, we will be together with two better individuals.（最好，我要向我的父母和妻子表示最诚挚的感谢。曼彻斯特的每个周末，我会和父母视频分享周中发生的事，隔着屏幕我可以感受到思念的感觉。未来，我会照顾好自己，保持健康，享受生活，维持一个好心态无论遇到什么困难。我在曼彻斯特遇到了我的真爱，她留在曼城陪伴我走过了很久，但我们可能不得不分离一段时间，我在新加坡，你在曼城，请千万照顾好自己，不要为我担心，我相信当我们学业结束我们会带着更好的自己重逢

Introduction

As a novel tool for engineering devices with on-demand electronic properties, 2D heterostructures have received significant global interest in recent years. The introduction of interlayer twist offers a new degree of freedom to tune the electrical properties of 2D crystal stackings, among which, Graphene - hBN superlattice is our focus in this thesis.

Hexagonal boron nitride (hBN), as an ideal substrate for graphene owing to its atomically smooth surface and fine stability[2–4], has the lattice structure similar to graphene. Their lattice mismatch is only 1.8%, which enables the creation of a moire pattern by aligning the lattice of hBN with that of graphene. The resulting periodicity of the superlattice is 10 times greater than the lattice of graphene. This opened up the possibility to study a lot of interesting phenomena, such as second Dirac points[5], Hofstadter butterfly[6–8] in magnetic fields and Brown - Zak oscillation[9,10] persisting up to boiling water temperatures. When the twist angle between graphene and hBN gets close to zero, graphene will adjust itself to follow the lattice of hBN resulting in a commensurate state[11]. This local displacement also breaks the sublattice symmetry. As a result, the bandgap opening on the graphene neutrality point is observable.[8]

The first paper in the thesis reported the strong Umklapp electron-electron scattering (UEE scattering) in the graphene-hBN superlattice. UEE scattering is the scattering process in which the momentum of electrons is transferred to the crystal lattice thus providing a finite resistance on graphene. Compared to the pristine graphene lattice, the larger superlattice periods correspond to the smaller reciprocal lattice. Between two neighbouring superlattice periods, UEE scattering is prone to occur. The resulting contribution of resistance strongly depends on the temperature and shows a quadratic dependence in a wide temperature range which was extracted in our paper. At room temperature, UEE scattering has already become the dominant factor of carrier mobility. Hence the observation in this paper has extensive significance for the engineering of graphene superlattice-based devices

To further control the properties of graphene heterostructures, additional degree of freedom can be introduced by aligning graphene lattice to lattice of hBN on both sides together. In this structure, the bandstructure of graphene can be tuned not only by double moire patterns but also by the differential supermoires originated from the interaction between two Moire periods. In this way, the limitation of moire pattern period due to the graphene- hBN lattice mismatch can be overcome. The

resulting supermoire periods can be controlled arbitrarily to desired size. Correspondingly, the energy spectrum of monolayer graphene can be engineered at arbitrarily low energies.

Section 3.3 details the current data and analysis on double aligned graphene heterostructures determined in this study. The multiple peaks in the carrier concentration dependence of R_{xx} and sign reversals in R_{xy} indicate the periods of moire and supermoire. These are consistent with the measured fundamental frequencies of Brown zak oscillation.

In addition to the graphene - hBN alignment, twisted $NbSe_2$ heterostructures have been studied. In Section 3.4, $NbSe_2$ was used as a model system, whereby a new general method for scalable synthesis of high-quality monolayer superconductors has been reported. To prove the high quality of $NbSe_2$ printed in such method, the transport device of twisted printed $NbSe_2$ was measured against its exfoliated counterpart. The critical current of superconductivity with respect to the magnetic field shows the significant magnetic field dependent oscillation from which the frequency of Aharonov–Bohm oscillation can be extracted.

Fabrication of CVD graphene and its twisted 2D heterostructures has been explored with two studies. Section 3.5 tried to solve the puzzle of surface contamination by a post-growth method which exploited the adhesive force of an activated-carbon-based lint roller on the graphene surface. It was found that the polymer residue can be significantly eliminated through this approach. As a result, the electrical properties of such a pure graphene device are dramatically improved. Following Section 3.5, Section 3.6 reported an *ex situ* nucleation strategy to control the second layer nucleation with respect to the first layer. The quality of the resultant twisted graphene was kept very well, with mobility up to 68,000 $cm^2\,V^{-1}\,s^{-1}$ at room temperature.

Chapter 1 Basics of 2D Electrical Measurement

Introduction

In this chapter, general knowledge for different kinds of samples and measurement methods are referred to.

First, the nearly free model is introduced, whereby the carrier density in the *k*-space of the 2-dimensional electron gas is calculated and the distribution function *f(Ek)* evolving with the temperature is discussed. This model has many applications in transport measurement, such as the gate model of the transistor sample, the temperature smearing of fine information and the Fermi level shift. Then the difference between metals and semiconductors is mentioned with their transport characteristics, extending to the 2-carrier model. Shubnikov-de Haas oscillations(SdH), as a kind of magnetic oscillations, is described by Lifshitz-Kosevich (LK) formula. This chapter also illustrates the concept of quasiparticles in regard to its broad application in the weakly interacting many-body system. Different fermion quasiparticles and boson quasiparticles are summarised and listed briefly. The typical term of electron quasiparticles are referred to by explaining the usage of the effective mass. Finally, the Van der Pauw geometry is explained together with hall bar structure and Corbino geometry.

1.1 Nearly Free Electron Model

In the 2D free electron gas model, electrons propagate freely in the *x* and *y* directions and strongly bounded in the *z*-direction. If the boundary conditions in the *z*-direction are infinite, this can be treated as a quantum well model. Electron energy is quantised when the width of the quantum well is less than or equal to the electron wavelengths. Due to the discrete energy levels of the quantum well model $E_n = \frac{\hbar^2 k_n^2}{2m^*} = \frac{\hbar^2}{2m^*}(\frac{n\pi}{d})^2$ where E_n is the discrete energy of confined electrons, k_n is the wavenumber and m^* is the effective mass, the small quantum well width *d* will give a large gap ΔE_n between two levels, hence, electrons in the *z*-direction are usually confined in the ground state. In practical experiments, the 2D crystals are usually encapsulated between stable materials with huge band gaps such as hBN whilst measurements are conducted at helium temperatures to ensure the boundary conditions of the *z*-direction and to minimize the temperature smearing of the presentation of energy levels.

In the *x* and *y* direction, most materials with Schrodinger fermions have the dispersion relation

$$E_F = \frac{\hbar^2 k_F^2}{2m^*} \tag{1}$$

Graphene with massless Dirac fermions has

$$E_F = \hbar v_F k_F \tag{2}$$

where m^* is the effective mass and k represents the wavenumber of the dispersion

The free electron model in x and y directions provides the simplest dispersion relation as shown in Fig.1 (a). The translational symmetry in real spaces is transformed into the translational symmetry in k-space. Considering the periodic potential on the free electrons moving in the crystal lattices, the resultant translational invariance in k-space gives the following corrected dispersion relation

$$E_{vk} = \frac{\hbar^2 k^2}{2m^*} = \frac{\hbar^2 (k + G)^2}{2m^*} \qquad (3)$$

where G is the periodic reciprocal lattice vector as depicted by the blue curve in Fig.1 (b), m^* is the effective mass and k represents the wavenumber of the dispersion.
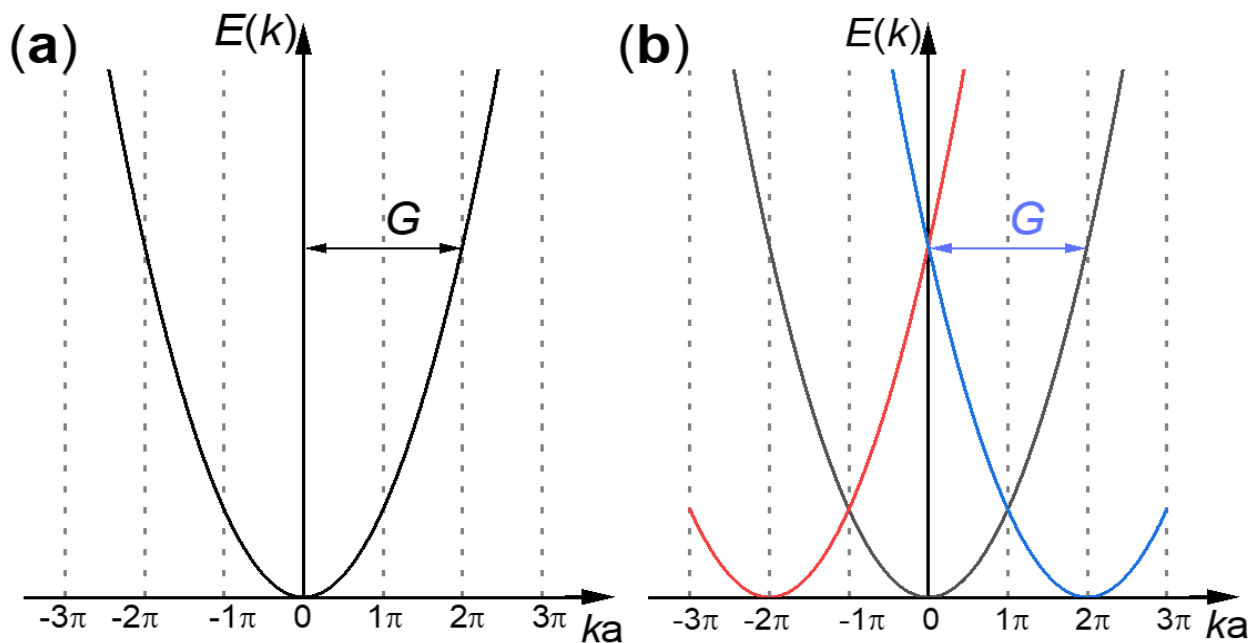

Fig.1 The diagram of the band structures in (a) extended zone, (b) repeated zone

The crossing point of each $k=\pm n\pi/a$ depicts the edge of each Brillioun Zone (BZ) at which the electron waves are Bragg scattered resulting in the zero-group velocity. Thus, the bandgap opens up and the different energy states are isolated as shown in Fig.2. Meanwhile, the dispersion relation away from the zone edge is still similar to the free electron model.

Essentially, compared to the free electron model, the nearly free electron model just introduces the weak periodic potentials caused by the lattice of crystals. The detailed explanation can start from plane waves of electrons to the two standing waves formed on the zone boundaries. The differing

electrostatic energies results in the bandgap opening.

In comparison to the nearly free electron model considering the weak periodic potential, the tight-binding model assumes the strong lattice potentials on electrons, in which the electrons are bound to the lattice cores strongly and rarely jump between atoms through the unique quantum-mechanical approach. The tight-binding model is generally applied to theoretical simulations of band structures
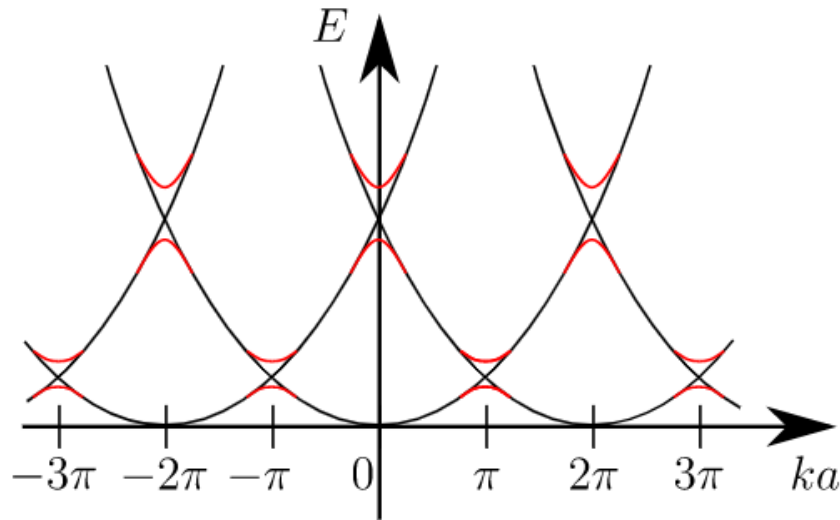

Fig.2 The illustration of the energy dispersion in two models. Red curves indicating the scattering by the lattice periodic potential shows the difference between the free electron model and the nearly free electron model. The bandgap is opened on these crossing points while the parabolic relation $E_{vk} = \frac{\hbar^2 k^2}{2m^*}$ is maintained to a large scale away from the crossing points.

1.2 Carrier Density for 2D Crystals and its Modulation in Transport Measurement

According to the nearly free electron model, the electron movements in 2D crystals can be regarded as the motions confined by the periodic boundary conditions originating from periodic lattice potential. This boundary condition is called the Born-von Karman periodic boundary condition in which the wavefunction of electrons is translationally invariant between two neighbouring periods. The electron state distribution in k-space is shown as follows
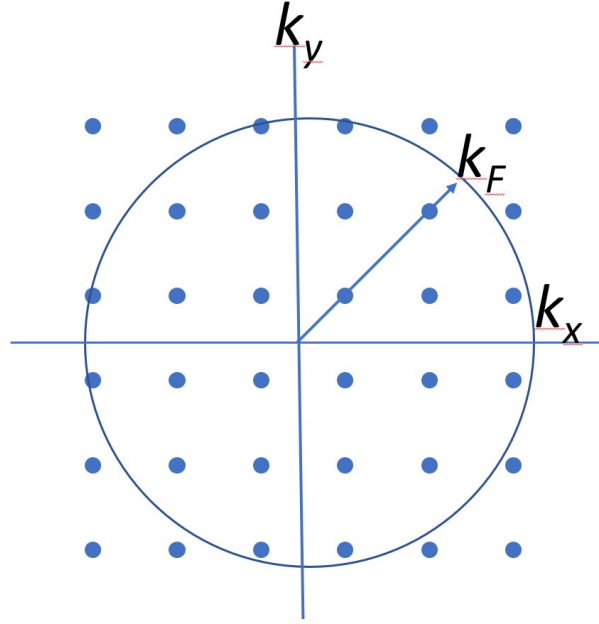
Figure 3 The diagram of *k*-space. The grid points represent the states of electrons and the circle represent the Fermi energy corresponding to k_F

$$k_x = \frac{2\pi n_x}{L_x} \qquad (4)$$

$$k_y = \frac{2\pi n_y}{L_y} \qquad (5)$$

where n_x and n_y are integers and L_x and L_y are the sizes of the sample.

In Fig.3, the grid points within the circle of wave vector k_F correspond to the electron states with energies smaller or equal to the Fermi energy. By calculating the number of points enclosed within the k_F circle for a unit area in the real space, the relationship between wave vector k_F and carrier density *n* is deduced through the following equation

$$k_F = \sqrt{\left(\frac{4\pi n}{g_s g_v}\right)} \qquad (6)$$

where g_s and g_v are the spin degeneracy and valley degeneracy, respectively.

All the above deductions are based on the assumption that all states within the k_F circle are 100% occupied by electrons. This only occurs at absolute zero temperature.

For different band structures, the dispersion for Schrodinger fermions and graphene can be written as

$$E_F = \frac{\hbar^2 k_F{}^2}{2m^*} = \frac{\hbar^2 \left(\frac{4\pi n}{g_s g_v}\right)}{2m^*} \tag{7}$$

$$E_F = \hbar v_F k_F = \hbar v_F \sqrt{\left(\frac{4\pi n}{g_s g_v}\right)} \tag{8}$$

Our field-effect transistor samples can be modelled as a parallel-plate capacitor for which the introduced carrier density Δn_{2D} is tuned linearly with the gate ΔV_g.

$$\Delta n_{2D} = \frac{\varepsilon \varepsilon_0}{ed} \Delta V_g \tag{9}$$

Where d is the thickness of the capacitor, primarily the thickness of SiO$_2$ and hBN in our samples, ε is the relative permittivity and ε_0 is the vacuum permittivity.

When the low-temperature premise disappears, an additional factor of occupation function is required to describe the behaviour of electrons.

$$n = \int_{E_C}^{E_F} g(E) dE f(E) \tag{10}$$

Where the $g(E)$ is the density of states with the constant value $\frac{m^*}{\pi \hbar^2}$ for the 2D case. The product $g(E)dE$ is the number of quantum states in the energy interval between E and $E+dE$ per unit cell. *Fig.4* shows the occupation function of fermions in the finite temperature, known as Fermi-Dirac distribution

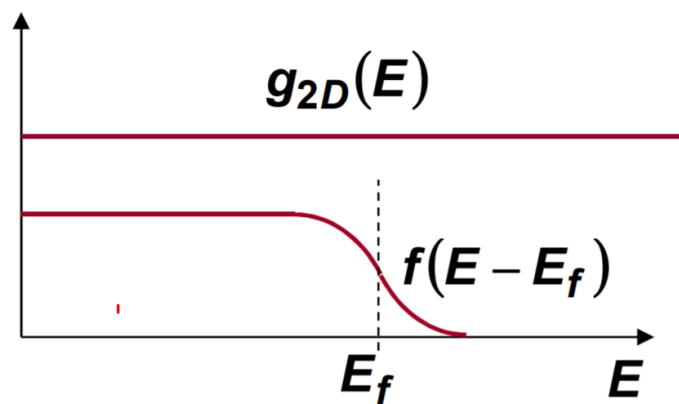$$f(E) = \frac{1}{1 + e^{\frac{(E - E_F)}{kT}}} \tag{11}$$

Fig.4 The distribution function $g_{2D}(E)$ and Fermi-Dirac distribution function $f(E-E_f)$ of the density of states in the finite temperature.

With the temperature increasing, electrons disperse to occupy the states of the higher energies above Fermi energy while leaving holes just below the Fermi energy. This temperature smearing effect lead to the reduction of the measurement resolution. If the explored propertiesrequires the high resolution of characterization of the band structures, the gate sweeping cannot detect it differentiably enough and instead gives the averaged information on a larger energyrange. On the contrary, at temperatures approaching absolute zero, the occupation function of electrons tends to fully occupy the states below the Fermi level and totally vacate the states above. In this case, only the electrons proximal to the Fermi-edge are able to contribute to the conduction. The passing of Fermi level across the different band structures provides an elaborate depiction.

1.3 Metals, Semiconductors and Multiple Carrier model

1.3.1 The Transport of Metals and Semiconductor

The gating effect on metals

The analysis described in Section 1.2 regarding carrier density tuning is only suitable for metals whereby the Fermi energy level situates within bands. In the practical measurement, the gating is not always effective to tune the metals electrically. For graphene, the gate modulation is powerful enough as the carrier density for pristine graphene is around zero. The dielectric SiO_2 and hBN provide the gate tunning range in the order of 10^{12} cm^{-2}, which is sufficient to observe most phenomena for graphene. Yet, the intrinsic carrier concentration of most 2D metals exceeds the order of 10^{13} cm^{-2}. Although ionic liquid gating can dope up to 10^{14} cm^{-2}, this method still has many disadvantage. Contamination will be introduced to influence the sample's intrinsic properties.[12] Therefore, gate modulation is fairly impractical in most metal tuning scenarios. Moreover, for most multilayer metals, the gate-induced electric field is screened by the first layer neighbouring the dielectric. Dispersion then occurs, resulting in different carrier concentrations on different layers.

The Transport of Metals

Since the conductivity for the metal in the Drude model is proportional to the product of carrier density and the scattering time, the scattering time has to be considered also. Scattering time is defined as how long charge carriers are ballistically accelerated by the external electric field until there is a collision that changes the direction of the charge carrier. This process is highly dependent

on acoustic phonons. Since atom vibrations will be completely frozen at absolute zero temperature in the temperature measurement of helium-4, this factor is minimised.[13]

In a not 'clean' system, any chargeable impurities will scatter electrons by Coulomb force. This scattering significantly depends on the number of charges whose existence is independent of temperature, and consequently, impurity scattering cannot be eliminated by low temperatures. If the influence of an 'unclean' system needs to be alleviated from the measurement, the fundamental solution would be to fabricate a 'clean' sample. Scattering due to imperfections, such as surface roughness, defects, and charge trapping sites, follows a similar process of resolution

Besides, there are other kinds of scattering not appearing commonly. For high-quality graphene samples, the electron-electron scattering plays an important role at low temperatures after the cooling down kills the phonon.[14] In some compound semiconductors with a polar nature, the electric field arising from the distortion of the sample unit cell due to the external strain deflects the travelling electrons.[13] In the Section 3.2, the Umklapp electron-electron scattering provides a finite resistance in the graphene-hBN superlattice.

The transport of semiconductors

Since the Fermi level of a semiconductor is positioned within bandgaps, the carrier density of the semiconductor is dependent on the position of the Fermi level relative to the band edge and the temperature which excites electrons jumping to the bands.

$$n \propto e^{-\frac{\Delta E}{2kT}} \qquad\qquad (12)$$

where T is the temperature and ΔE is the energy difference between the Fermi level and the band.

Equation (12) shows an exponentially decreasing relationship between n and T. The mobility μ, which depends on scattering time, has less dependence with T, as this usually varies linearly in a similar manner to metals. Therefore, n (T) is the dominant factor. As a result, our resistivity measurement also varies exponentially with T. Based on the measurement of temperature dependence, the

position of the Fermi level can be determined within bands (metals) or within bandgaps (semiconductors or insulators). The basic profile of temperature dependence is shown in Fig.5 [13]
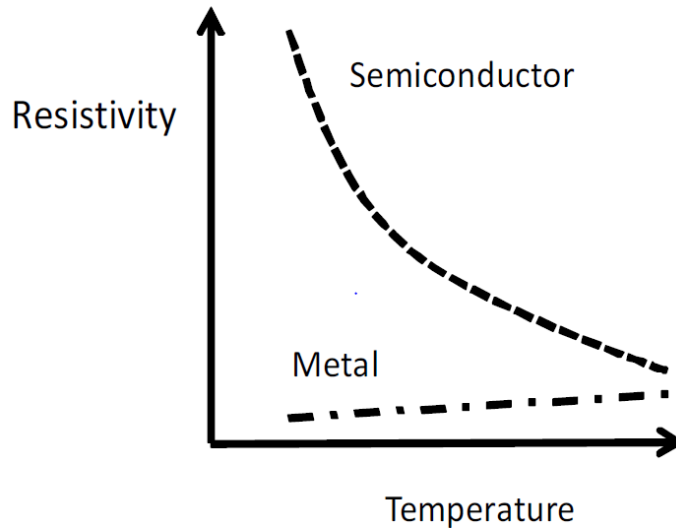

Fig.5 The general temperature dependence of resistivity for metals and semiconductors.

1.3.2 Capacitance of the field-effect device and the gating effect of transistors

In terms of the potential induced by the gate, the concepts of geometrical capacitance and quantum capacitance become evident. Geometrical capacitance is governed by a dielectric independent of the gate, while quantum capacitance relies on the crystal band structure and therefore varies with gate modulation. The total capacitance of this parallel plate capacitor model is given by

$\frac{1}{C_t} = \frac{1}{C_g} + \frac{1}{C_q}$ where C_g and C_q represent the geometrical capacitance and quantum capacitance, respectively.[15]

The total potential difference caused by total capacitance is the difference between the Fermi levels of the gate and sample. In physics, this is the total free electron energy difference. Geometrical capacitance induces the pure electrical potential on each electron, and so, the energy change of all electrons occurs concurrently, resulting in the energy of the whole band structure shifting collectively. However, the relative position of the Fermi levels in each band structure remains the same. Contrastingly, quantum capacitance results in a relative shift of the Fermi level. Electrons introduced to the negative side occupy the higher energy states, whilst electrons eliminated from the

positive side leave the lower energy states vacant. Physically, geometrical capacitance originates from the formation of dipoles from the dielectric, following the process of $Q = C_d V_g$, where C_d and V_q represent the dielectric capacitance and Galvani potential, respectively. Contrarily, quantum capacitance derives from the variation of the chemical potential $\Delta u_i = Q/(\rho e)$. The corresponding voltage is determined as $V_q = \Delta u_i/e = Q/(\rho e^2)$, where ρ refers to the density of states of the low-density-of-states material. Hence, the definition of quantum capacitance is represented by $C_Q = \rho e^2$.[16]

For normal crystals with parabolic dispersion, quantum capacitance is calculated as shown in Equation (13).[16]

$$C_Q = \frac{g_v \mathrm{m}^* \mathrm{e}^2}{\pi \hbar^2} \qquad (13)$$

For graphene with Dirac massless fermions, the quantum capacitance depends on the carrier density. When $E_F \gg kT$, the Fermi level is distant from the Dirac point and is measured at low temperatures, the quantum capacitance is shown in Equation (14). [17]

$$C_Q = e^2 \frac{2}{\pi} \frac{e V_{ch}}{\pi (\hbar v_F)^2} \qquad (14)$$

Quantum capacitance is negligible in the metal-insulator-metal capacitor due to the high carrier concentrations of metal. As the introduction or loss of electrons is inconsequential, so is the chemical energy change. However, in the context of the low-density-of-states system, quantum capacitance is of significance. The quantum capacitance of semiconductors, graphene, or semimetals varies with the gate. In terms of graphene, quantum capacitance is distinctly altered around Dirac points and in quantising magnetic fields.

In our transport measurement, a single SiO₂ gate architecture is usually employed. To lessen the disorder caused by inhomogeneous electric gating, a graphite gate is applied.[18] By applying this dual gate geometry, the displacement field and the carrier density can be tuned separately. Resultantly, the measurement has an additional degree of freedom, and this has become a common strategy for bilayer graphene.[19,20]

1.3.3 Two-carrier model

The analysis described in the previous section pertains to contexts where the Fermi levels are positioned in the bands or bandgaps, but is limited to a single carrier case where the Fermi level of crystals scans across the band of only one orbital or bandgap. However, for some materials, the bands of different orbitals can be overlapped in the region accessible by the solid gate. For example, the WTe$_2$ band structure is shown in Fig.6.
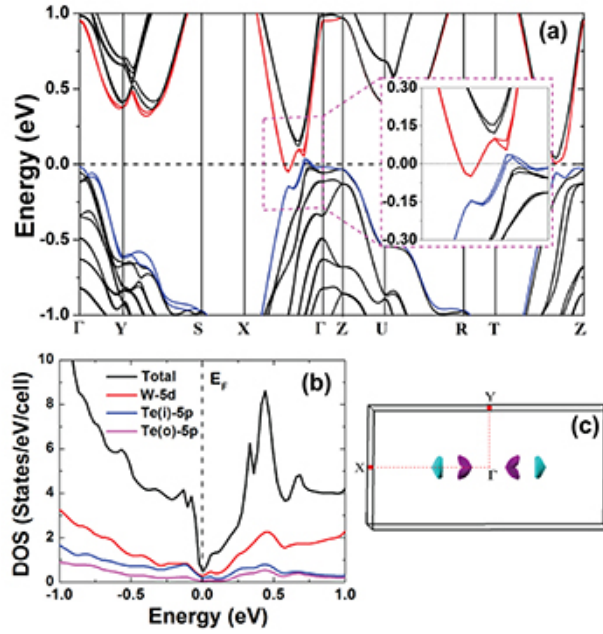

Fig.6 Bulk WTe$_2$ (a) band structure; (b) total and partial density of states (DOS); (c) Fermi surface adapted from [17].

Fig.6 shows that the atomic shells W-5d and Te-5p both contribute to the conduction. In Fig.6b, the theoretically stimulated density of states displays the contributions from different carriers.

In our transport measurement, the concentration of different carriers can be split. By applying small magnetic fields, the resistivity and hall resistance under the two-band model can be fitted in accordance with Equation (15) and Equation (16).[17]

$$\rho_{xx} = \frac{1}{e} \frac{(n\mu_e + p\mu_h) + (n\mu_e\mu_h^2 + p\mu_e^2\mu_h)B^2}{(n\mu_e + p\mu_h)^2 + (p-n)^2\mu_e^2\mu_h^2B^2} \tag{15}$$

$$\rho_{xy} = \frac{1}{e} \frac{(p\mu_h^2 - n\mu_e^2)B + (\mu_h^2\mu_e^2)(p-n)B^3}{(n\mu_e + p\mu_h)^2 + (p-n)^2\mu_e^2\mu_h^2B^2} \tag{16}$$

These equations refer to the 2-carrier case of electrons and holes. In the context of electrons and electrons, and holes and holes, the formula is similar. Since these two equations contain only four

unknown parameters, the results will produce inadequate accuracy. Alternatively, the field dependence at high fields can be an effective supplement. The Lifshitz-Kosevich (LK) formula is often employed to fit the SdH oscillation for effective mass extraction.

1.4 Shubnikov-de Haas oscillation, Landau level and Lifshitz-Kosevich (LK) formula

SdH oscillation occurs when free electrons behave like a harmonic oscillator in the conditions of low temperatures and intense magnetic fields. As the magnetic fields increase, finally fully developed Landau levels form and the quantum hall effect is reached. SdH oscillation orginates from the Landau quantisation which is the quantum quantisation of the cyclotron motion of electrons under intense magnetic fields and low temperatures, whereby the electrons only occupy the discrete energy levels corresponding to certain orbits. The Hamiltonian for weakly interacting electrons under the influence of the magnetic field can be written as follows:[13]

$$\hat{H} = \frac{1}{2m}(\hat{p} - q\hat{A}/c)^2 \tag{17}$$

When the perpendicular magnetic field is applied on 2D crystals, the energy eigenvalue in the z-direction is ignored.[19]

$$\hat{H} = \frac{\hat{p}_x^2}{2m} + \frac{1}{2m}(\hat{p}_y - \frac{qB\hat{x}}{c})^2 \tag{18}$$

$$\hat{H} = \frac{\hat{p}_x^2}{2m} + \frac{1}{2}m\omega_c^2(\hat{x} - \frac{\hbar k_y}{m\omega_c})^2 \tag{19}$$

Replacing the *qB/mc* with the cyclotron frequency ω_c enables the equation to become a typical model of a quantum harmonic oscillator, which always owns the discrete energy levels-Landau levels:

$$E_n = (n + \frac{1}{2})\hbar\omega_c \tag{20}$$

Due to the boundary condition of the sample edge, LLs bend upwards near the edge. The Fermi level situated between two LLs in the bulk will cut the bent LLs on the sample edge, which forms edge states.[15]

The LK formula is often used to describe SdH oscillations, which comprise five parts: 1) magnetisation and torque, 2) curvature factor, 3) damping terms r_t, 4) dingle term R_D, and 5) the spin splitting factor R_S.[18]

$$\Omega \propto R_T R_D R_S \times \text{magnetisation and torque} \times \text{curvature factor} \qquad (21)$$

Magnetisation and torque refers to the measurement of the perpendicular or parallel area of magnetisation and torque, in regard to magnetic fields. If our sample is measured perpendicular to fields without rotation, this term can be ignored.

Likewise, curvature factor accounts for the Fermi surface curvature, and therefore, is irrelevant unless the angle-dependent measurement is applied.

Damping is a term that originates from temperature smearing. As shown in Fig.4, the occupation function at non-zero temperature broadens to the order of $k_B T$, relative to the step function at zero temperature. At this point, as the Fermi level is no longer a strict boundary differentiating the occupied and unoccupied states, different oscillations of different carrier densities around the Fermi level will interfere with each other, which reduces the oscillation amplitude value by the factor shown below:

$$R_T = \left(\frac{X}{\sinh(X)} \right) \qquad (22)$$

$$X = \frac{2\pi k_B T p m^*}{e\hbar B} \qquad (23)$$

where m^* is the effective mass governed by electron-phonon scattering and electron-electron scattering. Damping can be applied to extract the effective mass by fitting the temperature dependence of the envelope of the oscillation; this then allows these two types of scattering to be investigated. [18]

It should be acknowledged that the parameter of X is essentially the ratio between temperature smearing $k_B T$ and the Landau level spacing $e\hbar B/ m^*$. Based on the function $X/\sinh(X)$, the damping effect increases with the ratio; this explains why measurement of the SdH oscillation requires a low temperature of < 50K and high magnetic fields. The oscillation is more observable in sample materials that naturally have a smaller effective mass.

The dingle term R_D is governed by the impurity or defect scattering, as shown in Equation (24):

$$R_D = \exp\left(\frac{2\pi k_B T_D p m_b}{e\hbar B} \right) \qquad (24)$$

where m_b is the band mass (applied in cyclotron motion in magnetic fields), τ is the scattering time, and $T_D = \hbar/2\pi k_B \tau$ is the dingle temperature which is set to imitate the influence of the real temperature on electron-phonon scattering. Impurities in a sample result in smaller values of τ, and thus, T_D is larger. This results in the suppression and widening of Landau levels.

The spin splitting factor R_S acknowledges the Zeeman splitting of Landau levels, whereby the spacing is $\Delta E = g\mu_B B$; in this case, g is the total degeneracy of electrons.

Parabolic dispersion relation leads to the reduction factor due to the interference between two close oscillations:

$$R_S = \cos(\frac{\pi g p m_b}{2 m_s}) \qquad (25)$$

where m_s only refers to the electron-electron interaction. When the electron-electron interplay is irrelevant, m_s approaches $m*$.[22]

$$\Delta R_{xx}(T,B) \propto \frac{\alpha T/\Delta E_N(B)}{sinh\left(\frac{\alpha T}{\Delta E_N(B)}\right)} e^{-\frac{\alpha T_D}{\Delta E_N(B)}} \qquad (26)$$

In our measurement, R_T and R_D are the main damping factors for the fitting. The envelope of oscillation amplitude is fitted by Equation (26), which extracts the damping factor with respect to T or B, as either fixed B fitting T or fixed T fitting B.
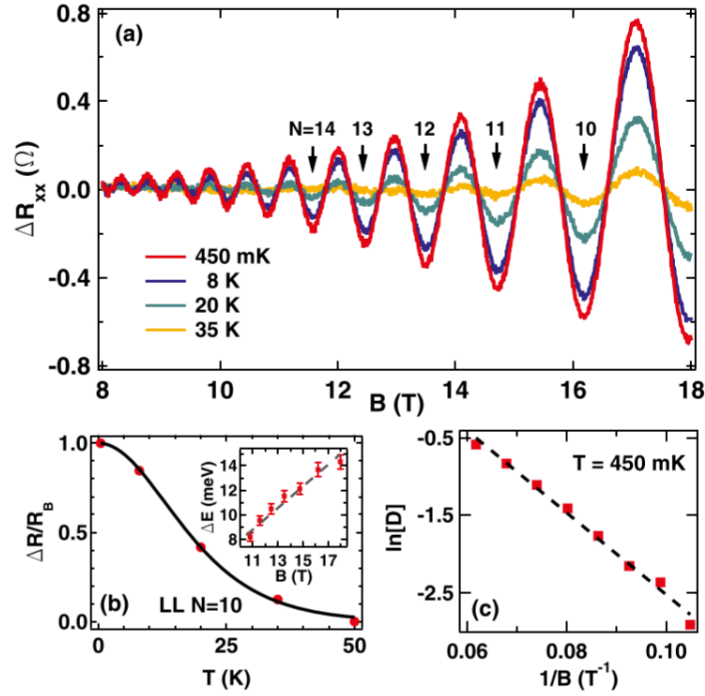
Fig. 7 Adapted from [19] (a) The subtracted Shubnikov de Haas oscillations at different temperatures, (b) The temperature dependence of the oscillation amplitude at N=10, Inset: The fitted ΔE of different oscillations N with respect to B, and (c) The 1/B fitting of ln(D) at 450K $D = \Delta R_{xx} B sinh\left(\frac{\alpha T}{\Delta E_N(B)}\right)$.

The simple model of 1-carrier crystals shown in Fig.7 can be used as an example: firstly, the R_{xx} vs B at different temperatures are subtracted from the background by a polynomial fitting. The deducted $\Delta R_{xx}(B)$ should oscillate at approximately 0. Then, specific oscillation peaks or valleys are selected to fix B. In Fig.7, the significant Landau level index number N=10 is chosen at different temperatures. This temperature dependence is fitted by $\frac{\alpha T/\Delta E_N(B)}{sinh\left(\frac{\alpha T}{\Delta E_N(B)}\right)}$, where $\Delta E_N(B) = \hbar eB/m^*$ is the energy gap between N and $(N+1)^{th}$ Landau levels; this becomes the constant by fixing B at this point. To obtain the most accurate value of ΔE_N, the linear fitting can be applied to determine the average of the energy gaps calculated from the different N^{th} Landau levels. The inset of Fig.7 (b) depicts this method. Thus, the effective mass can be derived from the slope of the 1/B dependence. [18]

Following the establishment of the effective mass of materials based on the temperature dependence of ΔR_{xx}, the dingle term can provide the scattering time at specific temperatures using magnetic field dependence. However, the B dependence associated with damping must first be removed. Based on Equation (26), a new term is created: $D = \Delta R_{xx} B sinh\left(\frac{\alpha T}{\Delta E_N(B)}\right)$. Using the slope

of *ln*(*D*) *vs 1/B* facilitates the extraction of $T_D = \hbar/2\pi k_B\tau$. Based on this, the scattering time and its corresponding mobility can be derived. At temperatures higher than the helium-4 boiling point, the scattering time includes both temperature-dependent scatterings and temperature-independent scatterings; yet when the temperature cools to below 2K, the former scattering is obsolete, and only the latter type, describing impurity scattering, survives.

By calculating the period of (*1/B*) of every peak or valley, the fundamental frequency B_F can be deduced, followed by the carrier density of SdH oscillation as $n(SdH) = geB_F/h$. In this equation, degeneracy *g,* including spin degeneracy and valley degeneracy, are important factors, but there is no involvement in the Hall effect. By comparing these two *n*, the degeneracy of electrons in this crystal can be determined.

In the context of a 2-carrier case, extracting the effective mass is a more challenging concept. The superposition of two or more oscillations makes it difficult to determine the envelope of each individual oscillation. Therefore, FFT (Fast Fourier Transformation) can be applied to distinguish the different frequencies that have merged. Equation (27) is useful to attempt direct fitting for oscillations, as opposed to establishing the envelope of the oscillations by LK formula. Using FFT of the data for (*1/B*) dependence transforms the X-axis from real 1/*B* to frequency B_F. Meanwhile, the Y-axis usually remains as amplitude. The two frequencies, B_{F1} and B_{F2} with maximum amplitude, can be extracted for two terms. Their corresponding carrier densities can then be deduced.[20]

$$\Delta R_{xx} \propto R_{T1}R_{D1} \sin\left(\frac{2\pi B_{F1}}{B} + \varphi\right) + R_{T2}R_{D2}\sin(\frac{2\pi B_{F2}}{B} + \varphi) \qquad (27)$$

At various temperatures, the field dependences can be fitted to simultaneously obtain effective mass and carrier lifetime. However, this method is relatively complex, as ideally only one parameter would be fit at one time. Since the R_D only involves field dependence, and effective mass is usually temperature-independent, the amplitude of oscillations will only involve a variable R_T with constant parameter m^* at the fixed field. To maximise this advantage, the amplitude of FFT is extracted as shown in Fig.8. [20]
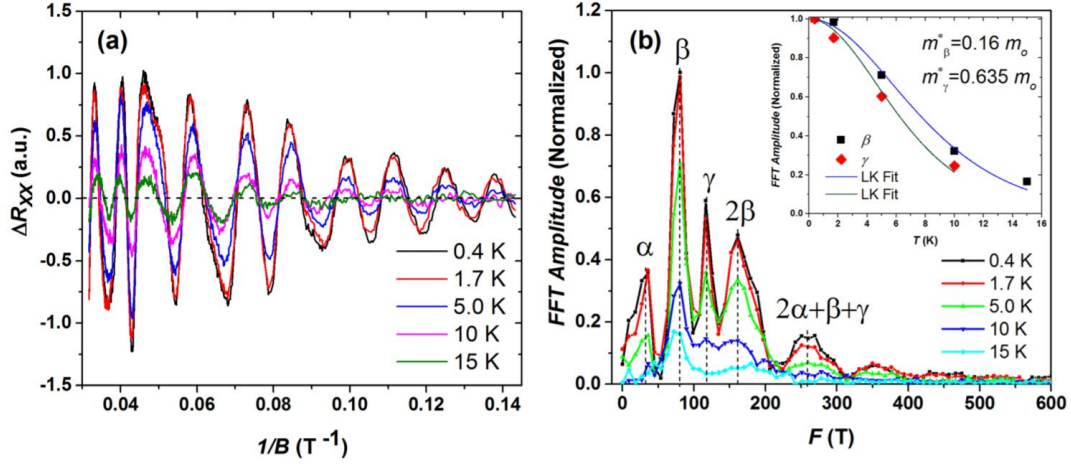
Fig.8 An example of effective mass extraction. (a) SdH oscillations after subtracting the background, (b) FFT spectrum of the oscillations in (a) Adapted from [20].

In the case of FFT of ΔR_{xx} versus $1/B$, three frequencies $\alpha, \beta,$ and γ are distinguished. It should be noted that the higher harmonics and their combinations, such as 2β and $(2\alpha + \beta + \gamma)$, also have significant peaks; however, these are established frequencies. The amplitudes of the three frequencies are essentially the average of corresponding oscillations in Fig.8 (a), which can be used for temperature fitting as the inset shows.

Once the effective mass has been determined, fitting the ΔR_{xx} function to derive the carrier lifetime becomes a simpler process. Moreover, the temperature dependence of scattering time also becomes obtainable.

Essentially, by fitting the SdH oscillations with the LK formula, the quantity effective mass and scattering time, and therefore the mobility and carrier density, can be established. When the SdH oscillation includes two or more oscillations, the 2-band model should be considered. The first stage should utilise the Hall effect, as fitting R_{xx} and R_{xy} at small magnetic fields deducts separate mobilities and carrier concentrations. Furthermore, higher fields that trigger SdH oscillations allows the use of the LK formula, assisted by FFT to split the carrier densities, effective masses, scattering times, and further effective mobilities.

In the real measurement of this study, the mixing of SdH oscillation with other smaller oscillations is a common phenomenon. To determine the origin of this event, oscillations deriving from other sources should initially be considered, such as BZ oscillation[9], magnetophonon oscillations,[23] and multiple Dirac points caused by the intersection of Landau levels. The usual approach to this

investigation involves measuring the magnetoresistance at different temperatures and different gates. If the results eliminate these options, other artificial factors of the 2-carrier model should be considered, such as the different carrier densities in different layers. The screening effect of samples found that carriers in different layers experience different gate influences vertically. If the samples are not uniform, are contaminated in certain regions, or the vicinity of contacts is doped, different horizontal regions will include different concentrations, and can potentially form p-n junctions[24,25]. These vertical and horizontal inhomogeneities can also create an additional oscillation with a different frequency. If the results of all these factors deem them irrelevant, the 2-carrier model should be carefully considered, especially for semimetals with overlapped band structures.

1.5 Quasiparticles and Effective mass

The analysis in the previous section used the effective mass in most instances where the formula required a quantity of mass. Before going into details of the effective mass, a general physical quantity known as 'quasiparticles' will be introduced, which comprises the most fundamental idea and mode of thought in a weakly-interacting quantum many-body system.

Solids consist of three elementary particles: neutrons, protons, and electrons. Only electrons participate in conduction. Quasiparticles do not exist, as instead, they are created artificially to simplify the complicated system. There are two keywords associated with the quasiparticle system: weakly interacting and many-body.

A single electron travelling in a weakly-interacting system is influenced by the presence of all other electrons, nuclei, and other external factors. If these influences are considered together in terms of motion and energy, the theoretical environment becomes too complicated. Therefore, the concept of quasiparticles was introduced to incorporate all the weak interactions on electrons into their effective mass. As a result, the movement of different crystals will behave like electrons with different effective masses, moving smoothly within free electron gas following the simplest dispersion relation *E(k).* Specifically, the electron quasiparticle is introduced to contain the influence of crystals on the 'free' electrons. The holes quasiparticles are special for the conduction to be carried by the valence band of semiconductors or the hole band of semimetals, for which the effective mass is negative and electron charge is positive. A polaron is employed to describe the motion of conduction electrons in ionic crystals.[26] Overall, quasiparticles are a mathematical tool created with the purpose to transform

the complicated weakly interacting system of real particles into the non-interacting system of totally free particles. [27,28]

A further motivation for the use of quasiparticles is the impossible direct description of all particles and their correlations in a 'many-body' system. In a real measurement, even a small graphene channel with a size of several nanometres would contain at least 10^{11} electrons. To better depict the information of such systems, treating every particle independently is vital. As with the previous analysis, applying the quasiparticle concept denotes the independent movement of every electron quasiparticle in a free electron gas, devoid of any interplay. This refers to a fermion quasiparticle.

In regard to boson quasiparticles, also known as 'collective excitations', the Boltzmann distribution is employed and the same notion of quasiparticles can be applied. For a given quantum system, the energy distribution is discrete with the ground state and many excited states with higher energies above the ground states. At absolute zero temperature, oscillation is absent on the lattice. The ground states accommodate all the electron states. At any higher temperatures, the lattice vibration will be triggered. To simplify the complicated oscillation influence, the phonon concept is introduced as a type of elementary excitation, and is essentially a quantum of the sound wave. When one phonon is added to the lattice, the crystal vibrates very slightly in a particular frequency, and the lattice will be in a low-lying excited state. More generally, the excited states can possess any integer number of phonons, which are all treated independently. This process allows a basic understanding of the simplified lattice vibration. In reality, the excitation energy borders on the accurate sum of all identical phonons but fails to attain the legitimate value. Some perturbations need to be introduced, such as phonon-phonon scattering.

Effective mass simplifies the movement behaviours of the electron quasiparticles by illustrating that electrons with different effective masses act like free electrons and are only influenced by an external electric field or magnetic field. The interactions due to the intrinsic properties of materials will be contained in the effective mass; this is not associated with real mass and is simply a mathematical contraption. The value of the effective mass is determined by the band structures and is also reversely defined by the relationship between the external force and group velocity. The group velocity represents the velocity of the whole electron system, or in the context of waves, refers to the propagation speed of electron wavefunctions. Mathematically, group velocity is the phase velocity of the wave packet envelope.

$$v_g = \frac{dE}{dp} = \frac{dE}{\hbar dk} \qquad (26)$$

If an external force caused by the electric field is applied, the formula for effective mass is derived, as shown below:

$$F = m^* \frac{dv_g}{dt} \qquad (27)$$

$$m^* = \frac{1}{\frac{d^2E}{\hbar^2 dk^2}} \qquad (28)$$

In Equation (27), *F* only refers to the external force, as the crystalline force is already contained in the wavefunction of electrons represented by group velocity v_g. It has been established that the parabolic dispersion *E*(*k*) corresponds to the constant m^*, while other *k* dependence results in a varying effective mass. Since graphene contains Dirac massless electrons, this formula is not applicable. For the 2D case, the carrier density has a direct relationship with effective mass $\frac{g_v m^*}{\pi \hbar^2}$.

As a basic property of crystals, effective mass essentially represents the band structure of the outermost shell of atoms and characterises the movement of most free electrons in crystals.

1.6 Various Transport Geometries and Transport Measurement Methods

1.6.1 Transport Geometry: Van der Pauw Method, Hall bar, and Corbino

In terms of practical measurements, the geometry of the Hall bar is the most common configuration. However, the Van der Pauw method is also significant. At times, the limitation of fabrication and the lower requirement of measurement result in a rectangular or circle sample also being employed without etching.

Resistivity transport measurement is a weighted averaging of the local resistivities of the whole measured section. Different sample shapes have different current distribution, and thus, are suitable for use with various methods to obtain the average and eliminate the inhomogeneity. Our transport measurement consists of the 2-probe method and the 4-probe method. The difference lies in the integration or separation of current-carrying electrodes and voltage-sensing electrodes. The measured results derived from 2-probe sensing include the impedance, capacitance, and resistivity

of two loads. Therefore, this approach is generally less accurate. However, sometimes contact resistance plays an important role in our measurement, and therefore, if the main focus is the contact resistance or edge channels, which are closely related to contacts, this method would be applicable. Comparatively, 4-probe sensing only measures the impedance of the chosen area targeted by the voltage-sensing loads; therefore, this method produces higher accuracy. The principle of 4-probe sensing is that for most instruments, such as lock-in or nanovoltmeter, almost no current will flow through the voltage sensing ends. As a result, the voltage variation induced by the contact is negligible. To achieve this principle, the sample resistance between two sense leads must be considerably smaller than the input resistance of the measuring instruments.

When the 4-probe measurement is applied, the resistance distribution of the sample shape, the contact position, and its size all take effect. The local resistivity in different areas contribute to different weighting; the resistivity of a specific area can be determined based on Equation (30).

$$\rho_{average} = \iint \rho(x,y)f(x,y)dxdy \qquad (30)$$

where $\rho(x,y)$ denotes the local resistivity of the specific location, and $f(x,y)$ is the weighting function depending on the sample shape and the arrangements of the contacts' position and size.

Regarding homogeneous resistivity and linear 4-probe arrangement, the resistance in the sensing direction is commonly known as $\rho = RW/L$. For general cases where contacts are positioned on the perimeter of the 2D sample with a random shape, the Van der Pauw method is primarily implemented.[41,42]
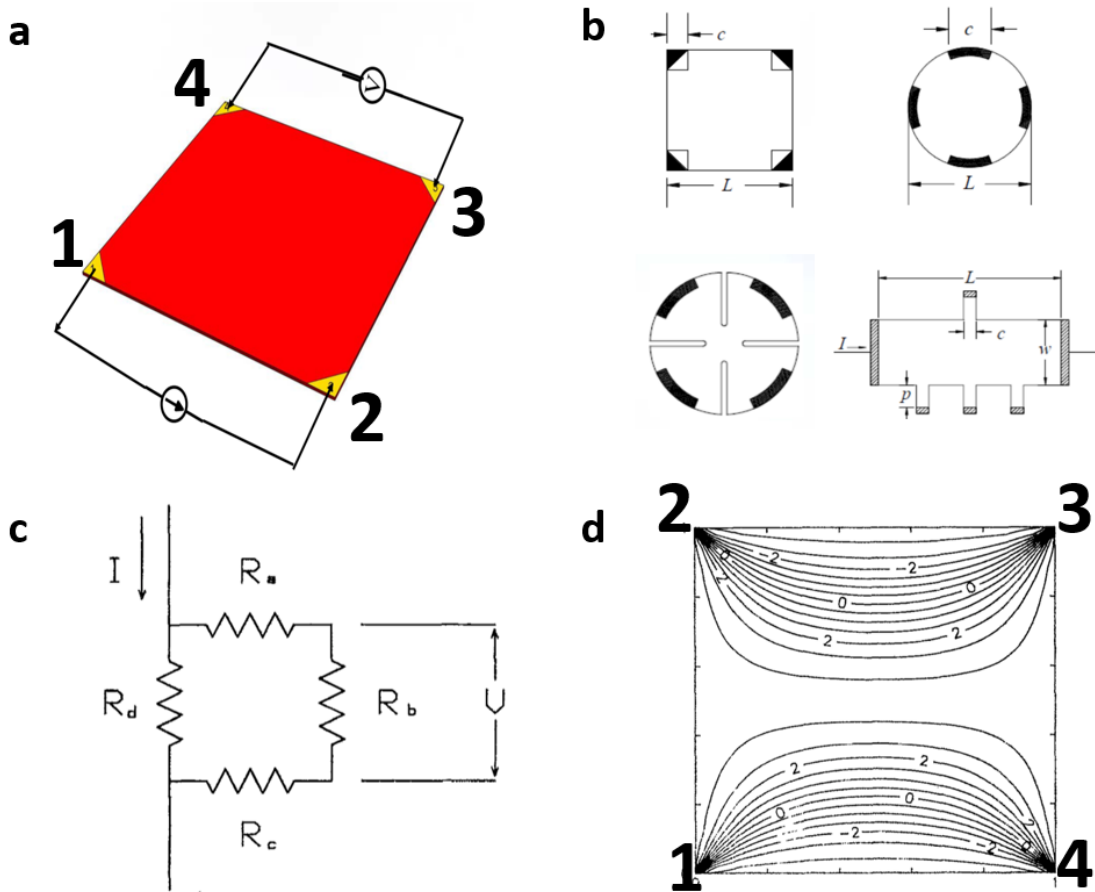
Fig.9 Van Der Pauw method (a) general schematic of the Van Der Pauw measurement (b) various sample shapes (c) an intuitive understanding of the resistivity distribution, adapted from [60] (d) the contour of the weighting map, whereby the negative index labels the negative weighting, adapted from [60]; current is applied from 1 to 2 and the subsequent voltage drop between 4 and 3 is measured.

In the Van der Pauw theorem, the general formula of the resistivity shown in Fig.9 (a) is represented in Equation (31).

$$\rho = \frac{\pi}{Ln2}\left(\frac{V_{34}}{I_{12}}\right) \qquad\qquad (31)$$

However, this formula assumes that the contacts are equally spaced and that the sample is symmetrical. If a higher level of accuracy is required, other measurement strategies can be used to estimate the inhomogeneity, and therefore, derive a more accurate average of the resistivity.

Firstly, reversing the polarity of the current or voltage leads (I_{12} to I_{21}, or V_{34} to V_{43}) removes the background resistance offset in direct current (DC) measurement; this is independent of the measurement direction, such as the background noise of instruments or the thermoelectric effect

resulting from temperature distribution. If the resistance of the swapped polarities produces a significant deviation, then this indicates that these two factors are active. By taking the average value, the offset is eliminated.

Secondly, the voltage leads and current leads can be swapped (I_{12}, V_{34} to V_{12}, I_{34}). By comparing both resistances, the contacts and sample portions that do not meet the aforementioned assumption of equal spacing and symmetry, respectively, can be identified. If the difference between the two resistance values is of a suitably small degree of deviation, the sample can be considered as relatively high quality.

Thirdly, both the vertical and horizontal resistances (I_{12}, V_{34} to I_{23}, V_{14}) can be measured. In this way, the contribution difference from the weighting function $f(x,y)$ of the different areas can be estimated and mitigated to a large scale. To average all the above factors, Equation (32) is used.

$$R_{average} = \frac{(R_{12,34} + R_{21,43} + R_{34,12} + R_{43,21}) + (R_{23,14} + R_{32,41} + R_{14,23} + R_{41,32})}{8}$$

(32)

Regarding measuring Hall resistance, establishing the value of V_{13} / I_{24} is sufficient. The above techniques to improve accuracy can also be implemented with an additional method of trying both positive and negative magnetic fields and calculating the average.

As Fig.9 (b) shows, the contacts should be fabricated on the perimeter of the sample if the Van der Pauw method is applied. The size of the contacts largely affects the systematic errors of the results. As the ratio of c/l increases, the error of R_{sheet} and R_H grows exponentially, therefore denoting positive correlation. Hence, minimising the contact size is important for systematic error reduction.[43] Usually, c/l should be less than 1/6. For a square sample with c/l = 1/6, rectangular contacts produce a systematic error of 2% for R_{sheet}, while triangular contacts produce a systematic error of 1%, and circular samples also produce a systematic error of R_{sheet} of approximately 1%. Contrastingly, the error of Hall resistance R_H is greater, at 15% for both square and circular samples. Cloverleaf shape samples result in a distinct reduction in systematic error, yet the fabrication process for this shape has higher requirements. For the normal Hall bar, the error of R_{xx} and R_{xy} measurements is minimal. However, the error of mobility can sometimes be magnified by the calculation. The premise $p>>c$, $w>3c$, and $L>4w$ can ensure the systematic error nears zero.

Compared to Van der Pauw geometry, Hall bar geometry is considerably more accurate and powerful. The longitudinal resistance R_{xx} and Hall resistance R_{xy} are well separated with multiple bars to measure them concurrently. The design of armbars minimises the side effect produced by the contact size. Nevertheless, it is difficult to etch the sample in a clean region. A minimum of six arms is required to minimise the misalignment of opposite bars, as well as reasonable contact configuration, and a bar with adequate length, to avoid the limiting condition of bubbles, defects, and wrinkles. Moreover, it is possible that the sample material may be sensitive to air or light, which is a further limitation, as the etching process may expose the edges of the sample.

Fig.9 (c) and (d) show an intuitive phenomenon. Current is applied from 1 to 2, and the voltage drop between 3 and 4 is measured; resultantly, the contour of weighting function f(x,y) in Fig.9 (d) clearly depicts negative contribution as shown by the index of -2, which means the local resistivities ρ(x,y) on the f(x,y) = -2 curves are contributing negatively to the average resistance. This is illustrated by the model in Fig.9 (c), as the current flows vertically through R_d with the voltage sensed on R_b. The measurement of resistance is given as follows:

$$R = \frac{V}{I} = \frac{R_b R_d}{R_b + R_d + R_a + R_c} \qquad (33)$$

Equation (33) shows that the value of R is inversely proportional to R_a and R_c. Consequently, the negative contours are perpendicular to the direction of current flow. In regard to the local resistivity, the more constituents perpendicular to the current direction, the more likely it will negatively contribute to the averaged resistance. To avoid this effect, the use of 4-probe voltage-sensing leads between current-carrying leads void of any perpendicular constituents can be implemented; this is the most common measurement arrangement on Hall bars. When measuring the plasmon related phenomenon, the nonlocal measurement containing perpendicular contribution is often applied.

As shown in Fig.10, the Corbino geometry is designed to specifically avoid the edge state influence, and therefore will probe the bulk properties of 2D materials solely and directly. Currently, it is mainly used to measure the quantum Hall effect, as it provides a much higher resolution for both integer and fractional quantum Hall effects compared with Hall bar geometry. The Corbino geometry allows observations of the quantum Hall effect in lower magnetic fields, whilst distinguishing more filling fractions.[44, 45] If a study required the splitting of the edge state and bulk state of a particular phenomenon, the Corbino geometry would be utilised. To further split the bulk and edge states, the

side gate can also be considered. The electrical properties on the edge can be effectively tuned without majorly influencing the bulk section.[46]
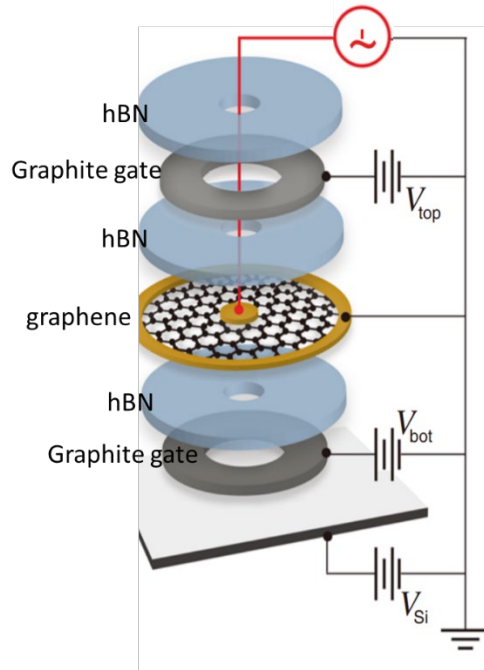

Fig.10 Corbino geometry with graphite dual-gate

1.6.2 Tunnelling measurement

Tunnelling measurements are based on the quantum tunnelling regime, which originates from the Heisenberg uncertainty principle. It can be solved directly by the Schrodinger equation by inserting different potential functions into the equation and solving the wavefunction in terms of potential V and particle energy E. Tunneling is solved in the condition of $E < V$. The transmission coefficient for an electron passing through the potential barrier is shown as:

$$T(E) = e^{-2\int_{x_1}^{x_2} dx \sqrt{\frac{2m}{\hbar^2}[V(x)-E]}} \qquad (34)$$

where x_2 and x_1 determine the thickness of the potential barrier, which is the middle insulator thickness. $V(x)$ represents the property of the insulator, which is mainly related to its band structure distribution on the x-direction, and is usually a constant for homogeneous samples. E is the work function of conductors on both sides. Based on this equation, the tunnelling current for low bias can be derived, as shown in Equation (35).

$$I(d) \sim V_{bias} exp(\frac{2\sqrt{2m(V_{barrier} - E)}}{\hbar} d) \qquad (35)$$

where d is the thickness of the middle insulator, and V_{bias} is the bias applied on tunnelling devices. Equation (35) clearly shows that the thickness of the insulator is important: inadequate thickness results in break-down risk, making it difficult to control the bias during measurement, whilst excessive thickness results in the tunnelling current being too small. Temperature smearing and other systematic noise influence the presentation and detection of meaningful phenomena. However, the thickness is dependent on each sample, and therefore, is often variable.

The tunnelling device consists of metal-insulator-metal structures. The example of a graphene-hBN-graphene device can be used to discuss the general basic rules and principles.
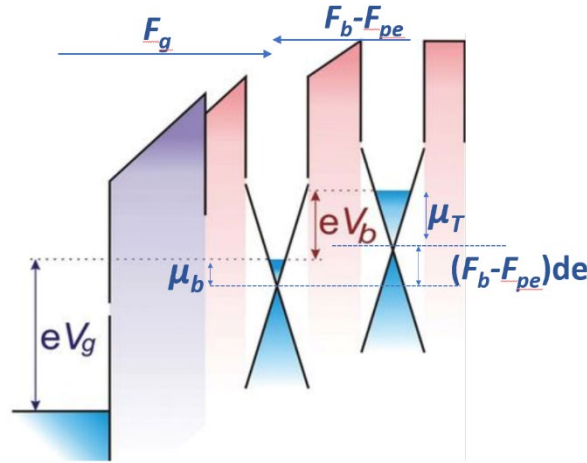
Fig.11 Schematic of the tunnelling regime of graphene-hBN-graphene device. Adapted from [47].

Fig.11 shows the tunnelling regime of Fermi level shifting induced by back gate V_g and bias V_b. The basic formula includes the Gauss theorem and energy equation. The Gauss theorem equations for both the bottom graphene layer and top graphene layer are given by Equation (36) and Equation (37), respectively.

$$\varepsilon(F_g - F_b + F_{pe}) = 4\pi n_b e \qquad (36)$$

$$\varepsilon(F_b - F_{pe}) = 4\pi n_T e \qquad (37)$$

where F_b and F_g denote the electrical fields caused by bias voltage and gate voltage, and F_{pe} denotes the remaining electrical field penetrating the bottom graphene monolayer. n_T and n_b represent the introduced number of electrons by the electric field.

The total energy applied by the sourcemeter is the sum of Coulomb energy and chemical potential.[48,47,49]

$$eV_b = \mu_T - \mu_B + \left(F_b - F_{pe}\right)ed \qquad (38)$$

$$eV_g = \mu_B + e^2(n_T + n_B)D/\varepsilon\varepsilon_0 \qquad (39)$$

where d is the thickness between two graphene layers, and D is the thickness between the back gate and the bottom graphene layer. In Equation (36), the second term Coulomb energy is transformed to the form of carrier densities $e^2(n_T + n_B)D/\varepsilon\varepsilon_0$. This set of energy equations can be incorporated to fit V_g vs V_b. In terms of the graphene Dirac relativistic electrons, $\mu \propto \sqrt{n}$ is applicable, but for most fermions, $\mu \propto n$ is more appropriate.

1.6.3 Capacitance measurement

Measuring capacitance is an effective probe to determine the available density of states in 2D electron gas; its principle is described in Section 1.3.2. The measured total capacitance is the reciprocal sum of the quantum capacitance and geometrical capacitance. Geometrical capacitance corresponds to the contribution of electrical potential energy, originating from the formation of dipole moments in dielectric materials, while quantum capacitance corresponds to the contribution of chemical potential, originating from the introduction of carriers. Therefore, variation in the density of states, in regard to the gate, can be directly displayed through the capacitance measurement. Since the Dirac points and the filling factor lines involve the drop of the density of states, the Landau fan, which indicates the filling factors of Landau levels, can also be determined from the capacitance measurement.[53,54]
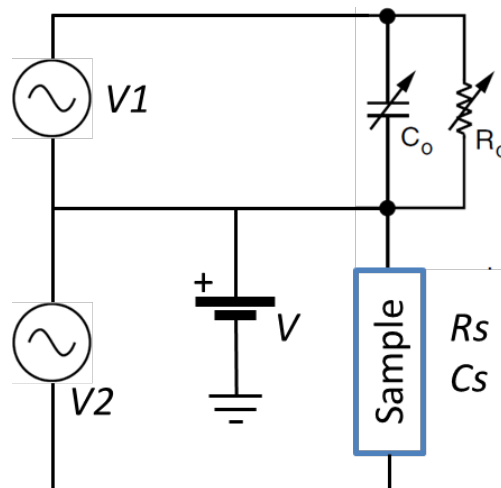
Capacitance measurement is conducted through the capacitor bridge, whereby C_0 and R_0 in the microprocessor are adjusted to attain a ratio of $V1/V2$ with the sample's R and C. The relationship of $C_0 R_0 = RC$ is maintained continuously under the condition of $V_1 = V_2$ when the bias V is tuned.

Chapter 2 Measurement Instruments

2.1 Cryogenic system

The cryogenic system, as the basic setup for our low-temperature and high-magnetic-field measurements, consists of a cryostat, pumping lines, cables, lock-in amplifiers, voltage/current source meters, nanovoltmeters, computers with LabVIEW and the sample insert. Two types of cryostats are used and classified as a wet and dry cryostat.

2.1.1 Wet Cryostat

(a)

(b)

(c)
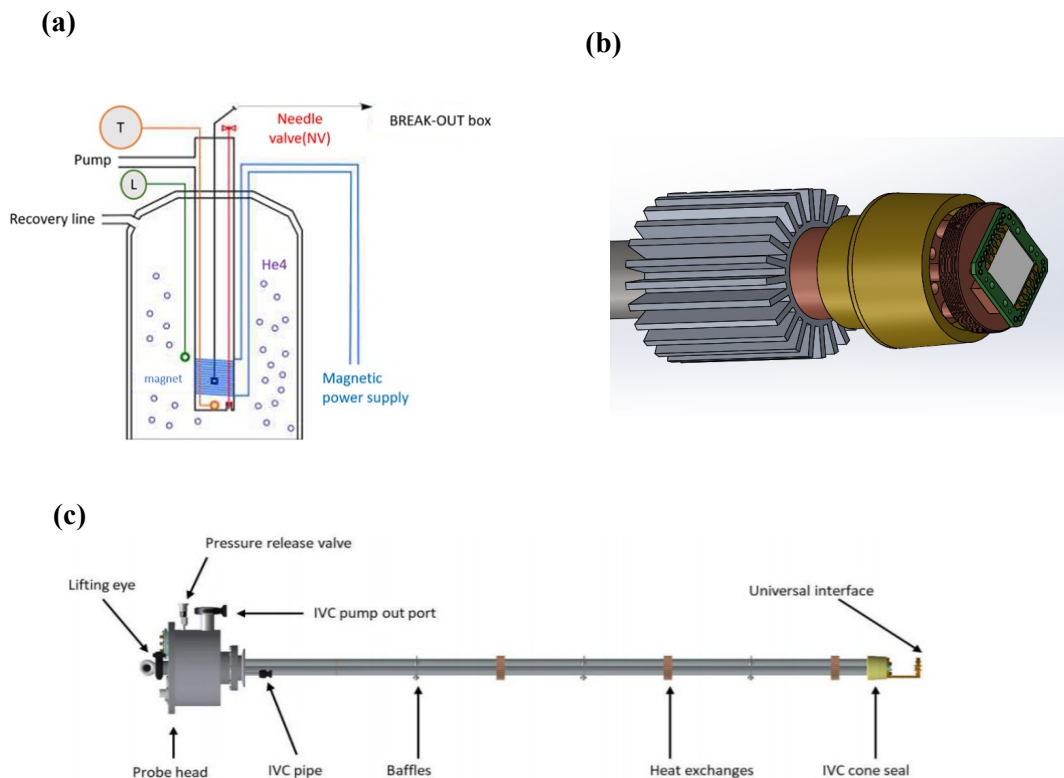
Fig.13 The simple schematic of the (a) wet cryostat, (b) the sample holder of the insert and (c) a typical insert

The term 'wet cryostat' means that this kind of cryostat does not have a closed cycle of Helium flow, rather the sample area is cooled by flowing liquid helium . The regular transfer of liquid helium is required. Its operation is described as Fig.13 (a). The liquid helium in the tank has two outlets. One is to collect evaporated helium gas to send to the recovery line and the other is for flowing of helium through the VTI and into the recovery line. In this process, the sample holder is directly in contact with flowing helium and is cooled to below liquid helium temperature. The thermal exchange plate shown in Fig.13 (c) enhances this thermal contact. Since the low pressure due to the pump can further decrease the boiling point of the liquid, the bottom of VTI usually is able to approach temperatures down to 2K. The final stable temperature is dependent on the thermal balance between the cooling power of the helium flow, controlled by a needle valve and heat dissipation which is determined by the loading of the insert and the sealing and isolation of the whole cryostat. The thermal isolation baffle on the insert in Fig.13.(c) can help reduce thermal contact with the outside enviroment. If the thermal load of the insert is not heavy, the temperature of this kind of cryostat can reach 1.5K approximately.

The procedures for sample loading is described in the following. First, the fabricated sample is bonded on achip carrier. The chip carrier is then assembled on the sample holder of the insert. Before loading, the sample holder has to be pumped down in vacuum to avoid any external contamination. A vacuum brass can shown in Fig.14 will be pumped through the IVC pump out port. Unless the bottom of the VTI is at room temperature, the insert has to be loaded gradually to avoid any temperature-induced change on the sample. During the process of cooling down the sample, we just adjust the needle valve to control the cool down rate. After the temperature reaches liquid helium temperatures, the flow rate should be reduced to reach a minimum of 1.5K.
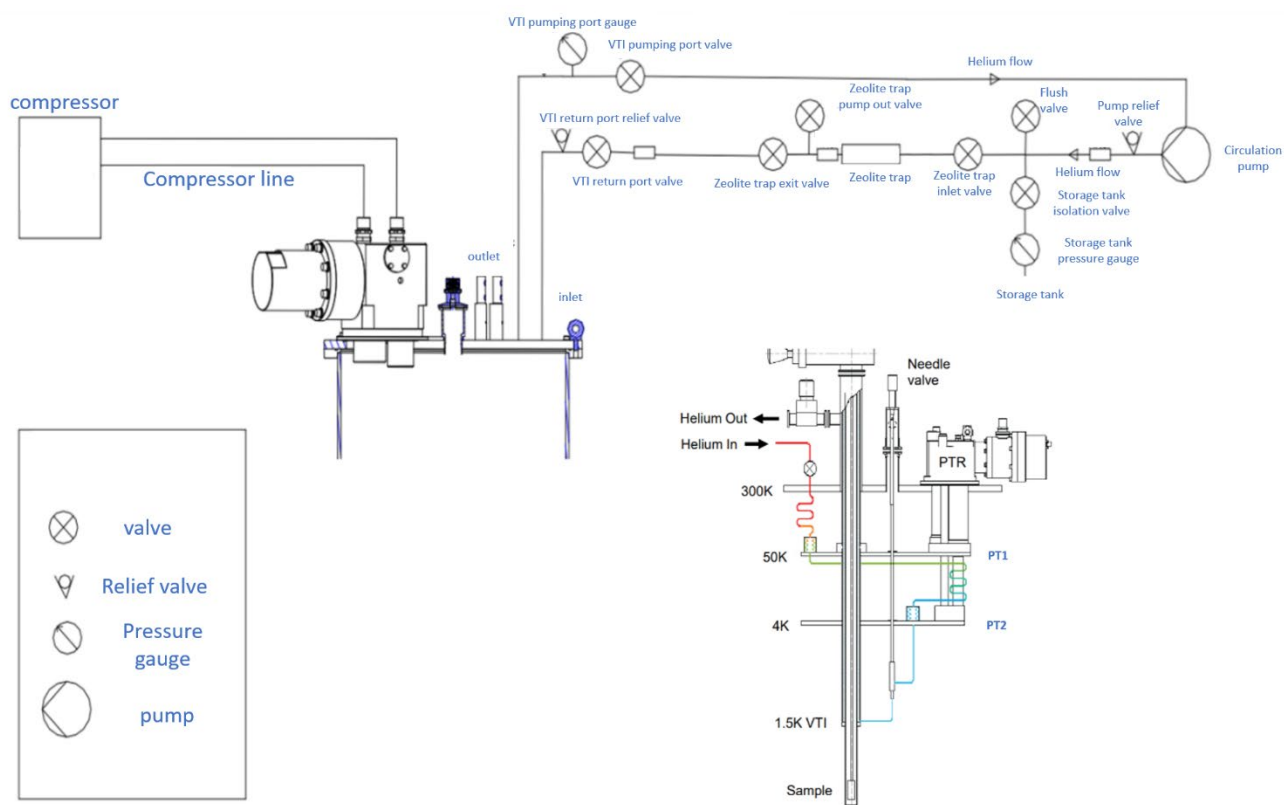
2.1.2 Dry Cryostat

Fig.14 The schematic of the whole layout of dry teslatron cryostat consisting of the helium circulation line and the compressor line. Reference from the manual of the Oxford instrument Teslatron PT 1.5 K Quantum Research Platform.

Dry cryostat means that this cryostat has a closed circle of Helium flow. It does not need the periodical filling of Helium. Simply speaking, the dry teslatron cryostat consists of two circles, a compressor circle and a helium circulation circle. The compressor circle can be understood as a general Carnot cycle with its adiabatic expansion process taking effect in the cold head of cryostat. This absorbs heat to the circulated helium and cools down the whole system. The circulation circle connects the cold head and VTI to cool down VTI to base T.

Helium compression path: When the cold head is operational, the compressor is used to pressurise the helium. Within the cold head, the high-pressure helium expands adiabatically over a short period of time. Specifically, a valve in the cold head of the pulse tube is bordered by high-pressure helium on one side and relatively low-pressure helium on the other side. The valve is opened and closed at a frequency of 1.4Hz, which is controlled by the solenoid valve. Whenever the valve is opened, a small quantity of the high-pressure helium gas transfers across to the low-pressure side, and expands rapidly. Following this, the temperature of the flowing helium decreases to a lower value than the

other components of the cryostat; therefore, the heat from the system is absorbed and returned to the compressor. In the compressor, the low pressure, expanded helium will be pressed again, whilst the water-cooling loop will take the heat away from the compressor simultaneously, releasing the heat to a separate water-cooling machine. After this process, the resulting high-pressure helium returns to the cold head, and the process continues to repeat

Helium circulation cycle: The variable temperature sample chamber in the system is cooled down by a separate helium path. This path is controlled externally by a series of valves and circulation pumps. The external circulation pump is connected to the closed circle, and the helium extracted from one end of the system is returned to the other end to form a circulation loop, whereby the switch and the rate of helium flow can be controlled by several port gauges and valves. Removal of contamination in the helium flow is achieved through a zeolite trap prior to circulation. When the system is turned off, the helium gas in the circulation cycle is stored in the storage tank, as depicted in Fig.14.

Helium entering the internal area of the system flows through the cold heads PT1 and PT2 (Fig.14) and is cooled to 4K over a two-stage process. When the temperature is below 4.2K, the helium liquefies into liquid helium, flows through the needle valve, and is then pumped by the circulation pump outside the circulation path. Prior to being pumped out, liquid helium coils around the variable temperature sample chamber to enable sufficient heat exchange. Considering these two factors, the variable temperature sample chamber can reach as low as 1.5K. Any contamination in the helium flowing through this closed loop will be cleaned by a zeolite trap.

Superconducting magnet: The liquid helium-free superconducting magnet is directly connected to PT2 by a copper column. The minimum temperature of PT2 is less than 4K. Due to the strong thermal conductivity of copper,, the superconducting magnet can be cooled to below 4K and enter the superconducting state.

2.1.3 Helium-3 inserts
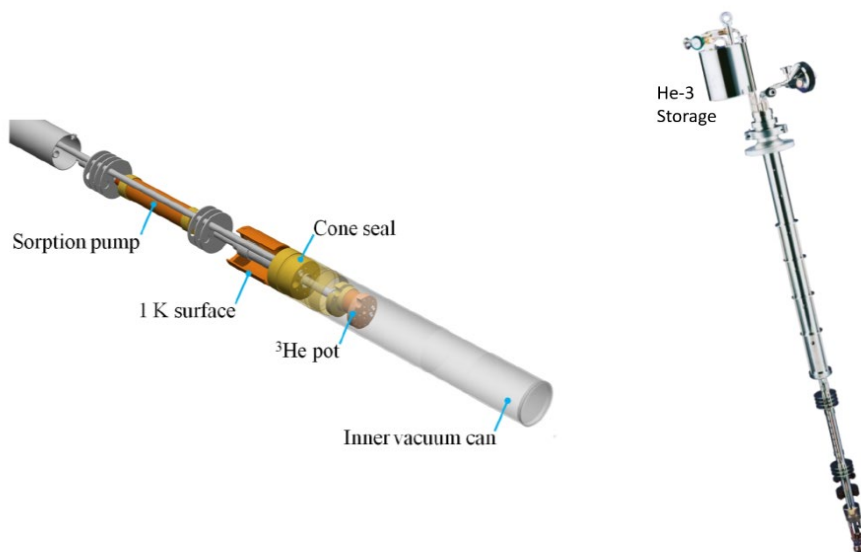
Fig.15 The schematic of the He-3 insert. Adapted from the manual of Oxford Instrument helium-3 insert.

Due to the lower boiling point of He-3 at 3.2K, the helium-3 insert can cool down the sample to 0.3K. Considering the extremely expensive price of He-3, it is typically used in a closed-circle scheme. Before cooling down, the He-3 gas is stored in the top can outside the cryostat. When the part inside the cryostat is cooled down by the flowing He-4 gas, the lower pressure in the bottom will push the top He-3 gas going down continuously, accumulated in the charcoal of the sorption pump. By heating the sorption pump, the released He-3 is liquified around the 1K-surface which is designed to enhance the thermal exchange with outside He-4. After the He-3 condensation, the sorption pump is cooled down. The charcoal in it starts to absorb the He-3 gas, and acts as a pump, pumping the He-3 pot to the lower pressure. At this stage, by adjusting the flow rate of He-4 flowing outside the insert, the temperature of He-3 pot can be stabilised at 0.3K. The material with good thermal conductivity contacts the He-3 pot to the sample holder, finally cooling down the sample temperature to 0.3K. Since the amount of He-3 in this closed-system is limited, when all the helium gas is collected by the charcoal, the temperature will go up and the re-condensation needs to be redone to achieve 0.3 K.

2.2 Measurement Instruments

(a)

(b)

(c)
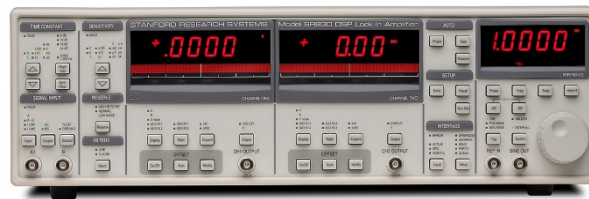
Fig.16 The measurement equipments (a) Nanovoltmetre (b) Source meter 2600 (c) SR 830 Lock-in, and

Fig.16 shows the common measurement instruments we often use. Classified by the current type, the electrical measurements are classified into two categories, direct current measurement (DC) and alternating current measurement (AC). The AC measurement usually gives more accurate results by locking to a single frequency. But since it is measured with the sin function of voltage, it can only measure resistance assuming that the voltage-current relationship (*I-V* curve) is linear. The sample with too big resistance, the order above 100 kΩ and Schottky contacts cannot meet this premise. Before the AC measurement, it is always meaningful to check the *I-V* curve by DC methods.

2.2.1 AC measurement

The AC measurement is usually performed by using a lock-in amplifier. To measure the small signal, amplifier and phase-sensitive detection (PSD) is used. After amplification, the noise will be magnified together with respect to the bandwidth. The current lock-in amplifier applies a phase-sensitive detector (PSD) strategy to minimize the noise by detecting the signal at a super small bandwidth. The principle is that a reference signal with the same frequency and phase is multiplied by the signal.

$$V_{psd} = V_{sig}V_L sin(\omega_r t + \theta_{sig})sin(\omega_L t + \theta_{ref})$$

$$= \frac{1}{2}V_{sig}V_L cos([\omega_r - \omega_L]t + \theta_{sig} - \theta_{ref})$$

$$- \frac{1}{2} V_{sig}V_L cos([\omega_r + \omega_L]t + \theta_{sig} + \theta_{ref} \qquad (40)$$

where the ω_L, $\theta_{ref,}$ and V_L are the parameters of the reference signal and ω_r, θ_{sig} and V_{sig} belong to the sample signal. After passing through a low pass filter, this product will reduce to

$$\frac{1}{2}V_{sig}V_L cos([\omega_r - \omega_L]t + \theta_{sig} - \theta_{ref}) \qquad (41)$$

Theoretically, θ_{sig} should be the same as θ_{ref} and ω_r should be the same as ω_L so the V_{sig} is derived. In our real measurement, we can either input the TTL sync of source lock-in or the sine signal of measured voltage to the measuring lock-in as a reference $V_L sin(\omega_L t + \theta_{ref})$. Unless the sample's perturbation on the source current is too high, the former will be chosen. In this case, any problems introducing some frequency deviation and phase variation will result in the gap between the source voltage waves and measured one. If the frequency deviates a lot, the time dependence of the measured resistances will have a big oscillation. If this oscillation is negligible, we can take it for granted. The phase variation can be measured by the 'out phase Y' which is designed in the dual PSD regime in that $X = V_{sig}cos(\theta_{sig} - \theta_{ref})$ and $Y = V_{sig}sin(\theta_{sig} - \theta_{ref})$. Ideally, X should be equal to the sample resistance and Y should be zero. If the phase variation is considerable, Y will increase and X will decrease. The ratio of X/Y increases. Usually, when this ratio is smaller than 1/10, the measurement can be trusted quantitatively. If larger, only the qualitative phenomenon can be determined. In the case of large sample resistance, bad ohmic contacts, there builds a large capacitance in the whole circuit and any problems from the source leads to measurement leads can increase the phase variation of the signal, leading to strong artefacts. Due to the cut frequency *f=1/RC*, a smaller frequency should be used so that co-axial cables and the isolation of outside conductors can effectively avoid the phase variation.

2.2.2 DC measurement

The DC measurement is conducted by the source meter and nanovoltmeter. The sourcemeter, applied as a voltage source, can measured the current with the resolution around 1nA. The nanovoltmeter, used as a voltage probe, has a relatively big noise usually containing a large offset.

This voltage offset contained in the measured values is usually removed by the current resersal.

Compared to the AC measurement locking the specifc frequency, the high-frequency noise largely affects the collected results even with the low pass filters in the instruments. To further mitigate the noise, an additional *RC* filter is usually utilized between samples and instruments.

Chapter 3 Alignment of graphene-hBN superlattice

Introduction

Graphene, first exfoliated in reference [55,56], became a groundbreaking foundation and opened various epoch-making researches. It was first exfoliated on the SiO_2, etched into the multi-terminal hall bar and lithographically contacted with the golden contacts. Later the use of hBN largely preserves the electric properties of pristine graphene[2]. As the first paper [2] reporting hBN substrate illustrated, the graphene on hBN has mobility two orders higher than that on SiO_2. With the development of the Van der Waals heterostructures, the graphene-hBN superlattice attracts much attention from researchers.

3.1 Graphene

Graphene is a gapless semiconductor that hosts quasiparticles that move relativistically with a zero effective mass and follow linear energy dispersion governed by the Dirac equation[57,58]. The conduction and valence bands are perfectly symmetrical and described by the same Dirac equation which results in the Klein tunnelling[59]. The exceptional transportability comes from the distinct crystals hybridization in which the '*s*' and '*p*' orbitals hybridize to form sp^2 orbitals with one spare p_z orbital. The sp^2 orbitals form the hexagonal lattice through the creation of covalent bonds with three neighbouring carbon atoms The spare p_z orbital forms a π bond with the neighbouring atom whose electrons propagate freely in the graphene plane. This is the origin of the exceptional conductivity property differing from the graphite counterpart.[58]
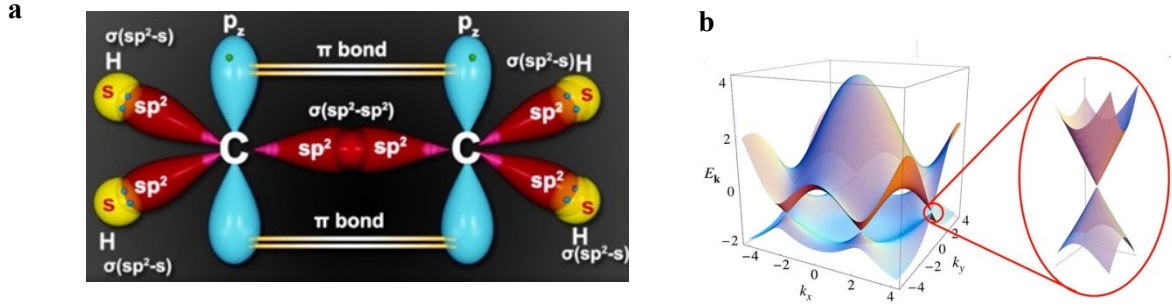
Fig.17 **a** The hybridization of graphene **b** The band structure of graphene. Graphene has a unique *sp²* hybridization with single layer atoms arranged in a 2D crystal honeycomb lattice. Electronic dispersion of this honeycomb lattice is shown in **b** with the inset of zoom-in of the bandstructure close to the Dirac point. adapted from[80]

The honeycomb structure results in the unique band structure of graphene. It contains two kinds of sublattice A and B which have quantum mechanical hopping directly resulting in the overlapping bands. They are intersected forming the Dirac point with no gap. The initial theoretical paper in 1947[60] derived this result by calculating the quantum hopping of electrons between neighbouring sites in the π bonds of the graphene lattice. Its result is shown in Fig.17.(b). This paper identified that three electrons in the *sp²* trigonal bonding do not contribute to the conduction. Only the one *$2p_z$* electron needs to be considered. By considering the hopping occurring between sublattice A and B, the tight-binding approximation gives the dispersion relationship of graphene.[60]

$$E_{\pm}(\vec{k}) = \pm\gamma\sqrt{3 + 2\cos(\sqrt{3}k_y a) + 4\cos(\sqrt{3}k_y a/2)\cos(3k_x a/2)}$$

(42)

where $\gamma = 2.8$ eV is the hopping energy between sublattices A and B which is the nearest-neighbour hopping energy. After considering the next nearest-neighbour hopping energy, the parameter γ' is introduced.

$$E_{\pm}(\vec{k}) = \pm\gamma\sqrt{3 + 2\cos(\sqrt{3}k_y a) + 4\cos(\sqrt{3}k_y a/2)\cos(3k_x a/2)} + \gamma'(2\cos(\sqrt{3}k_y a)$$
$$+ 4\cos(\sqrt{3}k_y a/2)\cos(3k_x a/2))$$

(43)

If $\gamma' = 0$, the energy spectrum will be symmetric around $E_{\pm}(\vec{k}) = 0$. If not, the electron-hole symmetry will be broken resulting in the asymmetric π and π^* bands. But the Hamiltonian near zero

will not be influenced. By expanding the Equation(43) in the energyregion close to zero, the linear dispersion is derived

$$E_{\pm}(q) = \pm v_F q \qquad (44)$$

Where q is the momentum and v_F is the Fermi velocity with a value of 10^6 m/s.[60]

In Fig.17 (b), there are six Dirac cones at which conduction bands and valence bands meet in the corners of the Brillouin zone with a linear dispersion. These six cones are classified as two different Dirac cones, K and K' points, known as Dirac points. This gives 4-fold degeneracy of graphene density of states – two valley degeneracies and two spin degeneracies.[61]

The gapless state on the Dirac point is protected by two symmetries, time-reversal symmetry and inversion symmetry. Any perturbation invariant under these two symmetries will not open the bandgap. When the sublattice equivalence is broken, the inversion symmetry is also broken. Then the bandgap is opened. The introduction of the Moire pattern by graphene-hBN superlattice is one way to do it.[61]

In contrast to graphene, hBN is a 2D material with a very wide bandgap around 6eV. Whilst it possesses a similar honeycomb structure to graphene, but the sublattice of boron and nitride is unequivalent, which destroys the sublattice symmetry. The small lattice mismatch to graphene of 1.8% is small enough to signify its role as a good substrate to impose a strain and periodic potential on graphene. Furthermore, factors such as the atomically flat surface between graphene and hBN, free the absence of defects of hBN, and the very high work function on the boundary due to hBN's significant bandgap, mean that the graphene - hBN superlattice has becomes a hotspot in heterostructure study .[2]

3.2 hBN-graphene single aligned heterostructure
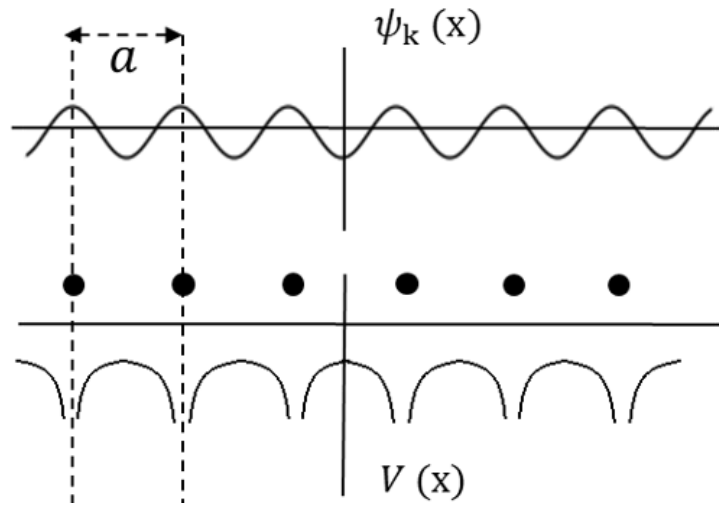
Fig.18 Schematic of a 1D linear array of ion cores evenly spaced by the distance *a*(middle solid dots) and its corresponding wavefunction ψ_k(x)and periodical potential *V*(x)   Taken from [15]

In the Section 1.1, discussing the Nearly free electron model, the energy dispersion E(k) is explained by Fig.2. This detailed explanation derives from the Bloch theorem.

The crystal lattice's influence is described by the periodic potential. The 1D cases is shown by

$$U(x) = U(x + a) \tag{45}$$

Where *a* is the period of the crystal lattice.[15]

When this is applied to the Schrodinger equation, the following wavefunction is derived

$$\psi_k(x) = e^{ik.x}u_k(x) \tag{46}$$

Where $u_k(x)$ has the periodicity same as the periodic potential and *k* is the wavenumber. Furthermore, Equation (47) indicates that the wave function in some states, k, remains the same when electrons move by one lattice distance, a, in real space.[15]

$$\psi_k (x + a) = e^{ik \cdot a}\psi_k(x) \tag{47}$$

Extending to the 2-dimensional case, the wavefunction differing by multiples of one reciprocal lattice vector is identical ψ_{k+G} (**r**) = ψ_k(**r**) where **r** is the vector describing the position of electrons. This translational symmetry determines the periodicity of the Brillouin zone. Consequently, under ideal

conditions with defect-free crystals, T=0, electrons move devoid of scattering when passing these positively charged ions. The entire energy spectrum is periodic and can be described by the first Brillouin zone, as Fig.2 (c) shows.[15]

In addition, Fig.18 and Fig.2 depict the opening of the bandgap for the Schrodinger fermions, on the edge of every Brillouin zone. For graphene, the massless Dirac fermions possess a gapless Dirac point instead. In a pristine graphene lattice, the period $2\pi/a$ is too big, and therefore, is not accessible by the gate in our transport measurement. The superlattice period caused by moiré-induced periodic potentials is adequate enough to impose a small reciprocal period within the gate modulation range. Resultantly, this interesting phenomenon around the edge of the first Brillouin zone can be explored.[5]

In this thesis, the graphene–hBN superlattice is the primary focus. The secondary Dirac point appearing on the superlattice Brillouin zone edge was first discovered during scanning tunnelling microscopy (STM) characterisation at the Fermi energy of 0.3 eV, relative to the MDP.[5,62] The zero angle alignment between graphene and hBN allows a superlattice period of 14 nm due to the 1.8% lattice mismatch; this corresponds to the secondary Dirac point at 0.2 eV and can be easily achieved by gating. Due to replication of the MDP, the R_{xx} peak and R_{xy} charge reversal appear on the second Dirac point, as shown in Fig.20 (a) and (b). Specifically, at the charge neutrality point of Fig. (a), the zero carrier density produces a sharp resistivity peak. At larger carrier concentrations, satellite peaks appear on the hole and electron side at equal distances from the MDP when the Fermi level tuned by the gate reaches the superlattice zone edge. Hall resistance reflects the type of charge carriers, and in Fig. (b), the sign reversal is also on the same secondary Dirac points. An additional sign reversal occurring before the secondary Dirac point is Van Hove singularity[64]
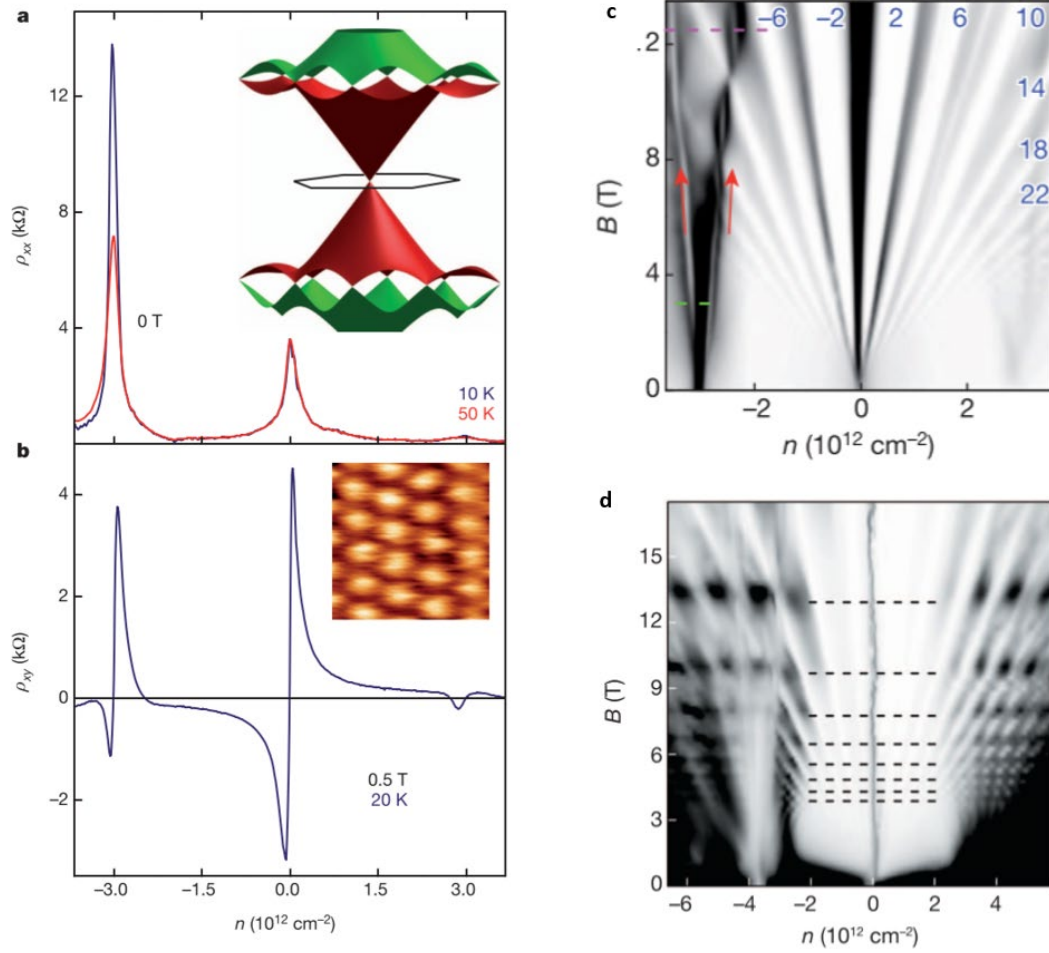
Fig.19 The transport properties of the graphene-hBN superlattice. **a** and **b:** The longitudinal resistivity ρ_{xx} and hall resistivity ρ_{xy} as a function of carrier concentration n. The secondary Dirac points on the hole side and electron side appears at the edge of the superlattice Brillouin zone depicted by the inset of **a**. c: Longitudinal resistivity, $\rho_{xx}(n, B)$ at 20K. d: Longitudinal conductivity, $\sigma_{xx}(n,B)= \rho_{xx}/(\rho_{xx}{}^2 + \rho_{xy}{}^2)$. The dashed lines indicate the indexes of Brown-Zak oscillations. Adapted from [6]

In magnetic fields, a characteristic length governs the quantum phenomena in a magnetic field; this is called the magnetic length $l_B = \sqrt{\frac{\hbar}{eB}} = \frac{26}{\sqrt{B}}$ nm. When other periods approach the magnetic length, certain interesting phenomena are likely to occur due to the interplay.

In Section 1.4, regarding SdH oscillation, the discrete Landau levels are discussed. At each Landau level, as many electrons as possible are accommodated. The degeneracy is calculated by $N = \Phi/\Phi_0$, where Φ is magnetic flux piercing the unit cell of materials, and Φ_0 is the constant flux quantum. Originating from this, Zak proposed the notion of magnetic translation[63]. The general principle was that when the magnetic field reaches certain values, such as the area enclosed by cyclotron motion

commensurate with the unit cell of lattice, translation symmetry in fields is achieved. As a result, the electrons move as if there is no magnetic field influence. These specific states occur at the magnetic fields that satisfy the condition of $\frac{\Phi}{\Phi_0} = \frac{p}{q}$, where p and q are both integers. Intuitively, this equation can be perceived as the magnetic flux of q unit cells piercing the flux quantum p times.

Following Zak's work, the theory of a self-similar fractal pattern called the Hofstadter butterfly was later developed. [64] This is a beautiful pattern that indicates interplay between magnetic length and lattice periods. Experimental progress on graphene-hBN superlattices has verified this theoretical prediction in recent years [10,9,7,8,6] The Landau fan in Fig.19 (c) and the dashed horizontal lines in Fig.18 (d) clearly show the Hofstadter butterfly and the BZ oscillations.

These exotic electronic properties predicted and observed on graphene superlattices are all based on the periodic potential that is significantly greater than the graphene lattice, as caused by the moiré pattern. Many single aligned hBN- graphene-hBN heterostructures have been measured in our research group, as depicted in the published article in Nature Physics: Excess resistivity in graphene superlattices caused by umklapp electron-electron scattering. This paper discussed the umklapp electron-electron (UEE) scattering in the graphene-hBN superlattice, whereby UEE scattering occurs easily between neighbouring superlattice Brillouin zones, which transfers electron momentum to the crystal lattice. This results in finite resistance. This regime was initially theoretically predicted and was then verified through temperature dependence experiments. This paper is significant as at room temperature, the UEE scattering becomes the dominant factor affecting mobility, which may contribute to the engineering of graphene-based devices in the future.

Paper 1 (published in Nature Physics, co-author)

My contribution: Most experimental figures were summarized from my measurements. The second author mentored me. We analyzed the transport results together.

Excess resistivity in graphene superlattices caused by umklapp electron–electron scattering

J. R. Wallbank[1], R. Krishna Kumar[1,2], M. Holwill[1,2], Z. Wang[2], G. H. Auton[1], J. Birkbeck[1,2], A. Mishchenko[1,2], L. A. Ponomarenko[3], K. Watanabe[4], T. Taniguchi[4], K. S. Novoselov[1,2], I. L. Aleiner[5], A. K. Geim[1,2] and V. I. Fal'ko[1,2]*

In electronic transport, umklapp processes play a fundamental role as the only intrinsic mechanism that allows electrons to transfer momentum to the crystal lattice and, therefore, provide a finite electrical resistance in pure metals[1,2]. However, umklapp scattering is difficult to demonstrate in experiment, as it is easily obscured by other dissipation mechanisms[1-6]. Here we show that electron–electron umklapp scattering dominates the transport properties of graphene-on-boron-nitride superlattices over a wide range of temperature and carrier density. The umklapp processes cause giant excess resistivity that rapidly increases with increasing superlattice period and are responsible for deterioration of the room-temperature mobility by more than an order of magnitude as compared to standard, non-superlattice graphene devices. The umklapp scattering exhibits a quadratic temperature dependence accompanied by a pronounced electron–hole asymmetry with the effect being much stronger for holes than electrons. In addition to being of fundamental interest, our results have direct implications for design of possible electronic devices based on heterostructures featuring superlattices.

In umklapp electron–electron (Uee) scattering, a crystal lattice gives a pair of interacting electrons a momentum kick such that

$$\mathbf{k}_1 + \mathbf{k}_2 = \mathbf{k}_3 + \mathbf{k}_4 + \mathbf{g} \qquad (1)$$

where $\hbar\mathbf{k}_{1,2}$ and $\hbar\mathbf{k}_{3,4}$ are the initial and final momenta of the two electrons near the Fermi level, respectively, and $\mathbf{g}$ is a non-zero reciprocal lattice vector of the crystal. In clean metals, normal electron–electron scattering, such that $\mathbf{g} = 0$, does not lead to a finite resistance because electron–electron collisions do not relax the momentum imparted to the electron system by the electric field (unless the charge carriers involved have the opposite polarity so that, for example, electrons scatter at thermally excited holes[7-9]). This can be understood by considering the case of head-on collisions along the direction of the electric field: if one electron is scattered backwards, the other must be scattered in the forward direction to conserve momentum, as illustrated in Fig. 1a (left) for Dirac electrons in one of the graphene valleys. In contrast, in umklapp processes (Fig. 1a, right), both electrons near the Fermi level can be scattered in the backward direction with the Bragg momentum, $\hbar\mathbf{g}$, transferred to the lattice. This behaviour originates from the peculiar nature of electrons in periodic potentials, whose momentum is conserved only up to one reciprocal lattice vector ($\hbar\mathbf{g}$).

Although recent theories predict a dominant role of Uee scattering in some classes of conductors[10,11], experimental evidence has so far been reported only for a few ultraclean metals[1,2] and in laterally modulated two-dimensional (2D) electron gases in GaAs/AlGaAs quantum wells[3-6]. In both cases, the umklapp contribution was relatively small and noticeable only at $T < 15\,\mathrm{K}$, being dwarfed by other thermal processes at higher T. In this report, we show both theoretically and experimentally that, in graphene moiré superlattices, Uee scattering dominates T-dependent resistivity over a wide range of carrier densities, n (a representative miniband[12-14] for Dirac electrons in graphene superlattices is shown in Fig. 1a, right).

The devices we studied (inset of Fig. 1b) were fabricated using standard methods for assembling encapsulated graphene/hexagonal boron nitride (hBN) heterostructures (see Methods) where a superlattice was engineered by aligning graphene with an hBN substrate. This produces a moiré pattern[15] due to the small lattice mismatch ($\delta \approx 1.8\%$) between the two crystals (inset of Fig. 1c), which in turn creates a superlattice potential with a period of around 15 nm for perfect alignment. The superlattice potential acts on charge carriers in the graphene and causes significant reconstruction of the electronic spectrum. In particular, a mini-Brillouin zone is created around the Dirac points of graphene[13,14], whose size is determined by the misalignment angle, θ, and resulting moiré period, λ. As the Brillouin zone is small compared to normal metals, Uee scattering becomes dominant in graphene/hBN superlattices. We present our results referring to 6 superlattice devices and, for comparison, a reference device in which the graphene and hBN axes were intentionally misaligned ($\theta > 15°$; $\lambda < 3\,\mathrm{nm}$). For aligned samples, λ was determined from the frequency of Brown–Zak oscillations using magnetotransport measurements[16] (Supplementary Section 1). At low T and small n, all of our devices exhibited high mobilities of up to 500,000 $\mathrm{cm^2\,V\,s^{-1}}$.

Figure 1b plots the resistivity ρ_{xx} as a function of doping (n) for 2 of our graphene devices at 10 K (solid lines) and 200 K (dashed). One of them is the reference, non-aligned sample (orange curves) whilst the other has a misalignment angle close to 0° and $\lambda \approx 15\,\mathrm{nm}$ (green). At low T, both devices exhibit comparable values of ρ_{xx} for small n, with sharp peaks at zero doping and the resistivity that drops off rapidly with increasing n for both electrons and holes (positive and negative n, respectively). The measured ρ_{xx} are rather similar except for additional satellite peaks that occur in the superlattice at $n = \pm n_0 = 8/\sqrt{3}\lambda^2$ because of secondary Dirac points located at the edges of the superlattice Brillouin zone. At 200 K, however, the two devices exhibit remarkably different behaviour even for $|n| < |n_0|$.

[1]National Graphene Institute, University of Manchester, Manchester, UK. [2]School of Physics & Astronomy, University of Manchester, Manchester, UK. [3]Department of Physics, Lancaster University, Lancaster, UK. [4]National Institute for Materials Science, Tsukuba, Japan. [5]Physics Department, Columbia University, New York, NY, USA. *e-mail: vladimir.falko@manchester.ac.uk
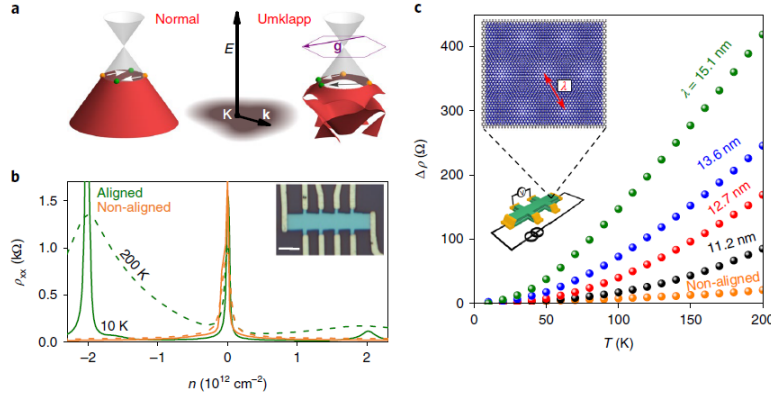
Fig. 1 | Umklapp scattering and excess resistivity in graphene superlattices. a, Normal electron–electron scattering for, for example, holes in graphene does not lead to resistivity (left), in contrast to the umklapp scattering for holes in a graphene superlattice (right). Here we also illustrate the superlattice Brillouin zone (purple hexagon) and superlattice minibands in the valence band of graphene. **b**, Longitudinal resistivity for non-aligned (orange) and aligned (green) graphene/hBN devices. Solid curves: low $T=10$ K. Dashed: 200 K. Inset: optical image of the superlattice device in **b**. Scale bar, 5 μm. **c**, T-dependent resistivity, $\Delta\rho$, at a fixed $n=-1\times10^{12}$ cm^{-2} for four superlattice devices and the non-aligned device (orange symbols). Error bars are smaller than the data points. Inset: device schematic and measurement scheme. The top illustration is a moiré pattern arising from 1.8% lattice mismatch in aligned graphene (blue) and hBN (grey) crystals.

In non-aligned graphene, the resistivity at 200 K is only marginally larger than that at 10 K. This weak T dependence stems from the low electron–phonon coupling intrinsic to the stiff atomic lattice of the graphene. In stark contrast, the superlattice device exhibits a huge increase in ρ_{xx}, which is accompanied by a pronounced electron–hole asymmetry. Such a behaviour cannot be attributed to electron scattering on thermally activated holes[7–9] because the effect is much stronger for doping away from the main Dirac point where the Fermi energy $\varepsilon_F > k_B T$ and the system behaves as a metal rather than a gapless semiconductor. To compare devices with different electronic quality, we analysed the T-dependent part of resistivity, $\Delta\rho$, by subtracting ρ_{xx} at the base T of 10 K from the measured data: $\Delta\rho = \rho_{xx}(T) - \rho_{xx}(10$ K). We have chosen 10 K to avoid an obscuring contribution from mesoscopic fluctuations at lower T. Figure 1c plots $\Delta\rho(T)$ for the studied devices at a fixed density of holes. There is a huge excess resistivity in the graphene superlattice that grows rapidly with the moiré period. As shown below, this behaviour can accurately be described by a dominant contribution from Uee scattering.

Figure 2a details our observations by plotting ρ_{xx} as a function of n (normalized by n_0) for four superlattice devices, focusing on the doping level $0.2n_0 < |n| < 0.7n_0$, away from the Dirac points, miniband edges and van Hove singularities. In this range of n, the reconstruction of the Dirac spectrum is weak and thermal excitations of carriers with the opposite sign of effective mass can be neglected[9]. The solid and dashed lines in Fig. 2a represent ρ_{xx} at 10 K and 100 K, respectively, whereas the coloured shaded areas emphasize changes in resistivity. Notably, the electron–hole asymmetry increases with n and, also, becomes more pronounced with increasing λ. Such asymmetry is absent in our reference graphene at any T. To emphasize this observation, Fig. 1c plots $\Delta\rho(100$ K) for these superlattice devices.

To explain this behaviour, we model Uee scattering for Dirac electrons in either the conduction ($s = +$) or valence ($s = -$) band of graphene using perturbation theory in both the electron–electron Coulomb interaction and moiré superlattice potential. The use of this approach is justified by considering that, in the range of densities $0.2n_0 < |n| < 0.6n_0$, the superlattice inflicts only a weak change on the Dirac spectrum and the Dirac velocity[13] as, for example, shown previously in angle-resolved photoemission studies

of graphene/hBN heterostructures[17,18]. In the perturbative approach, one can envisage an Uee process as a scattering event in which one of the electrons scatters into a state on the opposite side of the Fermi circle, whereas the other goes into an intermediate state with a much larger momentum (and therefore off the energy shell) and then is returned back to the Fermi line by Bragg scattering off the superlattice. The overall amplitude of such a process is accounted for by four Feynman diagrams, in which Bragg scattering can occur either before or after an electron–electron collision and involves either the first or second electron,

$$M_{ss'}^{\mathbf{g}_m} = M_{ss'}^{\mathbf{g}_m}(\mathbf{k}_1,\mathbf{k}_2,\mathbf{k}_3,\mathbf{k}_4) + M_{ss'}^{-\mathbf{g}_m*}(\mathbf{k}_3,\mathbf{k}_4,\mathbf{k}_1,\mathbf{k}_2) + M_{ss'}^{\mathbf{g}_m}(\mathbf{k}_2,\mathbf{k}_1,\mathbf{k}_4,\mathbf{k}_3) + M_{ss'}^{-\mathbf{g}_m*}(\mathbf{k}_4,\mathbf{k}_3,\mathbf{k}_2,\mathbf{k}_1)$$

$$M_{ss'}^{\mathbf{g}_m}(\mathbf{k}_1,\mathbf{k}_2,\mathbf{k}_3,\mathbf{k}_4) = \quad (2)$$

Here 〰 stands for the screened Coulomb interaction, ■ stands for the superlattice perturbation leading to Bragg scattering with momentum transfer $\hbar\mathbf{g}$ and ─── $= (\varepsilon - s'v|\mathbf{k}_1 + \mathbf{g}_m|)^{-1}$ describes the electronic propagator of the intermediate virtual state, where v is the Dirac velocity in graphene and $s' = \pm$ refers to the conduction and valence band, respectively. To account for the superlattice scattering, we employ the previously developed model[13,14] to describe electron scattering with the shortest six moiré superlattice reciprocal lattice vectors,

$$\mathbf{g}_{m=0,\cdots 5} = \left(-\sin\left[\phi + \frac{\pi m}{3}\right], \cos\left[\phi + \frac{\pi m}{3}\right]\right)g, \quad \text{where} \quad g = \frac{4\pi}{\sqrt{3}\lambda} \quad \text{and}$$

$$\phi = \arctan\left[\frac{\sin}{\delta + 1 - \cos}\right].$$

Hence, for the first diagram in equation (2), the intermediate state has a wavevector $\mathbf{p} = \mathbf{k}_1 + \mathbf{g}_m$, and the matrix element for superlattice scattering is

$$\blacksquare \equiv W(\mathbf{g}_m) = \frac{1}{2}\left[U_0 h_+ + i(-1)^m U_3 h_- + (-1)^m U_1 h_1\right] \quad (3)$$
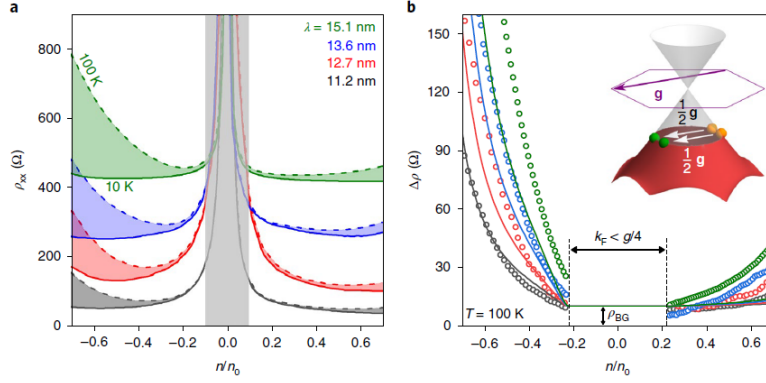
Fig. 2 | Electron–electron scattering and its electron–hole asymmetry in graphene superlattices. a, Resistivity for different λ (colour-coded) as a function of density n. Their n_0 were between 2 and 3.7×10^{12} cm^{-2}. Solid curves: 10 K. Dashed: 100 K. The curves for $\lambda = 13.6$ and 15.1 nm are offset for clarity by 200 and 400 ohm, respectively. The coloured shaded areas emphasize the T-dependent parts of ρ_{xx} for different λ. Data close to the neutrality points $n = 0$ and $\pm n_0$ are omitted (grey shading) because they exhibit activated behaviour of little interest for this study. **b**, Open circles show experimental $\Delta\rho(T)$ (same colour coding as in **a**). The error bars are smaller than the symbols. Solid curves: calculated Uee contribution. Note that a small density-independent offset of $\rho_{BG} = 10$ has been added to the theoretical curves to account for the resistivity generated by scattering at acoustic phonons in the Bloch–Grüneisen regime[19,24,25] . The inset depicts an umklapp process for the threshold density n_c such that $k_F = g/4$ where the momentum transferred to the superlattice corresponds to the exact backscattering of a pair of electrons (orange and green balls).

with $h_\pm = 1 \pm ss' e^{i(\vartheta_{k_1} - \vartheta_{p'})}$ and $h_1 = s e^{i\left(\vartheta_{k_1} - \frac{\pi m}{3}\right)} + s' e^{i\left(\frac{\pi m}{3} - \vartheta_{p'}\right)}$, determined by the chirality of the electron states and the sublattice structure of the superlattice Hamiltonian[13,14] (ϑ_k is the angle between $\mathbf{k}$ and the x axis) and U_i are the phenomenological parameters controlling the superlattice potentials. We use $U_0 = 8.5$ meV, $U_1 = -17$ meV and $U_3 = -14.7$ meV, which were determined from the previous independent study of transverse magnetic focusing in graphene/hBN superlattices[12].

For the Coulomb interaction in the first diagram of equation (2),

$$\equiv V(\mathbf{g}_m) = \frac{1 + ss' e^{i(\vartheta_{p'} - \vartheta_{k_3})}}{2} \frac{2\pi e^2/\kappa}{|\mathbf{k}_2 - \mathbf{k}_4| + q_{TF}} \frac{1 + ss' e^{i(\vartheta_{k_2} - \vartheta_{k_4})}}{2} \quad (4)$$

we use[19,20] with the Thomas–Fermi wavevector $q_{TF} = \frac{4e^2 k_F}{\nu\kappa}$, and the dielectric constant of hBN, $\kappa \approx 3.2$. Then, the first diagram in equation (2) is given by

$$M_{ss'}^{g_m}(\mathbf{k}_1, \mathbf{k}_2, \mathbf{k}_3, \mathbf{k}_4) = \frac{W(\mathbf{g}_m) V(\mathbf{g}_m)}{s\nu|\mathbf{k}_1| - s'\nu|\mathbf{p'}|}$$

To determine the Uee contribution to resistivity, ρ_{Uee}, we use the Boltzmann transport theory[21] assuming the thermal energy $k_B T < \epsilon_F$ (Supplementary Section 2), which yields the tensor with $\alpha, \beta = x, y$.

$$\rho_{Uee}^{\alpha\beta} = \frac{h}{e^2} \frac{(k_B T)^2}{24\pi^2 \nu^4 k_F^2} \sum_{m=0,\cdots,5} g_m^\alpha g_m^\beta \int |\sum_{s'=\pm} M_{ss'}^{g_m}|^2 \frac{d\vartheta_{k_1} d\vartheta_{k_3}}{|\sin\vartheta_{24}|} \quad (5)$$

This expression was derived using the approximation $\mathbf{k}_i \approx k_F(\cos[\vartheta_{k_i}], \sin[\vartheta_{k_i}])$, where k_i are related by equation (1), and the scattering angle ϑ_{24} is such that

$$\cos(\vartheta_{24})$$
$$= \cos(\vartheta_{k_1} - \vartheta_{k_3})$$
$$- \frac{g}{k_F}\left(\frac{g}{2k_F} + \sin\left(\vartheta_{k_1} - \phi - \frac{\pi m}{3}\right) - \sin\left(\vartheta_{k_3} - \phi - \frac{\pi m}{3}\right)\right)$$

As a result of the three-fold rotational symmetry of graphene superlattices, the resistivity tensor is isotropic, that is, $\rho_{Uee}^{\alpha\beta} = \rho_{Uee} \delta^{\alpha\beta}$. We note that Uee scattering can occur only above the threshold $k_F > g/4$ (inset of Fig. 2b), which arises from the fact that all scattering states must be in the vicinity of the Fermi level, $k_i \approx k_F$ in equation (1) and yields the critical density $n_c = n_0 \pi/8\sqrt{3} \approx 0.227 n_0$ below which Uee scattering is not allowed.

Using the superlattice parameters U_i stated above, we calculated ρ_{Uee} for the specific experimental parameters in Fig. 2a. The results (solid curves in Fig. 2b) are in good agreement with the experiment, which is particularly impressive considering that no additional fitting parameters were used. Note that the deviations between the experiment and theory for electron doping in Fig. 2b are mostly due to a limited accuracy of our analytical method as the full numerical analysis shows (see Supplementary Fig. 5a). Furthermore, the analytical theory, equation (5), suggests that close to the threshold density $\rho_{Uee} \propto (|n| - n_c)^{3/2}$, which stems from the interplay between the size of the phase space available for Uee scattering and the 'chirality factor' (for example, $(1 + e^{i(\vartheta_{k_2} - \vartheta_{k_4})})/2$ in equation (4)) which suppresses the amplitude of backscattering[22]. The large asymmetry between ρ_{Uee} for electrons and holes arises from the fact that kinematic constraints dictate that the electron Bragg scattering by the superlattice must be almost backscattered (inset of Fig. 2b). The probability for such backscattering,

$$P \sim |U_1 - sU_3|^2 \quad (6)$$

is much higher in the valence band ($s = -1$) than the conduction band ($s = 1$) for the given U_1 and U_3 used in equation (3) so that the Uee process is much more effective for hole rather than electron doping. Note that this feature of Uee distinguishes itself from other scattering mechanisms including the potential disorder in the moiré superlattice[23], which results in almost electron–hole symmetric ρ_{xx} within the density range $-0.7 n_0 < n < 0.7 n_0$.

Our analysis predicts two further signatures of Uee scattering. First, for a given $|n| > n_c$, the efficiency of umklapp processes depends on λ such that $\rho_{Uee} \propto \lambda^4$. This behaviour is governed entirely
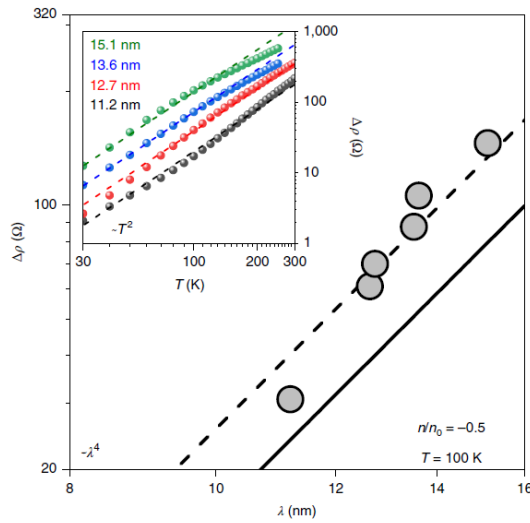
Fig. 3 | Characteristics of umklapp electron–electron scattering. The temperature-dependent part of the resistivity as a function of the moiré period for $n = -0.5n_0$ in all of our six superlattice devices. The circles are experimental data; the dashed line is the best fit of a λ^4 dependence to the data; and the solid line is the calculated Uee contribution to the resistivity (also proportional to λ^4). Inset: symbols are experimental data for the superlattice devices (colour-coded). The dashed lines are T^2 fits to the experimental data. Logarithmic scales are used in both the main plot and the inset. Standard deviations in our measurements are smaller than all of the symbols.

by the U_{ee} matrix element ($M_{ss''}^{g_m}$) and can be understood by counting the number of Bragg vector factors ($g \propto \lambda^{-1}$) that appear in equations (3)–(5), recalling that momenta k_F, $|\mathbf{k}_i|$ and $|\mathbf{p}|$ scale linearly with g for a fixed n/n_0. Figure 3 shows that the λ^4 dependence describes well the experimentally observed behaviour of $\Delta\rho$. This unusually strong dependence is one of the reasons why misaligned devices with small superlattice periods do not exhibit any discernible umklapp resistivity. Second, equation (5) yields a quadratic temperature dependence typical for electron–electron scattering in the Fermi liquid theory, $\rho_{Uee} \propto T^2$, in agreement with the experimental behaviour plotted in the inset of Fig. 3. The T^2 behaviour holds over a wide T range for all of our superlattice devices, showing the dominance of Uee scattering. However, at high $T > 150\,\text{K}$, one can see some deviations from the T^2 dependence. We attribute those to the thermal excitation of carriers with the opposite sign of effective mass, resulting in deviations of resistivity from the values described by equation (5). Indeed, these deviations become stronger as we approach either the main Dirac point ($|n| < 0.3n_0$) or van Hove singularities[13] ($|n| > 0.6n_0$) where scattering at thermally excited carriers of the opposite polarity starts playing a role.

Finally, we analysed the normal and umklapp (due to the moiré superlattice) scattering of electrons at acoustic phonons in graphene. The normal electron–phonon scattering, studied in detail previously[19,24,25], can result in approximately a $10\,\Omega$ contribution for the relevant n at $100\,\text{K}$ (the value used as an offset in Fig. 2b) and up to $30\,\Omega$ at $300\,\text{K}$. An additional scattering from phonons in the hBN may also contribute to the deviations. This is discussed in Supplementary Section 2C–E, where we consider a possibility that electrons scatter off acoustic phonons in graphene and hBN by transferring additional momentum $\hbar\mathbf{g}$ to the

moiré superlattice (Supplementary Fig. 5c). When analysing such processes, we took into account the intrinsic electron–phonon coupling (deformation potential) in graphene, piezoelectric coupling with deformations in hBN and dynamical variations of the moiré potential due to a mutual displacement of graphene and hBN, which are caused by vibrations of the two crystals. We find that the calculated phonon-induced umklapp resistivity is much smaller and has different dependences on T and λ, as compared to those caused by Uee scattering and observed experimentally (Supplementary Fig. 5).

To conclude, Uee scattering in long-period moiré superlattices degrades the intrinsic high-T mobility of graphene's charge carriers. This limits the potential applications of epitaxial grown graphene/hBN heterostructures[26], which are inherently aligned, for room-temperature high-mobility devices. To achieve high carrier mobility at room temperature, the 2D crystals that form the heterostructure should be misaligned. We expect that Uee scattering should strongly influence electron transport in twisted graphene bilayers, where superlattice effects have also been predicted[27,28] and recently observed[29–33].

Online content

Any methods, additional references, Nature Research reporting summaries, source data, statements of data availability and associated accession codes are available at https://doi.org/10.1038/s41567-018-0278-6.

References

1. Bass, J., Pratt, W. P. & Schroeder, P. A. The temperature-dependent electrical resistivities of the alkali metals. *Rev. Mod. Phys.* **62**, 645–744 (1990).
2. Gasparov, V. A. & Huguenin, R. Electron–phonon, electron–electron and electron–surface scattering in metals from ballistic effects. *Adv. Phys.* **42**, 393–521 (1993).
3. Messica, A. et al. Suppression of conductance in surface superlattices by temperature and electric field. *Phys. Rev. Lett.* **78**, 705–708 (1997).
4. Overend, N. et al. Giant magnetoresistance and possible miniband effects in periodic magnetic fields. *Physica B* **249–251**, 326–329 (1998).
5. Kato, M., Endo, A., Katsumoto, S. & Iye, Y. Two-dimensional electron gas under a spatially modulated magnetic field: A test ground for electron–electron scattering in a controlled environment. *Phys. Rev. B* **58**, 4876–4881 (1998).
6. Kato, M., Endo, A., Sakairi, M., Katsumoto, S. & Iye, Y. Electron–electron Umklapp process in two-dimensional electron gas under a spatially alternating magnetic field. *J. Phys. Soc. Jpn* **68**, 1492–1495 (1999).
7. Kashuba, A. B. Conductivity of defectless graphene. *Phys. Rev. B* **78**, 085415 (2008).
8. Fritz, L., Schmalian, J., Müller, M. & Sachdev, S. Quantum critical transport in clean graphene. *Phys. Rev. B* **78**, 085416 (2008).
9. Nam, Y., Ki, Dong-Keun, K., Soler-Delgado, D. & Morpurgo, A. F. Electron–hole collision limited transport in charge-neutral bilayer graphene. *Nat. Phys.* **13**, 1207–1214 (2017).
10. Rice, T. M., Robinson, N. J. & Tsvelik, A. M. Umklapp scattering as the origin of T-linear resistivity in the normal state of high-T_c cuprate superconductors. *Phys. Rev. B* **96**, 220502 (2017).
11. Aleiner, I. L. & Agam, O. Saturation of strong electron–electron umklapp scattering at high temperature. *Ann. Phys.* **385**, 716–728 (2017).
12. Lee, M. et al. Ballistic miniband conduction in a graphene superlattice. *Science* **353**, 1526–1529 (2016).
13. Wallbank, J. R., Patel, A. A., Mucha-Kruczyński, M., Geim, A. K. & Fal'ko, V. I. Generic miniband structure of graphene on a hexagonal substrate. *Phys. Rev. B* **87**, 245408 (2013).
14. Wallbank, J. R., Mucha-Kruczyński, M., Xi, C. & I., F. V. Moiré superlattice effects in graphene/boron-nitride van der Waals heterostructures. *Ann. Phys.* **527**, 359–376 (2015).
15. Yankowitz, M. et al. Emergence of superlattice Dirac points in graphene on hexagonal boron nitride. *Nat. Phys.* **8**, 382–386 (2012).
16. Krishna Kumar, R. et al. High-temperature quantum oscillations caused by recurring Bloch states in graphene superlattices. *Science* **357**, 181–184 (2017).
17. Wang, E. et al. Gaps induced by inversion symmetry breaking and second-generation Dirac cones in graphene/hexagonal boron nitride. *Nat. Phys.* **12**, 1111–1115 (2016).

18. Wang, E. et al. Electronic structure of transferred graphene/h-BN van der Waals heterostructures with nonzero stacking angles by nano-ARPES. *J. Phys. Condens. Matter* **28**, 444002 (2016).
19. Hwang, E. H. & Das Sarma, S. Acoustic phonon scattering limited carrier mobility in two-dimensional extrinsic graphene. *Phys. Rev. B* **77**, 115449 (2008).
20. Hwang, E. H. & Das Sarma, S. Dielectric function, screening, and plasmons in two-dimensional graphene. *Phys. Rev. B* **75**, 205418 (2007).
21. Ziman, J. M. *Electrons And Phonons: The Theory of Transport Phenomena in Solids* Sec. 9.14 (Oxford Univ. Press, Oxford, 1960).
22. Castro Neto, A. H., Guinea, F., Peres, N. M. R., Novoselov, K. S. & Geim, A. K. The electronic properties of graphene. *Rev. Mod. Phys.* **81**, 109–162 (2009).
23. DaSilva, A. M., Jung, J., Adam, S. & MacDonald, A. H. Transport and particle–hole asymmetry in graphene on boron nitride. *Phys. Rev. B* **91**, 245422 (2015).
24. Chen, J.-H., Jang, C., Xiao, S., Ishigami, M. & Fuhrer, M. S. Intrinsic and extrinsic performance limits of graphene devices on SiO_2. *Nat. Nanotech.* **3**, 206–209 (2008).
25. Wang, L. et al. One-dimensional electrical contact to a two-dimensional material. *Science* **342**, 614–617 (2013).
26. Yang, W. et al. Epitaxial growth of single-domain graphene on hexagonal boron nitride. *Nat. Mater.* **12**, 792–797 (2013).
27. Lopes dos Santos, J. M. B., Peres, N. M. R. & Castro Neto, A. H. Graphene bilayer with a twist: electronic structure. *Phys. Rev. Lett.* **99**, 256802 (2007).
28. Bistritzer, R. & MacDonald, A. H. Transport between twisted graphene layers. *Phys. Rev. B* **81**, 245412 (2010).
29. Li, G. et al. Observation of Van Hove singularities in twisted graphene layers. *Nat. Phys.* **6**, 109–113 (2010).
30. Kim, K. et al. Tunable moiré bands and strong correlations in small-twist-angle bilayer graphene. *Proc. Natl Acad. Sci. USA* **114**, 3364–3369 (2017).
31. Sanchez-Yamagishi, J. D. et al. Quantum Hall effect, screening, and layer-polarized insulating states in twisted bilayer graphene. *Phys. Rev. Lett.* **108**, 076601 (2012).
32. Rode, J. C., Smirnov, D., Schmidt, H. & Haug, R. J. Berry phase transition in twisted bilayer graphene. *2D Mater.* **3**, 035005 (2016).
33. Cao, Y. et al. Unconventional superconductivity in magic-angle graphene superlattices. *Nature* **556**, 43–50 (2018).

Acknowledgements

Author contributions

This study was consummated by J.R.W., V.I.F. and A.K.G.; J.R.W, I.L.A and V.I.F. have developed theory for the studied effect. hBN was provided by T.T. and K.W. The devices were fabricated by M.H., G.H.A. and J.B. Transport measurements were performed by R.K.K., Z.W. and A.M. under the supervision of K.S.N., L.A.P. and A.K.G. All authors have contributed to the discussions of results. The manuscript was written by J.R.W, R.K.K., V.I.F. and A.K.G.

Competing interests

The authors declare no competing interests.

Additional information

3.3 hBN-graphene-hBN double aligned heterostructure

When the single aligned hBN-graphene-hBN heterostructure is fabricated, one side of hBN is intentionally misaligned by 15 degrees. This study attempted to align both sides of hBN to graphene to create double aligned samples, as this would result in one more degree of freedom. This structure initiated the progress of three layer-aligned heterostructures. In the below paper, the band structure showed the double moiré pattern phenomena, as well as the signatures of a differential supermoiré resulting from the interaction between two moiré patterns. The signatures include multiple R_{xx} peaks, R_{xy} sign reversals, sets of Landau fan, and multiple fundamental frequencies corresponding to BZ oscillations. In terms of atomic force microscopy (AFM) and Raman spectroscopy, a double hexagonal pattern in the Fourier transform of AFM and broadened full width at half maximum were observed.

Paper 2 (published in Science Advance, first author)

My contribution: The main person who performed all transport measurements, analyzed and understood the data, cooperated with the theorists, participated in the manuscript writing and replied to the editor's review.

Composite super-moiré lattices in double aligned graphene heterostructures

Authors: Zihao Wang[1]*, Yi Bo Wang[1]*, J. Yin[1], Y. Yang[2], L. Lin[2], M. Holwill[2], J. Birkbeck[2], D. J. Perello[2], S. Xu[2], J. Zultak[2], R. V. Gorbachev[1,2,3], A. V. Kretinin[2,4], T. Taniguchi[5], K. Watanabe[5], S. V. Morozov[6], M. Anđelković[7], S. Milovanović[7], L. Covaci[7], F.M. Peeters[7], A. Mishchenko[1,2], A. K. Geim[1,2], K. S. Novoselov[1,2], V. I. Fal'ko[1,2,3], A. Knothe[2]†, C. R. Woods[1,2]†

* These authors contributed equally.

† Corresponding Author (CRW: colin.woods@manchester.ac.uk, AK: angelika.knothe@googlemail.com)

Affiliations:

[1]School of Physics and Astronomy, University of Manchester, Oxford Road, Manchester, M13 9PL, UK

[2]National Graphene Institute, University of Manchester, Oxford Road, Manchester, M13 9PL, UK

[3]Henry Royce Institute for Advanced Materials, Oxford Road, Manchester, M13 9PL, UK

[4]School of Materials, University of Manchester, Oxford Road, Manchester, M13 9PL, UK

[5]National Institute for Materials Science, 1-1 Namiki, Tsukuba, 305-0044, Japan

[6]Institute of Microelectronics Technology RAS, Chernogolovka 142432, Russia

[7]Department of Physics, University of Antwerp, Groenenborgerlaan 171, Antwerp, Belgium

Abstract: When two-dimensional atomic crystals are brought into a close proximity to form a van der Waals heterostructure, neighbouring crystals can start influencing each other's electronic properties. Of particular interest is the situation when the periodicity of the two crystals closely match and a moiré pattern forms, which results in specific electron scattering, reconstruction of electronic and

excitonic spectra, crystal reconstruction, and many other effects. Thus, formation of moiré patterns is a viable tool of controlling the electronic properties of 2D materials. At the same time, the difference in the interatomic distances for the two crystals combined, determines the range in which the electronic spectrum is reconstructed, and thus is a barrier to the low energy regime. Here we present a way which allows spectrum reconstruction at arbitrary energies. By using graphene which is aligned simultaneously to two hexagonal boron nitride layers, one can make electrons scatter in the differential moiré pattern, which can have arbitrarily large wavevector and, thus results in spectrum reconstruction at arbitrary low energies. We demonstrate that the strength of such a potential relies crucially on the atomic reconstruction of graphene within the differential moiré super-cell. Such structures offer further opportunity in tuning the electronic spectra of two-dimensional materials.

Main Text:

Van der Waals heterostructures allow combining different two-dimensional (2D) materials into functional stacks(*1, 2*), which has already produced a range of interesting electronic(*3, 4*) and optoelectronic(*5-8*) devices and resulted in the observation of exciting physical phenomena. The large variety of the heterostructures is mainly due to the large selection of 2D materials. However, the assembly of van der Walls heterostructures allow one extra degree of freedom: apart from the selection of the sequence of the 2D crystals – the individual crystals can be differently oriented with respect to each other. Previously such control over the rotational alignment between crystals resulted in the observation of the resonant tunnelling(*9-11*), a renormalisation of exciton binding energy(*12*) insulating(*13*) and superconducting(*14*) states.

Probably one of the most spectacular results of the rotational alignment between different 2D crystals is the observation of the band-reconstruction due to electron scattering on the moiré pattern in graphene aligned with hexagonal boron nitride (hBN). Because the lattice constants of graphene and hBN are relatively close to each other, the alignment between the two crystals leads to the formation of a moiré pattern(*15, 16*) with relatively small wavevector, which results in the appearance of the secondary Dirac points(*17-19*) in the electronic spectrum. Furthermore, the strong van der Waals interaction also leads to the atomic reconstruction of the graphene lattice(*20-23*). Unfortunately the characteristic energies at which the electronic spectrum can be reconstructed are

given by the difference between the lattice constants of graphene and hBN, which doesn't allow changes to be made to the low energy part of the spectrum.

Here, we demonstrate how we can gain further control over the band reconstruction of graphene by utilising the differential between two moiré patterns (super-moiré) created by top and bottom hBN in hBN/graphene/hBN heterostructures. Such super-moiré patterns are not related to the difference in the lattice constants between the two crystals and thus can be of any arbitrary wavenumber, which makes it possible to arrange the spectrum reconstruction at arbitrary low energies.

To this end we created encapsulated graphene devices where the graphene layer was aligned to both bottom and top hBN layers (alignment angles θ^α and θ^β). The fabrication and transfer procedures have been previously described in (*24*) with the exception that not only the bottom but also the top hBN is now crystallographically aligned to the graphene. In brief, we started by identifying the top-hBN layer on SiO$_2$. We then use a thin film of PPC on PDMS to lift the hBN from its substrate. This film then facilitates bringing the top-hBN into contact with a graphene crystal, Fig. 1a,b. We use very long and straight edges of the crystals to identify crystallographic axes and align them using a commercially available transfer rig(*25*). The graphene can then be lifted away from its substrate, Fig. 1b. At this point, we perform atomic force microscopy(*15, 16, 20*) and Raman spectroscopy(*26*) experiments on the hBN/graphene bilayer to confirm the alignment. One such AFM image is presented in Fig. 1e, clearly showing the characteristic hexagonal pattern (the Fourier transformation is shown in Fig. 1h). The crystals are then aligned and brought into contact with a second thin hBN-layer (typically less than 1.5 nm or 5 atomic layers thick), Fig. 1b. This layer is also lifted away from its substrate leaving a triple layer on the thin polymer film, Fig. 1c. We then perform AFM and Raman characterisation again. Fig. 1f and Fig. 1i are an example of one of our double-aligned moiré AFM images and its Fourier transformation for the case of the second hBN layer being 1 atomic layer thick, which allows one to see both moiré patterns simultaneously. Although not immediately clear in the real-space image, the Fourier transformation clearly shows two sets of peaks corresponding to two hexagonal patterns (red and green dashed hexagons), as also schematically shown on Fig. 1d. The triple layer is then misaligned (~15°) and placed on top of a thick substrate-hBN (Fig. 1c). Finally, we use standard lithographic techniques to create the hall-bar geometry.
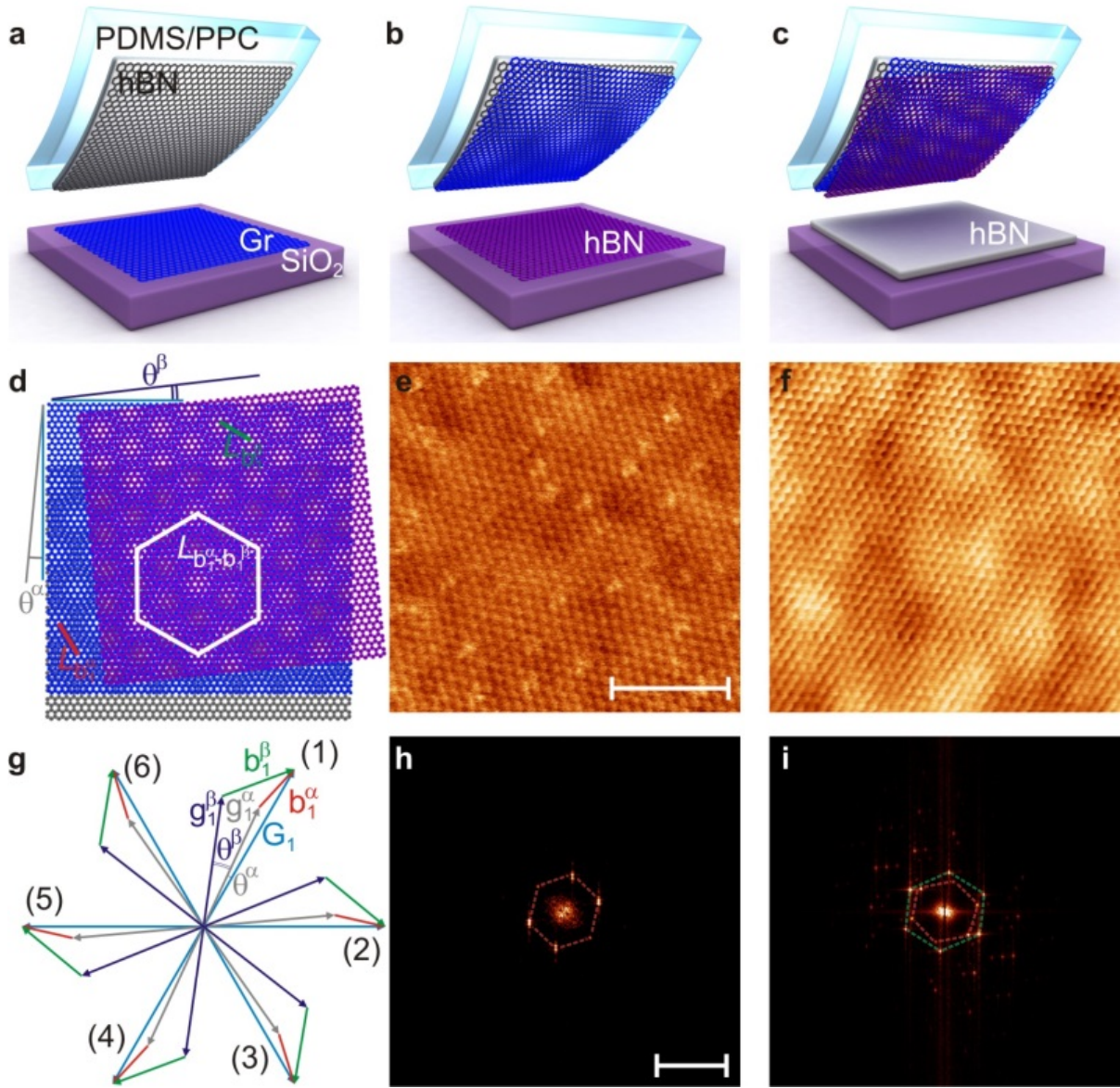
Fig. 1: Device fabrication and characterisation. *a Step (1) A thick hBN layer is aligned and used to pick up graphene. b Step (2) a thin-hBN layer is aligned and picked up forming a triple layer. c Step (3) The heterostructure is placed on top of a thick-hBN layer at 15° rotation angle (The substrate). d Illustration of the two individual moiré patterns and super-moiré pattern for three overlapping hexagonal lattices. e AFM image of the moiré pattern after the graphene is picked up. This shows only one moiré periodicity. f AFM image of the moiré patterns after the second thin-hBN is picked up. Here periodicities due to both hBN layers are visible. g Reciprocal space image of graphene's first Brillouin zone. G_1 (blue), g_1^{α}(grey), and g_1^{β} (purple) are the reciprocal lattice vectors for graphene and the α and β hBN layers, respectively. α and β are at angles θ^{α} and θ^{β} relative to graphene. b_1^{β} (green) is the moiré between graphene and the β hBN. b_1^{α} (red) is the moiré between graphene and the α hBN. h Fourier transformation of the image in e, displaying only one hexagonal periodic pattern (red dashed hexagon). i Fourier transformation of the image in f, showing two sets of distinct hexagonal patterns (red and green dashed hexagons). The scale bar in e is 100nm (f shares this scale). The scale bar in h is 0.2nm^{-1} (i shares this scale).*

The longitudinal resistance (R_{xx}) as a function of carrier concentration is presented on Fig. 2a. Here, apart from the resistance peak associated with the main Dirac point(27), several additional peaks can be seen. Most of such peaks correspond to the change of sign of the transversal (Hall) resistance (R_{xy}) measured in non-quantised magnetic field, Fig. 2b. Typically, if graphene is aligned with only one hBN, a single moiré pattern is produced, and only one secondary Dirac point for electrons and one for holes can be seen at concentrations which correspond to the wavevector determined by the periodicity of the moiré pattern(15-19). Aligning graphene to both the top and the bottom hBN will produce two moiré patterns (if θ^{α} and θ^{β} are not equivalent), which should result in two secondary Dirac points for electrons and two for holes. However, if electrons can feel potential from both moiré patterns simultaneously, then second order processes can be allowed, which would result in the reconstruction of the electronic spectrum at many other wavevectors.
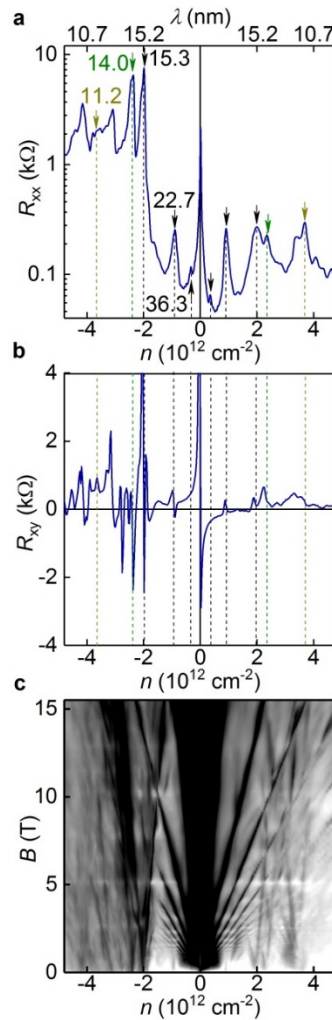
Fig. 2: Transport properties of doubly-aligned hBN/graphene/hBN device. a R_{xx} as a function of n for one of our devices with b ≈ 15.3nm ($\phi_1 = 0^0$), b' ≈ 14.0nm ($\phi_2 = 0.4^0$). Lattice mismatch, δ, is taken as 1.64%. The moiré and super-moiré peaks are marked by arrows and also labelled with

their periods on hole side in the unit of nanometres. The position of the peaks is symmetric w.r.t holes and electrons. The top axis mark is labelled in the size of the moiré pattern which corresponds to the particular carrier concentration. Dashed lines correspond to the arrows and can be traced to those in (b). **b**. R_{xy} for the same device measured at B=0.2T. The dashed lines can be traced to the arrows in (a) and correspond to the particular peaks in R_{xx}. **c** Fan diagram $\sigma_{xx}(n, B)$ for the same device. All measurements are done at T=1.7K

In quantized magnetic fields, Landau fans can be seen to originate from these peaks, Fig. 2c. The Landau fans for most peaks exhibit both positive and negative indexes (positive and negative slopes in Fig. 2c), which suggests that those are indeed originating from the additional Dirac points and not from the higher order zone edges(*28*).

To interpret these additional peaks we recall that the perfectly aligned graphene on hBN should produce moiré pattern with approximately 14nm periodicity, which corresponds to carrier concentration $n \approx 2.3 \times 10^{12}$ cm^{-2}. Thus, for our double-aligned graphene we interpret the most pronounced peaks at $\pm 1.98 \times 10^{12}$ cm^{-2} and $\pm 2.34 \times 10^{12}$ cm^{-2} as coming from the moiré patterns from the top and bottom hBN layers.

The periodicity of a moiré pattern, L, can be related to the carrier concentration required to reach edge of its first Brillouin zone by, $n_{SDP} = \frac{8}{\sqrt{3}L^2}$. Utilising this, we get periodicities of 15.3nm and 14.0 nm respectively for the two most prominent features. The moiré periodicities are dependent upon both the lattice constant mismatch and the alignment angle, as given by $b^{\alpha,\beta} = \left| \boldsymbol{b}_n^{\alpha,\beta} \right| = \frac{4\pi}{\sqrt{3}a} \sqrt{\delta^2 + \theta^{\alpha,\beta^2}}$, where $\boldsymbol{b}_n^{\alpha,\beta} = \boldsymbol{G}_n - \boldsymbol{G}_n^{\alpha,\beta}$ (n=0,..,5) are the moiré reciprocal lattice vector between the α or β hBN layer (with reciprocal lattice vectors $\boldsymbol{G}_n^{\alpha,\beta}$) and graphene (with reciprocal lattice vectors $\boldsymbol{G}_n$), δ is graphene-hBN lattice constant mismatch, $\theta^{\alpha,\beta}$ is the misalignment angle for α or β, and a is graphene's lattice constant. Interestingly, one of the observed periods is larger than that could be expected for graphene aligned with hBN (~15.3nm, see(*15-20*)). We attribute this slightly larger moiré period to stretching of graphene as it interacts more strongly with the two aligned hBN layers. Since the angle is zero, or sufficiently close to zero ($\delta \gg \theta$), we may calculate a new δ. In this case, the lattice mismatch to achieve the periodicity of 15.3nm should be ~1.64%. This corresponds to ~ 0.15% strain in the graphene crystal.

Then we would like to notice the small peaks at $\pm 0.35 \times 10^{12}$ cm^{-2} which corresponds to the largest differential moiré pattern. From the carrier concentration we can infer a periodicity of 35 nm. Further
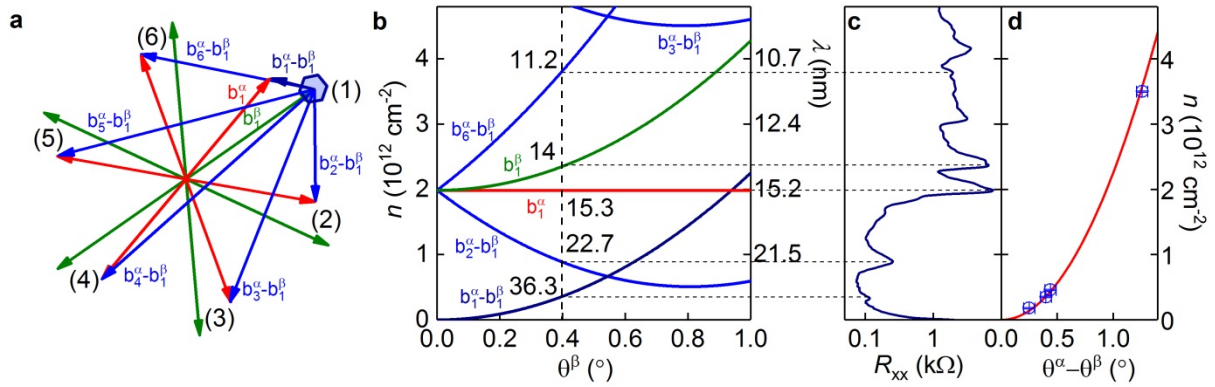
Fig. 3: Super-moiré geometry. *a* Reciprocal-space image of the area around graphene's K-point. b_m^α (green) and b_m^β (red) for m=1,2..6 are the graphene-hBN moiré reciprocal lattice vectors. $b_1^\alpha - b_m^\beta$ (blue) are the six super-moiré reciprocal lattice vectors. The blue hexagonal area indicates the $b_1^\alpha - b_1^\beta$ first Brillouin zone. *b* Carrier concentration of the first Brillouin zone edge for the two moiré and four lowest-energy super-moiré features as a function of θ^β (δ=1.64%, θ^α=0°). *c* R_{xx} peak positions in carrier concentration. Dashed lines connect values of carrier concentration for θ^β =0.4 in *b* to the position in *c*. Each line matches a peak. *d* carrier concentration of the $b_1^\alpha - b_1^\beta$ super-moiré feature vs $\left|\theta^\alpha - \theta^\beta\right|$ for four of ours samples (blue circles) andby calculation (red line).

still, there is a pronounced peak at approximately ±0.90x10^{12} cm^{-2}, which would yield a period of 22.7nm. These features represent previously impossible periodicities for the graphene/hBN moiré pattern.
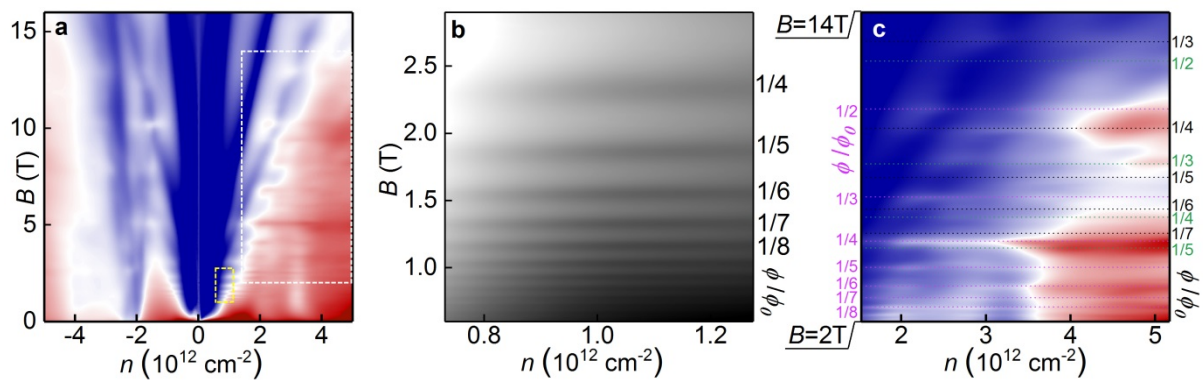
Fig. 4: Brown-Zak oscillations in one of our doubly-aligned hBN/graphene/hBN devices. *a* Map of $\sigma_{xx}(n, B)$. *b* Zoom in into the low field part of the map, marked by yellow rectangle in (a). The Brown-Zak oscillations correspond to a moiré structure with periodicity of 22.7nm and the fundamental field is 9.3T. *c* Zoom in into the high field part of the map, marked by white rectangle in (a). The Brown-Zak oscillations correspond to a moiré structures of different periodicities are

marked by dashed lines of different colours. Black - 15.3nm (B$_F$=20.5T), green 14.0nm (B$_F$=24.2T) and brown – 11.2nm (B$_F$=38T). All measurements are done at T=70K.

In Fig. 3a, we schematically describe the geometric origin of the super-moiré features. $\boldsymbol{b}_m^\alpha$ and $\boldsymbol{b}_k^\beta$ (red and green vectors, m=1,2,..6, k=1,2,..6) are the α and β moiré patterns. Their combination produces six new super-moiré patterns by the combinations of the vectors. In Fig. 3a we highlight the $\boldsymbol{b}_1^\alpha - \boldsymbol{b}_k^\beta$ vectors (blue). In Fig. 3b we present the position of the moiré and super-moiré zone edges in carrier concentration as a function of the angle between the second hBN layer (θ^β) and graphene for the case when the first hBN layer is held at zero angle mismatch ($\theta^\alpha = 0$), and $\delta = 1.64\%$, as calculated. For θ^β=0.4°, the features correspond exactly to the observed peaks in R_{xx} (as shown by the dotted lines connecting Fig. 3b and Fig. 3c), and sign reversal of R_{xy}, thus revealing the presence of new secondary Dirac points in the low energy electronic spectrum. Such low energy peaks originate from the differential super-moirés, $b_1^\alpha - b_1^\beta$, $b_1^\alpha - b_6^\beta$, and $b_1^\alpha - b_2^\beta$. Further, in Fig. 3d, we show the position of the R$_{xx}$ peak in carrier concentration for the $b_1^\alpha - b_1^\beta$ super-moiré, against the calculated angle between the two hBNs ($|\theta^\alpha - \theta^\beta|$). This peak is unique because its period is independent of the graphene sheet as it is geometrically identical to moiré pattern between the two hBN layers. As expected, Fig. 3d shows the peak position for four of our samples (blue circles) follows exactly expectation (red line).

To check that all these peaks indeed originate from the spectrum reconstruction because of scattering on the additional periodic potential we measured the Brown-Zak oscillations at elevated temperatures (*T*) where cyclotron oscillations are suppressed, Fig. 4. At *T*>70K oscillations independent of the carrier concentration can be clearly seen. At low fields *B*<2.5T (Fig. 4b) the oscillations are clearly periodic in 1/*B* with the fundamental field *B$_f$*=9.3T. Assuming a hexagonal unit cell, such fundamental field can be calculated to correspond to moiré periodicity of 22.7nm, which corresponds to the peak in R_{xx} at *n*=±0.90x10^{12} cm^{-2}, Fig. 2a.

The behaviour at high fields is more complex, as several Brown-Zak oscillations which originate from different periodicities overlap. However, by taking the periodicities which correspond to the most prominent peaks in R_{xx} at *B*=0 (15.3nm, 14nm and 11.2nm, see Fig. 2a) we could identify most oscillations in terms of fractions of the flux quantum per the corresponding plaquette, labelled in Fig. 4c. Thus, the graphene-hBN moiré periods (14.0 and 15.3 nm) and super-moiré periods (11.2 nm, 22.7 nm, and 36.3 nm) each give features attributable to secondary Dirac points at well understood values of carrier concentration. Also they produce clear Brown-Zak oscillations for unitary flux

through moiré unit cells for the 11.2 nm, 14.0 nm, 15.3 nm, and 22.7 nm periods.

Further to our previous observations, we would like to note that there are several unexplained features in R_{xx} (Fig. 2a) and R_{xy} (Fig. 2b), most pronounced at $n_e \approx \pm\ 3.2\text{x}10^{12}\text{cm}^{-2}$ and $n_e \approx \pm\ 4.1\text{x}10^{12}\text{cm}^{-2}$. One possible explanation for these features is higher order moiré periodicities, that is, moiré patterns between super-moiré periods. However, the probability of such multiple scattering events diminishes strongly. Likewise, there could exist features due to super-moiré patterns between further zone edges (2nd, 3rd,… Brillouin zone edges of the graphene/hBN moirés) or a more exotic superlattice phenomenon.

Theoretically (29), moiré effects on graphene can be described in terms of a periodic superlattice (SL) potential applied to Dirac electrons produced by incommensurable lattices of two (top and bottom) hBN flakes,

$$\hat{H} = v\boldsymbol{p} \bullet \boldsymbol{\sigma} + \sum_{j=\pm} \sum_{n=0\ldots5} \left[U_0^j + (-1)^n \left(iU_3^j \sigma_3 + U_1^j \frac{\boldsymbol{a}_n \bullet \boldsymbol{\sigma}}{a} \right) \right] e^{i\boldsymbol{b}_n^j \bullet (r + j\frac{R}{2})} e^{i\boldsymbol{G}_n \bullet \boldsymbol{u}(r,R)}. \tag{1}$$

Here, σ_3 and $\boldsymbol{\sigma} = (\sigma_1, \sigma_2)$ are Pauli matrices acting in the sublattice space of graphene's Bloch states; j=± identifies layers α (+) and β (-); U_0^j, U_1^j, and U_3^j parameterise a smoothly varying moiré potential, the asymmetric sublattice on-site energies, and hopping between A and B sublattices, respectively (based on the earlier studies(30-32), $U_0^j \approx 8.5$ meV, $U_1^j \approx -17$ meV, $U_3^j \approx -15$ meV for $\theta^j \ll \delta$). Vector $\boldsymbol{R}$ describes the phase shift between moiré produced by hBN flakes α and β.

From this, the super-moiré periods for the individual moiré SLs (α, β) in graphene originate in two ways. One is due to the quantum mechanical interference, which appears in the second order perturbation theory. In this case, Eq. (1) allows for the electron scattering from the combined j=± superlattices with the Bragg vectors $\boldsymbol{b}_n^\alpha - \boldsymbol{b}_m^\beta$. These comprise of different moiré SL reciprocal vectors, leading effectively to the SLs with Fourier components described in Fig. 1g and 3a. The second possibility is the reconstruction of graphene, which leads to a displacement field, $\boldsymbol{u}(r, \boldsymbol{R})$, generating mixing of the moiré SL's reciprocal vectors. When this is considered, the longest period super-moiré SL ($m = 1, k = 1$) that determines the low-energy part of graphene spectrum can be described by following SL potential,

$$\hat{H}_{1,1}^P \approx -12U_3\omega_{as}\sigma_3 - \sum_m \left[2U_3\omega_{as}\sigma_3 + \frac{4U_3U_1}{vb} + i\frac{2U_1^2}{vb}\frac{\boldsymbol{b}_n \bullet \boldsymbol{\sigma}}{b} \right] e^{i\boldsymbol{b}_m^\alpha \bullet \boldsymbol{R}} e^{i(\,\boldsymbol{b}_m^\alpha - \boldsymbol{b}_m^\beta) \bullet \boldsymbol{r}}$$

$$\hat{H}_{1,1}^{AP} \approx \sum_m \left[i(-1)^m 2U_0\omega_{as} - \frac{4U_3U_1}{vb} + i\frac{2U_1^2}{vb}\frac{\boldsymbol{b}_n \bullet \boldsymbol{\sigma}}{b} \right] e^{i\boldsymbol{b}_m^\alpha \bullet \boldsymbol{R}} e^{i(\,\boldsymbol{b}_m^\alpha - \boldsymbol{b}_m^\beta) \bullet \boldsymbol{r}} \tag{2}$$
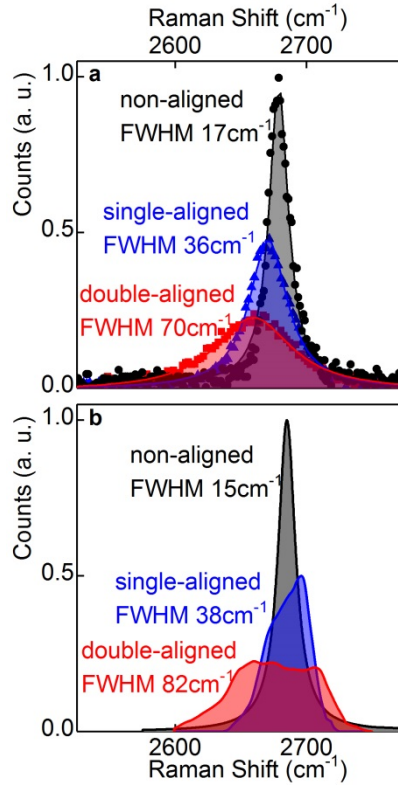
Fig. 5: Strain distribution in the aligned graphene-hBN heterostructures. *Raman spectra (2D-peak region) for an unaligned sample (grey), single-aligned sample (blue), and double-aligned sample (red). (a) Experimental results. (b) Molecular dynamics relaxation simulations.*

This expression was derived for $\theta^\beta \ll \delta$ for both parallel (P) and antiparallel (AP) mutual orientations of the two hBN crystals (hence, approximately, $\boldsymbol{b}_m^\alpha - \boldsymbol{b}_m^\beta \perp \boldsymbol{b}_m^{\alpha,\beta}$), and, here, ω_{as} parameterises the amplitude of inversion asymmetric component of strain.

Vital to this description is the understanding that the displacement field $\boldsymbol{u}(r, \boldsymbol{R})$ develops due to the competition between stacking-dependent van der Waals adhesion, of graphene and hBN, and elasticity of graphene. Previous work (*20, 21*) has identified that the crystals form a 2D fixed-density commensurate state when graphene and hBN are close to perfect alignment. The effect relies upon strain, and thus $\boldsymbol{u}(r, \boldsymbol{R})$, modulating with a period matching that of the moiré pattern to minimise adhesive and elastic energy. The commensurate state is characterised by hexagonal domains with increasingly sharp domain walls near ϑ=0, observed in PeakForce atomic force microscopy (*33*), and broadening of the 2D-peak in the Raman spectrum (*20, 26*).

To evaluate the degree of strain within our super-moiré samples we have employed Raman spectroscopy. In Fig.5a we show the 2D-peak and its full-width half-maximum (FWHM) for a typical unaligned sample (black circles), a sample aligned to one hBN (blue triangles), and one of our doubly aligned samples (red squares). In the case that the two hBN layers may be treated entirely

independently, the signature in the Raman spectrum would remain unchanged from the singly-aligned case (FWHM (2D) ~36 cm^{-1}). However, it is clear that when a second aligned hBN layer is added, the width of the 2D-peak increases by a factor of ~ 2, Fig 5a. We attribute this to restructuring of strain within the super-moiré unit cells. This observation supports the proposed model of the two moiré patterns mixing through strain fields. Therefore, $\boldsymbol{u}(r, \boldsymbol{R})$ should have periodicities described by b_m^α (α-moiré), b_k^β (β-moiré), and $b_m^\alpha - b_k^\beta$ (super-moirés). This is also supported by molecular dynamics simulations of the relaxation in the doubly aligned systems, as shown in Fig. 5b, where the Raman spectra of simulated relaxed configurations is presented (see Supplementary Materials).

To conclude, graphene's electronic spectrum is significantly altered by scattering from super-moiré structures described by the pre-existing moiré between graphene and its substrate and encapsulating hBN layers. These alterations may be considered in two ways; as double scattering events from both graphene-hBN moiré patterns, or as single scattering events from a reconstructed graphene layer. Such super-moiré potential can be of arbitrarily small wavevector (unlike moiré potential from single hBN aligned with graphene), which allows modification of the graphene band structure at arbitrarily low energies.

References

1. A. K. Geim, I. V. Grigorieva, Van der Waals heterostructures. *Nature* **499**, 419-425 (2013).

2. K. S. Novoselov, A. Mishchenko, A. Carvalho, A. H. Castro Neto, 2D materials and van der Waals heterostructures. *Science* **353**, aac9439-aac9439 (2016).

3. L. Britnell *et al.*, Field-effect tunneling transistor based on vertical graphene heterostructures. *Science* **335**, 947-950 (2012).

4. Y. Cao *et al.*, Unconventional superconductivity in magic-angle graphene superlattices. *Nature* **556**, 43 (2018).

5. L. Britnell *et al.*, Strong light-matter interactions in heterostructures of atomically thin films. *Science* **340**, 1311-1314 (2013).

6. F. Withers *et al.*, Light-emitting diodes by band-structure engineering in van der Waals heterostructures. *Nat. Mater.* **14**, 301-306 (2015).

7. F. Withers *et al.*, WSe2 light-emitting tunneling transistors with enhanced brightness at room temperature. *Nano Lett.* **15**, 8223-8228 (2015).

8. T. Low *et al.*, Polaritons in layered two-dimensional materials. *Nature Materials* **16**, 182 (2016).

9. T. L. M. Lane, J. R. Wallbank, V. I. Fal'ko, Twist-controlled resonant tunnelling between monolayer and bilayer graphene. *Appl. Phys. Lett.* **107**, 203506 (2015).

10. J. R. Wallbank *et al.*, Tuning the valley and chiral quantum state of Dirac electrons in van der Waals heterostructures. *Science* **353**, 575-579 (2016).

11. A. Mishchenko *et al.*, Twist-controlled resonant tunnelling in graphene/boron nitride/graphene heterostructures. *Nature Nanotechnology* **9**, 808 (2014).

12. E. M. Alexeev *et al.*, Resonantly hybridized excitons in moire superlattices in van der Waals heterostructures. *Nature* **567**, 81-86 (2019).

13. Y. Cao *et al.*, Correlated insulator behaviour at half-filling in magic-angle graphene superlattices. *Nature* **556**, 80-84 (2018).

14. Y. Cao *et al.*, Unconventional superconductivity in magic-angle graphene superlattices. *Nature* **556**, 43-50 (2018).

15. J. M. Xue *et al.*, Scanning tunnelling microscopy and spectroscopy of ultra-flat graphene on hexagonal boron nitride. *Nat. Mater.* **10**, 282-285 (2011).

16. M. Yankowitz *et al.*, Emergence of superlattice Dirac points in graphene on hexagonal boron nitride. *Nat. Phys.* **8**, 382-386 (2012).

17. L. A. Ponomarenko *et al.*, Cloning of Dirac fermions in graphene superlattices. *Nature* **497**, 594-597 (2013).

18. C. R. Dean *et al.*, Hofstadter's butterfly and the fractal quantum Hall effect in moire superlattices. *Nature* **497**, 598-602 (2013).

19. B. Hunt *et al.*, Massive Dirac fermions and Hofstadter butterfly in a van der Waals heterostructure. *Science* **340**, 1427-1430 (2013).

20. C. R. Woods *et al.*, Commensurate-incommensurate transition in graphene on hexagonal boron nitride. *Nat. Phys.* **10**, 451-456 (2014).

21. C. R. Woods *et al.*, Macroscopic self-reorientation of interacting two-dimensional crystals. *Nat. Commun.* **7**, 10800 (2016).

22. M. Yankowitz, K. Watanabe, T. Taniguchi, P. San-Jose, B. J. LeRoy, Pressure-induced commensurate stacking of graphene on boron nitride. *Nature Communications* **7**, 13168 (2016).

23. M. Yankowitz *et al.*, Dynamic band-structure tuning of graphene moiré superlattices with pressure. *Nature* **557**, 404-408 (2018).

24. T. Uwanno, Y. Hattori, T. Taniguchi, K. Watanabe, K. Nagashio, Fully dry PMMA transfer of graphene onh-BN using a heating/cooling system. *2D Materials* **2**, 041002 (2015).

25. Y. Cao *et al.*, Quality heterostructures from two-dimensional crystals unstable in air by their assembly in inert atmosphere. *Nano Lett.* **15**, 4914-4921 (2015).

26. A. Eckmann *et al.*, Raman fingerprint of aligned graphene/h-BN superlattices. *Nano Lett.* **13**, 5242–5246 (2013).

27. K. S. Novoselov *et al.*, Electric field effect in atomically thin carbon films. *Science* **306**, 666-669 (2004).

28. R. K. Kumar *et al.*, High-temperature quantum oscillations caused by recurring Bloch states in graphene superlattices. *Science* **357**, 181-184 (2017).

29. J. R. Wallbank, A. A. Patel, M. Mucha-Kruczynski, A. K. Geim, V. I. Falko, Generic miniband structure of graphene on a hexagonal substrate. *Phys. Rev. B* **87**, 245408 (2013).

30. M. Lee *et al.*, Ballistic miniband conduction in a graphene superlattice. *Science* **353**, 1526-1529 (2016).

31. R. K. Kumar *et al.*, High-order fractal states in graphene superlattices. *Proc. Natl. Acad. Sci. U. S. A.* **115**, 5135-5139 (2018).

32. J. R. Wallbank *et al.*, Excess resistivity in graphene superlattices caused by umklapp electron-electron scattering. *Nat. Phys.* **15**, 32-36 (2019).

33. B. B. Pittenger, N. Erina, C. Su, in *Application Note #128*. (2012).

Supplementary Information

Composite super-moiré lattices in double aligned graphene heterostructures

Contents:

Additional experimental materials

Additional fabrication details

Details of super-moiré Analysis

Details of Tight-Binding model used

Details of Raman spectroscopy simulations

More examples of double alignment

Following from our analysis in the main text, we can extend the comparison between the calculated periodicities to the electronic transport characteristics of three more devices. Fig. S1 shows longitudinal resistance R_{xx}, hall resistance R_{xy} and their corresponding theoretical fittings of four samples; the device of the main text (Fig. S1a), and three others (Fig. S1b-d). All of these samples are encapsulated graphene heterostructures with perfect alignment in one side graphene-hBN contact surface. From the perfectly aligned moiré period, we can fit δ. The fitted parameters are shown in Supp. Table 1.

We compare R_{xx} and R_{xy} data to confirm the presence of secondary Dirac points, whose signature has both a peak in the R_{xx} data and a reversal of sign in R_{xy}. The coexistence of these features rules out other features in the moiré minibands (*5*).

	Figure label	Lattice mismatch	Second twist angle
Sample 1	**a**	1.64%	0.4^0
Sample 2	**b**	1.66%	0.44^0
Sample 3	**c**	1.69%	1.25^0
Sample 4	**d**	1.71%	0.25^0

Supplementary Table 1: δ and θ^β for each device. *Lattice mismatch, δ, and angle of the second hBN, θ^β, for each device in Fig. S1.*

Many R_{xx} peaks are observable with good agreement with the calculated periods. The amplitudes of the R_{xx} peaks for super-moiré are typically smaller than those of the moiré Dirac points. This is particularly pronounced on the hole side where the amplitude ratios, shown in Fig S4, result in a big difference between peaks of moiré and super-moiré. The R_{xx} features match with features in R_{xy}, indicating the presence of a new Dirac point. Many of the super-moiré features in R_{xy} do not reverse the sign entirely – however this may be explained as a result of the weakened amplitude of the super-moiré scattering process.
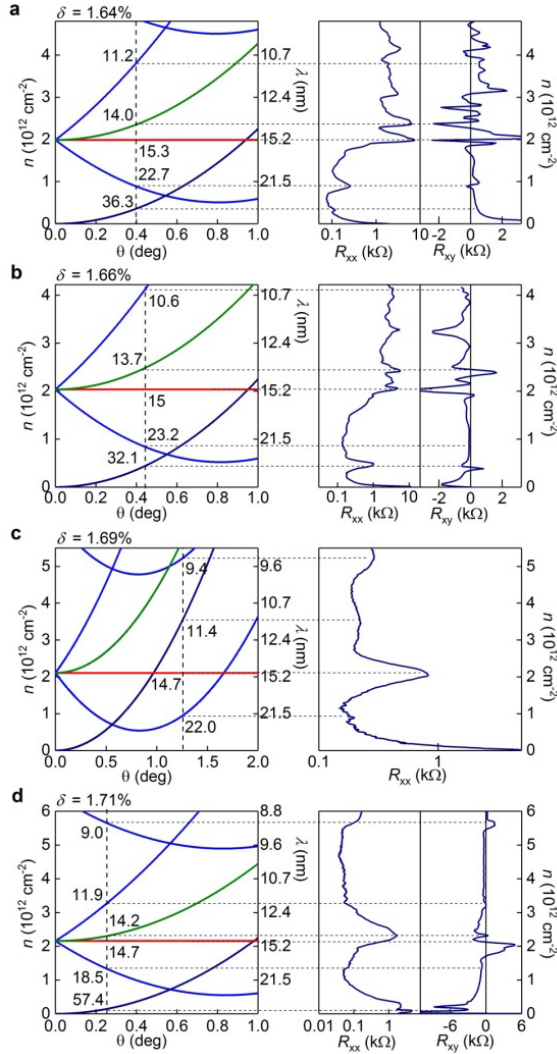
Supplementary Figure 1: Transport properties of doubly-aligned encapsulated graphene devices. a shows the calculated dependence on θ^β of the moiré and super-moiré periodicities. Dashed lines are a guide for the eye linking intersections with $\theta^\beta = 0.4$ to the R_{xx} and R_{xy} data. This is a reproduction of Fig. 3b and 3c from the main text. b Same as a for device two, $\theta^\beta = 0.44$. c same as a for device three, $\theta^\beta = 1.25$. d same as a for device 4, $\theta^\beta = 0.25$.

Different fundamental frequencies of Brown-Zak oscillations

Previous literature reported the Brown-Zak oscillations (BZO) as a robust method to study the periodic potential applied on the graphene, for which maxima in σ_{xx} occurs following $\frac{B}{B_F} = \frac{p}{q}$ where fundamental frequency $B_F = \frac{\phi_0}{S}$, p, q are integers, S is the area of unit cell (6, 7). Here we employ BZO to probe the unit cell resulting from moiré and super-moiré periodicities. The key point is to extract the different frequencies corresponding to different unit cells, and then calculate the periodicity by assuming it corresponds to a hexagonal area.

As reported in (7), with p, q increasing, the amplitude of BZO decays exponentially due to the smaller group velocity and larger super unit cell. Usually p = 1 is much more prominent than p = 2, 3... It is experimentally difficult to realise observations of the p=1, q=1, oscillations in singly-aligned graphene on hBN since the fundamental frequency is ~24T. Further, the BZO would be

more visible at high carrier densities, high T (up to 150K), and in an electron doped graphene. The increased observation of the BZO at high temperature is due to the smearing of the electronic energy distribution which removes the influence of quantum phenomenon (Landau quantization). The BZO survive because they transport oscillations, rather than a quantum oscillation.

In our BZO maps (Fig. S2), the oscillation corresponding to an aligned graphene-hBN moiré is clearest. It is unobservable at carrier densities around Main Dirac points (MDP). However, other frequencies start to appear around the carrier densities of their corresponding R_{xx} peaks. Also, many BZO may be distinguished more clearly at high densities on electron-doped side of the main Dirac point ($n>4.5e12$ cm^{-2}) where the landau fan from the various Dirac point is unobservable. In Fig. S2b, the oscillations of the second largest super-moiré start to appear around its R_{xx} peak 0.9e12cm^{-2} (Fig.S1.**a**). In this range, only one frequency occurs at small magnetic fields, so it can be easily extracted. Then, around $n = 2.0e12$ cm^{-2}, shown in Fig.S2.**c**, the frequency of perfectly aligned graphene-hBN moiré pattern becomes dominant. To distinguish other frequencies, higher n and higher B are both required. In Fig.S2.d, we neglect the two frequencies that have already been extracted in the small n. Another two frequencies are observed. In total four distinct periodicities are observable; 2 moirés, and 2 super-moirés.
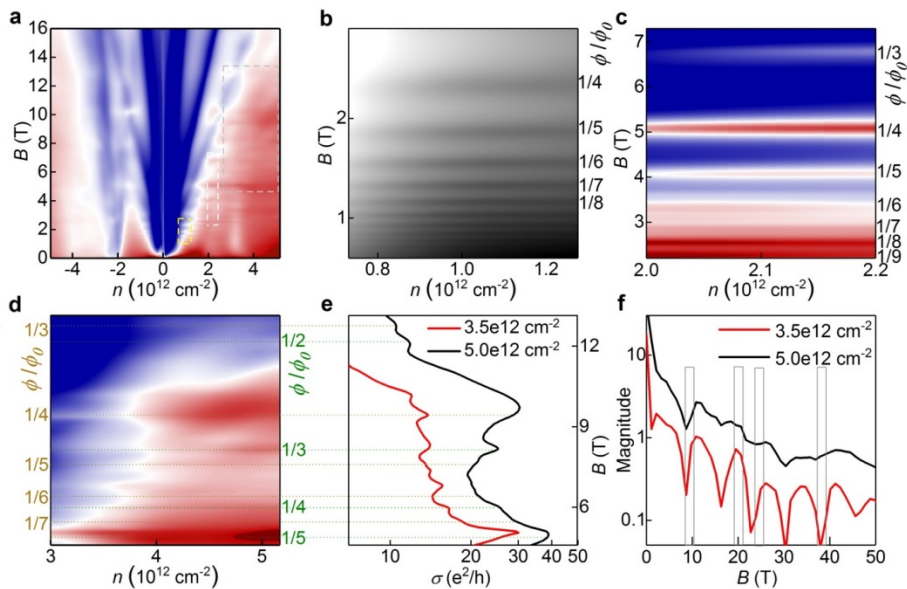
Fig.S2 Brown-Zak Oscillations in sample 1. *This sample is the Same the main text. **a** σ_{xx} as a function of carrier concentration and magnetic field (Scale: blue to red 0.5 e^2/h to 70 e^2/h). **b, c** and **d** are zoom-in of the region marked by the yellow, white, and grey dashed lines, respectively (scales: blue to red, 7 e^2/h to 37 e^2/h.) **e** Two magnetic field sweepings at carrier densities*

3.5e12cm^{-2} and 5.0e12cm^{-2}, with dotted lines connecting the peaks of two sweepings to the maxima in the map. *f* The FFT of the two carrier densities in *e*. Grey bars mark our fundamental frequencies 9.3T, 20.5T, 24.2T and 38T.
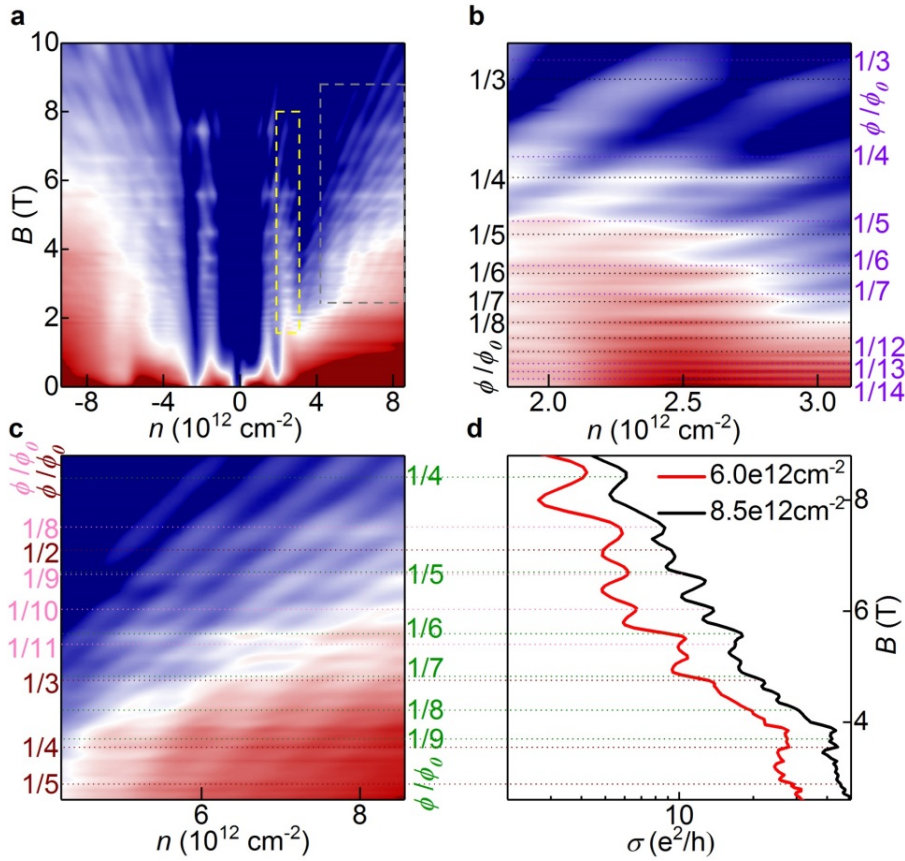
Fig.S3 Brown-Zak oscillations for sample 4. *a* σ_{xx} *map of carrier concentration and B-field of sample (scale: blue to red, 4 e^2/h to 150 e^2/h).* ***b*** *and* ***c*** *are zoom-in of the* ***a****, marked by the yellow and grey rectangles, respectively. (****b*** *scale: blue to red, 2.4 e^2/h to 30 e^2/h) (****c*** *scale: blue to red, 3.5 e^2/h to 50 e^2/h).* ***d*** *shows two magnetic field sweepings at carrier densities 6.0e12cm^{-2} and 8.5e12cm^{-2} with the same scale as* ***c****, dotted lines connecting the peaks of two sweepings to the maxima in the map. The Brown-Zak oscillations correspond to a moiré structures of different periodicities are marked by dotted lines of different colours. Black – 14.6nm (B$_F$=22.5T), violet – 14.2nm (B$_F$=23.8T), light pink – 8.9nm (B$_F$ =60.5T), green – 11.9nm (B$_F$=33.5T), red – 18.4nm (B$_F$=14.1T). The periods are similar with those derived by R$_{xx}$ and R$_{xy}$. All measurements are done at 35K.*
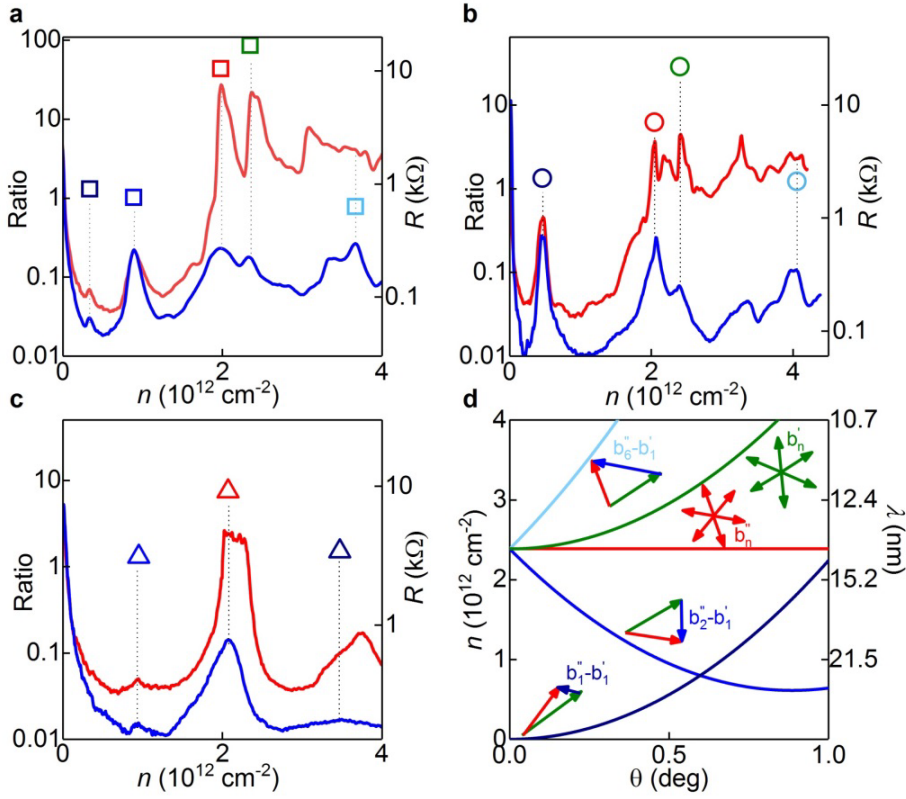
***Fig.S4 electron-hole symmetry in super-moiré features. a, b** and **c,** scatter plots represent the ratios between hole-side peak amplitudes and their electron-side counterparts with dashed lines connecting their corresponding peaks (red – hole-side, blue – electron-side). Different shapes point to different samples, **a** (square) – sample 1, **b** (circle) – sample 2 and **c** (triangle) – sample 3, same as Main text Fig.4. Different colours point to different moiré vectors and super-moiré vectors, shown clearly in **d**.*

Atomic force microscopy of other double aligned samples

We have made and measured many doubly-aligned samples. Each sample shows a double moiré pattern in the AFM images (Fig. S5 a-d), principally confirmed by the presence of two sets of independent spots in the Fourier transformation (Fig. S5 e-h). In each case the encapsulation hBN layer is thin (<5 layers). We do not observe the moiré pattern when the hBN is thick (10s of nm). The double alignment is further confirmed by electronic transport data – yielding several moiré and super-moiré features.
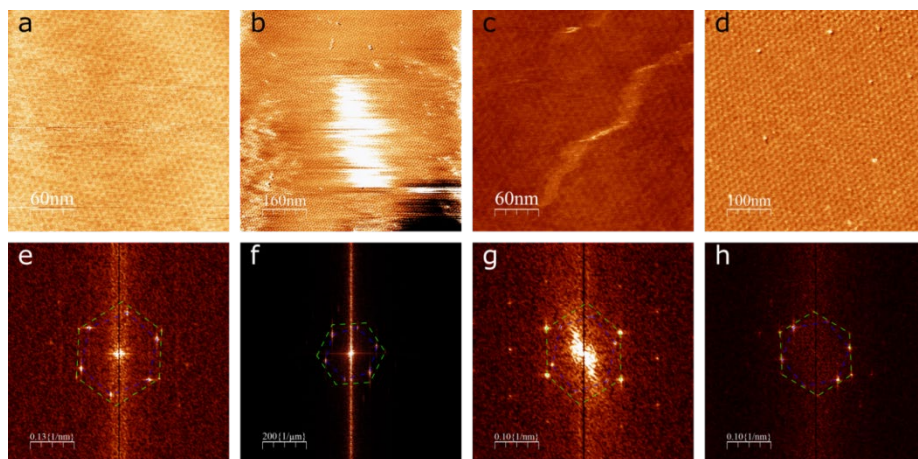
***Supplementary figure 5: Examples of double aligned samples. a, b, c, and d** AFM Young's Modulus images of super-moiré samples. In some cases, contamination is visible in the image. **e, f, g, and h** Fourier transformations of the images in **a, b, c, and d**, respectively. Each image shows two sets of hexagonal spots corresponding to distinct moiré periods.*

Sample Fabrication

Further to the sample preparation described in the main text, in Fig S6, the general process is shown step-by-step. We use PPC (sometimes PMMA) spun on a thick PDMS membrane to facilitate moving and orientating the flake. This membrane is used to pick up the first hBN layer. The crystal may then be positioned and aligned to graphene (Fig. S6a) before the two are brought into contact (Fig. S6b). Removing the membrane in a precise way then lifts the graphene off from its substrate (Fig. S6c). Further, we can invert the membrane and perform various characterisation techniques on the half-assembled heterostructure (Fig S6d). The previous steps (Fig S6a-d) may be repeated multiple times to produce increasingly complex heterostructures. Finally, the stack of crystals is positioned (Fig S6e) and brought into contact with a final 'substrate' hBN (Fig S6f). The membrane is removed (Fig S6g) and all the crystals are left on a SiO_2 wafer (Fig S6h).
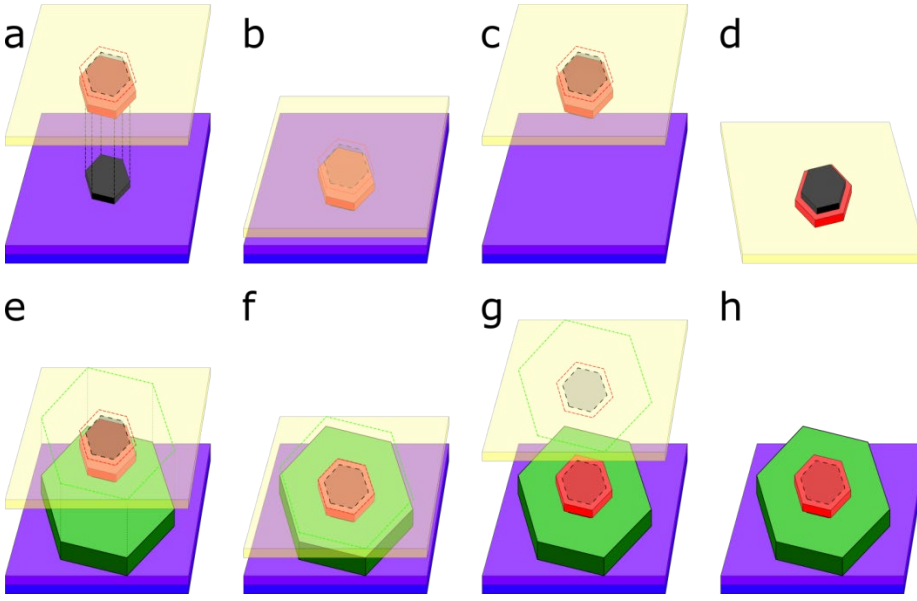
***Supplementary Figure 6: illustration of a typical heterostructure fabrication process. a** A thin top-hBN (red) is aligned over a graphene flake (black). **b** The crystals are brought into contact. **c** The graphene and hBN are lifted away from the substrate. **d** The membrane is inverted and may be characterised by AFM and Raman spectroscopy. **e** once all the crystals are assembled on the membrane, the stack is aligned over a final substrate hBN layer (green). **f** The crystal are brought into contact. **g** The membrane is removed slowly. **h** All the crystals are left on the SiO2/hBN substrate. The PPC/PDMS membrane is yellow, the Silicon is blue, and Silicon dioxide is purple.*

Analysis of super-moiré peaks

The analysis of moiré patterns in hBN-GR-hBN was done following an approach described in Ref. (*8*). The methodology is based on the Fourier analysis of moiré patterns appearing when two hexagonal lattices are combined. A hexagonal lattice can be described using the function

$$f(\vec{r}) = \frac{1}{9} + \frac{8}{9}\cos\left(\frac{1}{2}\vec{k}_1\vec{r}\right)\cos\left(\frac{1}{2}\vec{k}_2\vec{r}\right)\cos\left(\frac{1}{2}\vec{k}_3\vec{r}\right) \quad (25)$$

where $\vec{k}_1 = k[1,0]$, $\vec{k}_2 = k[-1,1]$, $\vec{k}_3 = k[0,-1]$, with $k = 4\frac{4\pi}{a\sqrt{3}}$, and a is the lattice constant. This function contains spatial frequencies at 0 (zero order), and $\vec{k}_1$, $\vec{k}_2$, $\vec{k}_3$ (first order). Higher order frequencies can be obtained when considering functions f^2 (second order) and f^3 (third order), or even f^n (n-th order). It is important to note that a perfect lattice would contain harmonics of infinite order with an amplitude in the Fourier transform that's inversely proportional to the order of the harmonic. Using the description of a lattice from Eq. (25), the moiré pattern defined by combining two of such lattices can be expressed as a product between functions f_1 and f_2. The Fourier

transform of this product would reveal which spatial frequencies appear, and subsequently which are the possible moiré patterns.

We approach the problem of the trilayer heterostructures by considering two moiré patterns (one made by graphene and top hBN and the second one made by graphene and the bottom hBN) as the two lattices and following the approach explained above. Let's define the moiré reciprocal vectors, $\vec{m}_{1,2}$ and $\vec{n}_{1,2}$ corresponding to graphene and hBN layers rotated by an angle θ_1 and θ_2, respectively,

$$\vec{m}_i = \vec{g}_i \begin{bmatrix} \cos\theta_1 & -\sin\theta_1 \\ \sin\theta_1 & \cos\theta_1 \end{bmatrix} \frac{\vec{g}_i}{(1+\delta_1)} \qquad (26)$$

and

$$\vec{n}_i = \vec{g}_i \begin{bmatrix} \cos\theta_2 & -\sin\theta_2 \\ \sin\theta_2 & \cos\theta_2 \end{bmatrix} \frac{\vec{g}_i}{(1+\delta_2)}, \qquad (27)$$

where $i = 1,2$, $\vec{g}_i$ are the reciprocal vectors of the graphene lattice, and δ_i are the relative ratios of unit cell lengths between graphene and the two hBN lattices. The super-moiré reciprocal vectors that correspond to different spatial periodicities can be defined as a difference between harmonics of different order (any two combinations of the underlying moiré vectors $\vec{m}_i$ and $\vec{n}_i$). Unlike the moiré pattern between graphene and hBN, the three layer problem (hBN-GR-hBN) (within a certain range of small rotation angles) results in higher order beating frequencies in the low frequency range, suggesting the emergence of structures with larger periodicity than the main pattern defined by the difference $\vec{m}_1$ - $\vec{n}_1$ (or $\vec{m}_2$ - $\vec{n}_2$). Fig. 7 shows an example of frequency spectra obtained for $\theta_1 = 0^0$ and $\theta_2 = 0.8^0$.
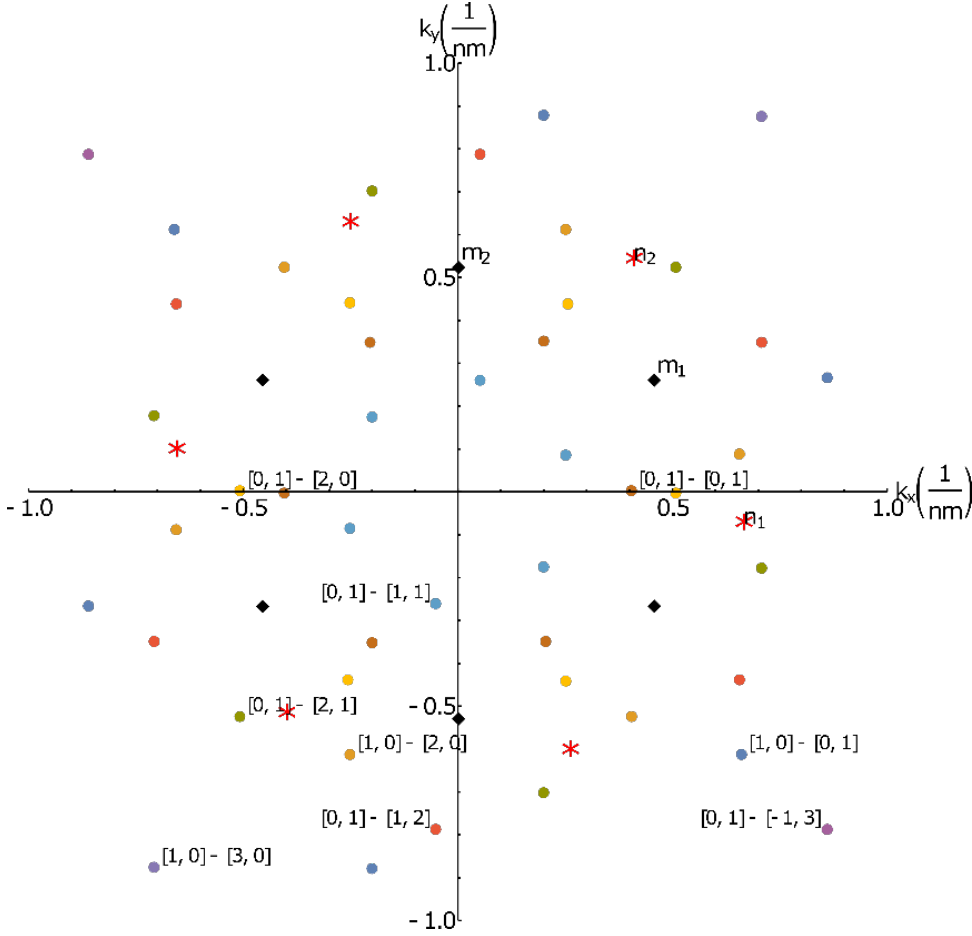
Supplementary Figure. 7: *Frequency analysis of different harmonics of hBN-gr-hBN structure. The reciprocal vectors of moiré patterns are marked with $m_{1,2}$ using $\theta_1 = 0^0$ (diamonds) and $n_{1,2}$ using $\theta_2 = 0.8^0$ (stars) while the super-moiré harmonics are labelled as a difference between relative coordinates [p, q]–[r, s].*

Dominant super-moiré harmonics that fit the experimentally observed features are labelled in Fig. 8. They emerge as the difference between the moiré harmonics of different orders, as shown in the previous plot. Here, we show the super-moiré periods calculated using the following relation $\lambda = \frac{4\pi}{\sqrt{3}|\vec{k_1}|}$, (4)

where $\vec{k_i} = (p\vec{m}_1 + q\vec{m}_2) - (r\vec{n}_1 + s\vec{n}_2)$, where p, q, r, s are integers.
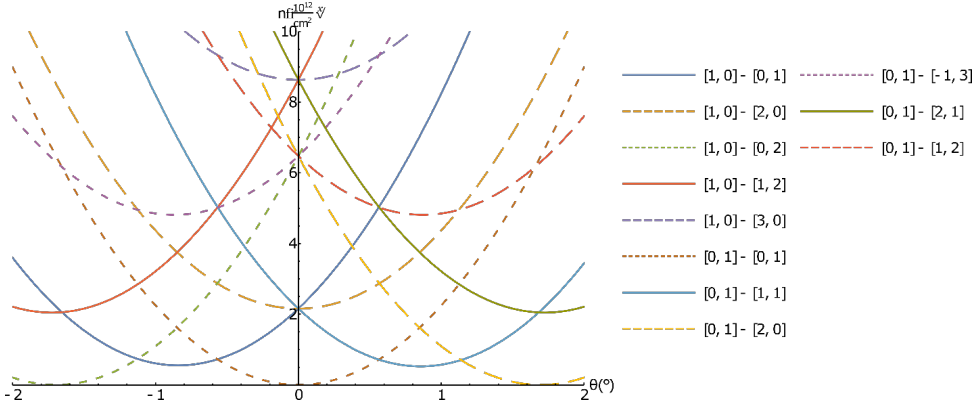
Supplementary Figure 8. *Super-moiré periods corresponding to different harmonics obtained using different combination of [p, q]−[r, s] shown in the inset.*

Tight-binding model

Tight-binding calculations are performed using standard tight-binding Hamiltonian given by

$$H = -\sum_{i,j} t(\vec{r}_i, \vec{r}_j) c_i^\dagger c_j, \qquad (28)$$

with

$$t(\vec{r}_i, \vec{r}_j) = V_\pi \left[1 - \left(\frac{\vec{d}\vec{e}_z}{d}\right)^2\right] + V_\sigma \left(\frac{\vec{d}\vec{e}_z}{d}\right)^2, \qquad (29)$$

using

$$V_\pi = V_\pi^0 e^{-\frac{d-a_0}{\delta}}$$

$$V_\sigma = V_\sigma^0 e^{-\frac{d-d_0}{\delta}}$$

where $V_\pi^0 = -2.7$ eV, $V_\sigma^0 = 0.48$ eV are the intralayer and interlayer hopping integrals, respectively. $\vec{d}$ is the bond vector between sites i, j, a_0 is the equilibrium bond length of each material, and $\delta = 0.3187a_0$ is chosen to fit the next-nearest intralayer hopping value. Hoppings within the layer are considered up to the second nearest neighbour while the interlayer hoppings are considered within the radius of $1.5d_0$, where d_0 is the equilibrium interlayer distance. This radius is chosen due to the fact that hoppings outside this radius contribute only to a small energy shifts of the spectra, without modifying it significantly. However, neglecting the above mentioned hoppings results in a considerable gain in calculation time due to a reduced number of non-zero elements in the Hamiltonian.

Molecular dynamics simulations and Raman shift calculations

Molecular dynamics simulations are performed for the singly-aligned hBN/graphene and the double-aligned hBN/graphene/hBN by allowing the relaxations of both hBN and graphene layers. We used

the bond-order Brenner potentials for the graphene layer, Tersoff potentials for the B-N interaction in the hBN layers and the Morse potential developed in Ref. (*9*) for the inter-layer interactions. The simulations are performed within the "large-scale atomic/molecular massively parallel simulator" (LAMMPS) (*10, 11*) by considering a disk of radius 120nm. We fix the atoms in a boundary region of 2nm but allow the relaxation of all other atoms. The total energy is minimized until the forces are below 10^{-6} eV/Å. Results of simulations are shown in Fig. 9 where we plotted bond lengths of the relaxed graphene layer in the case of single and double aligned system.
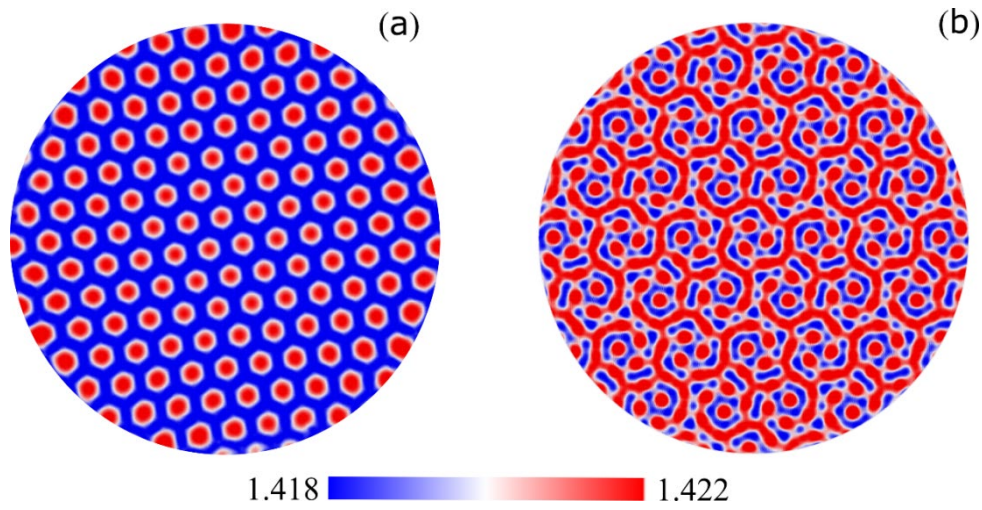
Supplementary Figure 9. *Bond lengths in (a) single ($\theta = 0.4°$) and (b) double ($\theta_1 = 0$ and $\theta_2 = 0.4°$) aligned hBN/graphene/hBN system.*

Using the relaxed structures, we calculate the shift of the 2D peak. Calculations are performed using the prescriptions given in Ref. (*12-14*). First, we obtain the strain tensor $\varepsilon(\boldsymbol{r})$ which is employed to extract the shift of the 2D peak as

$$\Delta\omega_{2D} = -\omega_{2D}^0 \gamma_{2D} \varepsilon_h, \qquad (30)$$

where ω_{2D}^0 is the 2D frequency of the unstrained graphene, $\gamma_{2D} = 3.55$ [5] , and $\varepsilon_h = \varepsilon_{xx} + \varepsilon_{yy}$ is the hydrostatic component of the strain tensor. This method has been applied to three different systems: graphene aligned with both hBN layers, graphene aligned with top hBN layer, and non-aligned system (Fig. 5b red, blue, and black curve, respectively). A histogram of the shifts has been produced and the Lorentzian fitting to the obtained data was performed.

References

1. D. A. Cosma, J. R. Wallbank, V. Cheianov, V. I. Fal'ko, Moiré pattern as a magnifying glass for strain and dislocations in van der Waals heterostructures. *Faraday Discussions* **173**, 137-143 (2014).

2. J. R. Wallbank, A. A. Patel, M. Mucha-Kruczynski, A. K. Geim, V. I. Falko, Generic miniband structure of graphene on a hexagonal substrate. *Physical Review B* **87**, 245408 (2013).

3. M. Mucha-Kruczyński, J. R. Wallbank, V. I. Fal'ko, Heterostructures of bilayer graphene and h-BN: Interplay between misalignment, interlayer asymmetry, and trigonal warping. *Physical Review B* **88**, 205418 (2013).

4. X. Chen *et al.*, Dirac edges of fractal magnetic minibands in graphene with hexagonal moir\'e superlattices. *Physical Review B* **89**, 075401 (2014).

5. L. A. Ponomarenko *et al.*, Cloning of Dirac fermions in graphene superlattices. *Nature* **497**, 594-597 (2013).

6. R. Krishna Kumar *et al.*, High-temperature quantum oscillations caused by recurring Bloch states in graphene superlattices. *Science* **357**, 181 (2017).

7. R. Krishna Kumar *et al.*, High-order fractal states in graphene superlattices. *Proceedings of the National Academy of Sciences* **115**, 5135 (2018).

8. P. Zeller, S. Günther, What are the possible moiré patterns of graphene on hexagonally packed surfaces? Universal solution for hexagonal coincidence lattices, derived by a geometric construction. *New Journal of Physics* **16**, 083028 (2014).

9. G. Argentero *et al.*, Unraveling the 3D Atomic Structure of a Suspended Graphene/hBN van der Waals Heterostructure. *Nano Letters* **17**, 1409-1416 (2017).

10. S. Plimpton, Fast Parallel Algorithms for Short-Range Molecular Dynamics. *Journal of Computational Physics* **117**, 1-19 (1995).

11. S. J. Plimpton, A. P. Thompson, Computational aspects of many-body potentials. *MRS Bulletin* **37**, 513-521 (2012).

12. S. Reich, J. Maultzsch, C. Thomsen, P. Ordejón, Tight-binding description of graphene. *Physical Review B* **66**, 035412 (2002).

13. T. M. G. Mohiuddin *et al.*, Uniaxial strain in graphene by Raman spectroscopy: G peak splitting, Gr\"uneisen parameters, and sample orientation. *Physical Review B* **79**, 205433 (2009).

14. T. Vincent *et al.*, Probing the nanoscale origin of strain and doping in graphene-hBN heterostructures. *2D Materials* **6**, 015022 (2018).

3.4 Alignment of twisted NbSe$_2$

Additional twisted heterostructures were studied during my PhD, including twisted CrI$_3$, MoS$_2$-MoSe$_2$, and NbSe$_2$. This paper reported a new general method for the scalable synthesis of high-quality monolayer transition metal dichalcogenide (TMD) superconductors. To determine the quality of this novel printed NbSe$_2$, my research team measured the twisted printed NbSe$_2$ devices in comparison to exfoliated NbSe$_2$ counterpart. Unlike the period of Δ($1/B$) in the graphene superlattice, the observed oscillation extracted from the I_c - B mapping was reported to be the period ΔB.

Paper 3 (published in Nature material, co-author)

My contribution: Performed the transport measurement for the exfoliated twisted NbSe$_2$ samples and analyzed these data.

Printable 2D superconducting monolayers

Jing Li[1,3,†], Peng Song[1,†], Jinpei Zhao[2,†], Kristina Vaklinova[3,†], Xiaoxu Zhao[4,†], Zejun Li[1], Zhizhan Qiu[1], Zihao Wang, Li Lin Meng Zhao[5], Tun Seng Herng[4], Yuxin Zuo[4], Win Jonhson[4], Wei Yu[1], Xiao Hai[1], Pin Lyu[1], Haomin Xu[1], Huimin Yang[1], Cheng Chen[1], Stephen J. Pennycook[4], Jun Ding[4], Jinghua Teng[5], A. H. Castro Neto[2,3], Kostya S. Novoselov[2,4]* and Jiong Lu[1,3]*

[1]Department of Chemistry, National University of Singapore, 3 Science Drive 3, Singapore 117543, Singapore.

[2]Department of Physics, National University of Singapore, Singapore 117551.

[3]Centre for Advanced 2D Materials and Graphene Research Centre, National University of Singapore, Singapore 117546.

[4]Department of Materials Science & Engineering, National University of Singapore

9 Engineering Drive 1, Singapore 117575, Singapore.

[5]Institute of Materials Research and Engineering, Agency for Science, Technology and Research

(A*STAR), 2 Fusionopolis Way, Innovis, Singapore 138634, Singapore.

Two-dimensional superconductivity (2DSC) is one of the most fascinating fields in condensed matter research due to extreme importance of quantum fluctuations and the complex nature of the collective electronic behavior. In particular, 2D non-centrosymmetric superconductors such as monolayer transition metal dichalcogenides (TMDs) exhibit unconventional pairing symmetries and anomalous magnetic response, and thus are irreplaceable when creating van der Waals heterostructures with untrivial quantum properties. However, they are often susceptible to structural disorder and environmental oxidation that destroy electronic coherence and provide technical challenges in the creation of the complex van der Waals heterostructures for devices. Furthermore, large-scale synthesis of highly crystalline atomic layers is another difficulty that hinders the exploitation of those materials in scientific and industrial applications. Herein we report a general approach for a scalable synthesis of highly uniform and crystalline superconducting TMD monolayers via a mild electrochemical exfoliation method using bulky organic ammonium cations solvated with neutral solvent molecules as co-intercalants. Using $NbSe_2$ as a model system, we achieved a high monolayer yield (>70%) of large-sized single crystal flakes of up to 300 μm under optimized exfoliation conditions. In order to demonstrate the versatility of our process, we fabricated twisted $NbSe_2$ van der Waals heterostructures, which demonstrate high stability, good interfacial properties and a critical current that is modulated by magnetic field when one flux quantum fits to an

integer number of moiré cells. Finally, 2DSC atomic layers can be formulated into high quality inks for patterning wafer-scale 2D superconducting wire arrays and creating 3D superconducting composites with desirable morphologies using 2D and 3D printing technologies, respectively. Our work presents a versatile and scalable route for the production of a variety of solution-processable and highly crystalline 2DSCs in monolayer limit towards the fabrication of large-area superconducting junctions and device arrays.

2D TMD superconductors provide a new platform for the investigation of new quantum physics and exotic superconductivity owing to their confined geometry, broken spatial inversion symmetry combined, in many cases, with a strong spin-orbit coupling.[1-5] Van der Waals heterostructures (vdWHs) based on such crystals allow creation of artificial, strongly correlated, materials with full control over the symmetry and the dimensionality of the resulting structures[6, 7]. The exploration of these systems may lead to the discovery of new atomically-thin superconductors with exotic states and novel superconducting mechanisms.[8-12] However, while the figure-of-merits of highly crystalline 2DSCs set them apart from the conventional 2DSCs with granular and amorphous structures,[13-15] the bottleneck of this field has been the lack of a general and facile approach for the production of high quality atomic layers of 2DSCs in large amount for practical applications.[1] Recently, advances in thin film synthesis technologies have enabled the preparation of 2DSC TMD monolayers via different fabrication approaches including mechanical exfoliation[10], molecular beam epitaxy (MBE)[8, 11], chemical vapor deposition (CVD)[16-18] and chemical intercalation[19-23]. Unfortunately, none of these approaches offers simultaneous excellent crystallinity, high production yield, scalability of as-prepared flakes and ease of incorporation into the final devices, which severely hampers further advancement in this field. These constrains have motivated us to devise a general and versatile approach for the production of high quality atomic layers of 2DSCs in large amount for the fabrication of basic vdWHs and for the potential use in quantum devices.

Here, we demonstrate a universal method of electrochemical exfoliation of bulk TMDs using quaternary ammonium cations as a cathodic intercalant towards the production of a wide range of high quality monolayer 2DSCs including $Nb(Se/Te)_2$, $Ta(S/Se)_2$, $Ti(S/Se)_2$, and $MoTe_2$[4, 10, 24, 25] and their one-step incorporation into basic vdWHs.

The entire exfoliation process in solution-phase can efficiently prevent the degradation of air-sensitive metallic TMDs, thus can yield monolayer and few-layer flakes.[26-28] Electrochemical exfoliation involving the use of charged ions (eg, alkali and tetraheptylammonium cations) has been utilized to exfoliate graphite, semiconducting and other types of TMDs into thin flakes[19, 20]. However, the intercalation of TMDs with a large amount of charged species often leads to undesirable outcomes such as phase transition and degradation of crystal quality with a low monolayer yield[23]. In this regard, the key advance of our approach lies in the maximization of the efficient intercalation of neutral polar solvent molecules (eg, propylene carbonate, PC) in TMDs carried by an ultra-low concentration of organic ammonium cation (eg, tetrapropylammonium, TPA). (Supplementary Fig S10-13) This strategy not only allows for sufficient intercalation but also significantly reduces the excessive charging and structural damage of the TMD hosts arising from charged intercalants[21, 22], which is crucial for the exfoliation of high-quality and large-size 2DSC sheets with a high monolayer yield (Fig. 2b). Protective properties of intercalants and the high quality of the resulting flakes allow natural protection of basic vdWHs–twisted NbSe2 crystals, which demonstrate excellent interfacial properties and where the critical supercurrent is an oscillatory function of the external magnetic field. We attribute such behaviour to the formation of the Moiré pattern at the interface between the two crystals. The oscillations are observed to be an integer number of flux quanta that fits to the integer number of Moiré cells at any point of time.

Fig. 1 illustrates the cathodic exfoliation of layered bulk TMDs into monolayer and few-layer 2DSCs using quaternary ammonium cations. Tetrabutyl ammonium (TBA) dissolved in PC (0.05 M)

was used for a demonstration of cathodic exfoliation of more than 7 types of bulk TMD materials. Upon applying a voltage of -5 V, these layered materials show a rapid volumetric expansion and exfoliation into thin flakes (Fig. 1a). To better understand the crystallinity of intercalated materials, we performed scanning tunnelling microscopy (STM) imaging of the TBA-intercalated 2DSCs drop-cast onto the SiO_2/Si substrate with the pre-patterned Au electrodes (Supplementary Fig. 2). Large-scale STM image (Fig. 1b) reveals bright protrusions randomly scattered over the whole surface. At a low sample bias, we managed to resolve the intact atomic lattice in both flat and protrusion regions (Supplementary Fig 2b). This suggests that bright features are presumably associated with uniformly intercalated molecules buried under $NbSe_2$ surface layer, which can be rinsed off with solvent under sonication. Seven prototypical 2DSCs materials, including $Nb(Se/Te)_2$, $Ta(S/Se)_2$, $Ti(S/Se)_2$, and $MoTe_2$ were cathodically exfoliated, which demonstrates a generality of this method towards the synthesis of 2DSCs.

The thickness and crystallinity of as-exfoliated flakes were analysed to further evaluate the exfoliation efficiency of 2DSCs in Supplementary Fig. 3-9. Fig. 1c-h show the AFM images and line-profiles of as-exfoliated 2DSC monolayers. We note that all the layered TMD materials show a fast expansion and exfoliation behaviours but with a slightly different statistical thickness distribution, presumably attributed to the different interlayer bonding strength among all these TMDs. Due to the excellent conductivity of SC bulk materials as compared to semiconducting TMDs, we achieved a remarkable intercalation efficiency with a high yield (>80%) of 1-5 layers of 2DSC thin films as evidenced by a statistical analysis of multiple AFM images (Supplementary Fig 3-9). STEM imaging was then conducted to assess the density of atomic defects of as-exfoliated flakes. Large-view STEM images of monolayer TaS_2 (Fig. 1i) and $TiSe_2$ (Fig. 1j) flakes reveal nearly perfect atomic lattice with a very low defect density. The high crystallinity of all the other 2DSC monolayers are also confirmed by STEM images as shown in Supplementary Fig. 3-9. Our STEM

results reveal that the crystallinity of exfoliated 2DSC monolayers is superior to the monolayer flakes grown by MBE[8] and CVD[17] methods.

We now focus on NbSe$_2$,[8, 10, 29] a prototypical 2D superconductor as a model system to carry out a systematic investigation of the exfoliation efficiency and crystallinity of thin flakes as well as their superconducting properties. Under the optimized exfoliation condition (tetrapropyl ammonium (TPA) of 150 ppm, at -4 V), (Supplementary Fig. 14-17) a small portion of large-sized single crystal monolayer NbSe$_2$ (~300 µm) can be acquired via a direct detachment from the cathode. Note, that this is larger than the monolayer NbSe$_2$ flake obtained by CVD and mechanical exfoliation.[17] TPA-intercalated NbSe$_2$ laminates (Supplementary Fig. 17) can be readily exfoliated into monolayer[3] (>75% yield) and few-layer flakes dispersed in a wide range of solvents via a mild sonication for 30 seconds (Supplementary Fig. 18-19). These large-sized monolayer flakes were further deposited onto a carbon grid for TEM and STEM characterization (Supplementary Fig. 20). Large-view STEM-ADF image (Fig. 2d) of NbSe$_2$ flake reveals a long-range periodic bright (Se$_2$) and dim (Nb) dots arranged in the honeycomb lattice with the atomic defect density lower than that of monolayer grown by CVD growth (Supplementary Fig S21).[17] Selective area electron diffraction (SAED) was performed to probe the crystallinity of exfoliated flakes (Fig. 2e). Grain boundaries or disorders are absent in all the flakes studied, as verified by the observation of the same diffraction pattern with nearly identical orientation (±1.0º) for several randomly-chosen regions (Fig. 2c), which further confirms the exfoliated monolayer is a single crystalline flake.

As-exfoliated NbSe$_2$ flakes were patterned into a Hall-bar geometry with Cr/Au electrodes using e-beam lithography for low-temperature transport measurements. Fig. 2f shows the temperature dependence of the longitudinal resistance (R_{xx}) for a representative monolayer NbSe$_2$ flake at zero magnetic field. The residual resistance ratio (RRR), defined as the ratio between resistance at 300 K (R_{300K}) and resistance at the normal state resistance right above the transition temperature (R_{7K} in this

case), is an indicator of crystal quality.[17] Strong scattering from impurities and defects leads to a large residual resistance and thus a small RRR.[1] As-exfoliated NbSe$_2$ monolayer reveals a RRR of 3.5, smaller than that of mechanically-exfoliated NbSe$_2$ (~10)[10] but larger than the CVD-grown NbSe$_2$ (< 2)[17], suggesting a low density of defect/disorder in the exfoliated NbSe$_2$ monolayer. A negligible defect/disorder in NbSe$_2$ monolayer also results in a low resistance (~ 200 Ω/sq) at 7 K, well below h/$4e^2$ $\approx$ 6450 Ω that associated with the disorder-induced superconductor-insulator transition.[14, 30]

The superconducting transition temperature (T_c) of exfoliated NbSe$_2$ monolayer is determined to be ~3.2 K. Note that T_c was defined as the temperature where resistance drops to the half of normal state resistance (R_{7K}). Similarly, the upper critical field (H_{c2}) at finite temperature is defined as the field corresponding to half of R_{7K}. Fig. 2g and Supplementary Fig. 23 shows the temperature dependent R_{xx} under out-of-plane ($H_\perp$) and in-plane ($H_{//}$) magnetic field, respectively. The monolayer NbSe$_2$ exhibits a strong anisotropy in the superconductivity under the parallel ($H_{//}$) and perpendicular ($H_\perp$) magnetic fields. Fig. 2h shows the H_{c2}-Tc phase diagram for both $H_\perp$ and $H_{//}$. A linear correlation between temperature and $H_{c2}^\perp$, can be modelled by the 2D Ginzburg–Landau (GL) theory:[10, 29]

$$H_{C2}(T) = \frac{\phi_0}{2\pi\xi_{GL}^2(0)} \left(1 - \frac{T}{T_c}\right) \qquad (1)$$

where $\xi_{GL}(0)$ is the zero-temperature GL in-plane coherence length and ϕ_0 is the magnetic flux quantum. A fitting of experimental data ($H_{c2}^\perp$- Tc) to equation (1) yields an in-plane coherence length of $\xi_{GL}(0)$ = 16 nm, larger than the sample thickness (~1 nm) by a factor of 16. Such a long coherence length indicates a strongly suppressed depairing effect of orbital magnetic effect associated with $H_{//}$ in line with the characteristics of 2D superconductivity.[10] It is noted that $H_{c2}^{//}$ is greatly enhanced which goes beyond the Pauli paramagnetic limit ($H_p \sim 1.84\ T_c$), consistent with the Ising

superconductivity protected by Ising spin-orbit coupling.[10, 31] Current excitation measurements (Fig. 2i) shows that the *V-I* curve evolves from a linear to a power-law dependence ($V \propto I^{\alpha}$), in good agreement with Berezinskii-Kosterlitz-Thouless (BKT) model for 2D superconductors. The BKT transition temperature (T_{BKT}) is determined to be 2.9 K at $\alpha=3$ (Supplementary Fig. 24). All the transport data confirm that large-sized as-exfoliated monolayer $NbSe_2$ behaves as 2D Ising superconductor with a high crystallinity comparable with mechanically exfoliated flakes.[10]

The majority of monolayer TMDs superconductors are intrinsically air-sensitive, posing a formidable challenge towards their real applications[1, 6, 32]. Typically, a protection layer[33, 34] or sample preparation in the inert environment[10] is required for the device fabrication and characterisation of monolayer 2DSCs. In contrast, 2DSC monolayer suspensions show a significantly enhanced stability and processability, which permits sample processing in ways that would otherwise be difficult or impossible (Supplementary Fig. 25). In our case, excellent solvent protection prevents the air-degradation of vulnerable 2DSC monolayers in the solution phase, which allows for the synthesis and sample processing in ambient condition.

This property also helps enormously in the fabrication of vdWHs and their devices. Generally, fabrication of 3D stacks of air-sensitive 2D crystals is a very challenging task, which has to be undertaken in glove-boxes or vacuum chambers within a short period of time[6, 35]. In contrast, protective properties of the solvent significantly enhance the lifetime of the flakes in ambient conditions[26, 28]. At the same time, the self-cleaning properties of the 2D crystals[36] efficiently remove the residual solvent, leaving the interface to be very clean. In order to demonstrate these advantages of our preparation method, we created twisted flakes of $NbSe_2$ and studied their transport properties.

The device was first prepared by drop-casting the TPA-exfoliated $NbSe_2$ flakes on the surface of Si/SiO_2 (300 nm of oxide). We then selected the overlapping flakes and deposited Ti/Au (3 nm/80 nm) contacts on various parts of the sample using the standard lithography procedure. All manipulations of

the sample were conducted under the ambient conditions. The transport properties of one of our devices are presented in Fig 3. The device consists of the two overlapping flakes–the top flake (outlined with orange, two-layer thick) and middle one (outlined with cyan, three-layer thick). The magnetic dependence of the differential resistance (dV/dI) and the temperature dependence of the resistance for a single flake resistance are presented in Fig 3b,f. Note that the magnetic field dependence of the critical current for both flakes is very weak in the field range presented.

Fig 3c,d presents the magnetic field dependence of the junction, where the current is directed from one flake to another. The critical current associated with the superconducting to normal transition for each flake can be seen. On the overlapping flakes the superconducting to normal transition has a strong oscillatory behaviour as a function of magnetic field. We attribute this transition to the superconducting/normal transition at the interface between the two flakes. Different junctions have different periods of the oscillations. Thus, oscillations coming from junction 2 have a period of B=8mT, which can be converted to a specific area A as A= Φ_0/B, where Φ_0 = h/(2e) is the superconducting magnetic flux quantum ($\Phi_0 \sim 2$ mT·μm^2) resulting in A=0.25 μm^2. We associate this specific area with the formation of the moiré pattern at the interface between the two closely-aligned flakes (Fig 3e).

The observed behaviour of the critical current in the presence of the applied magnetic field is reminiscent of the effect of a magnetic field on a frustrated superconducting Josephson junction array with triangular symmetry[37]. The controlling parameter in this case is the so-called *frustration* fraction that is defined as $f = B\ A/\ \Phi_0$, where A is the area of the moiré unit cell. For such arrays the critical current is periodic in Φ_0 (which we associate to the two large peaks in Fig. 3h at B $\sim \pm$ 8 mT) and has extra peaks at special frustration factors due to the formation of crystal vortex lattices[38]. For the triangular lattice the strongest secondary peak occurs at f = ½[39]. As shown in Fig. 3h, we possibly observe peaks at B $\sim$ -5 mT, -12mT, 12mT corresponding to $f \sim$ -0.5, -1.5, 1.5 as expected. Hence, our results are consistent with the proposed picture that the Moiré pattern between two slightly-twisted crystals act as a periodic Josephson junction array with the period of the moiré lattice (Fig. 3e). We

estimate from the area of the total overlapping interface ($\sim 10 \ \mu m^2$), we estimate that there are hundreds of Moiré-Josephson junctions formed between crystals that are described in terms of a frustrated classical 2D X-Y model with triangular symmetry.

Both individual thin flakes and the junction demonstrate the same transition temperature as bulk NbSe2, suggesting that the protective properties of TPA and self-cleaning mechanism at the interface enables the survival of these flakes during the lengthy fabrication process without encapsulation support. This will open a new avenue of simplified fabrication of NbSe2 devices, which will definitely lead to new and exciting physics observed in such materials.

Moreover, the dispersion of monolayer NbSe2 superconductors in solvents allows them to be in excellent compatibility with current thin film fabrication and printing technologies.[40, 41] As shown in Fig. 4a, TPA-intercalated NbSe2 samples can be readily dispersed in various solvents with just a mild sonication (Supplementary Table 1). The prepared materials can then be used in ink formulation for both 2D inkjet and 3D printing technologies (Supplementary Fig S27-29). Fig. 4b-d demonstrate that a wafer-scale NbSe2 superconducting wires can be patterned on a 4-inch SiO2 substrate using inkjet printing. AFM image reveals a continuous film with relatively uniform in-plane stacking for the printed NbSe2 flakes. Subsequently, an array of electrodes was deposited onto these printed atomic layers to evaluate their superconducting properties. Similar to NbSe2 bulk[10], printed NbSe2 film (~100 nm in thickness) shows an upper critical field $H_{c2}^{\perp}$~4.4 T (Fig 4f) and a linear $H_{c2}^{\perp}$-T_C dependence. However, the in-plane magnetic response of printed NbSe2 film resembles that of the NbSe2 monolayer with an upper critical field $H_{c2}^{//}$ far exceeding its BCS Pauli paramagnetic limit (H$_P$) (Fig 4g), suggesting the 2D superconductivity nature of the printed NbSe2 film[10]. The printed NbSe2 film also exhibits a high transition temperature (T_C~6.8 K) and high upper critical field ($H_{c2}^{\perp}$~4.4 T, $H_{c20}^{//}$~29 T). In addition, individual re-stacked few-layer NbSe2 flakes also reveal the co-existence of bulk-like transition temperature (TC~6.5 K) and monolayer-like upper critical field ($H_{c20}^{//}$~30 T) (Supplementary Fig S31), presumably attributed to the formation of interlayer

Josephson junctions with contribution from Pauli paramagnetism and spin-orbit scattering in 2D TMD superconductors42.

CONCLUSION

In summary, we have successfully developed a universal and mild electrochemical exfoliation approach for the scalable production of a library of highly crystalline 2D superconducting monolayers in solution phase. The single crystal domain size and crystallinity of as-exfoliated 2DSC monolayers are comparable to (in some cases, even superior to) the monolayer flakes obtained by other method including CVD and MBE growth. Moreover, 2DSC monolayer suspension shows a remarkably enhanced environmental stability and solution processability. These materials can be readily integrated with the current 2D and 3D printing technologies for the fabrication of wafer-scale superconducting device arrays, which offers a huge technological potential beyond the reach of the existing materials.

Methods

   Cathodic intercalation of layered materials with quaternary ammonium cations (QUATs): cathodic intercalation of layered TMDs in the QUAT-based electrolyte was carried out in a two-electrode system using an electrochemical workstation (CHI 760E).[26] Typically, a bulk TMD crystal with the size of ~ 2×2×1 (length × width × thickness) mm^3 was fixed on a Pt clip as cathode and a Pt wire served as anode. For a general exfoliation of 2DSCs, tetrabutyl ammonium tetrafluroborate (TBABF4) dissolved in propylene carbonate (PC) with a concentration of 0.05 M was used as electrolyte. To exfoliate 2DSCs, a voltage of -5 V *Vs* Pt wire was applied on cathode for 30 min.

Subsequently, the delaminated flakes from electrode will be subjected to bath sonication at 100 W for 30 seconds for a further exfoliation. All the solvents and ammonium ions were purchased from Sigma Aldrich (>99% of purity) and used as received. The layered materials were bought from HQ graphene and used as received.

NbSe$_2$ Ink formulation for 2D ink-jet printing. TPA-intercalated NbSe$_2$ flakes were sonicated and rinsed in acetone followed by a centrifugation at 12000 rpm for 20 min to remove all the residual intercalant and solvent. Subsequently, NbSe$_2$ flakes were re-dispersed in N,N-Dimethylformamide (DMF) under a sonication for 5 min. NbSe$_2$ dispersion was then filtrated through a filter membrane to remove the large-sized (>2 µm) flakes. Fujifilm Dimatix Materials Printer (DMP-2850) equipped with a 10 picoliter nozzle cartridge is used to print and pattern as-obtained NbSe$_2$ ink into superconducting wires. An electrode array (Cr/Au (3/80 nm) was patterned on printed NbSe$_2$ wires using laser lithography (Microtech Laser Writer LW405B).

NbSe$_2$ Ink formulation for 3D printing. TPA-exfoliated NbSe$_2$ flakes were mixed with commercial Genesis resin (Tethon 3D) for ink formulation (1 wt% of NbSe$_2$). Digital light projector (DLP) technology was used for printing of 3D superconducting objects with the setting parameters as follows: light intensity (33.4 mW/cm^2); slice thickness (0.05 mm) and exposure time (5 s) in each slice.

Characterization: The morphology of exfoliated 2DSC flakes is characterized by SEM (FEI Verios 460 operated at 2 kV and 100 pA), AFM (Bruker Multimode 8 in Ar glove-box and DIMENSION FastScan in air) and HRTEM (FEI Titan 80-300 S/TEM operated at 200 kV). Raman spectroscopic measurements (WITec Alpha 300R) were performed at room temperature with a laser excitation at 532 nm and power of <300 µW. Scanning transmission electron microscopy-annual dark field

(STEM-ADF) was performed using an aberration-corrected JEOL-ARM200F, equipped with a cold field emission gun, operated at 60 kV. The convergence semiangle of the probe was ≈ 30 mrad. STEM-ADF images of metal diselenide, and metal disulfide were collected using a half-angle range from ≈ 85 to 280 mrad, and ≈ 30 to 110 mrad, respectively. XPS was carried out with SPECS XR-50 X-ray Mg Kα (1253.7 eV) source. Hall-bar devices were fabricated with a standard electron-beam lithography procedure combined with thermal evaporation for the patterning metal electrodes consisting of Cr/Au of 3/80 nm. Temperature dependent resistance of Hall-bar device was measured in an Oxford Teslatron PT 12 cryostat. The magnetization of $NbSe_2$ power or 3D printing structures were characterized using a SQUID (quantum design MPMS 3) magnetometer with a temperature range of 2-300 K and an applied field range of -5,000 to 5000 Oe.

Author contributions

J.Lu supervised the project. J.Li. K.S.Novoselov. and J.Lu. conceived the research and wrote the paper. J.Li. and Z.J.Li. performed the cathodic intercalation and exfoliation experiment. P.Song. and J.Li. fabricated the Hall-bar and vdWHs device. P.Song. carried out the low-temperature transport measurement of Hall-bar devices and analysed the results, J.P.Zhao and K.Vaklinova. performed the low-temperature transport measurement of twisted $NbSe_2$ vdWHs devices. K.S.Novoselov and A.H Castro Neto analysed the transport results. X.X.Zhao. performed the STEM imaging of exfoliated

layered sheets and analysis. Z.Z.Qiu. assisted with the STM imaging of TBAs and TPAs intercalated

NbSe$_2$ structure. M.Zhao. performed inkjet printing of superconducting wires. Y.X.Zuo. and

W.Jonhson. carried out the 3D printing. T.S. Herng. assisted with the superconductivity

measurement of 2D and 3D printing structures. J.Li. performed the TEM, AFM and Raman

characterization. All authors discussed and commented on the manuscript.

Competing interests

The authors declare no competing interest.

Additional information

Supplementary information including detailed experimental procedures, characterization is available

in the online version of the paper.

REFERENCES

1. Saito Y, Nojima T, Iwasa Y. Highly crystalline 2D superconductors. *Nat Rev Mater* **2**, 16094 (2016).
2. Xu X, Yao W, Xiao D, Heinz TF. Spin and pseudospins in layered transition metal dichalcogenides. *Nat Phys* **10**, 343 (2014).
3. Xi X*, et al.* Strongly enhanced charge-density-wave order in monolayer NbSe$_2$. *Nat Nanotechnol* **10**, 765 (2015).
4. Li LJ, O'Farrell ECT, Loh KP, Eda G, Özyilmaz B, Castro Neto AH. Controlling many-body states by the electric-field effect in a two-dimensional material. *Nature* **529**, 185 (2015).
5. Qin S, Kim J, Niu Q, Shih C-K. Superconductivity at the Two-Dimensional Limit. *Science* **324**, 1314-1317 (2009).
6. Geim AK, Grigorieva IV. Van der Waals heterostructures. *Nature* **499**, 419-425 (2013).
7. Liu Y, Weiss NO, Duan X, Cheng H-C, Huang Y, Duan X. Van der Waals heterostructures and devices. *Nat Rev Mater* **1**, 1-17 (2016).
8. Ugeda MM*, et al.* Characterization of collective ground states in single-layer NbSe$_2$. *Nat Phys* **12**, 92 (2015).
9. Joe YI*, et al.* Emergence of charge density wave domain walls above the superconducting dome in 1T-TiSe$_2$. *Nat Phys* **10**, 421 (2014).
10. Xi X*, et al.* Ising pairing in superconducting NbSe$_2$ atomic layers. *Nat Phys* **12**, 139 (2015).
11. Ge J-F*, et al.* Superconductivity above 100 K in single-layer FeSe films on doped SrTiO$_3$. *Nat Mater* **14**, 285 (2014).
12. Saito Y, Kasahara Y, Ye J, Iwasa Y, Nojima T. Metallic ground state in an ion-gated two-dimensional superconductor. *Science* **350**, 409-413 (2015).
13. Graybeal JM, Beasley MR. Localization and interaction effects in ultrathin amorphous superconducting films. *Phys Rev B* **29**, 4167-4169 (1984).

14. Jaeger HM, Haviland DB, Orr BG, Goldman AM. Onset of superconductivity in ultrathin granular metal films. *Phys Rev B* **40**, 182-196 (1989).

15. Hebard AF, Paalanen MA. Magnetic-field-tuned superconductor-insulator transition in two-dimensional films. *Phys Rev Lett* **65**, 927-930 (1990).

16. Zhou J*, et al.* A library of atomically thin metal chalcogenides. *Nature* **556**, 355-359 (2018).

17. Wang H*, et al.* High-quality monolayer superconductor $NbSe_2$ grown by chemical vapour deposition. *Nat Commun* **8**, 394 (2017).

18. Lin H*, et al.* Growth of environmentally stable transition metal selenide films. *Nat Mater* **18**, 602-607 (2019).

19. Cai X, Luo Y, Liu B, Cheng H-M. Preparation of 2D material dispersions and their applications. *Chem Soc Rev* **47**, 6224-6266 (2018).

20. Han JH, Kwak M, Kim Y, Cheon J. Recent advances in the solution-based preparation of two-dimensional layered transition metal chalcogenide nanostructures. *Chem Rev* **118**, 6151-6188 (2018).

21. Peng J*, et al.* Very large-sized transition metal dichalcogenides monolayers from fast exfoliation by manual shaking. *J Am Chem Soc* **139**, 9019-9025 (2017).

22. Cullen PL*, et al.* Ionic solutions of two-dimensional materials. *Nature chemistry* **9**, 244 (2017).

23. Lin Z*, et al.* Solution-processable 2D semiconductors for high-performance large-area electronics. *Nature* **562**, 254-258 (2018).

24. Chen P*, et al.* Charge density wave transition in single-layer titanium diselenide. *Nat Commun* **6**, 8943 (2015).

25. Yu Y*, et al.* Gate-tunable phase transitions in thin flakes of 1T-TaS2. *Nat Nanotechnol* **10**, 270 (2015).

26. Li J*, et al.* Ultrafast electrochemical expansion of black phosphorus toward high-yield synthesis of few-Layer phosphorene. *Chem Mater* **30**, 2742-2749 (2018).

27. Kang J*, et al.* Solvent Exfoliation of Electronic-Grade, Two-Dimensional Black Phosphorus. *ACS Nano* **9**, 3596-3604 (2015).

28. Hanlon D*, et al.* Liquid exfoliation of solvent-stabilized few-layer black phosphorus for applications beyond electronics. *Nat Commun* **6**, 1-11 (2015).

29. Tsen AW*, et al.* Nature of the quantum metal in a two-dimensional crystalline superconductor. *Nat Phys* **12**, 208 (2015).

30. Fiory AT, Hebard AF. Electron mobility, conductivity, and superconductivity near the metal-insulator transition. *Phys Rev Lett* **52**, 2057-2060 (1984).

31. Lu JM*, et al.* Evidence for two-dimensional Ising superconductivity in gated MoS_2. *Science* **350**, 1353 (2015).

32. Li Q, Zhou Q, Shi L, Chen Q, Wang J. Recent advances in oxidation and degradation mechanisms of ultrathin 2D materials under ambient conditions and their passivation strategies. *J Mater Chem A* **7**, 4291-4312 (2019).

33. Cao Y*, et al.* Quality Heterostructures from Two-Dimensional Crystals Unstable in Air by Their Assembly in Inert Atmosphere. *Nano Lett* **15**, 4914-4921 (2015).

34. Khestanova E*, et al.* Unusual Suppression of the Superconducting Energy Gap and Critical Temperature in Atomically Thin $NbSe_2$. *Nano Lett* **18**, 2623-2629 (2018).

35. Cao Y*, et al.* Quality heterostructures from two-dimensional crystals unstable in air by their assembly in inert atmosphere. *Nano Lett* **15**, 4914-4921 (2015).

36. Kretinin A*, et al.* Electronic properties of graphene encapsulated with different two-dimensional atomic crystals. *Nano Lett* **14**, 3270-3276 (2014).

37. Garland RKBaJC. Effect of magnetic-field-induced frustration on the superconducting transition of proximity-coupled arrays. *Physical Review B*, 7827 (R) (1986).

38. Jayaprakash STaC. Josephson-junction arrays in transverse magnetic fields. *Physical Review Letters*, 1999 (1983).

39. Strout WYSaD. Two-dimensional superconducting arrays in a magnetic feild: effects of lattice structures. *Physical Review B*, 158 (1985).
40. Bonaccorso F, Bartolotta A, Coleman JN, Backes C. 2D-Crystal-Based Functional Inks. *Adv Mater* **28**, 6136-6166 (2016).
41. Macdonald E*, et al.* 3D Printing for the Rapid Prototyping of Structural Electronics. *IEEE Access* **2**, 234-242 (2014).
42. Klemm RA, Luther A, Beasley M. Theory of the upper critical field in layered superconductors. *Phys Rev B* **12**, 877 (1975).
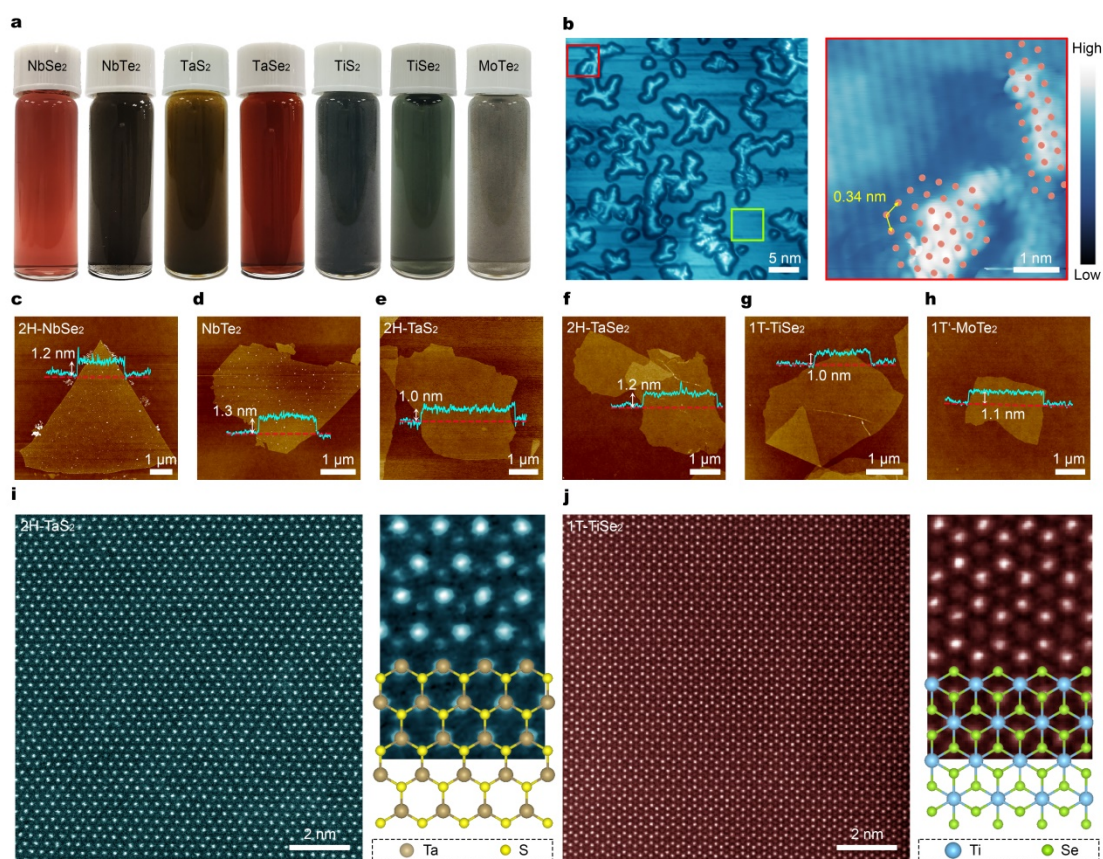
Fig. 1 A general synthesis of 2D superconducting monolayers via cathodic exfoliation. a, Photographs of a series of exfoliated 2DSCs dispersed in PC solvent. **b**, large-area (left image) and magnified-view (from the area labelled with red square) STM imaging of TBA-intercalated $NbSe_2$. Atomic lattice of $NbSe_2$ in green square can be seen in Supplementary Fig 2. Tunnelling parameter: -2.2 V, 10 pA (large-area image); -0.15 V, 80 pA (magnified-view image). **c-h,** AFM images and height profiles of various exfoliated 2DSC monolayers using TBA cations as electrochemical intercalant. Atomic-resolution STEM-ADF images of as-exfoliated (**i**) $2H$-TaS_2 and (**j**) $1T$-$TiSe_2$ monolayer. Close-up STEM-ADF image with the corresponding atomic model is presented in the right panel. Scale bars, 5 nm (**b,** left image), 1 nm (**b,** left image), 1 μm (**c-h,** AFM images) and 2 nm (**i-j,** STEM images).
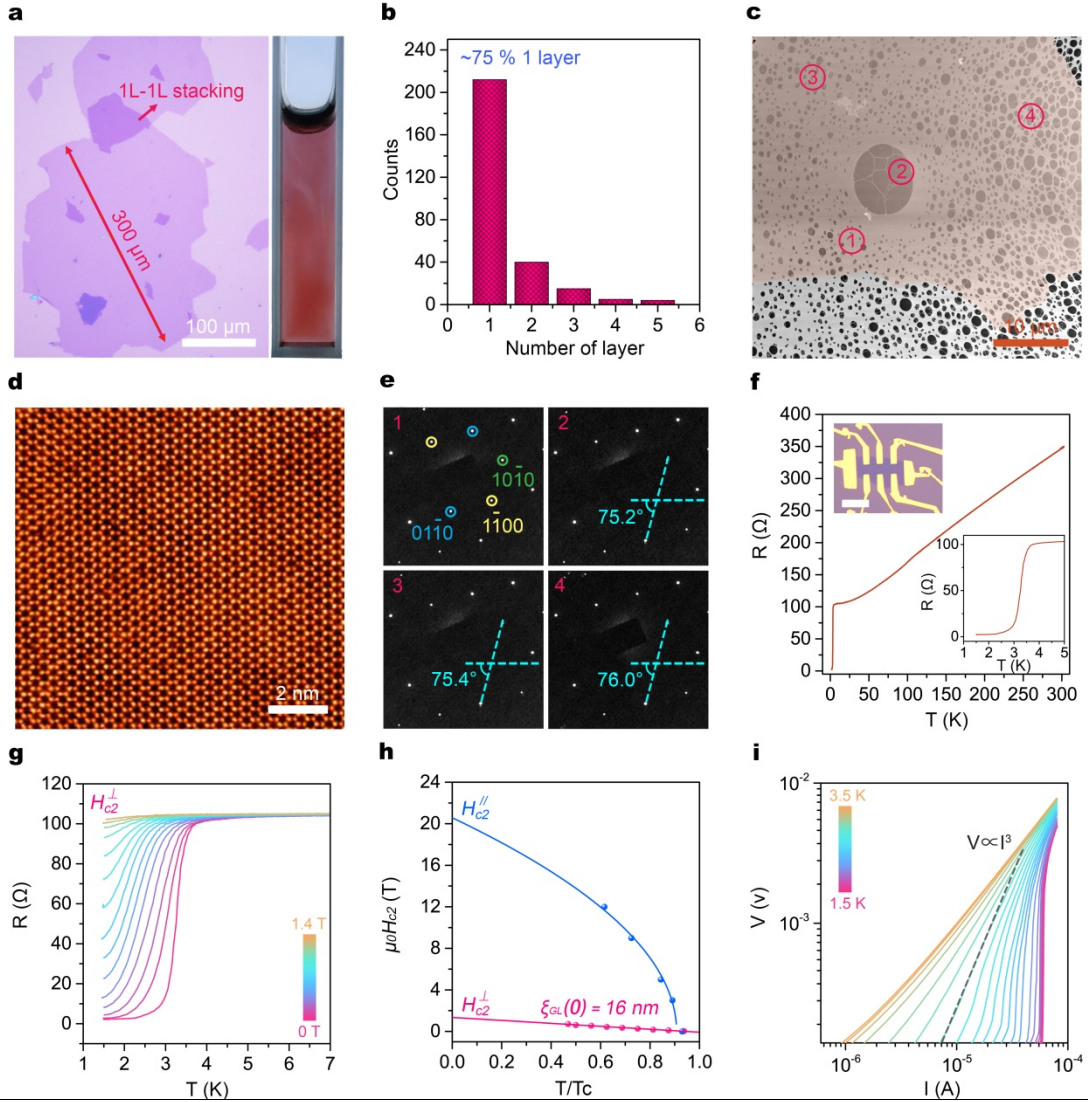
Fig. 2 Structural and superconductivity characterization of highly crystalline NbSe₂ monolayer
a, Optical microscopic image of a representative large-sized NbSe₂ monolayer (~300 μm). Right inset: exfoliated NbSe₂ flakes in PC. **b,** Histogram of the thickness distribution of as-exfoliated NbSe₂ flakes. **c,** SEM image of as-exfoliated NbSe₂ flake (highlighted in false colour) drop-cast onto a TEM grid. Zoom-in SEM image in Supplementary Fig 20.**d,** Atomically-resolved STEM-ADF image shows the intact lattice of monolayer NbSe₂. **e,** The corresponding SAED patterns are acquired from various regions marked in panel (**c**). The angle between [01$\bar{1}$0] direction and horizontal axis is indicated in each panel. **f,** T-dependent longitudinal resistance (R_{xx}) for a monolayer NbSe₂ device. Upper inset: optical microscopic image of a typical monolayer NbSe₂ Hall-bar device. Lower inset: Resistance detail from 1.5 to 7 K. **g,** T-dependent R_{xx} of a monolayer NbSe₂ device under different perpendicular magnetic field ranging from 0 to 1.4 T. **h,** T-dependent upper critical field H_{c2} under out-of-plane ($H_\perp$) and in-plane ($H_{//}$) magnetic fields. The solid lines: the fitting based on Ginzburg-Landau theory. **i,** Voltage-current (V-I) characteristics at different temperatures on a logarithmic scale. Dashed line indicates the expected $V \propto I^3$ behaviour at the Berezinskii-Kosterlitz-Thouless (BKT) transition. Scale bars, 100 μm (**a**), 10 μm (**c**), 2 nm (**d**) and 20 μm (**f**).
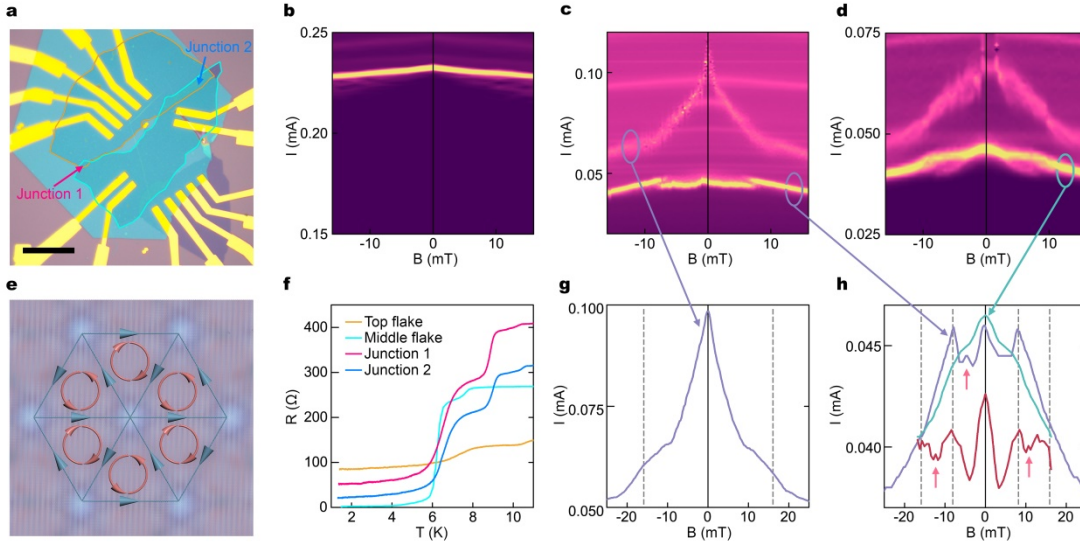
Fig. 3 Josephson junction arrays in van der Waals heterostructures based on twisted NbSe₂. a, Optical microscopic image of one twisted NbSe$_2$ device. The cyan border line marks a three-layer thick NbSe$_2$ flake and orange border line marks a two-layer thick NbSe$_2$ flake. The overlapping regions of the two flakes form two Josephson junctions arrays. Gold contacts were deposited on NbSe$_2$ flake and then this device was covered with hBN (green region). **b**, Differential resistance of middle flake (marked by cyan in **a**) versus current and magnetic field. Superconductivity transition is conspicuous here and the critical current has linear dependence on magnetic field. Colour scale from purple to yellow: 0 Ω - 3 kΩ. **c**, Differential resistance measured when current is sent from the top flake (marked by orange in **a**) to the middle flake (marked by cyan in **a**) versus current and magnetic field. Superconductivity transition associated with junction 1 and 2 are visible here and have oscillatory dependence on magnetic field. Colour scale from purple to yellow: 0 - 600 Ω. **d**, Same as **c** just for a different configuration of the contacts. **e**, Schematics of the vortex configuration for the case of half flux quanta per moire unit cell. The arrow indicates direction of supercurrent flow. Current flow will form a closed loop in one triangular with the adjacent triangular having the opposite vortex. **f**, Resistance across two flakes and two junctions are measured with temperature going down. Superconducting transition appears in all the four parts. **g**, Dependence of the critical current of junction 1 as a function of magnetic field. Extracted from **c**. **h**, Dependence of the critical current of junction 2 as a function of magnetic field for different contacts configurations (purple curved is extracted from **c** and green curve -from **d**). For clarity, parabolic background was subtracted from the green curve, resulting in the red curve. Grey lines are equidistant and mark position of the peaks. Green arrows mark peaks observed at half-integer values of frustration fraction. Measurements in **b**,**c**,**d**,**g**,**h** are done at 1.3 K.
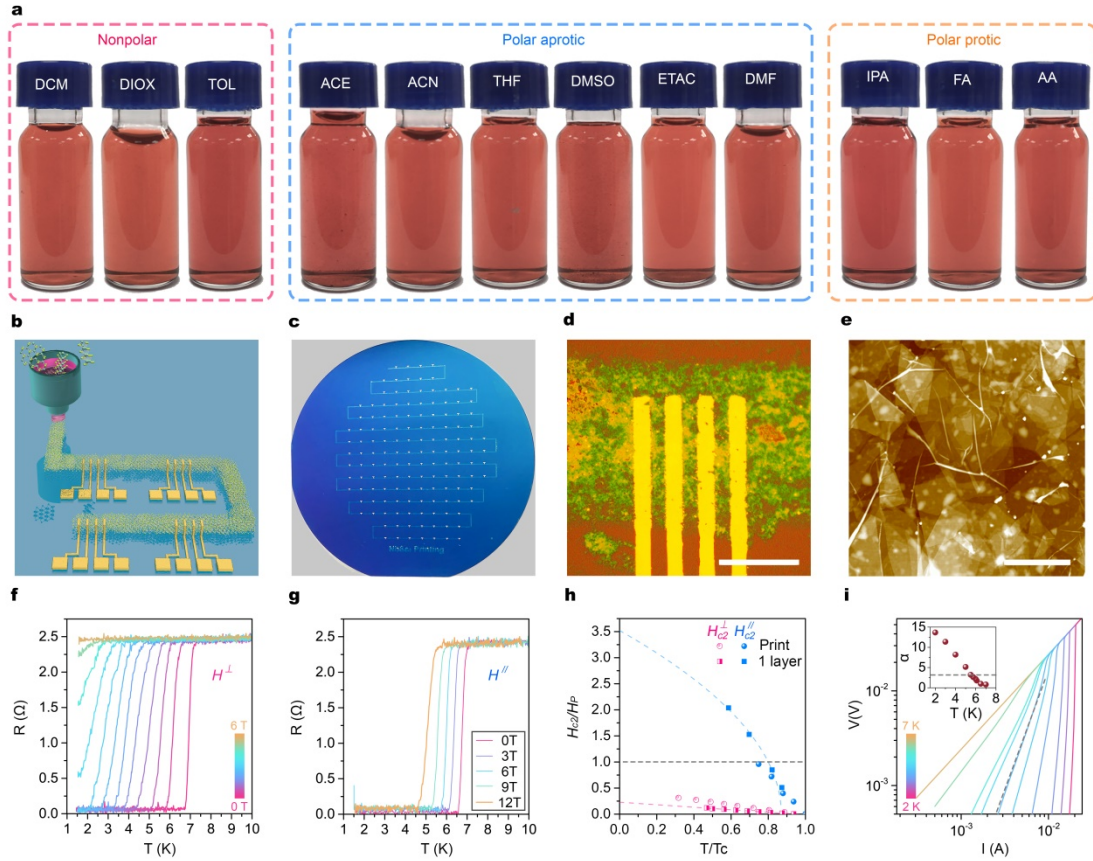
Fig. 4 Printing the exfoliated NbSe₂ flakes. a, Dispersion of exfoliated NbSe$_2$ flakes in a diversity of solvents. Note: the full name for these solvent are provided in Supplementary Table 1. **b,** Schematic illustration, (**c**) digital photograph, (**d**) optical microscopic image and (**e**) AFM morphology of a printed large-area superconducting NbSe$_2$ wire on a 4-inch SiO$_2$/Si wafer. (**f-i**) 2D superconductivity of printed NbSe$_2$ film. **f-g,** T-dependent longitudinal resistance (R_{xx}) of a printed NbSe$_2$ film under different (**f**) out-of-plane ($H_\perp$) and (**g**) in-plane ($H_{//}$) magnetic field. **h,** The critical field H_{c2}/H_p as a function of transition temperature T_c/T_{c0} for printed NbSe$_2$ film under out-of-plane ($H_\perp$) and in-plane ($H_{//}$) magnetic fields. The critical field H_{c2} and the critical temperature T_c are normalized by the BCS Pauli paramagnetic limit H_p and T_{c0} respectively for comparison. **i,** Voltage-current (V-I) characteristics at different temperatures on a logarithmic scale. Dashed line indicates the expected $V \propto I^3$ behaviour at the Berezinskii-Kosterlitz-Thouless (BKT) transition

Supporting Information

Printable 2D superconducting monolayers

Table of contents:

25.   *T-dependent R_{xx} of patterned NbSe$_2$ film using inkjet printing.*

26.   *2D superconductivity of re-stacked NbSe$_2$ monolayers.*

1. PC solvent for intercalation.
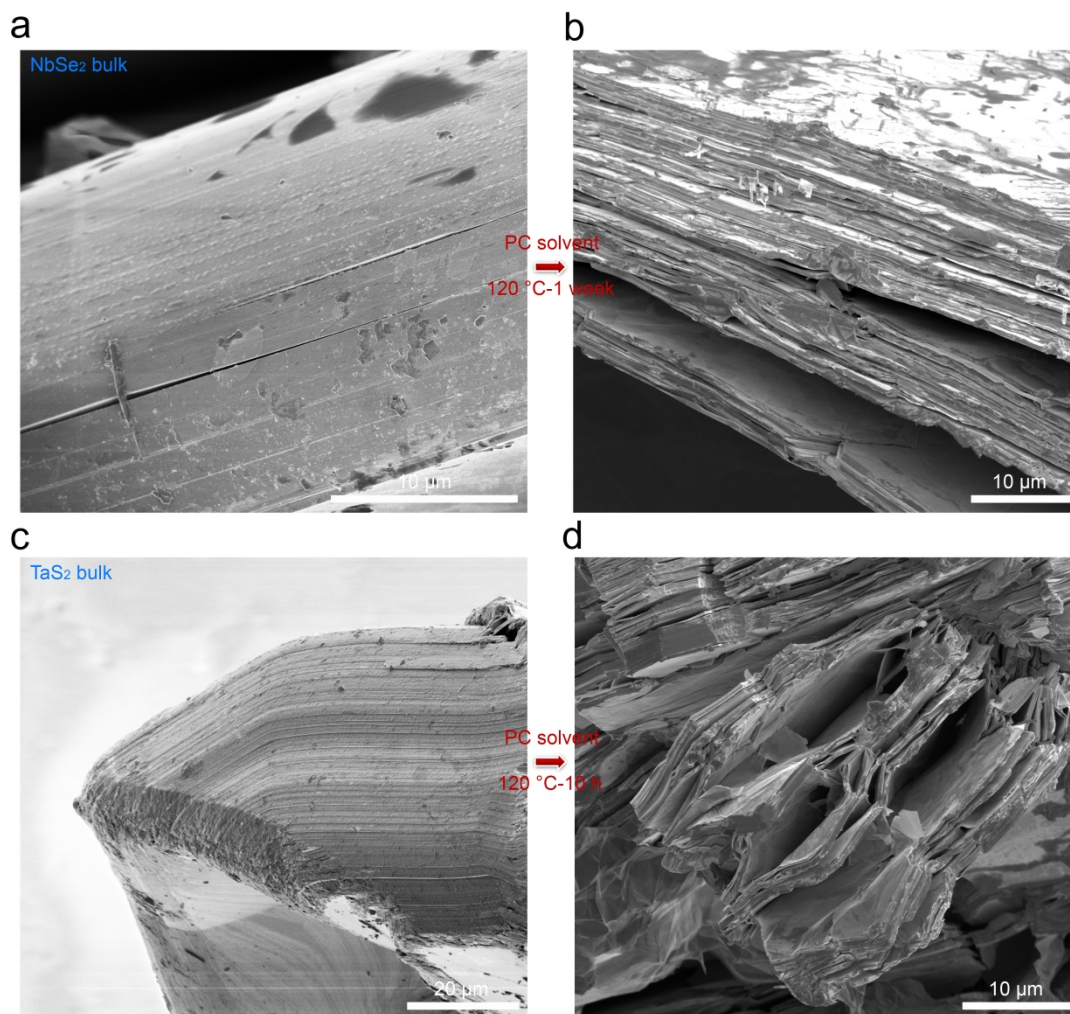
Fig. S1 SEM images of PC-intercalated SC bulks.

In this work, we tried to maximize the solvent intercalation of 2D materials, different from the previous intercalation strategies[1, 2]. The surface tension of propylene carbonate (PC) is 41.9 mJ/m^2, close to the surface energy of TMD crystals[3], which allows for an excellent dispersion of TMD sheets inside PC solvent. This is further supported by additional experimental observation that bulk $NbSe_2$ and TaS_2 crystals gradually swell and expand upon soaking in PC solvent, as shown in Fig. S1 (note the edge of bulk TMD crystal will open up in polar solvent, and thick flake can be obtained).

2. TBA-intercalated NbSe₂ for STM imaging.
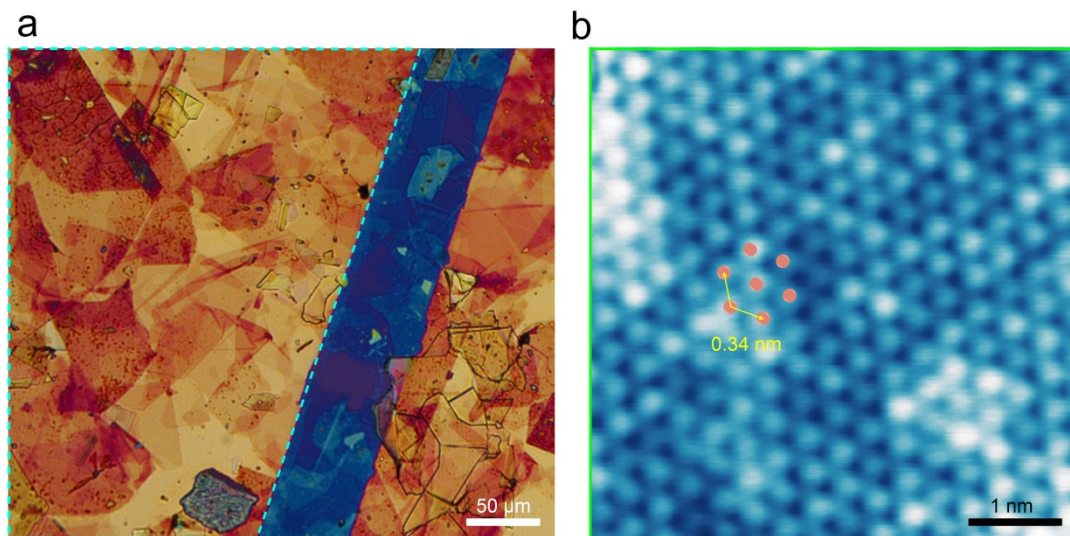
Fig. S2 TBA-intercalated NbSe$_2$ for STM imaging. **a**, Optical microscopic image of TBA-intercalated NbSe$_2$ flakes drop-cast onto a SiO$_2$ substrate with pre-patterned Au electrodes (80 nm thickness). The Au electrode is marked by dashed cyan line. **b**, STM imaging of TBA-intercalated NbSe$_2$ corresponds to the flat region marked by the green squares in Fig. 1b. Tunnelling parameter: -0.01 V, 260 pA (**b**).

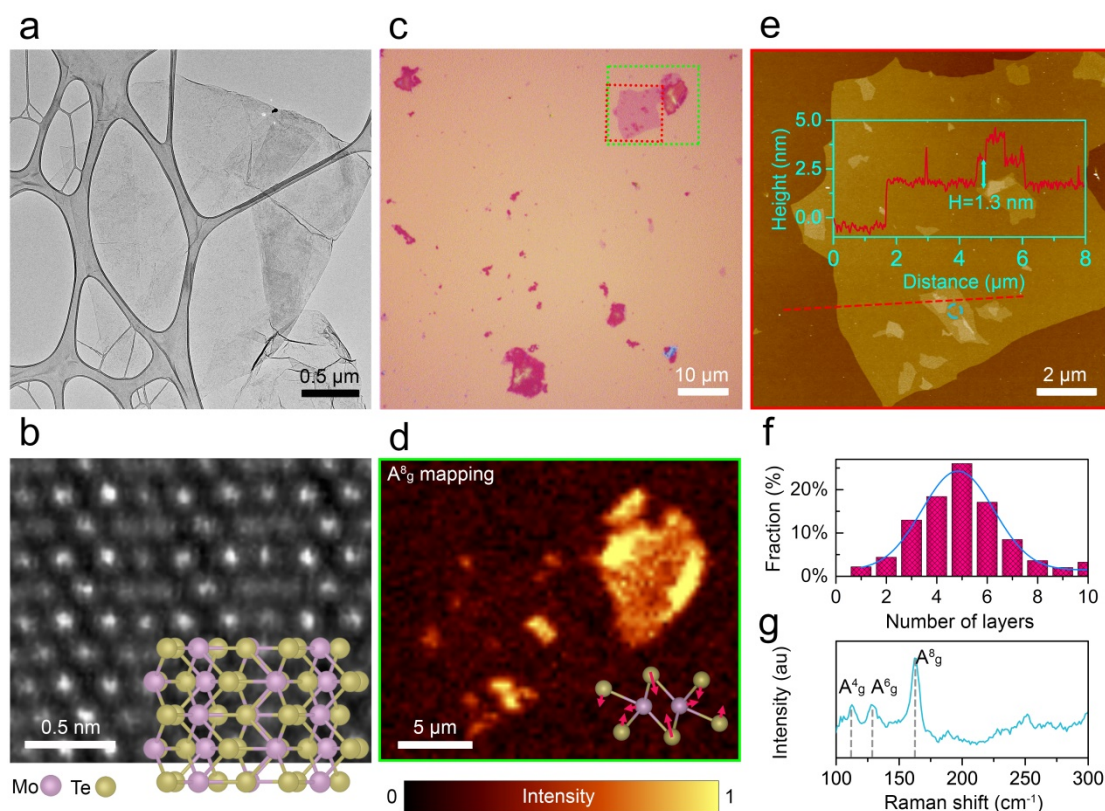# 3. Structure characterization of TBA-exfoliated 2DSCs.

3.1 NbSe₂.
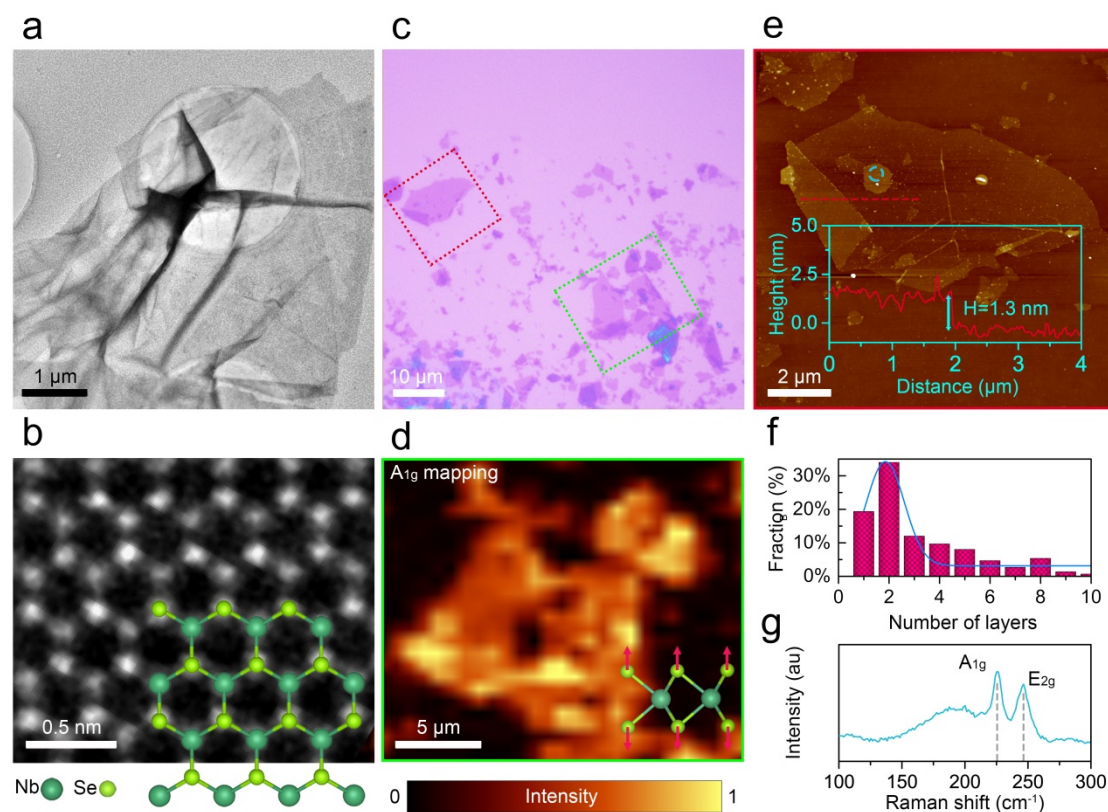
Fig. S3 Structure characterization of TBA-exfoliated NbSe₂ flakes. a-b, large-area TEM (**a**) and atomically-resolved STEM-ADF (**b**) images of TBA-exfoliated NbSe₂ monolayer. The corresponding atomic model of NbSe₂ monolayer is overlaid in the bottom of panel (**b**). **c**, Optical microscopic image of TBA-exfoliated NbSe₂ flakes drop-cast onto a SiO₂/Si substrate. **d-e**, The Raman mapping (**d**) and AFM topographic (**e**) images of the regions indicated by dashed-box in panel (**c**). Inset of panel (**d**) shows the A_{1g} Raman-active vibrational mode of NbSe₂.[4] Inset of panel (**e**) shows the cross-sectional height profile along the dashed line. **f-g**, The thickness distribution (**f**) and Raman spectrum (**g**) (in the area marked by dashed spot in panel (**e**)) of as-exfoliated NbSe₂ flakes.

3.2 NbTe₂.
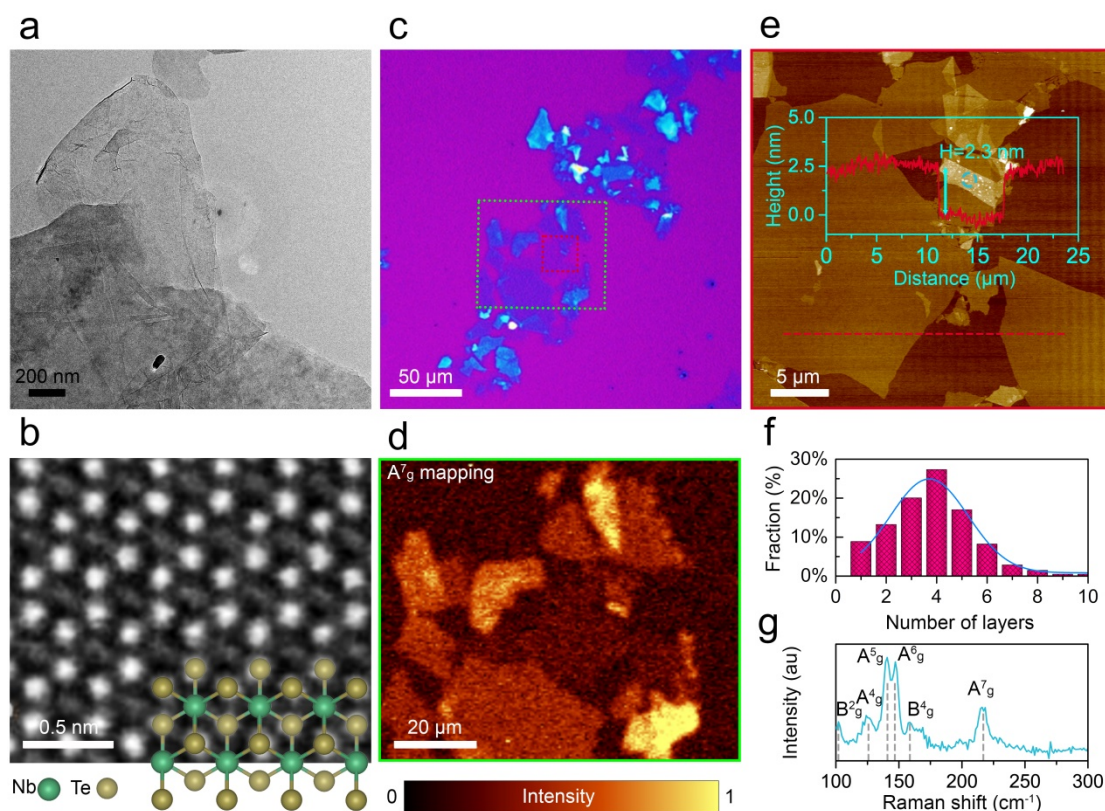


Fig. S4 Structure characterization of TBA-exfoliated NbTe₂ flakes. a-b, large-area TEM (**a**) and atomically-resolved STEM-ADF (**b**) images of TBA-exfoliated NbTe₂. The corresponding atomic model of NbSe₂ is overlaid in the bottom of panel (**b**). **c**, Optical microscopic image of TBA-exfoliated NbTe₂ flakes drop-cast onto a SiO₂/Si substrate. **d-e**, The Raman mapping (**d**) and AFM topographic (**e**) images of the regions indicated by dashed-box in panel (**c**). Inset of panel (**e**) shows the cross-sectional height profile along the dashed line. **f-g**, The thickness distribution (**f**) and Raman spectrum (**g**) (in the area marked by dashed spot in panel (**e**)) of as-exfoliated NbTe₂ flakes.[5]

3.3 TaS$_2$.
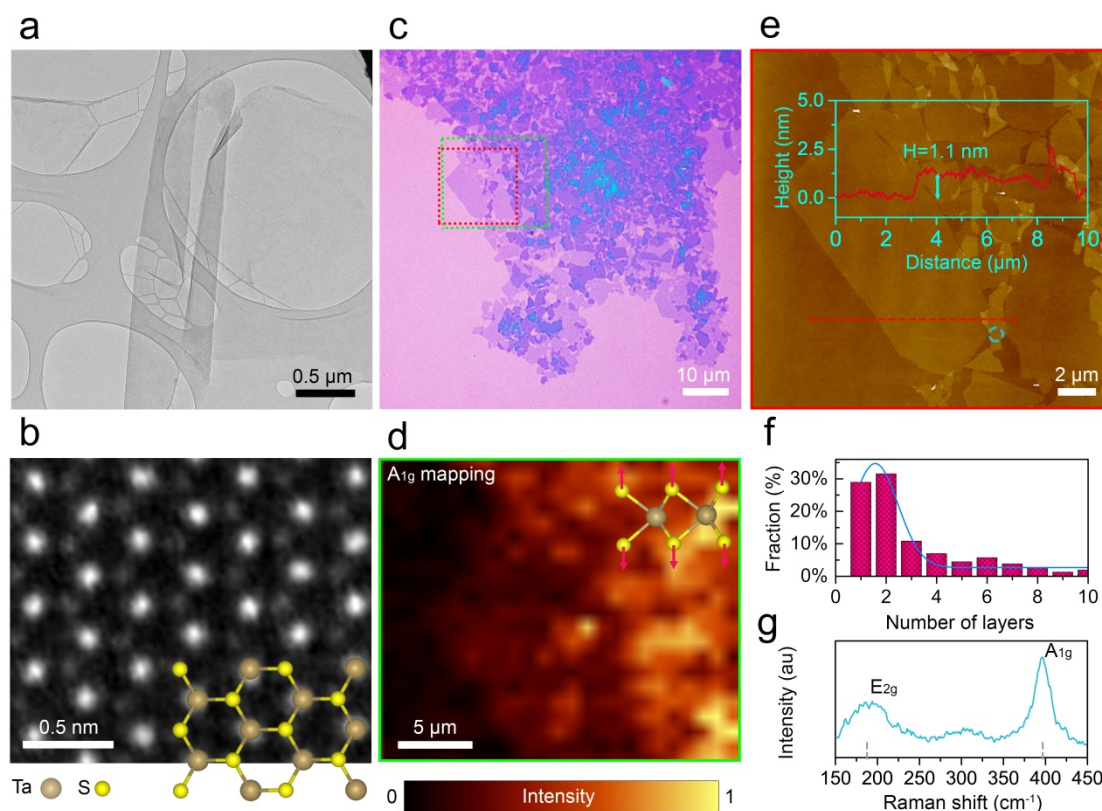
Fig. S5 Structure characterization of TBA-exfoliated TaS$_2$ flakes. a-b, large-area TEM (**a**) and atomically-resolved STEM-ADF (**b**) images of TBA-exfoliated TaS$_2$ monolayer. The corresponding atomic model of TaS$_2$ monolayer is overlaid in the bottom of panel (**b**). **c**, Optical microscopic image of TBA-exfoliated TaS$_2$ flakes drop-cast onto a SiO$_2$/Si substrate. **d-e**, The Raman mapping (**d**) and AFM topographic (**e**) images of the regions indicated by dashed-box in panel (**c**). Inset of panel (**d**) shows the A$_{1g}$ Raman-active vibrational modes of TaS$_2$.[6] Inset of panel (**e**) shows the cross-sectional height profile along the dashed line. **f-g**, The thickness distribution (**f**) and Raman spectrum (**g**) (in the area marked by dashed spot in panel (**e**)) of as-exfoliated TaS$_2$ flakes.

3.4 TaSe$_2$.
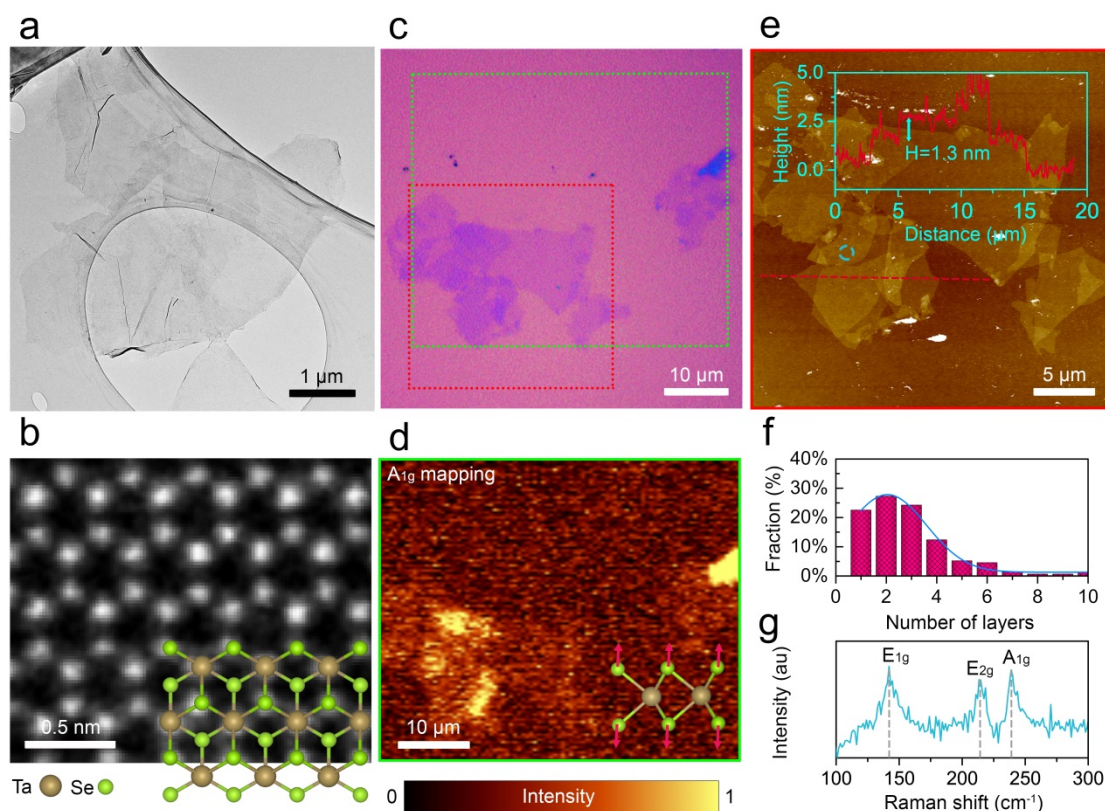
Fig. S6 Structure characterization of TBA-exfoliated TaSe$_2$ flakes. a-b, large-area TEM (**a**) and atomically-resolved STEM-ADF (**b**) images of TBA-exfoliated TaSe$_2$ flakes. The corresponding atomic model of TaSe$_2$ is overlaid in the bottom of panel (**b**). **c**, Optical microscopic image of TBA-exfoliated TaSe$_2$ flakes drop-cast onto a SiO$_2$/Si substrate. **d-e**, The Raman mapping (**d**) and AFM topographic (**e**) images of the regions indicated by dashed-box in panel (**c**). Inset of panel (**d**) shows the A$_{1g}$ Raman-active vibrational modes of TaSe$_2$.[7] Inset of panel (**e**) shows the cross-sectional height profile along the dashed line. **f-g**, The thickness distribution (**f**) and Raman spectrum (**g**) (in the area marked by dashed spot in panel (**e**)) of as-exfoliated TaSe$_2$ flakes.

3.5 TiS$_2$.
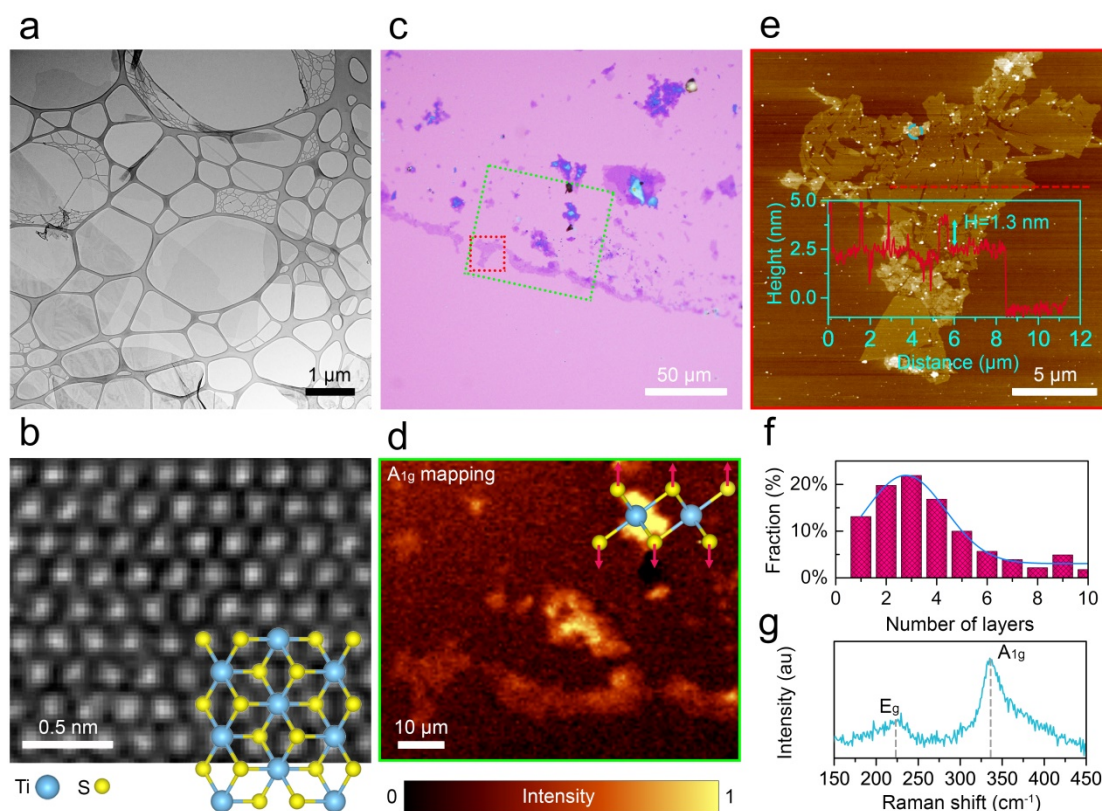
Fig. S7 Structure characterization of TBA-exfoliated TiS$_2$ flakes. a-b, large-area TEM (**a**), and atomically-resolved STEM-ADF (**b**) images of TBA-exfoliated TiS$_2$ flakes. The corresponding atomic model of TiS$_2$ is overlaid in the bottom of panel (**b**). **c**, Optical microscopic image of TBA-exfoliated TiS$_2$ flakes drop-cast onto a SiO$_2$/Si substrate. **d-e**, The Raman mapping (**d**) and AFM topographic (**e**) images of the regions indicated by dashed-box in panel (**c**). Inset of panel (**d**) shows the A$_{1g}$ Raman-active vibrational modes of TiS$_2$.[8] Inset of panel (**e**) shows the cross-sectional height profile along the dashed line. **f-g**, The thickness distribution (**f**) and Raman spectrum (**g**) (in the area marked by dashed spot in panel (**e**)) of as-exfoliated TiS$_2$ flakes.

3.6 TiSe₂.
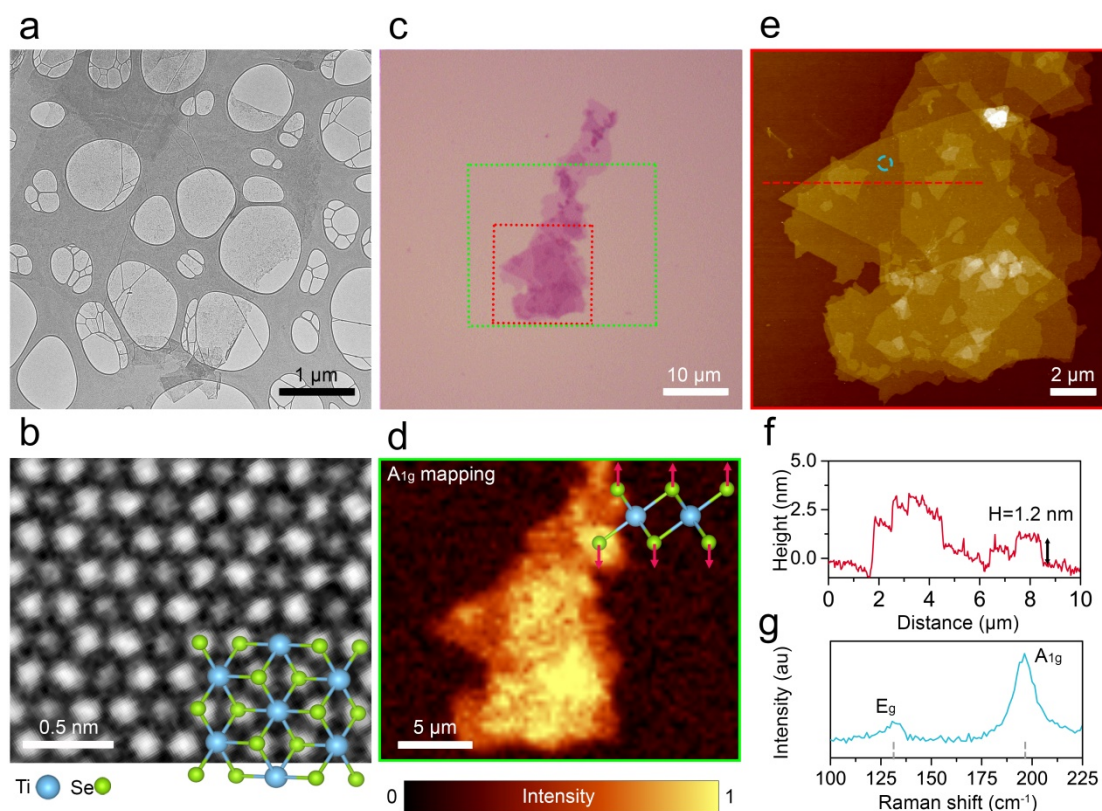
Fig. S8 Structure characterization of TBA-exfoliated TiSe₂ flakes. a-b, large-area TEM (**a**) and atomically-resolved STEM-ADF (**b**) images of TBA-exfoliated TiSe₂ monolayer. The corresponding atomic model of TiSe₂ monolayer is overlaid in the bottom of panel (**b**). **c**, Optical microscopic image of TBA-exfoliated TiSe₂ flakes drop-cast onto a SiO₂ substrate. **d-e**, The Raman mapping (**d**) and AFM topographic (**e**) images of the regions indicated by dashed-box in panel (**c**). Inset of panel (**d**) shows the A_{1g} Raman-active vibrational modes of TiSe₂.[9] Inset of panel (**e**) shows the cross-sectional height profile along the dashed line. **f-g**, The thickness distribution (**f**) and Raman spectrum (**g**) (in the area marked by dashed spot in panel (**e**)) of as-exfoliated TiSe₂ flakes.

3.7 MoTe₂.

Fig. S9 Structure characterization of TBA-exfoliated MoTe₂ flakes. a-b, large-area TEM (**a**) and atomically-resolved STEM-ADF (**b**) images of TBA-exfoliated MoTe₂ flake. The corresponding atomic model of MoTe₂ is overlaid in the bottom panel of (**b**).[10] **c**, Optical microscopic image of TBA-exfoliated MoTe₂ flakes drop-cast onto a SiO₂/Si substrate. **d-e**, The Raman mapping (**d**) and AFM topographic (**e**) images of the regions indicated by dashed-box in panel (**c**). Inset of panel (**d**) shows the A^8_g Raman-active vibrational modes of MoTe₂.[11] Inset of panel (**e**) shows the cross-sectional height profile along the dashed line. **f-g**, The thickness distribution (**f**) and Raman spectrum (**g**) (in the area marked by dashed spot in panel (**e**)) of as-exfoliated MoTe₂ flakes.

3.8 UV-vis spectra of exfoliated 2DSC sheets.
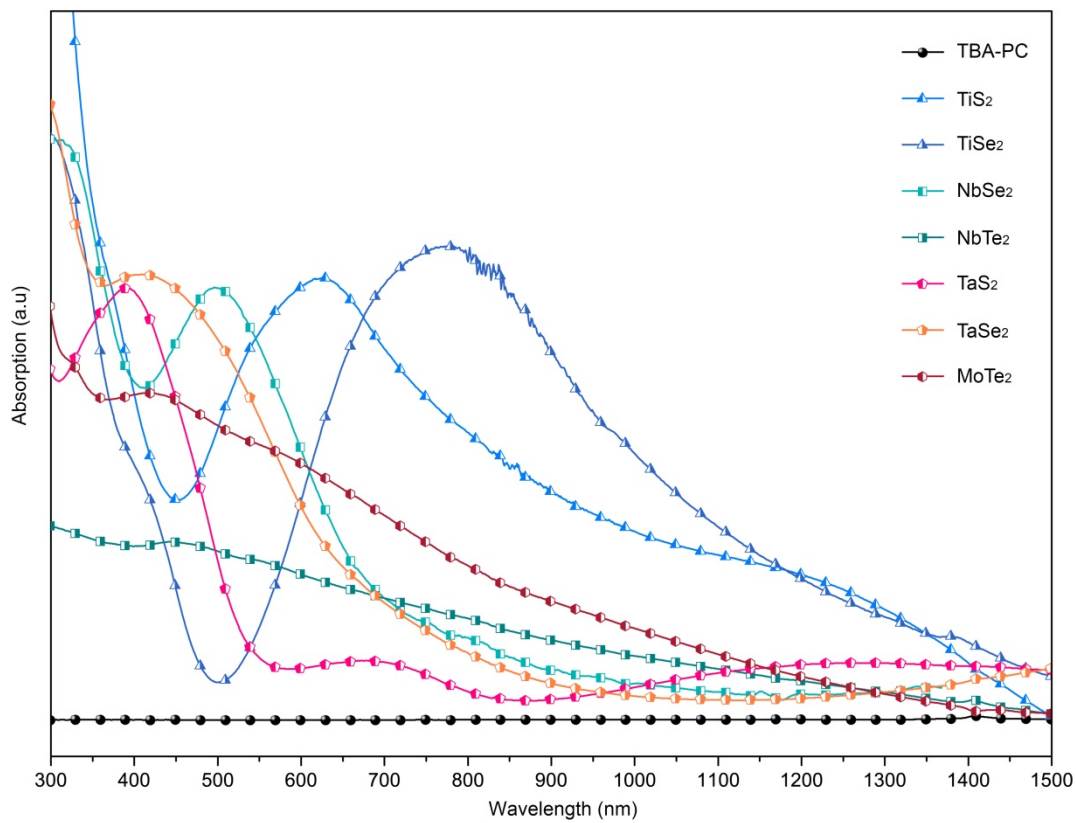
Fig. S10 UV-vis absorption spectra of as-exfoliated 2DSC flakes dispersed in PC solvent.

Metallic SC flakes often reveal a broad absorption spectrum ranging from 300 to 1500 nm. The prominent feature located between 400 to 800 nm can be assigned to the interband transitions from the p states in chalcogens and d states in transition metals[12, 13, 14, 15].

4. Intercalated NbSe$_2$ crystals as a function of the concentration of TPA.
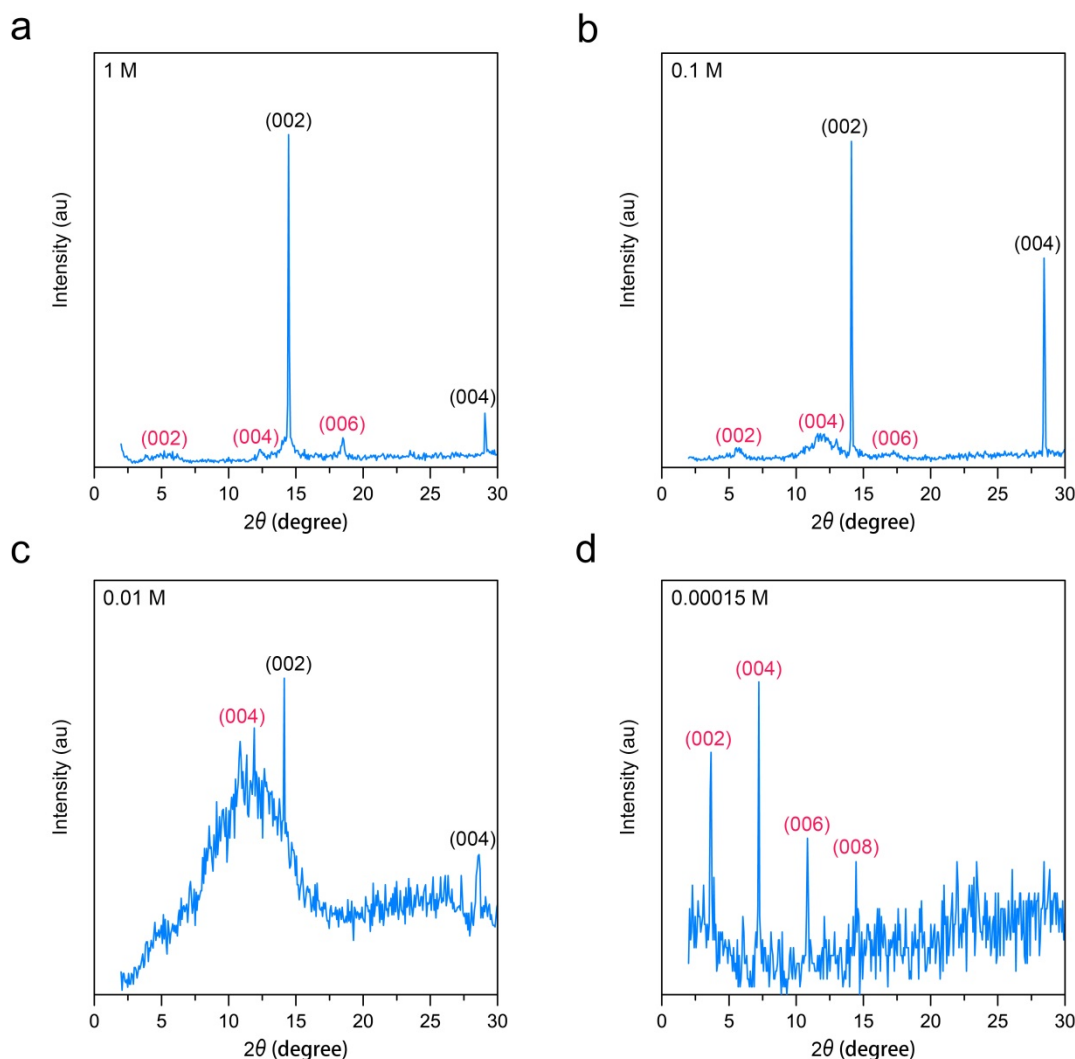
Fig. S11 XRD patterns of electrochemically-intercalated NbSe$_2$ sheets using a series of electrolytes with different concentrations of TPA in PC solvent. (00*l*) peaks associated with the original out-of-plane stacking in NbSe$_2$ are labelled in black, and intercalation induced new features are labelled in red.

To better understand the intercalation mechanism, we first used X-ray diffraction (XRD) to systematically investigate the structure of SC TMD crystals intercalated by a series of electrolytes with different concentrations of TPA in PC solvent (Fig. S11). The intensity of (*00l*) peaks (black label in Fig. S11) corresponding to the original out-of-plane stacking in bulk NbSe$_2$ crystals drops as a decrease of the concentration of TPA in electrolyte, suggesting that a diluted TPA-PC electrolyte favors a sufficient intercalation and thus leads to the exfoliation of thinner flakes. When the electrolyte with a concentration of 1.5×10^{-4} mol/L is used, the original

(*00l*) peaks disappears, indicating a complete intercalation of NbSe$_2$ bulk crystal. The interlayer distance is increased to ~2.4 nm (002 peak is located at 3.6 degree), providing a strong evidence for the successful delamination of each layer after electrochemical intercalation. Note a gentle sonication is not necessarily required to further delaminate these fully-intercalated TMDs but it can enable a fast separation of these weakly coupled 2D sheets for their dispersion in solvent.
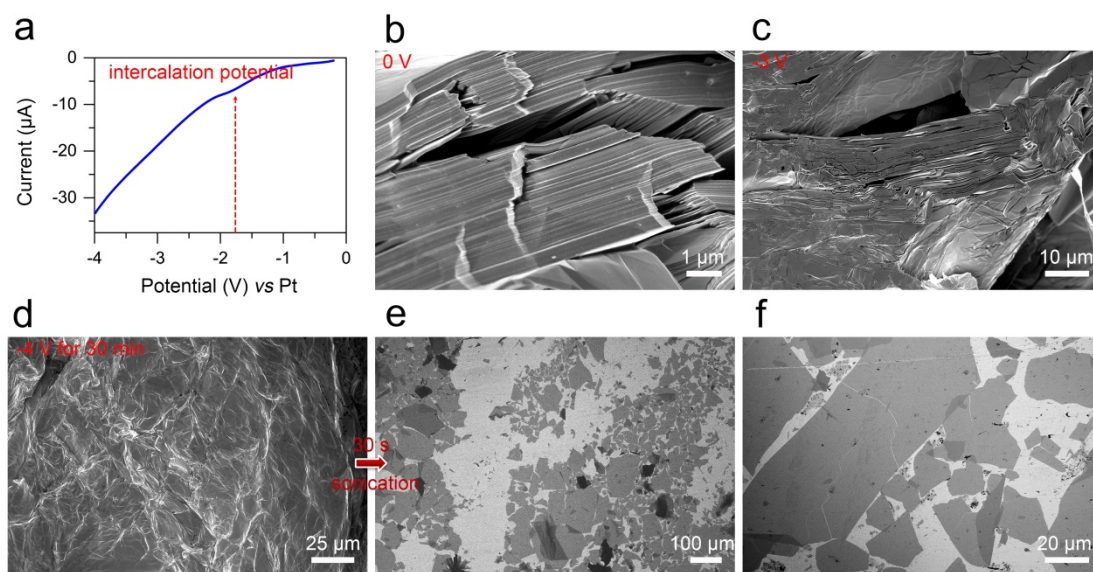
Fig. S12 Morphology evolution of bulk NbSe$_2$ under different cathodic voltages. a, Linear sweep voltammogram (scan rate: 0.1 V/s) of bulk NbSe$_2$ in PC electrolyte (1.5×10^{-4} mon/L TPABF$_4$), a intercalation potential of -1.8 V *Vs* Pt indicates the low intercalation barrier of solvated TPA into NbSe$_2$ galleries. **b-c,** SEM images of the edge of bulk NbSe$_2$ before (**b**) and after (**c**) the cathodic scan from 0 to -3 V. **d**, SEM image of the edge of bulk NbSe$_2$ after charging at -4 V for 30 min. **e-f,** SEM images of as-exfoliated NbSe$_2$ flakes.
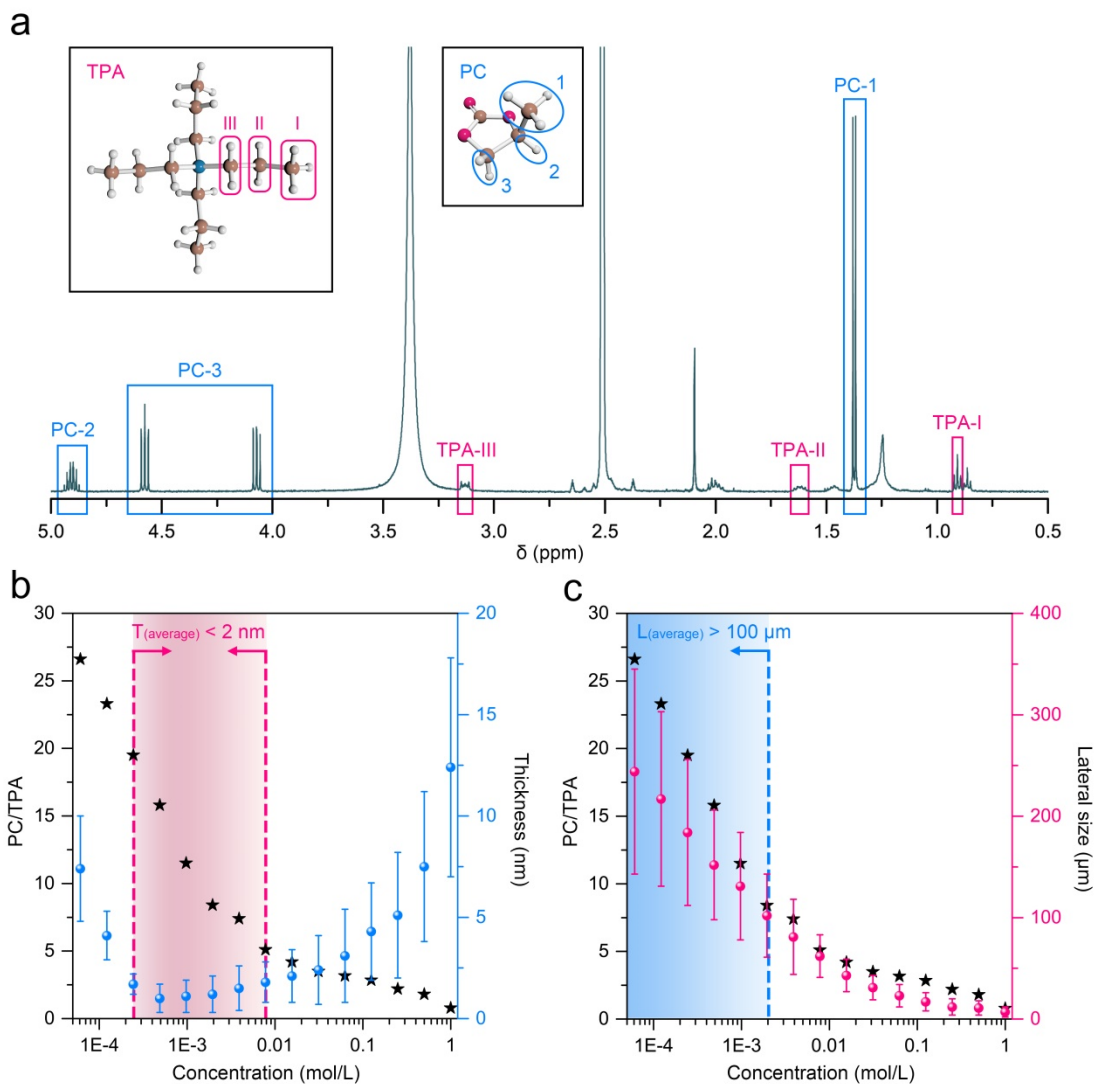
Fig. S13 The size/thickness distribution of as-exfoliated NbSe$_2$ flake as a function of the concentration of TPA in PC. a, ^{1}H NMR spectrum of intercalated species (PC and TPA) in the interlayer galleries NbSe$_2$ (1.5×10^{-4} mon/L TPA-PC is used for intercalation). The relationship between the (**b**) thickness and (**c**) size of exfoliated NbSe$_2$ sheets as a function of the concentration of TPA in PC. The error bars show the standard error.

To gain deep insight into the intercalation mechanism, we performed ^{1}H NMR test to measure the composition of intercalated species between the interlayer galleries of NbSe$_2$ (Fig. S13). The electrochemically-exfoliated NbSe$_2$ sheets were collected by filtration and then washed with acetone for three times to remove the electrolyte adsorbed on surface. A vacuum drying of these exfoliated NbSe$_2$ sheets at 30 °C for 1 h to remove the residual acetone solvent, followed by the sonication in DMSO-D6 to release the intercalants for the subsequent measurement of ^{1}H NMR spectra. As shown in Fig. S13b, a decrease of the concentration of TPA in PC results

in a monotonical increase of the ratio of intercalated PC:TPA. A diluted concentration of TPA in PC ranging from 1.5 to 20×10^{-4} mon/L enables a high intercalation degree of $NbSe_2$ crystal, and the resultant exfoliated 2D flakes show an average thickness below 2 nm (corresponding to 1-3 layers). A further dilution of the electrolyte ($<1.5\times10^{-4}$ mol/L) slows down the intercalation rate significantly and results in an insufficient intercalation and exfoliation (thick flakes produced). The correlation between the sizes of exfoliated $NbSe_2$ sheets and the ratio of intercalated PC:TPA confirms that the intercalation of a large amount of neutral PC solvent favors the production of the large-sized high-quality of monolayer 2D sheets.

5. The proposed intercalation mechanism of NbSe₂ in ultra-diluted TPA-PC electrolyte.
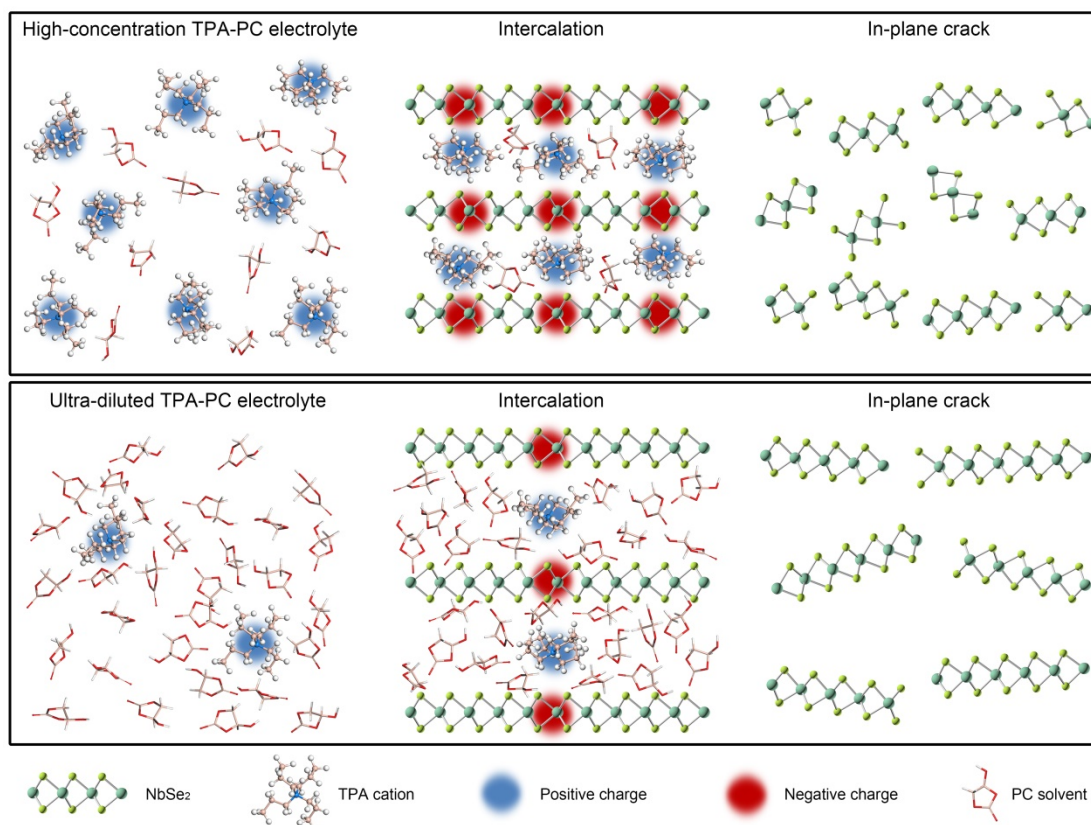
Fig.   S14

Proposed intercalation mechanism of NbSe₂ in ultra-diluted TPA-PC electrolyte.

The maximization of the efficient intercalation of neutral solvent molecules into the interlayer space of superconducting TMD bulk crystals can weaken or avoid the excessive charging and structural damaging of TMD materials arising from charged intercalants[1, 2]. This is crucial for the electrochemical exfoliation of high-quality and large-size 2DSC sheets[1, 2, 16]. The production of high-quality and large-sized 2D TMD-based superconducting monolayers can be achieved *via* the using an ultra-diluted concentration ($<20 \times 10^{-4}$ mol/L) of tetrapropylammonium cations (TPA) in a polar solvent. In this case, solvation of TPA cations by a large number of neutral solvent molecules as co-intercalants for the electrochemical exfoliation of TMD SC bulks (Fig. S13).

6. Large-sized 2DSC monolayers exfoliated in ultra-diluted TPA-PC electrolyte.
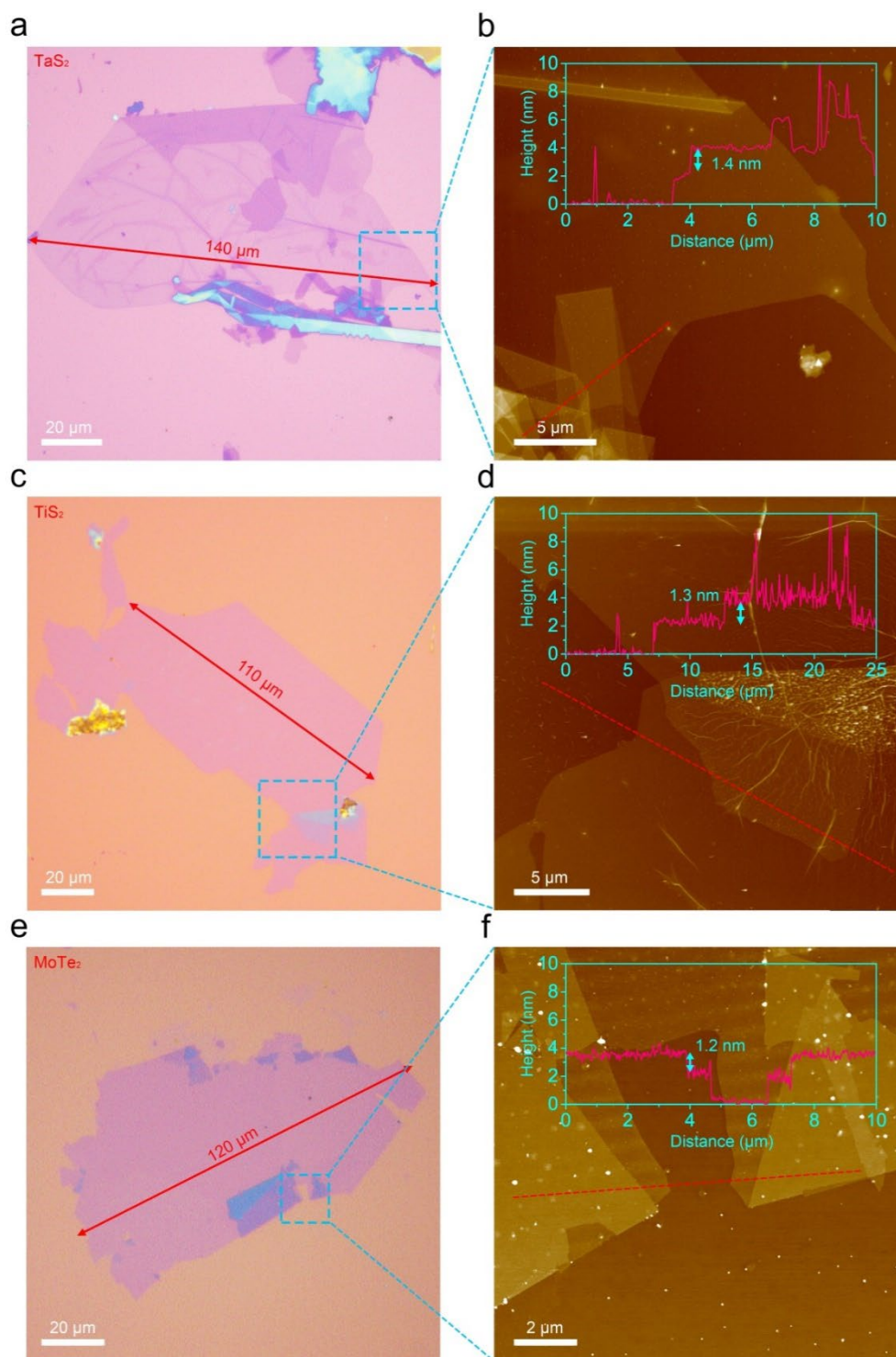
Fig. S15 Large-sized 2DSC monolayer exfoliated in ultra-diluted TPA-PC electrolyte. Optical microscopic (left panel) and AFM (right panel) images of several representative large-sized 2DSC exfoliated in TPA-PC electrolyte with the concentration ~2×10^{-4} mon/L.

7. TPA-intercalated NbSe₂ for STM imaging.

STM imaging provides a real-space distribution of the intercalated species. A closer examination reveals flat region (un-intercalated or re-stacked NbSe$_2$ during ultra-high vacuum pumping) and the bright feature with an apparent height of ~0.18 nm, (Fig. S16) ascribed to NbSe$_2$ intercalated by TPA-PC molecules.
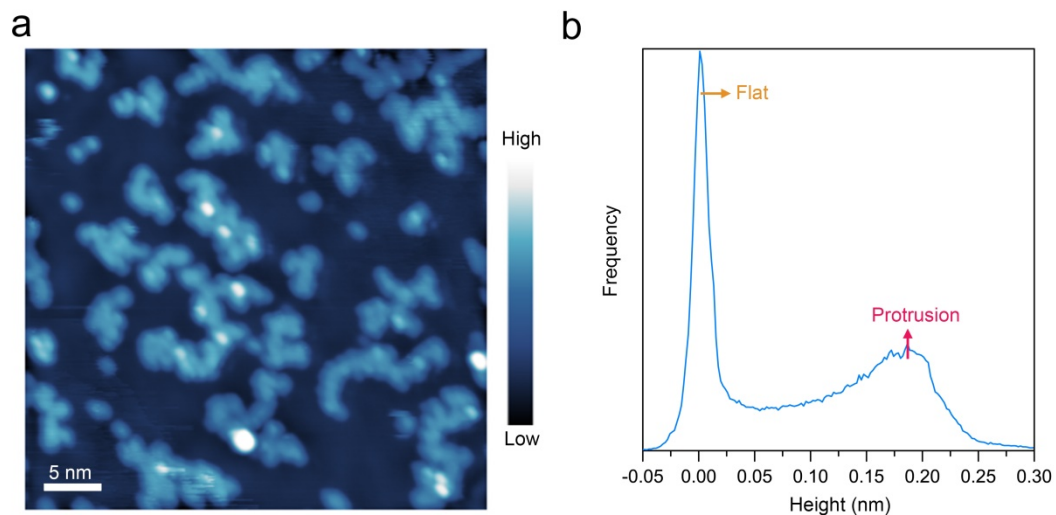
Fig. S16. (a) Large-scale STM image (tunneling parameter: -2.3 V, 10 pA) and (b) height histogram of TPA-PC intercalated NbSe$_2$ sample.

7. Quasi-monolayer structure of TPA-intercalated NbSe$_2$.
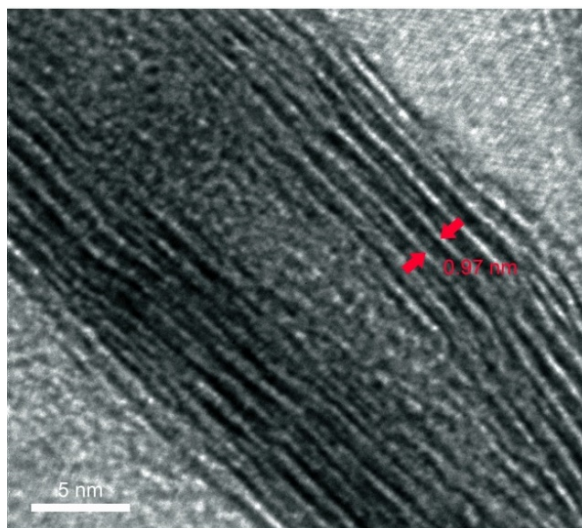
Fig. S17 Cross-sectional HRTEM image of TPA-intercalated NbSe$_2$.

8. Dispersion of TPA-intercalated NbSe$_2$ in PC solvent.
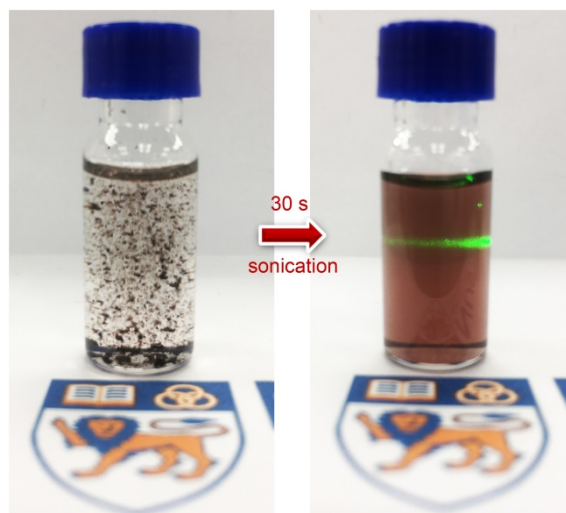
Fig. S18 Digital photographs of TPA-intercalated NbSe$_2$ before and after a sonication for 30 seconds.

9. Structure characterization of TPA-exfoliated NbSe₂.
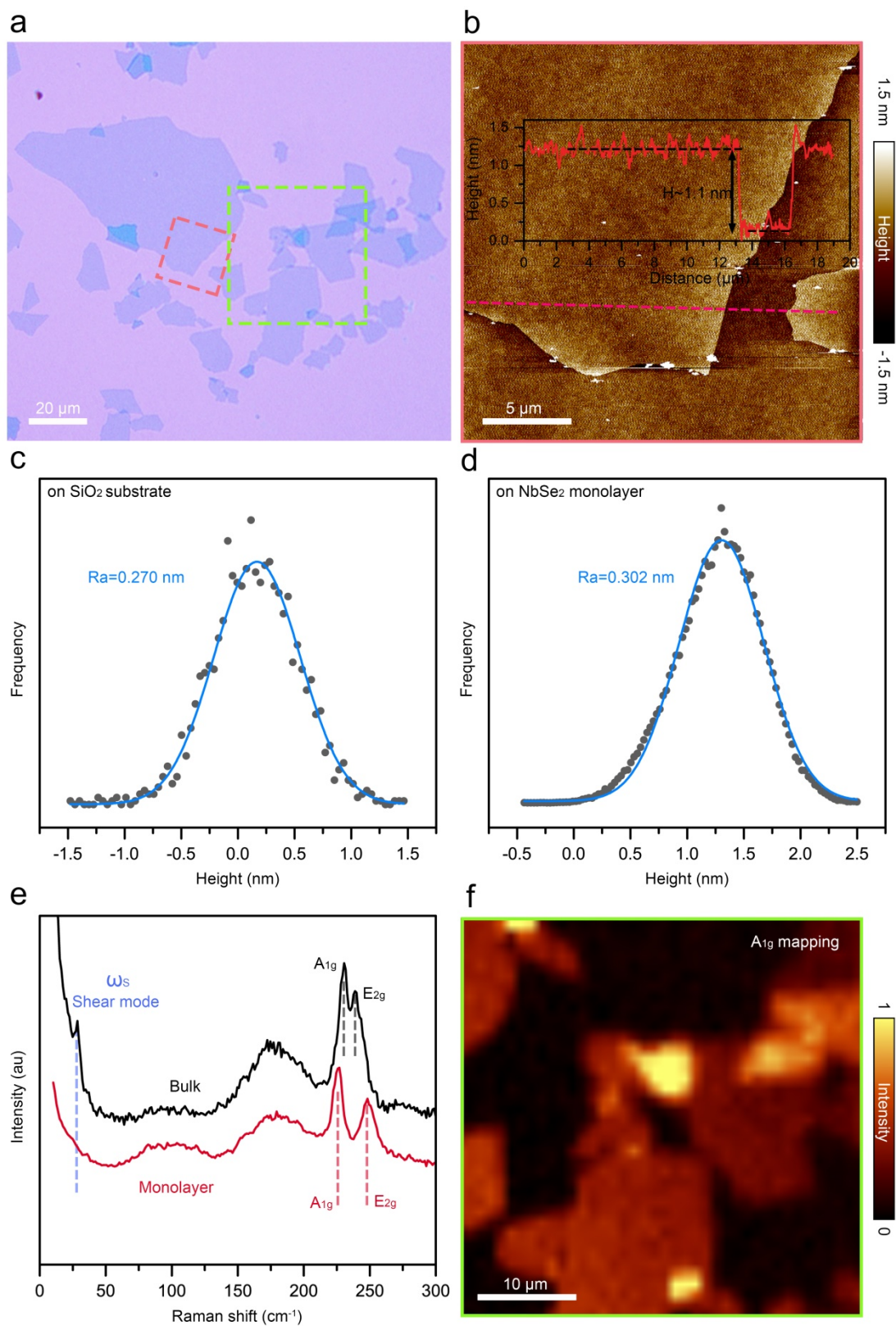
Fig. S19 a, Optical microscopic image of as-exfoliated NbSe₂ flakes drop-cast onto a SiO₂/Si substrate. **b**, AFM

topographic of the regions marked by red in panel (**a**). The height profile along the dashed line is superimposed in panel (**b**). **c-d**, Height histogram of (**c**) exfoliated $NbSe_2$ monolayer and (**d**) blank SiO_2 substrate. **e**, Raman spectra of $NbSe_2$ bulk and as-exfoliated flakes. The absence of the peak ~27 cm^{-1} (associated with the ω_s shear mode in multilayer stacked $NbSe_2$)[4] demonstrates a monolayer nature of as-exfoliated $NbSe_2$ flake. **f**, Raman mapping images (A_{1g} peak intensity) of the regions marked by green in panel (**a**).

We performed the statistics analysis for the surface roughness of as-exfoliated $NbSe_2$ monolayers and blank SiO_2 substrate using AFM (Fig. S19). The surface roughness of SiO_2 substrate and $NbSe_2$ monolayer is measured to be 0.270 nm (standard deviation σ~382 pm) and 0.302 nm (standard deviation σ~374 pm) respectively. This suggests that the morphology of as exfoliated $NbSe_2$ monolayers follows that of bottom SiO_2 substrate[17]. Additionally, we have checked the TPA-PC exfoliated $NbSe_2$ flakes by STM imaging. As shown in Fig. S20, the intercalated TPA and PC molecules can be removed after rinsing with PC or acetone solvents under a mild sonication (100 W) for 30 seconds. STM images reveal that the majority of surface of as-exfoliated $NbSe_2$ monolayer is clean, without the electrolyte residuals.
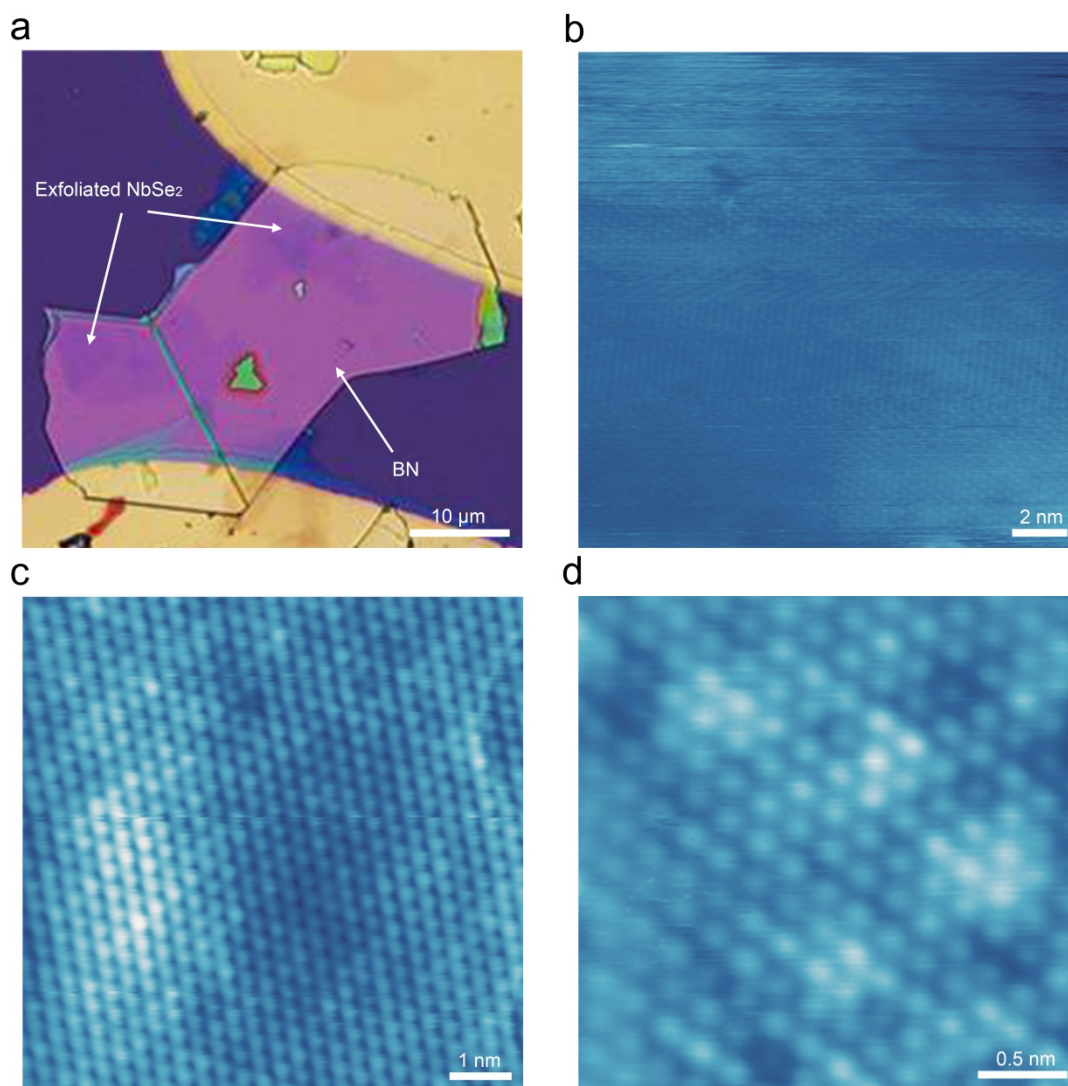
Fig. S20 STM imaging of the TPA-PC exfoliated NbSe₂ flakes. (**a**) Optical microscopic and (**b-d**) STM images of exfoliated NbSe₂ flakes drop-cast onto a *h*-BN flake. Tunneling parameter: -3 V, 10 pA (**b**), -0.05 V, 80 pA (**c**) and -2.5 V, 30 pA (**d**).

10. SEM imaging of the as-exfoliated NbSe$_2$ flake for SAED characterization.
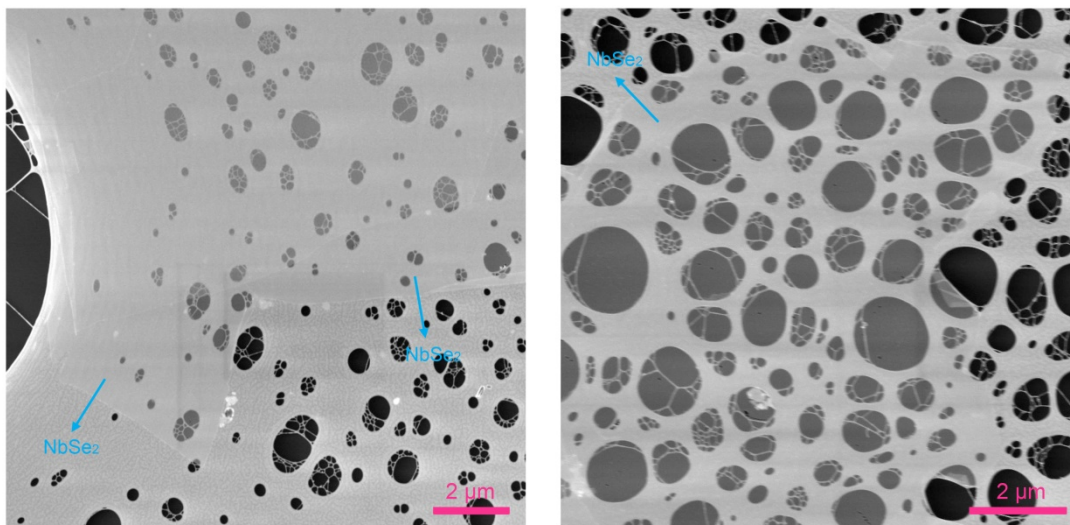
Fig. S21 Zoom-in SEM image of the as-exfoliated NbSe$_2$ flake for SAED characterization.

11. Defects density in as-exfoliated 2DSC monolayers.

| ● Metal | ● Dichalcogen | ● Single vacancy | ● Double vacancy |
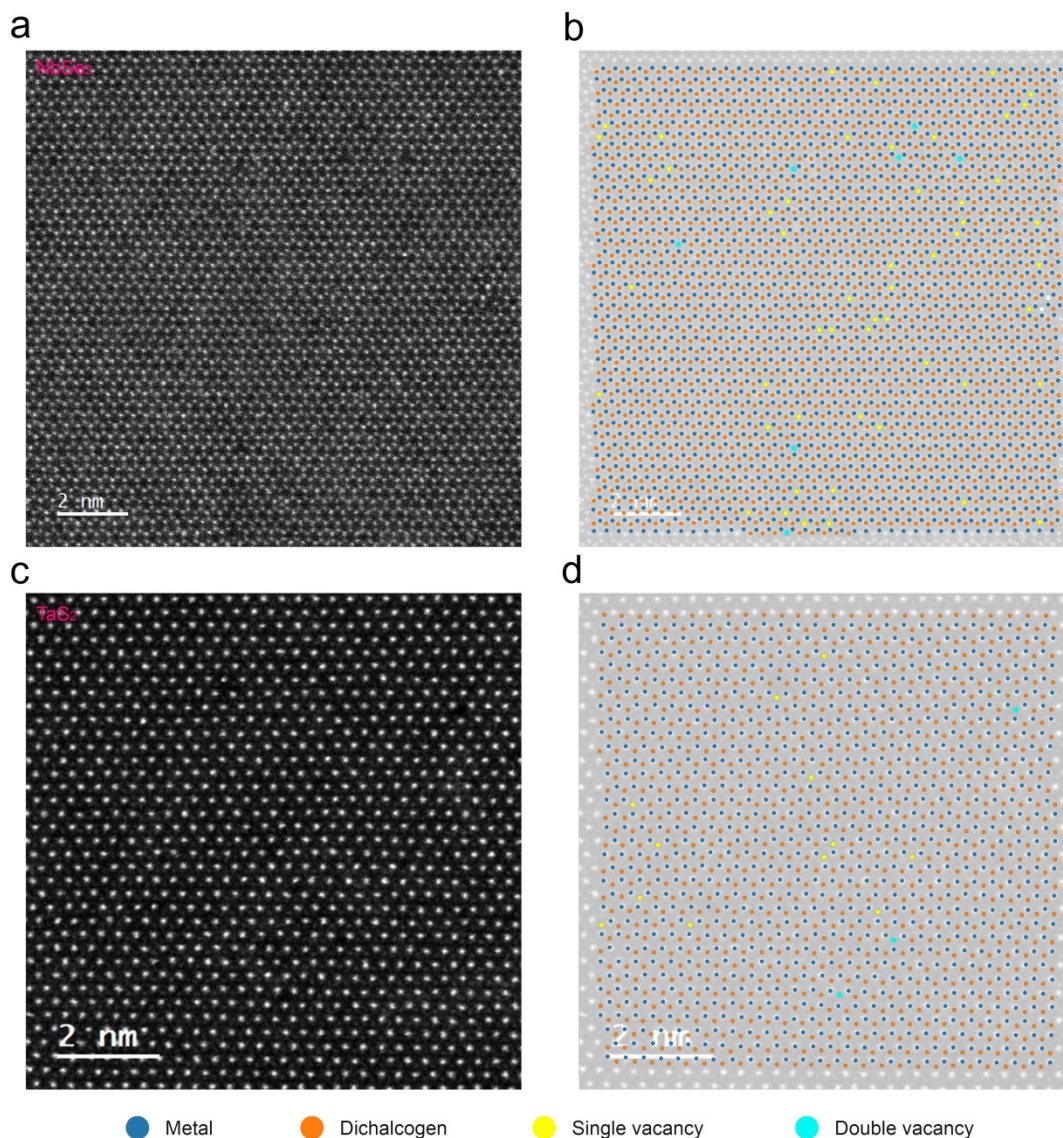
Fig.   S22

Representative STEM images (a, c) of exfoliated NbSe$_2$ and TaS$_2$ sheets with the corresponding (b, d) structural simulation by Python. The labels for the structure model, blue: metal, orange: dichalcogen (Se$_2$ or S$_2$), yellow: single vacancy (V$_{Se}$ or V$_S$) and cyan: double vacancy (V$_{S2}$ or V$_{Se2}$). The defect density for as exfoliated NbSe$_2$ is Se$_2$: V$_{Se}$: V$_{Se2}$=1:0.0331:0.005729, and defect density for as-exfoliated TaS$_2$ is S$_2$: V$_S$: V$_{S2}$=1: 0.0139: 0.00347.

To further evaluate the quality of as-exfoliated flakes, we have carried out a statistic analysis of multiple STEM images of exfoliated NbSe$_2$ and TaS$_2$ sheets to make a quantitative analysis of the defect density in our samples. Fig. S22 shows representative STEM images of exfoliated NbSe$_2$ and TaS$_2$ sheets with the corresponding atomic

model. The structural simulation *via* Python allows for the estimation of the chemical stoichiometry of exfoliated flakes (NbSe$_{1.96}$ and TaS$_{1.98}$ for exfoliated NbSe$_2$ and TaS$_2$ sheets, respectively).

12. XPS spectrum of as-exfoliated NbSe$_2$.
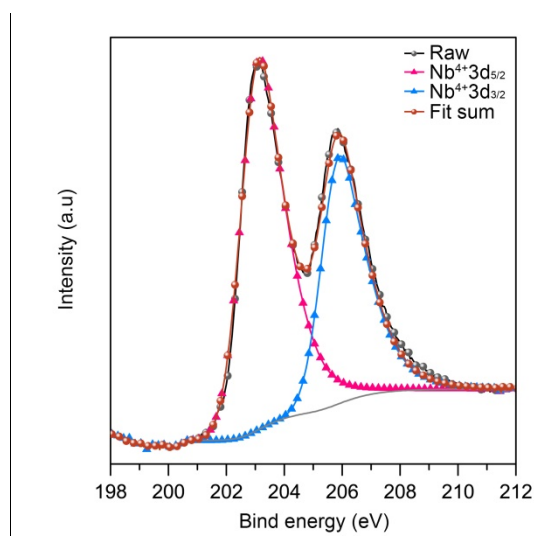
Fig. S23 XPS spectrum (Nb 3d) of freshly-exfoliated NbSe$_2$.

Fig. S23 shows the Nb 3d core-level XPS spectrum of as-exfoliated NbSe$_2$ flakes. The doublet features peaked at 203.1 and 205.8 eV can be ascribed to the characteristic Nb^{4+} 3d$_{5/2}$ and 3d$_{3/2}$ core-level spectrum of NbSe$_2$, respectively. The absence of sub-peaks at 207.2 (3d$_{5/2}$) and 209.6 (3d$_{3/2}$) eV associated with oxidation states of Nb^{5+} demonstrates a negligible oxidation of as-exfoliated NbSe$_2$ flakes.

13. Resistance of NbSe₂ monolayer as a function of out-of-plane ($H_\perp$) and in-plane ($H_{//}$) magnetic field.
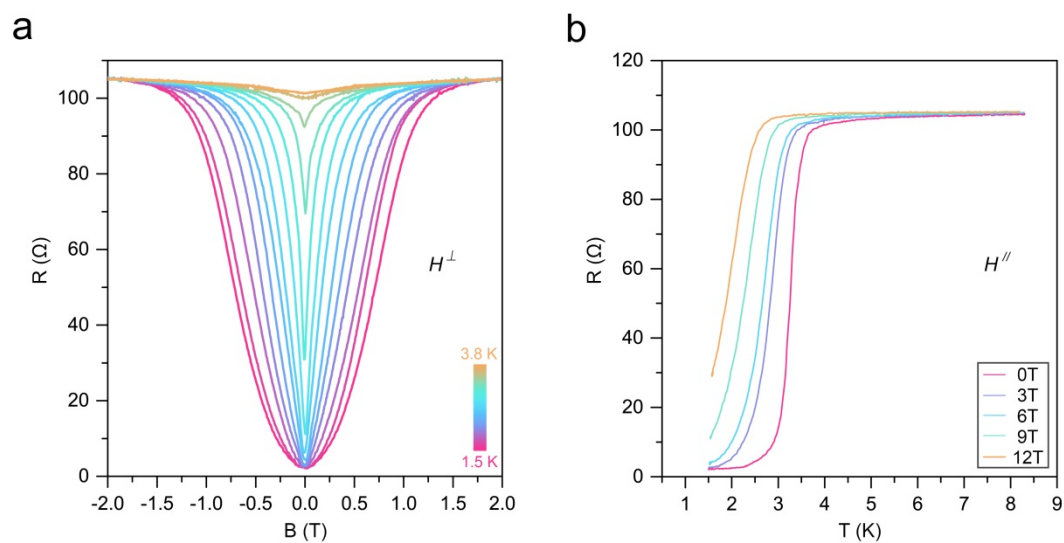
Fig. S24 a, Resistance (R_{xx}) of monolayer NbSe$_2$ device as a function of out-of-plane ($H_\perp$) magnetic field at different temperatures from 1.5 to 3.8 K. **b,** T-dependent R_{xx} of monolayer NbSe$_2$ device under different in-plane ($H_{//}$) magnetic fields ranging from 0 to 12 T.

14. Berezinskii-Kosterlitz-Thouless (BKT) model fitting of NbSe$_2$ monolayer.
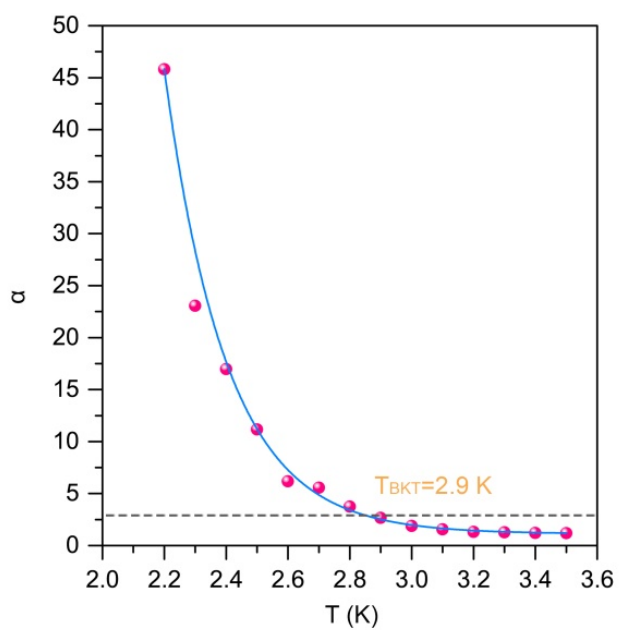
Fig. S25 Temperature-dependent exponent deduced from the V-I curve in Fig. 2i. The exponent α can be extracted from the slope of the V-I curves in Fig. 2i, and the BKT transition temperature T_{BKT} is estimated to be 2.9 K at $\alpha=3$.

15. Degradation of NbSe₂ monolayer in air.
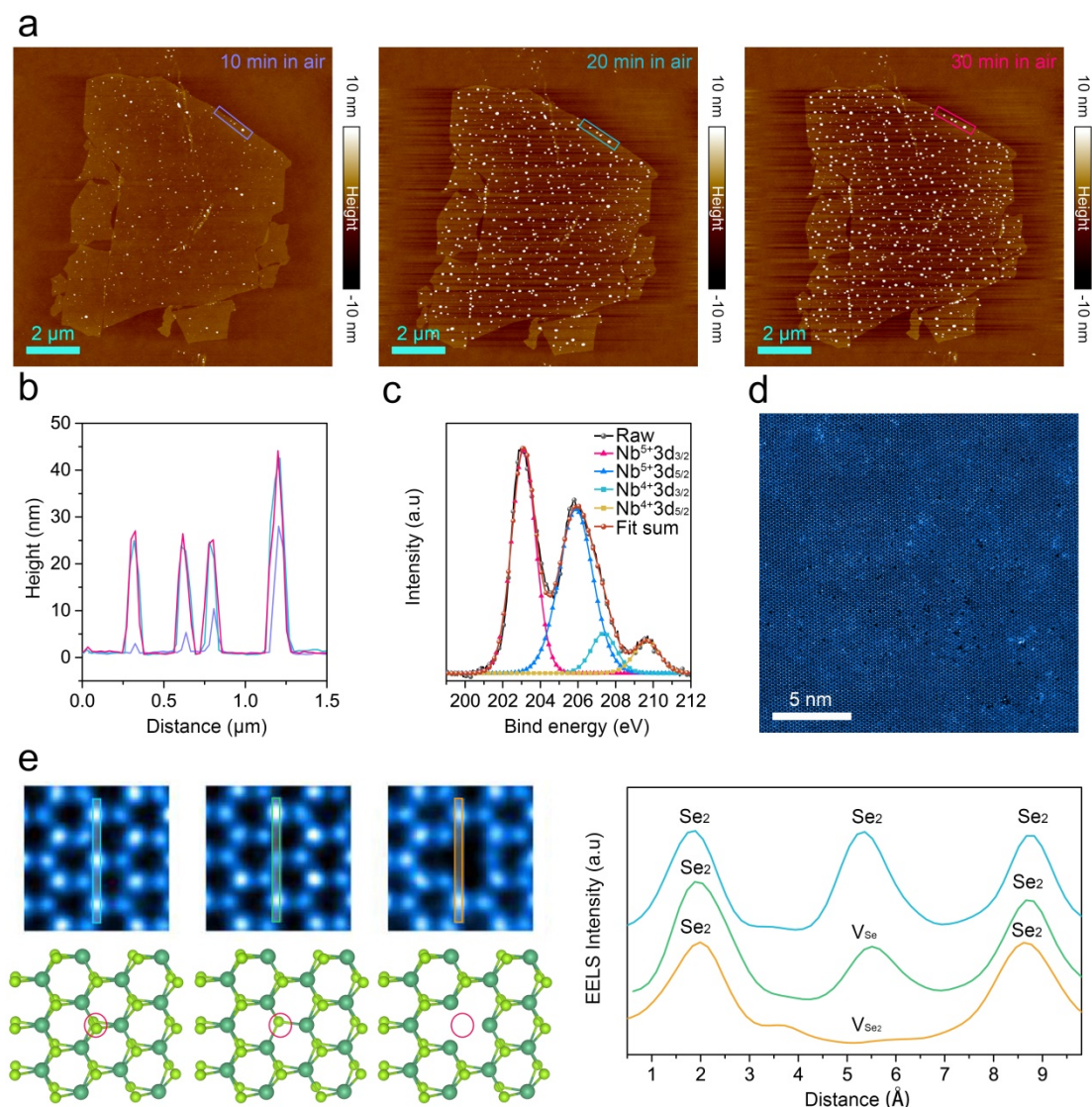
Fig. S26 Probing the degradation of NbSe₂ monolayer in air. (25 °C, 60% humidity) **a-b,** Time dependent AFM morphology (**a**) and corresponding height profiles (**b**) of exfoliated NbSe₂ monolayer exposed to air (note that as-examined flake has been thoroughly washed with acetone to remove solvent protection). **c**, XPS spectrum of as-exfoliated NbSe₂ flakes after exposure to air for 30 mins. **d**, STEM-ADF images of monolayer NbSe₂ after an exposure to air for 5 mins. **e**, STEM-ADF image of intact and defective area of NbSe₂ monolayer. Right panel displays the corresponding intensity profiles along marked lines in the STEM-ADF image (**e**).

16. Moiré patterns at the heterojunction of restacked NbSe$_2$ flakes.

Periodic moiré patterns in re-stacked NbSe$_2$ heterostructures can be observed *via* both STEM and STM imaging (Fig. S27-28), which indicates that large-scale clean interface with moiré pattern can be obtained in restacked NbSe$_2$ flakes.
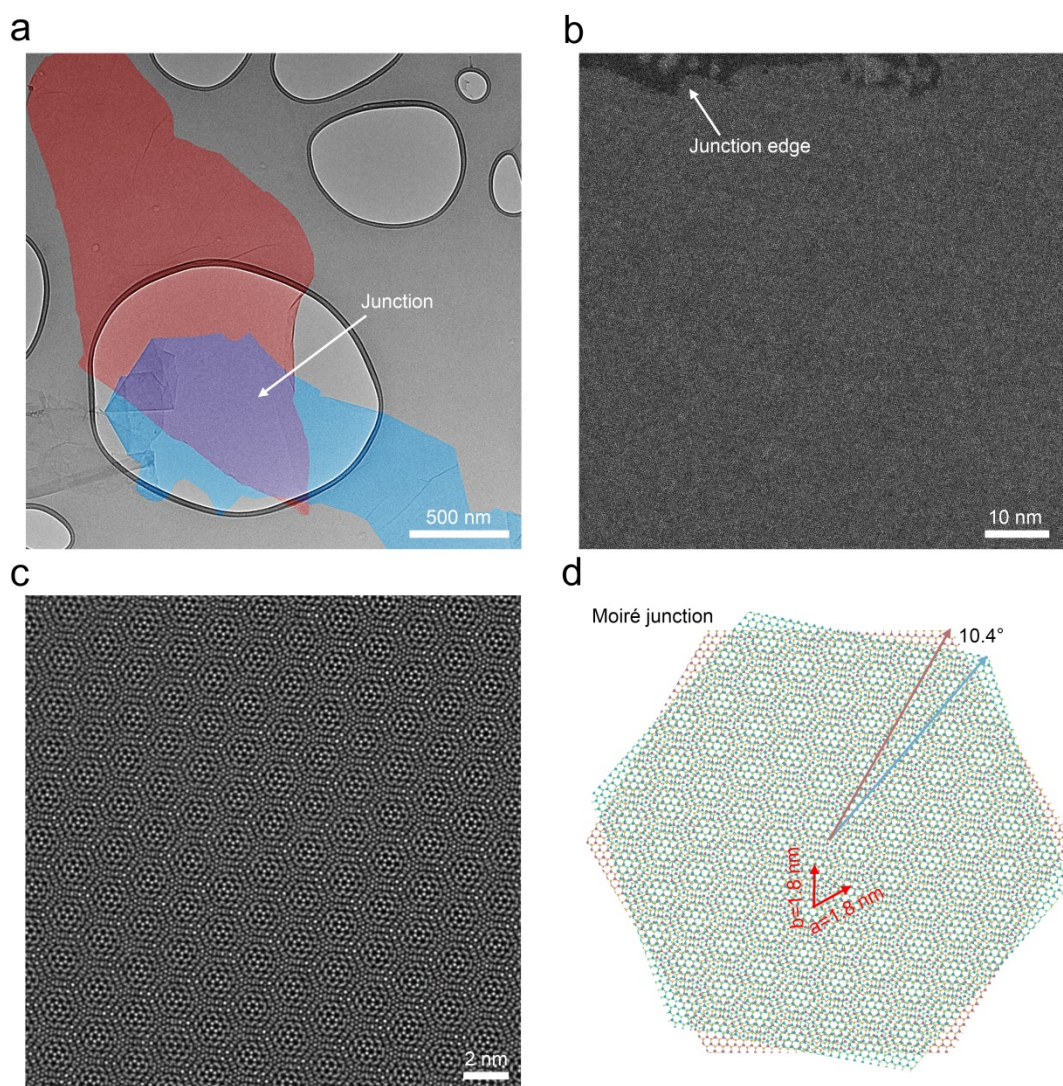

Fig. S27 STEM imaging of moiré patterns at the heterojunction of restacked NbSe$_2$ flakes. a, STEM image of the NbSe$_2$ junction structure formed by two TPA-PC exfoliated NbSe$_2$ flakes (highlighted in false colour of red and blue for each flake) drop-cast onto a TEM grid. (**b**) Large-scale and (**c**) zoom-in STEM images of a stacked moiré junction structure of NbSe$_2$ flakes with a twisted angle of 10.4° (**d**).
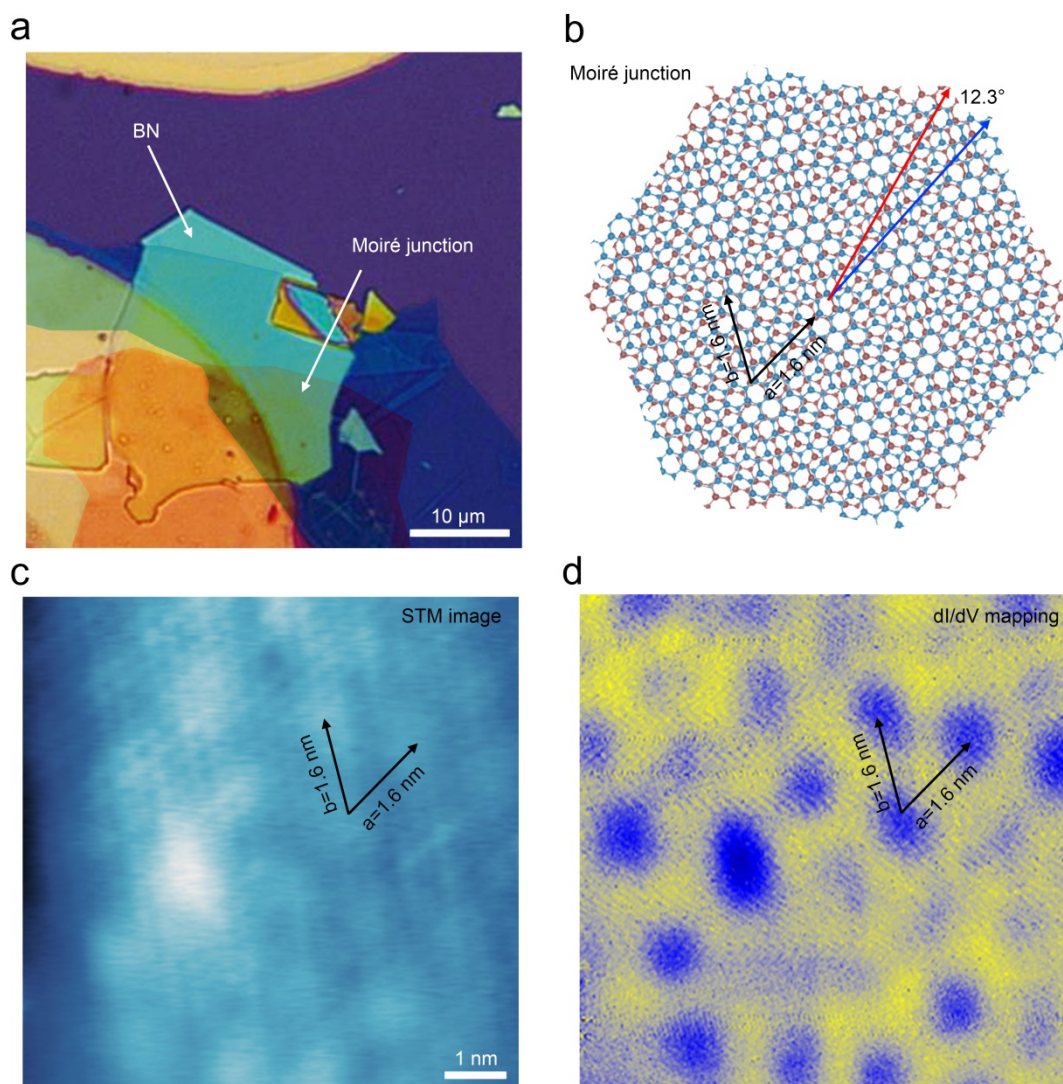
Fig. S28 STM imaging of moiré pattern of the restacked NbSe$_2$ flakes. a, Optical microscopic image of NbSe$_2$ moiré pattern at a twist angle of 12.3° (**b**) formed by two TPA-PC exfoliated NbSe$_2$ flakes (highlighted in false colour of blue and orange for each flake) drop-cast onto a *h*-BN flake. (**c**) STM and (**d**) *dI/dV* mapping images of the moiré pattern of the stacked NbSe$_2$ flakes at a twist angle of 12.3° (**d**).

17. Origin of the superconducting transition peaks in twisted NbSe₂.
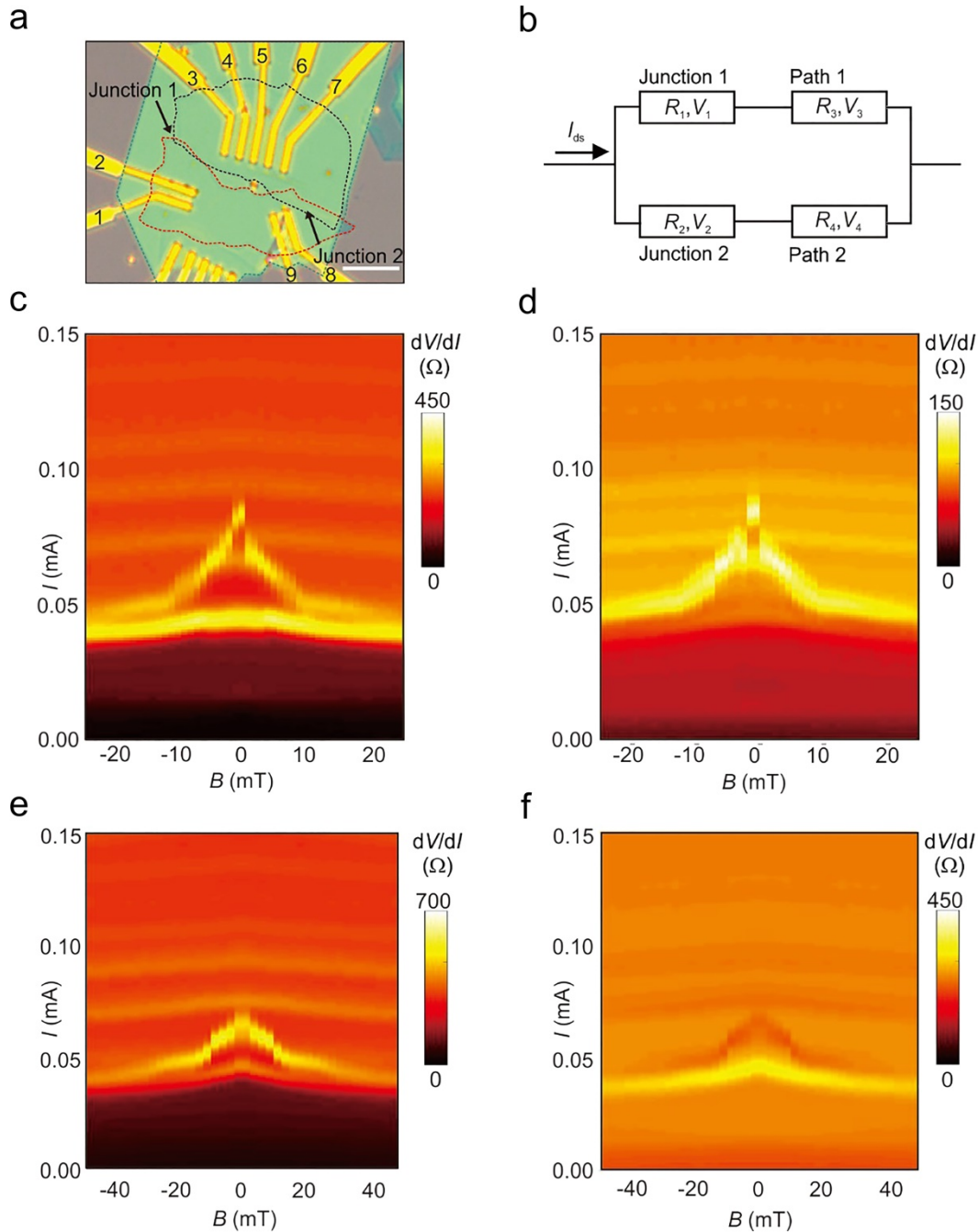
Fig. S29 a, Optical microscopic image of stacked NbSe₂ flakes, contacted with Ti/Au electrodes. Current is applied between the two flakes and voltage drop is recorded. The scale bar is 20 μm. **b**, Simple resistor model used to assign the transition peaks to the respective junctions. Since the two junctions are always connected in parallel, when current is applied across a junction, the current path and the magnitude of the detected signal are determined by the contact configuration and the difference in flake resistance. **c**, Two transition peaks in the

dV/dI *Vs* current and magnetic field are recorded with current contacts **5-1** and voltage contacts **7-8**. **d**, The lower transition peak disappears when the voltage signal is recorded with the contact pair **6-7** instead, indicating it originates from Junction 2. **e-f**, Similarly, when current is applied via **5-1** and voltage is recorded with **4-2**, across Junction 1, two transitions are visible, whereas moving the voltage probes to **5-4**, results in significant decrease of the higher-current transition peak, thus corroborating its origin from Junction 1.

18. Josephson junction arrays in van der Waals heterostructures based on mechanically exfoliated and twisted NbSe$_2$ flakes.

To support our data on the commensurate flux penetration and the formation of a network of Josephson junction arrays in twisted NbSe$_2$ flakes, we fabricated such twisted devices from mechanically exfoliated NbSe$_2$. Unlike the printed devices – the whole fabrication had to be done in glove box and the final device had to be encapsulated to avoid oxidation.

Twisted NbSe$_2$ devices (Fig. S30a-b) were assembled by the standard dry-transfer and tear-and-stack techniques, as reported previously[18, 19]. The preparation of the devices was carried out in an inert atmosphere provided by a glovebox. In brief, thin NbSe$_2$ flakes were first exfoliated onto oxidized silicon substrates (90 nm thickness of SiO$_2$). The thicknesses of NbSe$_2$ flakes were identified and selected *via* optical contrast. Then we used a double-layer polymer film of polypropylene carbonate (PPC) on polydimethylsiloxane (PDMS) to lift a flake of hexagonal boron nitride (*h*-BN), which was then used to lift the monolayer graphene crystal away from its substrate. Subsequently, we used a precision micromanipulator with a remote control to place the stacks (*h*-BN/Graphene) on top of the chosen few-layer NbSe$_2$ flake and make sure that the graphene covers only partial area of the NbSe$_2$. Then we quickly pealed the stack off the oxidized silicon substrate to tear the NbSe$_2$ flakes into two sections. The section without coverage of graphene remained on the substrate, which was rotated by 0.1° to 0.5° and then picked up by the stacks (*h*-BN/Graphene/NbSe$_2$). The resulting stack (*h*-BN/Graphene/twisted NbSe$_2$) was subsequently placed onto a larger *h*-BN crystal residing on the oxidized silicon substrate to achieve the full encapsulation. The assembled *h*-BN/Gr/twisted NbSe$_2$/*h*-BN heterostructures were removed out from the glovebox for device fabrication. Finally, the electron beam lithography was used to define the pattern in a shape of multiterminal Hall bars and the reactive ion etching was

used to selectively etch the *h*-BN on top of the monolayer graphene. As for metallic contacts, we deposited 3 nm Cr followed by 50 nm Au on top of the monolayer graphene (Fig. S30b).

The device was measured at T<0.3 K in a helium-3 system. The differential resistance (dV/dI) measurement shown in Figure R3d-e was conducted by sweeping DC current bias with 15 nA AC excitation mixed, while the 4-probe AC voltages on twisted and individual regions of $NbSe_2$ (Fig. S30b) were measured by lock-in, respectively. Fig. S30d presents the measurements on an individual $NbSe_2$ flake of three layers. One can see that the superconducting region at this temperature is limited only to the region of very small magnetic field and small critical currents. However, the twisted area demonstrates significantly larger critical current, which is able to survive in much larger fields. This can be understood as the critical temperature and critical current can be enhanced significantly in $NbSe_2$ flakes with an augment of the thickness[20] At the same time, the critical current as a function of magnetic field demonstrates oscillatory dependence. The period of the oscillation is $\Delta B \approx 0.22$ T. Assuming that the oscillations are caused by the specific distribution of the supercurrent in the arrays of the Josephson junction formed by moiré lattice, we can estimate the periodicity of the moiré pattern as $L=(\Phi_0/\Delta B)^{1/2} \approx 100$ nm, corresponding to a small twisted angle of ~0.2°. (here $\Phi_0 = h/(2e)$ is the superconducting magnetic flux quantum, $\Phi_0 \sim 2$ mT·μm^2)
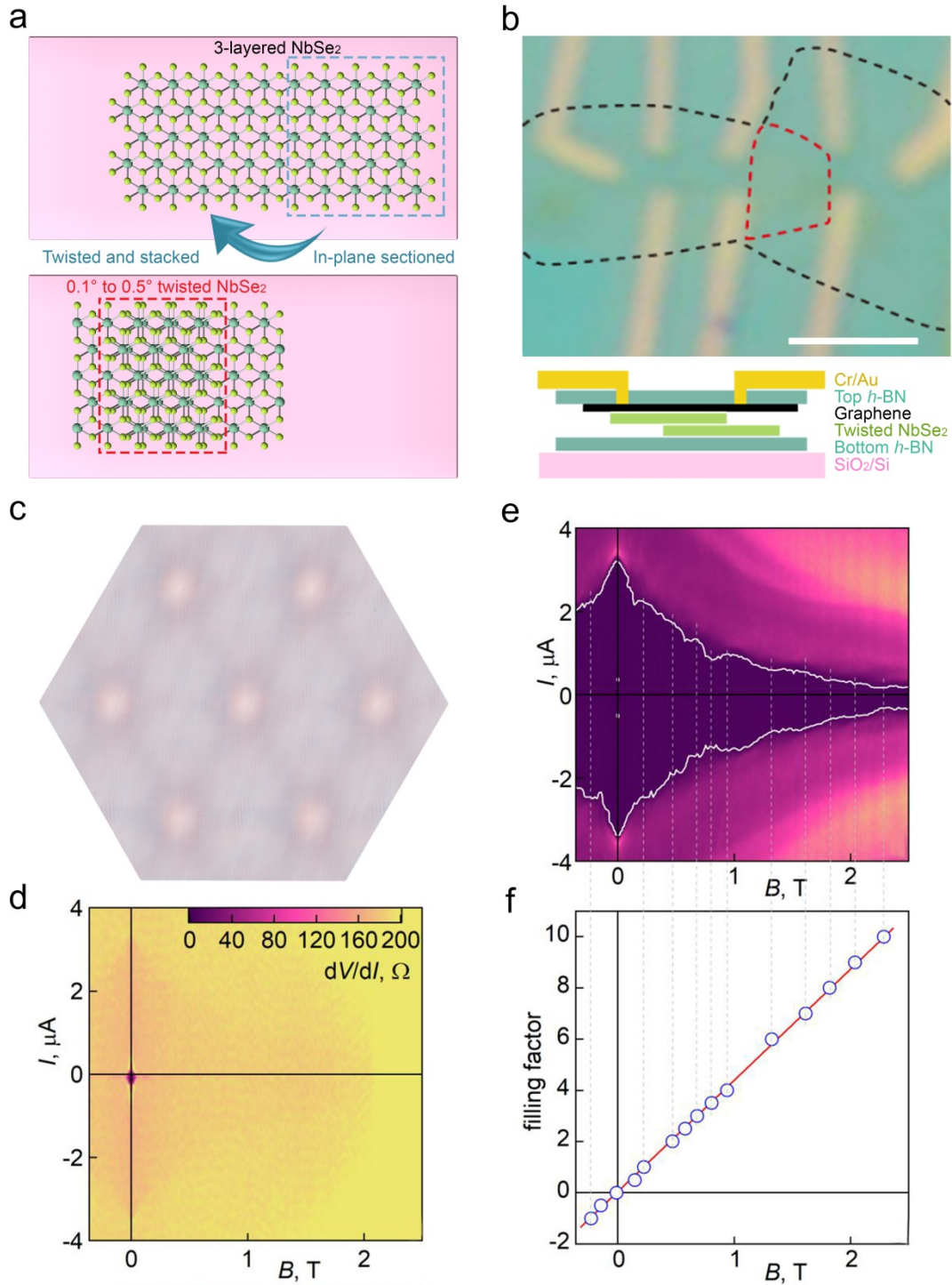
Fig. S30 Josephson junction arrays in van der Waals heterostructures based on mechanically exfoliated and twisted NbSe₂ flakes. (a) Illustration of the fabrication scheme and **(b)** optical microscopic image of the twisted NbSe₂ device. The black and red dashed curves in **(b)** outline the individual and twisted regions of mechanically exfoliated NbSe₂ flakes. Lower inset in **(b)** shows the schematic of twisted device. Scale bar, 2 μm. **c,** Schematic of the moiré pattern in the twisted NbSe₂ flake with a rotation angle of 0.2°. The differential

136

resistance ($\mathrm{d}V/\mathrm{d}I$) as a function of the current and magnetic field for the (**d**) individual and (**e**) twisted NbSe$_2$ flakes. The contours indicate the critical current, and the colour scales are the same in (**d**) and (**e**). **f**, The position of the maxima (integer indices) and minima (half-integer indices) as a function of the magnetic field.

## 19. Probing the stability of as-exfoliated NbSe$_2$ flakes dispersed in PC solvent.
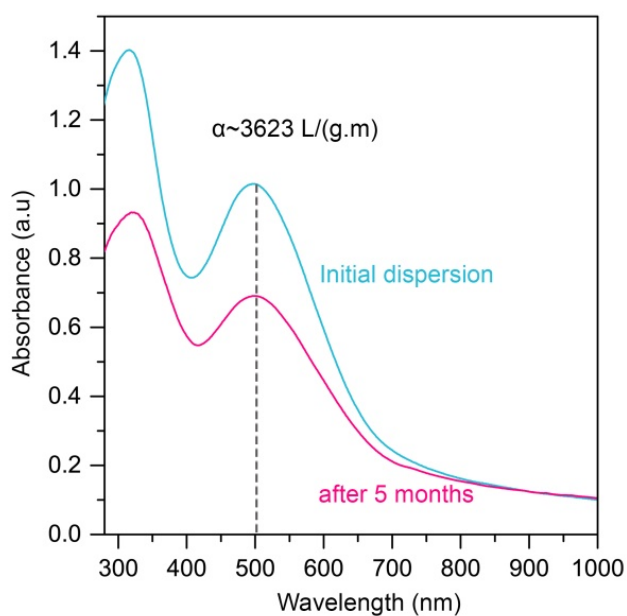
Fig. S31 UV-vis spectra of as-prepared NbSe$_2$ dispersed in PC solvent before (cyan line) and after (red line) a storage time of 5 months in air. UV-vis measurement demonstrates that ~60% of NbSe$_2$ flakes dispersed in PC can survive after a storage duration of 5 months in ambient conditions.

20. Dispersion of exfoliated NbSe$_2$ in a diversity of solvents.

Abbreviation	Full name	Polarity Index[21]
TOL	Toluene	2.4
DCM	Dichloromethane	3.1
IPA	Isopropyl Alcohol	4.0
THF	Tetrahydrofuran	4.0
ETAC	Ethyl Acetate	4.4
DIOX	1,4-Dioxane	4.8
ACE	Acetone	5.1
ACN	Acetonitrile	5.8
FA	Formic Acid	6.0
AA	Acetic Acid	6.0
DMF	N,N-Dimethyl Formamide	6.4
DMSO	Dimethyl Sulfoxide	7.2

Table 1 A list of solvents used for the dispersion of NbSe$_2$ in various solvents as shown in Fig. 4a.

21. Processibility of as-exfoliated NbSe₂ flakes in solution phase.
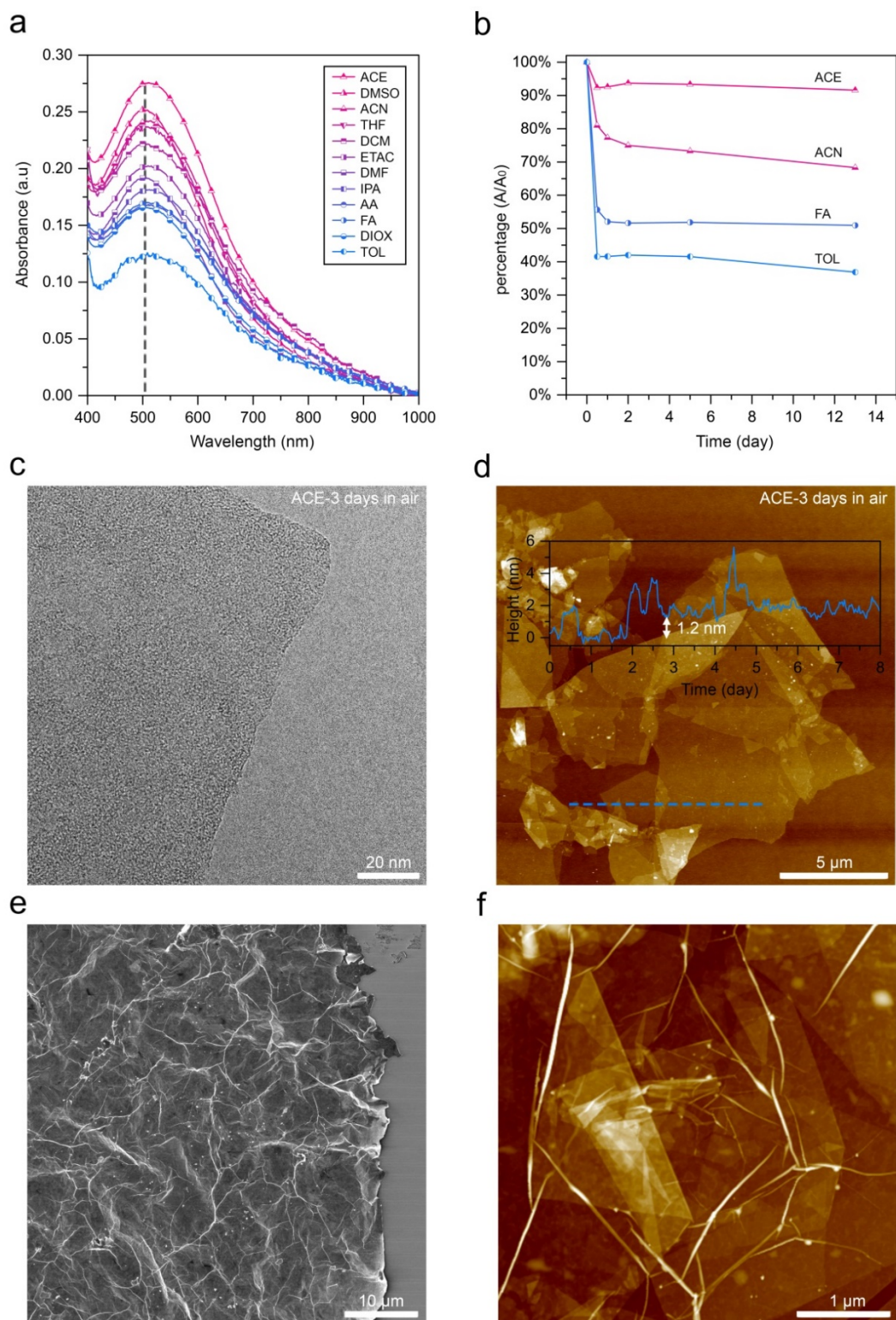
Fig. S32 The dispersion of exfoliated NbSe₂ sheets in different solvents and their solution processibility.
a, UV-vis spectra of as-exfoliated NbSe₂ sheets (~0.1 mg) re-dispersed in a variety of solvents (10 mL). **b**,

Time-dependence of UV-vis absorbance (at 508 nm, normalized to the initial absorbance A_0) after the storage in air. (**c**) TEM and (**d**) AFM images of NbSe$_2$ sheets stored in acetone for 3 days in air. (**e**) SEM and (**f**) AFM images of NbSe$_2$ film deposited on SiO$_2$ substrate *via* drop-casting (NbSe$_2$ dispersion in acetone).

We have provided the UV-vis spectra of exfoliated NbSe$_2$ sheets dispersed in a variety of solvents (Fig. S32a). The absorption feature peaked around 500 nm is originated from NbSe$_2$ thin flake dispersed in the solution[22]. The intensity variation of absorption feature around 500 nm can be used to track the stability of NbSe$_2$ sheets in solution medium. Therefore, we monitored the stability of NbSe$_2$ flakes dispersed in four representative solvent (acetone, acetonitrile, formic acid and toluene) using time-dependent UV-vis spectroscopy (Fig. S32b). We note that some portion of NbSe$_2$ sheets precipitate in the first 0.5 h in different solvents, presumably due to the over-saturation (the total amount of NbSe$_2$ exceeds the saturation concentration). After this, the maximal absorbance around 500 nm (normalized to its initial absorbance) exhibits excellent stability in air even up to fourteen days (decay < 1% per day), suggesting a great improvement in stability compared with the sheets directly exposed to air (degraded in mins, Fig. S26).

22. NbSe₂ ink for 3D printing.
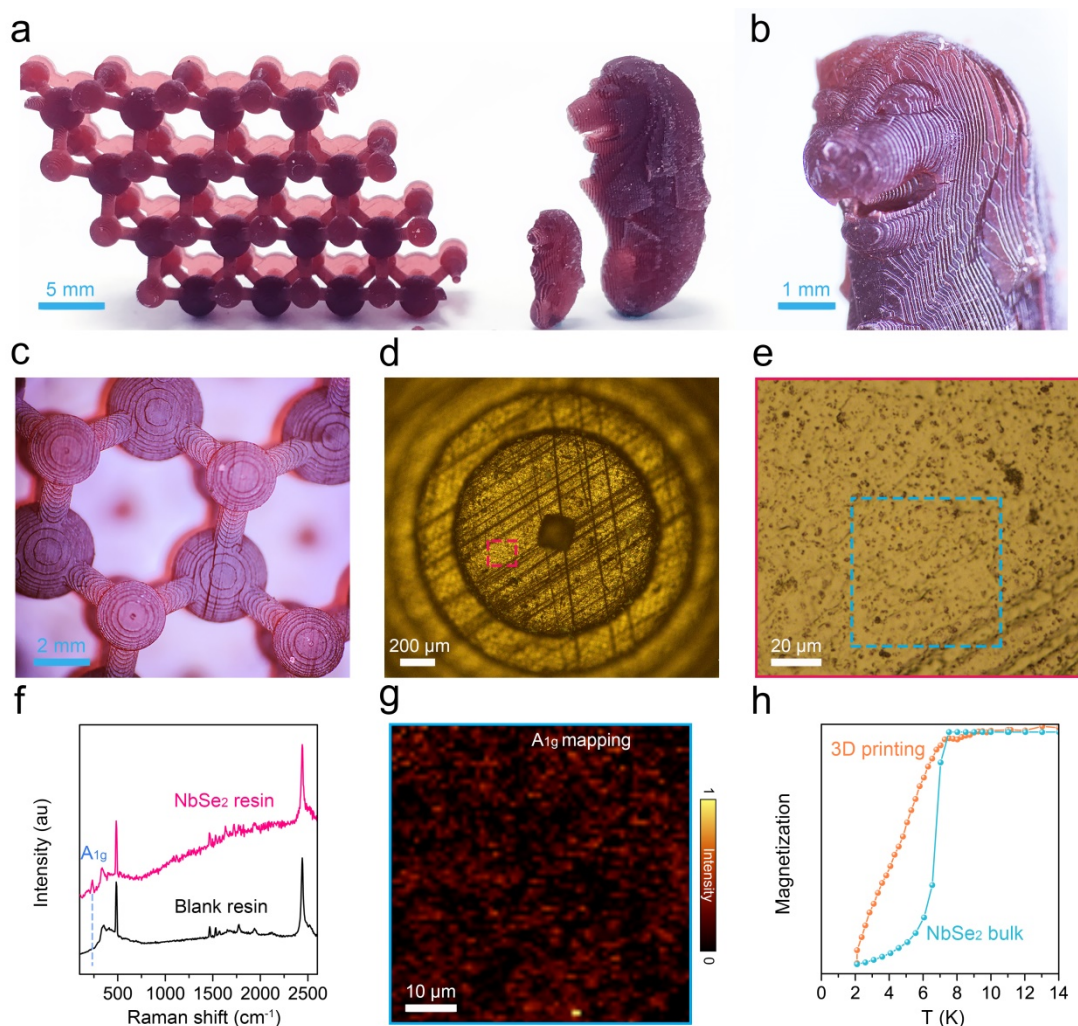
Fig. S33 3D printing of as-exfoliated NbSe₂ flakes. a-c, Digital photographs of a NbSe₂ atomic model and a Merlion statue by 3D printing. **d-e,** Optical microscopic images of 3D printed structures. **f,** Raman spectra of 3D printed structures with/without NbSe₂ sheets, the presence of the characteristic A_{1g} peak demonstrates the existence of NbSe₂ flakes in 3D printed matrix. **g,** Raman mapping acquired at the A_{1g} characteristic peak of NbSe₂. Uniform signal intensity indicates a good dispersion of NbSe₂ flakes in the printed structure. **h,** T-dependent magnetization of the NbSe₂ dispersed in 3D printed structure and bulk NbSe₂ sample under a magnetic field of 200 Oe.

141

**23. The size distribution of exfoliated NbSe₂ flakes in the printable ink for inkjet printing.**
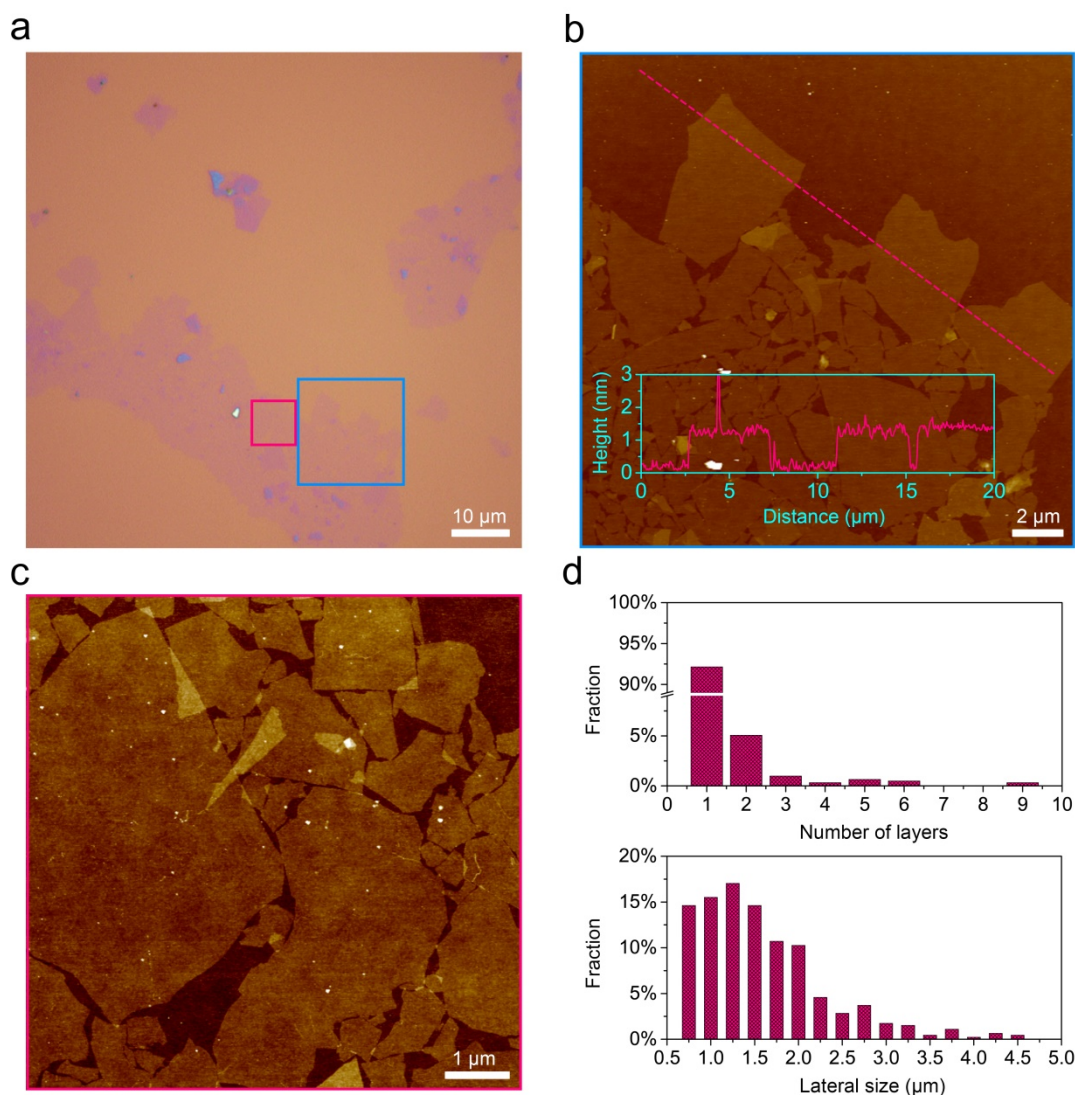
Fig. S34 The size distribution of exfoliated NbSe₂ flakes in the printable inks. a, Representative optical microscopic image and (**b-c**) AFM morphology of NbSe₂ flakes (corresponding to the area denoted with box in (**a**) *via* drop-casting as-prepared printable ink onto a SiO₂/Si substrate). **d**, The statistical distribution of vertical thickness and lateral size of NbSe₂ flakes in the printable inks.

24. T-dependent R_{xx} of patterned NbSe$_2$ film using inkjet printing.
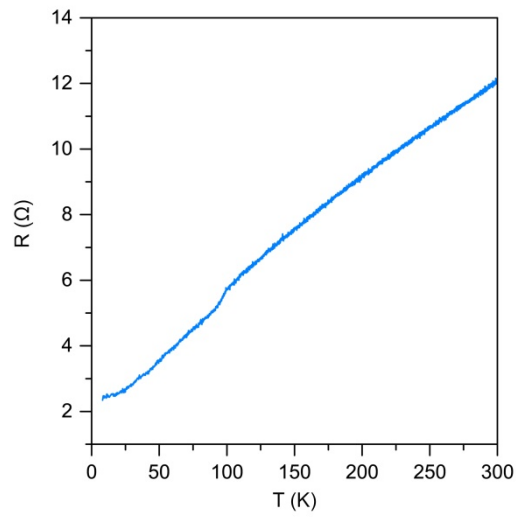
Fig. S35 T-dependent longitudinal resistance (R_{xx}) of patterned NbSe$_2$ film using inkjet printing.

25. 2D superconductivity of re-stacked NbSe₂ monolayers.

a

b

c

d

e

f
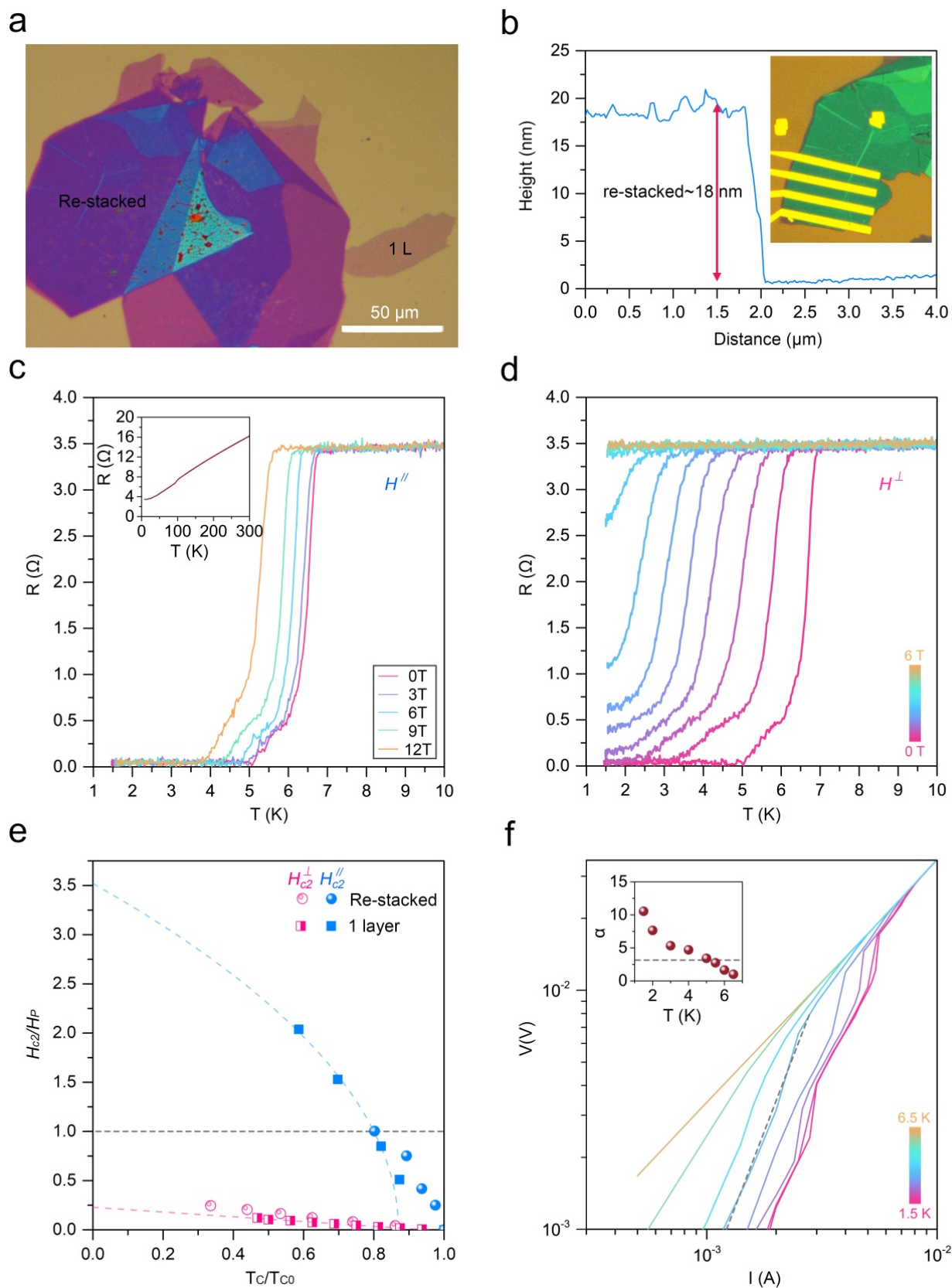
Fig. S36 2D superconductivity of re-stacked NbSe₂ sheets. (**a**) Optical and (**b**) AFM height profile of re-

stacked NbSe$_2$ monolayers. T-dependent longitudinal resistance (R_{xx}) of re-stacked NbSe$_2$ sheets under different in-plane ($H_{//}$) (**c**) and out-of-plane ($H_\perp$) (**d**) magnetic field. Inset shows the R_{xx} from 10 to 300 K. **e**, The critical field H_{c2}/H_p as a function of transition temperature T_c/T_{c0} for restacked NbSe$_2$ film under out-of-plane ($H_\perp$) and in-plane ($H_{//}$) magnetic fields. The dashed red and blue lines correspond to the fitting of monolayer NbSe$_2$ based on Ginzburg-Landau theory. The dashed grey line corresponds to the Pauli paramagnetic limit. **f**, Voltage-current (V-I) characteristics at different temperatures on a logarithmic scale. Dashed line indicates the expected $V \propto I^3$ behaviour at the Berezinskii-Kosterlitz-Thouless transition

Reference

1. Lin Z, *et al.* Solution-processable 2D semiconductors for high-performance large-area electronics. *Nature* **562**, 254-258 (2018).

2. Peng J, *et al.* Very large-sized transition metal dichalcogenides monolayers from fast exfoliation by manual shaking. *J Am Chem Soc* **139**, 9019-9025 (2017).

3. Shen J, *et al.* Liquid phase exfoliation of two-dimensional materials by directly probing and matching surface tension components. *Nano Lett* **15**, 5449-5454 (2015).

4. Xi X, *et al.* Strongly enhanced charge-density-wave order in monolayer NbSe$_2$. *Nat Nanotechnol* **10**, 765 (2015).

5. Barajas-Aguilar AH, *et al.* Crystalline structure, electronic and lattice-dynamics properties of NbTe$_2$. *Sci Rep* **8**, 16984 (2018).

6. Navarro-Moratalla E, *et al.* Enhanced superconductivity in atomically thin TaS$_2$. *Nat Commun* **7**, 11043 (2016).

7. Hajiyev P, Cong C, Qiu C, Yu T. Contrast and Raman spectroscopy study of single- and few-layered charge density wave material: 2H-TaSe$_2$. *Sci Rep* **3**, 2593 (2013).

8. Gao Z, *et al.* In Situ-Generated Volatile Precursor for CVD Growth of a Semimetallic 2D Dichalcogenide. *ACS Appl Mater Interfaces* **10**, 34401-34408 (2018).

9. Luo H, *et al.* Differences in Chemical Doping Matter: Superconductivity in Ti1–xTaxSe$_2$ but Not in Ti1–xNbxSe$_2$. *Chem Mater* **28**, 1927-1935 (2016).

10. Keum DH, *et al.* Bandgap opening in few-layered monoclinic MoTe$_2$. *Nat Phys* **11**, 482 (2015).

11. Kan M, Nam HG, Lee YH, Sun Q. Phase stability and Raman vibration of the molybdenum ditelluride (MoTe$_2$) monolayer. *PCCP* **17**, 14866-14871 (2015).

12. Rossi D, *et al.* Photoinduced separation of strongly interacting 2-D layered TiS2 nanodiscs in solution. *The Journal of Physical Chemistry C* **118**, 12568-12573 (2014).

13. Zhu Z, *et al.* Near-Infrared Plasmonic 2D Semimetals for Applications in Communication and Biology. *Adv Funct Mater* **26**, 1793-1802 (2016).

14. Han GH, *et al.* Absorption dichroism of monolayer 1T′-MoTe2 in visible range. *2D Materials* **3**, 031010

(2016).

15. Wu J, *et al.* Acid-assisted exfoliation toward metallic sub-nanopore TaS2 monolayer with high volumetric capacitance. *J Am Chem Soc* **140**, 493-498 (2018).

16. Cullen PL, *et al.* Ionic solutions of two-dimensional materials. *Nature chemistry* **9**, 244 (2017).

17. Lui CH, Liu L, Mak KF, Flynn GW, Heinz TF. Ultraflat graphene. *Nature* **462**, 339-341 (2009).

18. Kretinin A, *et al.* Electronic properties of graphene encapsulated with different two-dimensional atomic crystals. *Nano Lett* **14**, 3270-3276 (2014).

19. Kim K, *et al.* van der Waals heterostructures with high accuracy rotational alignment. *Nano Lett* **16**, 1989-1995 (2016).

20. Cao Y, *et al.* Quality heterostructures from two-dimensional crystals unstable in air by their assembly in inert atmosphere. *Nano Lett* **15**, 4914-4921 (2015).

21. Spangenberg B, Poole CF, Weins C. *Quantitative thin-layer chromatography: a practical survey*. Springer Science & Business Media (2011).

22. Hill HM, *et al.* Comprehensive optical characterization of atomically thin NbSe 2. *Phys Rev B* **98**, 165109 (2018).

3.5 CVD graphene and its twisted heterostructures

The improvement of CVD graphene fabrication has laid the foundation for the large-scale manufacture of graphene devices in industrial applications. Currently, the twisted heterostructures created directly by CVD have gained much attention. Our experimental studies found that growing twisted devices directly by CVD avoids the contingency of twisted angle caused by transfer and improves the efficiency of device fabrication. However, until now, this technique has remained at an immature stage. The quality of CVD graphene and the control of twisted angles still require further development to be suitable for practical applications. Paper 4 attempted to overcome the issue of surface contamination by a post-growth method that exploited the adhesive force of an activated-carbon-based lint roller on the graphene surface. Significant elimination of the polymer residue was identified, and thus, the transport properties of such graphene transistors have improved dramatically. Paper 5 reported an *ex situ* nucleation strategy to control the second layer nucleation, relative to the first layer, in the fabrication of twisted bilayer graphene. The results found that the control of the twisted angle was superior to those reported previously, whilst the quality of the twisted graphene was maintained well, with mobility up to 68,000 cm^2 V^{-1} s^{-1} at room temperature.

Paper 4 (Published in Advanced Material, Contributed equally)

My contribution: Performed the transport measurement for the CVD graphene and gave feedback to the fabrication side for any quality improvement.

A force-engineered lint roller for super-clean graphene

Luzhao Sun[1,2,#], Li Lin[1,#], Zihao Wang[3,#], Dingran Rui[4,#], Zhiwei Yu[5], Jincan Zhang[1,2], Yanglizhi Li[1,2], Xiaoting Liu[1,2], Kaicheng Jia[1], Kexin Wang[1], Linming Zheng[1], Bing Deng[1], Tianbao Ma[5], Ning Kang[4], Hongqi Xu[4], K. S. Novoselov[3], Hailin Peng[1,6]*, Zhongfan Liu[1,6]*.

[1] Center for Nanochemistry, Beijing Science and Engineering Center for Nanocarbons, Beijing National Laboratory for Molecular Sciences, College of Chemistry and Molecular Engineering, Peking University, Beijing 100871, P. R. China

[2] Academy for Advanced Interdisciplinary Studies, Peking University, Beijing 100871, P. R. China

[3] School of Physics and Astronomy, University of Manchester, Manchester M13 9PL, UK

[4] Beijing Key Laboratory of Quantum Devices, Key Laboratory for the Physics and Chemistry of Nanodevices, and Department of Electronics, Peking University, Beijing 100871, P. R. China

[5] State Key Laboratory of Tribology, Tsinghua University, Beijing 100084, P. R. China.

[6] Beijing Graphene Institute, Beijing 100094, P. R. China

Contamination is of concern when dealing with surface and interface technologies. Given that graphene is a two-dimensional (2D) monolayer material with an extremely large surface area, surface contamination may seriously degrade its intrinsic properties and strongly hindering the applications of graphene in surface and interfacial regions. However, large-scale and facile treatment methods for producing clean graphene film that preserve its excellent properties has been still unachieved. Herein, we report an efficient post-growth treatment method for selectively removing surface contamination to achieve a large-area super-clean graphene surface, enabled by a strong adhesive force of an activated-carbon-based lint roller upon graphene contaminations. The as-fabricated super-clean graphene, with a surface cleanness exceeding 90%, can be transferred to dielectric substrates with significantly reduced polymer residue, leading to superior optical and electrical properties.

Progress of modern semiconductor industry has its foundation on effective surface-cleaning techniques[1]. The rising applications of graphene and other 2D materials relies highly on the availability of super-clean surfaces, because surface cleanness has significant impacts on their properties and performances, especially in consideration of the 2D nature[2-7]. Although CVD-derived graphene film on metal foil exhibits promising properties[8,9], it still faces the serious issue of surface contamination, which strongly degraded the graphene properties[3,5,6].

Surface contamination of CVD-derived graphene films has three main origins: intrinsic

contamination that occurs during the CVD growth process (Supplementary Note 1), polymer residues introduced by transferring process from growth substrate to target substrate[10], and airborne contamination[5]. Many attempts have been made to remove the surface contamination of graphene, involving the Joule heating[11], annealing[10,12], plasma treatment[13,14]. However, only emphasizing the elimination of transfer-related contamination, these post-growth routines cannot thoroughly solve the issue of surface contamination, and to obtain super-clean graphene film on a large scale becomes a major hurdle in graphene research (Supplementary Table 1). In this paper, we obtain a meter-sized super-clean graphene film, relying on the direct effective cleaning of graphene on Cu foil to eliminate the intrinsic surface contamination, i.e., amorphous carbon[15], immediately following CVD growth. In this case, amorphous carbon can be successfully removed using an activated carbon-coating lint roller featured by a strong adhesive interaction with amorphous carbon. The successful removal of amorphous carbon would contribute to reducing the polymer residues on graphene during the transferring process, along with enhanced optical and electrical properties.

During the high-temperature CVD growth, the graphene surface would be contaminated with defective amorphous carbon with a thickness of around few nanometers (Supplementary Note 1 and Supplementary Fig. 1). Fortunately, the absence of relatively strong interaction between amorphous carbon and graphene surface promise a possibility of detaching them for obtaining a clean surface of graphene, as evident in the movement of amorphous carbon on graphene surface driven by the electron-beam (Supplementary Fig. 2 and Supplementary Video).

The lint roller, commonly used to remove the dust on clothes in daily life, is composed of one-sided adhesive paper with a strong interaction upon targeting contaminations. Inspired by this, an activated carbon-coating lint roller is fabricated to treat the graphene/Cu foil to obtain a clean graphene surface, relying on the strong interaction between activated carbon and amorphous carbon on graphene. In detail, activated carbon powder was coated on micron sized pores of commercially available Cu foam to achieve a high mass loading of activated carbon, where a binder is used to form a strong connection between Cu foam and activated carbon. The cleaning process of as-received large area of graphene on Cu foil was conducted by slowly rolling the foil directly under the activated carbon-coating lint roller at a temperature of 170 °C (Fig. 1a and Supplementary Fig. 3). A close contact between activated carbon

and contaminations on graphene is key for the successful removal of contaminations, due to their dense distribution on graphene surface. The close contact between amorphous carbon contamination of graphene and activated carbon of lint roller were indicated by the studies of cross-sectional transmission electron microscopy (TEM) and elementary dispersive spectrum (EDS) mapping, which lead to a strong interfacial adhesion force (Fig. 1b and Supplementary Fig. 4).

The removal of amorphous carbon contamination of graphene after lint rolling process can be revealed by atomic force microscopy (AFM). As shown in Fig. 1c, typical AFM image of common CVD graphene samples before the cleaning process indicates that amorphous carbon is universally distributed over the entire graphene surface at an average height of ~1.2 nm. In contrast, after post-treatment of lint rolling, a highly improved cleanness of graphene with reduced surface contamination can be confirmed by greatly improved surface flatness and the much narrower height distribution in AFM image (Fig. 1d and Supplementary Fig. 5).

We believe that the interfacial-force-engineered lint rolling process is key to for removing the amorphous carbon contamination and achieving the super-clean graphene surface. As well known, activated carbon has porous structure and functional groups (Supplementary Note 2 and Supplementary Fig. 6), enabling a stronger interaction with amorphous carbon than that between amorphous carbon and graphene surface[16], which ensure the success of detaching the amorphous carbon from graphene basal plane. To further confirm this, adhesion forces between activated carbon and amorphous carbon (F-$C_{activated}$-$C_{amorphous}$), and adhesion forces between amorphous carbon and graphene (F-$C_{activated}$-Gr) were measured, respectively (see Methods and Supplementary Note 2). As shown in Fig. 1e, we measured typical adhesive forces through the gradual approach of an amorphous-carbon-coated AFM tip towards the as-fabricated clean graphene or the activated carbon, respectively. As a result, F-$C_{activated}$-Gr with average value of 93.1 ± 10.9 nN is clearly smaller than F-$C_{activated}$-$C_{amorphous}$ (373.2 ± 158.0 nN) (Supplementary Fig. 7).

The efficient force-engineered lint rolling post-treatment allow for the fabrication of a large-area super-clean graphene surface. As shown in Fig. 1f, meter-scale super-clean graphene was obtained, and the cleanness was evaluated through the visualization of surface contamination using the TiO_2-deposition method[17,18] (Supplementary note 3, Fig. 1g and Supplementary Fig. 8). After transferring as-

received graphene onto the TEM grid, the high degree of surface cleanness of graphene film (can reach 99%) was further confirmed using high-resolution TEM (HR-TEM) (Fig. 1h and Supplementary Fig. 9). To test the recoverability of the activated carbon-coating lint-roller, a series of experiment were conducted and the cleanness of as-treated graphene could be maintained after at least 10 rounds. (Supplementary Fig.10).

The availability of super-clean graphene on Cu would enable the suppression of another contamination-polymer residues in the following transfer step for further applications. Normally, a transferring process of graphene from growth substrate to a dielectric substrate is required for further device fabrication and integration [19,20], in which a polymer medium such as poly(methyl methacrylate) (PMMA) is inevitably used to support the graphene film. This unfortunately results in a large amount of the PMMA residues on the as-transferred graphene surface[6], as evident in the AFM image of unclean graphene transferred onto atomically flat mica, where the polymer residue is clearly visible (Fig. 2a). The height distribution (Fig. 2b) was fitted with 3 Gaussian peaks, which can be assigned to graphene, amorphous carbon and PMMA residues, respectively. In contrast, almost no PMMA residues and amorphous carbon were found on the surface of the as-fabricated super-clean graphene after the transfer (Fig. 2c), as indicated by the similar height distribution of the as-transferred super-clean graphene with that of mica (Fig. 2d). Clearly, a removal of amorphous carbon before transfer ensure a reduction of transfer-related polymer residues. Figure 2e displays a photographic image of a super-clean-graphene film transferred onto a large-area (4 cm × 8 cm) mica substrate. The corresponding AFM images and the statistical data reveal a cleanness of 99% after the transfer (see Supplementary Fig. 11, and Fig. 2f, respectively). Furthermore, the PMMA residues on common as-transferred graphene samples can be still removed by the activated carbon-coating lint roller efficiently (Supplementary Fig. 12), showing the universality of our method.

The availability of a clean surface on a large scale would ensure enhanced electrical properties of graphene films. To characterize the quality of as-received graphene, firstly, no defect-related D peak were observed in Raman results, along with a large 2D/G ratio, confirming the high quality and monolayer nature of the obtained clean graphene film after the treatment[21] (Fig. 3a and Supplementary Fig. 13).

Contact issue and carrier mobility is two parameters, that dominate the electrical performance of graphene devices in applications of high-speed electronics[22]. In this regard, a graphene transistor array (inset of Fig. 3b) was fabricated for measuring the contact resistance. By using transfer length method (TLM)[23], we can extract the contact resistance at different gate bias (V_G - V_{Dirac}, V_{Dirac} = 15V) at room temperature (Fig. 3b and Supplementary Fig. 14), where the minimum contact resistance between clean graphene and metal (Pd/Au) reach 117.6 $\pm$ 32.5 Ω μm at V_G= V_{Dirac} – 37 V, which is comparable with the value of exfoliated graphene. The field-effect mobility of the as-received super-clean graphene on SiO_2/Si substrate is around 17,100 cm^2 V^{-1} s^{-1} at 1.9 K, which indicate the contribution of low level of contamination to improved electrical quality[24,25] (Supplementary Fig. 15). To further confirm the intrinsic mobility of super-clean graphene, the hBN-encapsulated graphene Hall bar devices with one-dimensional edge contact (inset of Fig. 3c) were fabricated using hot "pick-up" technique[26,27] (see Methods). By plotting the four-terminal resistance as a function of charge carrier density n, the extracted field effect mobility exceeds 400,000 cm^2 V^{-1} s^{-1} at 1.7 K (Fig. 3c), while the corresponding Hall mobility can be as high as 500,000 cm^2 V^{-1} s^{-1} (Supplementary Fig. 16). By performing magnetotransport measurements on the hBN-encapsulated graphene Hall bar device, the Landau fan and broken Landau level degeneracy can be well resolved (Fig. 3d), indicating the high quality of as-received super-clean graphene.

The reduced contamination also brings benefits on sheet resistance and optical transmittance, which are two important technological parameters in the application of transparent conductive film. The as-fabricated super-clean graphene film exhibits a lower sheet resistance (618.0 ± 19.6 Ω/□) than that of unclean graphene film (879.8.0 ± 173.7 Ω/□) (Fig. 3e), which is probably ascribable to an increase in carrier mobility and a better contact. As for the optical transmittance, the super-clean graphene transferred on quartz glass exhibited a average transmittance of 97.4 % at a wavelength of 550 nm, which is very close to ideal value of monolayer graphene[28] (Fig. 3f). By stacking three layers of graphene on polyethylene terephthalate (PET) substrate by layer-by-layer transfer techniques, the difference in transmittance between unclean and super-clean graphene can be clearly observable by naked eyes (Supplementary Fig. 17).

In summary, we developed and demonstrated an activated carbon-coating lint roller with a strong

adhesive force to successfully remove surface contamination on graphene surface. The as-treated graphene surface exhibited a high cleanness of 90% with low degree of polymer residue after transferring onto a functional substrate. The super-clean signature of the graphene film ensures considerably enhanced optical and electrical properties, providing a new material platform for various applications of graphene.

Methods

Graphene-film growth. Graphene films were grown on Cu foil using a low-pressure CVD system, as reported previously. Typically, 25-µm-thick Cu foil (99.8% purity, Alfa-Aesar #46365) was placed in a quartz tube furnace and heated to 1020 °C under a 500-sccm flow of Ar. The sample was then annealed for 30 min under a 500-sccm flow of H_2. Graphene was then grown for 20 min under a 100-sccm flow of H_2 and 1 sccm-flow of CH_4.

Graphene-film cleaning using the activated carbon-coating lint roller. An activated carbon-coating lint-roller was fabricated by binding activated carbon powder to porous Cu foam with poly(vinylidene fluoride) (PVDF, 1000 K). The mass ratio of activated carbon to PVDF was 6:1, and the binder solvent was N-methylpyrrolidone (NMP). Normal graphene on Cu foil was placed in a vacuum system and rolled by the as-fabricated activated-carbon lint roller at a temperature of 170 °C. The graphene surfaces were usually cleaned four times by this procedure.

Graphene transfer. The graphene film was transferred onto mica and SiO_2 with the assistance of PMMA. The graphene/Cu was spin-coated with PMMA at 2000 rpm and then baked at 170 °C for 5 min. After etching away the Cu foil with 1 M $Na_2S_2O_8$ solution and washing with deionised water, the PMMA/graphene was subsequently placed onto target substrates and the PMMA was dissolved using acetone. A "dry" transfer method was used to fabricate hBN-encapsulated graphene devices, including the native oxidation of Cu, "pick-up" graphene by hBN and drop down steps[26,27] (Supplementary Note 4). The graphene was transferred onto a TEM grid using a non-polymer-assisted method, as reported previously. Large-scale graphene films were transferred onto PET substrates with the assistance of thermal release tape.

Adhesion-force measurements. Adhesion force was measured in air on an MFP-3D atomic-force

microscope (Asylum Research) fitted with a graphene-coated microsphere probe. Graphene was first grown on copper microspheres under the same CVD growth conditions as used for graphene growth on copper foil. In order to fabricate the graphene-coated microsphere probe, a graphene-coated microsphere was then glued to an AFM cantilever (Nanosensor TL-FM), as previously reported[29]. The normal force constant (k = 2.82 N/m) was calibrated using the thermal-noise method[30].

Preparation of cross-sectional specimens for TEM. A dual-beam TEM instrument (FEI Strata DB 235), which combines a focused-ion beam (FIB) and a SEM column, was used to fabricate cross-sectional specimens of activated carbon/graphene/Cu foil. For initial surface protection during FIB scanning, the activated carbon/graphene/Cu sample was coated with a 30-nm-thick Cr layer by thermal evaporation. A 1-μm-Pt layer was then deposited at the selected region of the Cr/activated carbon/graphene/Cu structure as a protection layer as the sample was finally milled at thicknesses below 30 nm.

SEM and TEM measurements: SEM images were acquired on a scanning-electron microscope (Hitachi S-4800, accelerator voltage: 1–10 kV). The cross-sectional analysis of contact between activated carbon and amorphous carbon on graphene were conducted using aberration-corrected TEM (FEI Titan Cubed Themis G2 300) under 300 kV. The bright-field (BF) and high-angle annular dark-field (HAADF) images of graphene were acquired in the same aberration-corrected TEM under 80 kV.

Device Fabrication and Transport Measurements. To evaluate the electrical properties of our graphene sample, Hall bar devices were fabricated on the graphene crystal transferred onto 300-nm-thick silicon oxide with alignments marks. The flatness of each sample was verified by AFM. Electron-beam lithography (EBL) (Raith 150 2nd) and reactive ion etching (RIE) with O_2 (Trion Technology Minilock III) were employed to pattern graphene into a Hall bar geometry. After a PMMA mask (PMMA 950K A4 @ 4000 rpm) was patterned by EBL, Ti/Au (5/90 nm) electrodes were deposited by electron-beam evaporation (Kurte J. Lesker AXXIS). Electrical transport at room temperature was determined using a vacuum-probe station (Lake Shore TTP-4) with a Keithley semiconductor characterisation system (Model 4200-SCS). Electrical and magnetotransport data at low temperatures were acquired using a physical property measurement system (PPMS, Quantum Design DynaCool). Device resistance was measured using a lock-in amplifier (Stanford Research 830) with an ac driving current of 50–100 nA.

Figure Captions:

Figure 1 | Super-clean graphene treated by the activated carbon-coating lint roller. a, Schematic illustration of the activated carbon-coating lint roller designed for the roll-to-roll treatment of a graphene film on Cu foil (left). Note that, the contamination on common graphene sample (grey) can be peeled off by lint-roller (Left). Schematic illustration of contact model depicting activated carbon and unclean graphene on Cu foil (right). **b**, Cross-sectional EDS map of a contact area between activated carbon and graphene. **c,d**, AFM images of unclean (**c**) and super-clean graphene (**d**) on Cu foil. **e**, Typical measured adhesive forces of F-$C_{activated}$-$C_{amorphous}$ (red curve) and F-$C_{amorphous}$-Gr (blue curve). **f,g**, Large area visualisation of as-fabricated super-clean graphene through the selective deposition of TiO_2 particles (white dots in **g**); scale bar: 50 µm. **h**, HR-TEM image showing the atomically clean surface. Inset: lattice image of super-clean graphene with atomic resolution; scale bar: 2 nm.

Figure 2 | Suppression of polymer residue after graphene transfer. a,b, AFM images of unclean (a) and super-clean graphene (b) on mica. **c**, An as-obtained large-area super-clean graphene film transferred onto a 4-inch-sized mica substrate. **d,** Height Histogram of the the unclean graphene in (**a**) with multi-peak fits. **e**, Height distribution of the super-clean graphene in (**b**) and the bare mica substrate. **f,** Statistics of corresponding cleanness in **c**.

Figure 3 | Quality evaluation of as-fabricated super-clean graphene. a, Raman spectra taken from different position on the transferred super-clean graphene film. **b,** The contact resistance as a function of gate bias. Inset: SEM image of the TLM-measured graphene transistor array, where the channel lengths vary from 2 to 6 µm; scale bar: 2 µm. **c**, Resistivity of super-clean graphene encapsulated by hBN as a function of charge carrier density (n) at $T = 1.7$ K. Inset: schematic of Hall bar device of encapsulated graphene with one-dimensional contact. **d**, Derivative of the Hall resistivity R_{xy} with respect to n as a function of magnetic field B and n for the device in (c). The dash black lines clearly show Landau levels at filling factors ν = …, -10, -6, -2, 0, 2, 6, 10,…. **e**, Sheet resistances of unclean and super-clean graphene films transferred onto SiO_2/Si wafers; scale bar: 1 cm. **f**, UV-vis spectra of super-clean graphene films transferred onto quartz substrates. Inset: statistics of transmittance of graphene at wavelength of 550 nm.

References:

1. Reinhardt, K. A. & Reidy, R. F. *Handbook for cleaning for semiconductor manufacturing: fundamentals and applications*. (John Wiley & Sons, 2011)

2. Novoselov, K. S. *et al.* A roadmap for graphene. *Nature* **490**, 192-200 (2012).

3. Bolotin, K. I. *et al.* Ultrahigh electron mobility in suspended graphene. *Solid State Commun.* **146**, 351-355 (2008).

4. Pettes, M. T., Jo, I., Yao, Z. & Shi, L. Influence of polymeric residue on the thermal conductivity of suspended bilayer graphene. *Nano Lett.* **11**, 1195-1200 (2011).

5. Li, Z. *et al.* Effect of airborne contaminants on the wettability of supported graphene and graphite. *Nat. Mater.* **12**, 925-931 (2013).

6. Zhang, Z. *et al.* Rosin-enabled ultraclean and damage-free transfer of graphene for large-area flexible organic light-emitting diodes. *Nat. Commun.* **8**, 14560 (2017).

7. Kim, Y. *et al.* Remote epitaxy through graphene enables two-dimensional material-based layer transfer. *Nature* **544**, 340-343 (2017).

8. Bae, S. *et al.* Roll-to-roll production of 30-inch graphene films for transparent electrodes. *Nat. Nanotechnol.* **5**, 574-578 (2010).

9. Hao, Y. F. *et al.* The Role of Surface Oxygen in the Growth of Large Single-Crystal Graphene on Copper. *Science* **342**, 720-723 (2013).

10. Lin, Y. C. *et al.* Graphene annealing: how clean can it be? *Nano Lett.* **12**, 414-419 (2012).

11. Moser, J., Barreiro, A. & Bachtold, A. Current-induced cleaning of graphene. *Appl. Phys. Lett.* **91**, 163513 (2007).

12. Huang, L.-W. *et al.* Characterization of the cleaning process on a transferred graphene. *Journal of Vacuum Science & Technology A: Vacuum, Surfaces, and Films* **32**, 050601 (2014).

13.   Peltekis, N. *et al.* The effect of downstream plasma treatments on graphene surfaces. *Carbon* **50**, 395-403 (2012).

14.   Cunge, G. *et al.* Dry efficient cleaning of poly-methyl-methacrylate residues from graphene with high-density H2 and H2-N2 plasmas. *J. of Appl. Phys.* **118**, 123302 (2015).

15.   Robertson, J. Amorphous carbon. *Adv. in Phys.* **35**, 317-374 (1986).

16.   Bansal, R. C. & Goyal, M. *Activated carbon adsorption*. (CRC Press, 2005).

17.   Zhang, R. F. *et al.* Optical visualization of individual ultralong carbon nanotubes by chemical vapour deposition of titanium dioxide nanoparticles. *Nat. Commun.* **4**, 1727 (2013).

18.   Kim, K. *et al.* Selective metal deposition at graphene line defects by atomic layer deposition. *Nat. Commun.* **5**, 4781 (2014).

19.   Li, X. S. *et al.* Transfer of Large-Area Graphene Films for High-Performance Transparent Conductive Electrodes. *Nano Lett.* **9**, 4359-4363 (2009).

20.   Bonaccorso, F., Sun, Z., Hasan, T. & Ferrari, A. C. Graphene photonics and optoelectronics. *Nat. Photon.* **4**, 611-622 (2010).

21.   Malard, L. M., Pimenta, M. A., Dresselhaus, G. & Dresselhaus, M. S. Raman spectroscopy in graphene. *Phys. Rep.* **473**, 51-87 (2009).

22.   Schwierz, F. Graphene transistors. *Nat. Nanotechnol.* **5**, 487-496 (2010).

23.   Xia, F., Perebeinos, V., Lin, Y. M., Wu, Y. & Avouris, P. The origins and limits of metal-graphene junction resistance. *Nat. Nanotechnol.* **6**, 179-184 (2011).

24.   Morozov, S. V. *et al.* Giant intrinsic carrier mobilities in graphene and its bilayer. *Phys. Rev. Lett.* **100**, 016602 (2008).

25.   Chen, J. H., Jang, C., Xiao, S., Ishigami, M. & Fuhrer, M. S. Intrinsic and extrinsic performance limits of graphene devices on SiO2. *Nat. Nanotechnol.* **3**, 206-209 (2008).

26. Pizzocchero, F. *et al.* The hot pick-up technique for batch assembly of van der Waals heterostructures. *Nat. Commun.* **7**, 11894 (2016).

27. Banszerus, L. *et al.* Ultrahigh-mobility graphene devices from chemical vapor deposition on reusable copper. *Sci. Adv.* **1** (2015).

28. Nair, R. R. *et al.* Fine structure constant defines visual transparency of graphene. *Science* **320**, 1308-1308 (2008).

29. Liu, S. W. *et al.* Robust microscale superlubricity under high contact pressure enabled by graphene-coated microsphere. *Nat. Commun.* **8**, 14029 (2017).

30. Buut, H.-J. & Jaschke, M. Calculation of thermal noise in atomic force microscopy. *Nanotechnology* **6** (1995).

Correspondence and requests for materials should be addressed to Z.F.L. and H.L.P.

Competing financial interests

Figure 1

a

Amorphous carbon

Activated carbon

Cu foil

Unclean graphene   Super-clean graphene

b

Activated carbon

Graphene

Cu foil

Cu C

20 nm

c

Unclean graphene

5 nm
0 nm

d

Super-clean graphene

5 nm
0 nm

e

Force (nN)

$C_{amorphous}$ - Gr.

$C_{amorphous}$ - $C_{activated}$

Distance (μm)

f

1   2   3   4   5

g

1   2   3   4   5

h

200 nm

Figure 2

a Unclean graphene on mica

b

c Super-clean graphene on mica

d FWHM=0.13 nm

e Graphene on mica

f
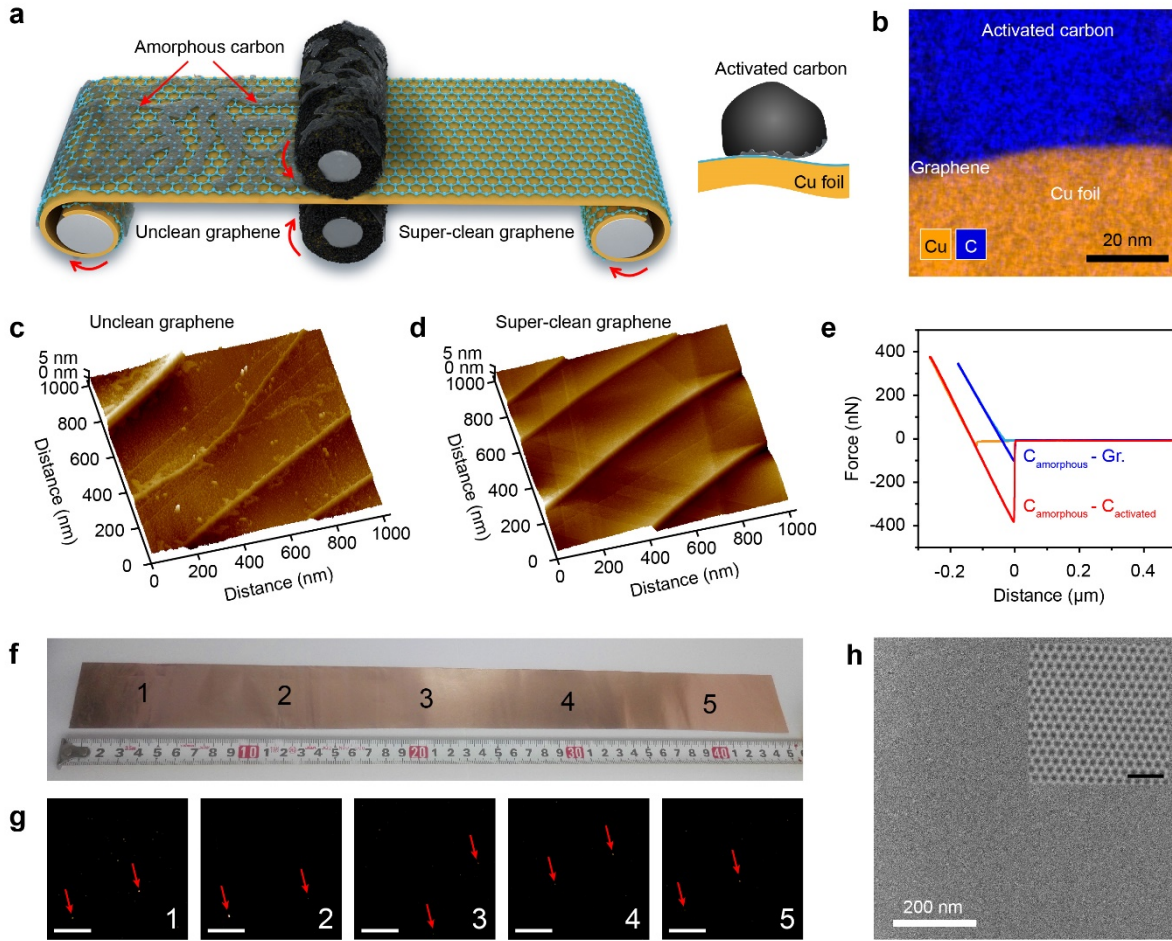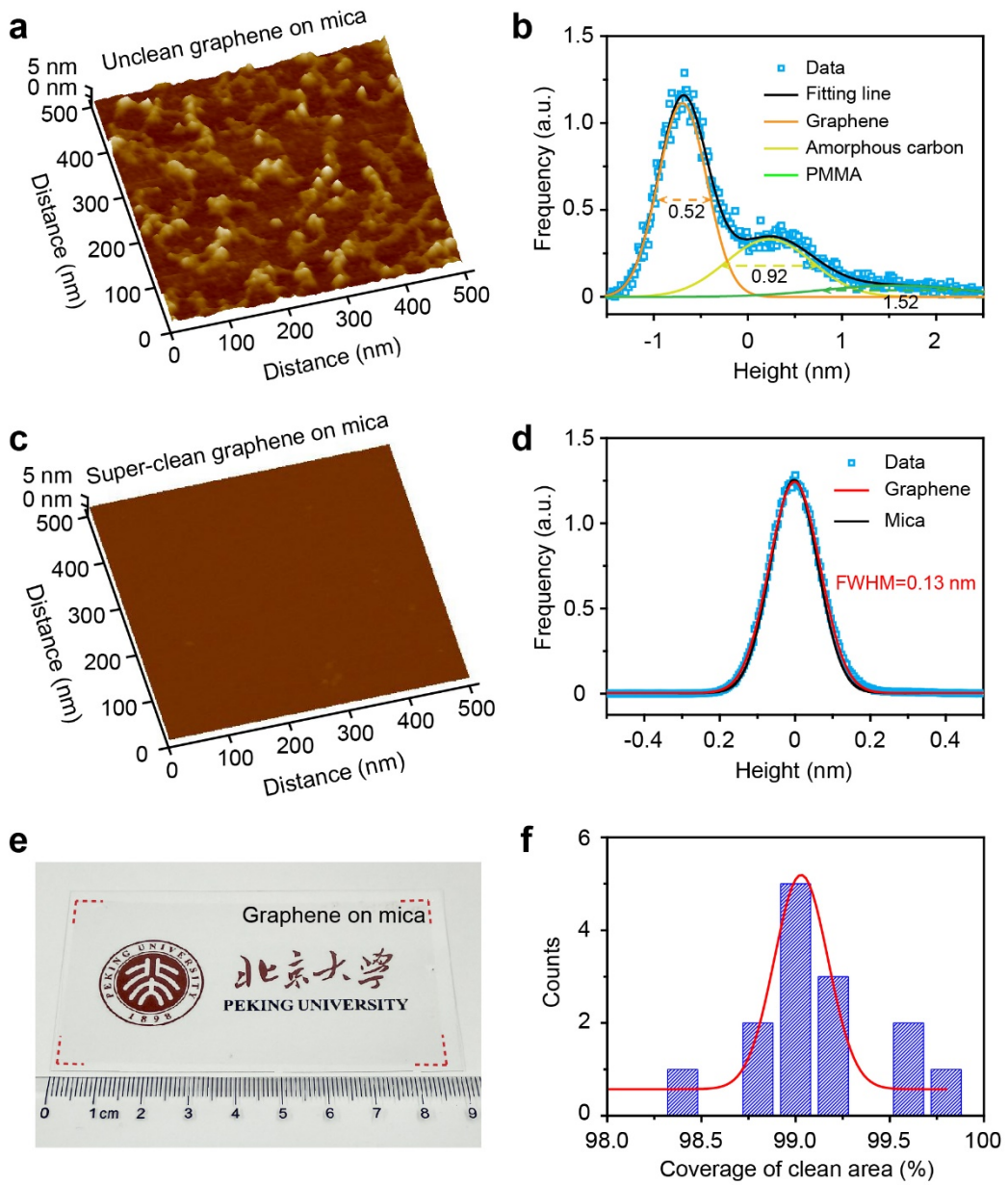
Figure 3
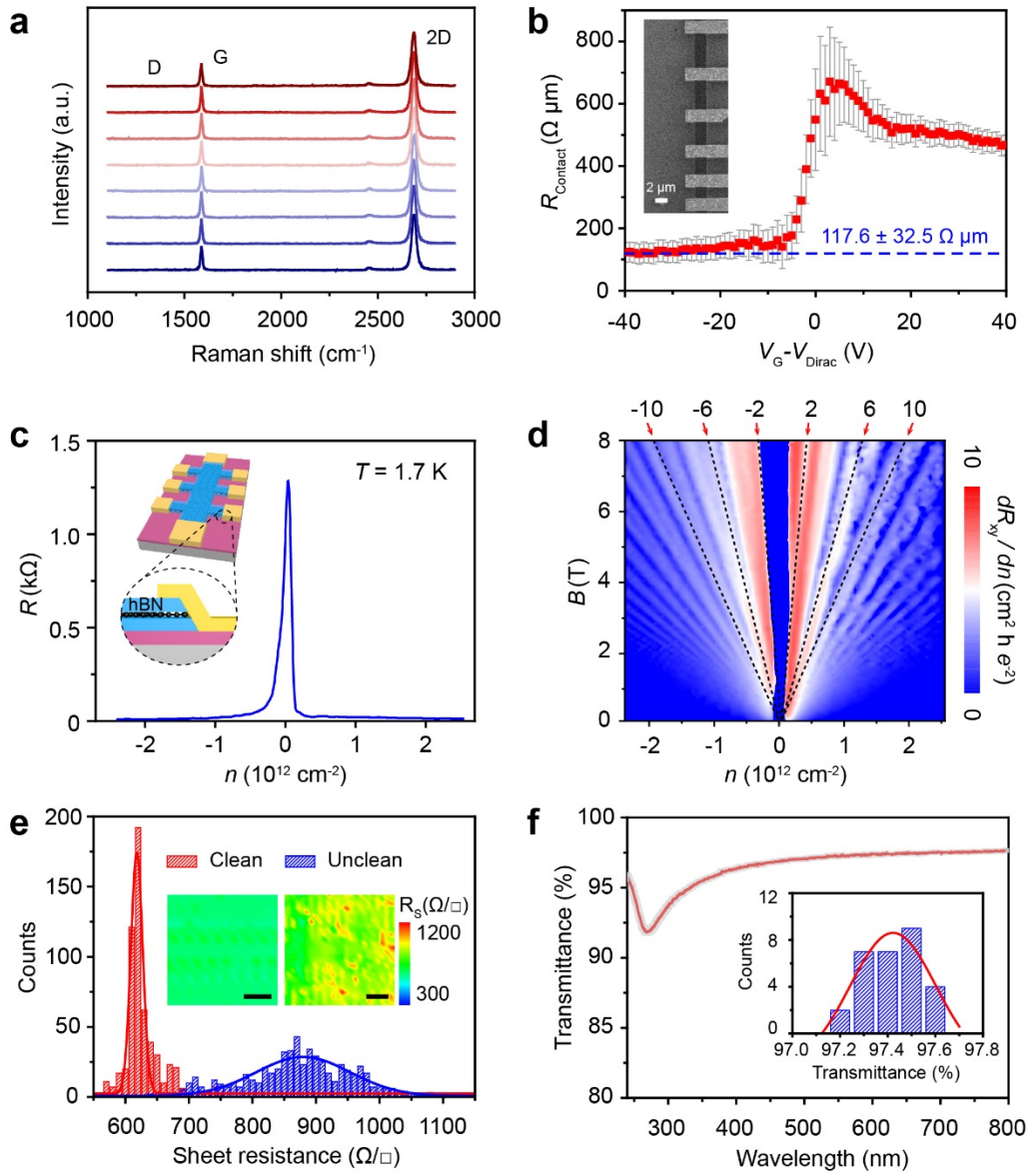
Supplementary information for:

A Force engineering lint-roller for super-clean graphene

Luzhao Sun[1,2#], Li Lin[1#], Zihao Wang[3#] Dingran Rui[4#], Zhiwei Yu[5], Jincan Zhang[1,2], Yanglizhi Li[1,2], Xiaoting Liu[1,2], Kaicheng Jia[1], Kexin Wang[1], Liming Zheng[1], Bing Deng[1], Tianbao Ma[5], Ning Kang[4], Hongqi Xu[4], Hailin Peng[1,6]*, Zhongfan Liu[1,6]*.

[1] Center for Nanochemistry, Beijing Science and Engineering Center for Nanocarbons, Beijing National Laboratory for Molecular Sciences, College of Chemistry and Molecular Engineering, Peking University, Beijing 100871, P. R. China

[2] Academy for Advanced Interdisciplinary Studies, Peking University, Beijing 100871, China

[3] School of Physics and Astronomy, University of Manchester, Manchester M13 9PL, UK

[4] Beijing Key Laboratory of Quantum Devices, Key Laboratory for the Physics and Chemistry of Nanodevices, and Department of Electronics, Peking University, Beijing 100871, P. R. China

[5] State Key Laboratory of Tribology, Tsinghua University, Beijing 100084, China.

[6] Beijing Graphene Institute, Beijing 100094, P. R. China

Correspondence to: zfliu@pku.edu.cn; hlpeng@pku.edu.cn

This supplementary information includes:

Supplementary note 1-3

Supplementary Table 1

Supplementary Figure 1-15

Reference (1-13)

Supplementary Note 1: Intrinsic contamination during CVD growth process.

CVD growth of graphene on Cu foil follows the surface mediated and self-limiting growth model which can be divided into elementary steps as follow: 1) adsorption of carbon precursor (such as CH_4) on Cu surface; 2) Gradually dehydrogenation of carbon precursor into C species (CH_3, CH_2, CH and C); 3)

surface diffusion and desorption of C species; 4) Nucleation on the active sites of Cu. 5) growth of graphene by adsorption of C species on the edges of graphene islands; 6) coalescence of graphene domains into continuous film[1]. As the graphene domains enlarge and merge into continuous film, the active Cu area gradually decreases, thus limiting the catalytic ability for the decomposition of carbon source and for the attachment of active carbon species onto graphene edges. Hence, the active carbon species in boundary layer would lead to the formation of amorphous carbon because the catalytic capability declines.

To further confirm the intrinsic contamination of CVD process and characterize the structure of the amorphous carbon, the normal CVD graphene sample was transferred onto TEM grid without any polymer assistance[2]. Subsequently, the normal CVD graphene sample covered by the amorphous carbon on graphene was characterized by high-resolution bright-field (BF) TEM images and high-annular dark-field (HAADF) images that acquired in a scanning transmission electron microscope (STEM) (Supplementary Fig. 1). Supplementary Fig. 1a shows the BF image of normal graphene with about 30%~50% clean area. The distribution shape of amorphous carbon on graphene is like a continuous net, but also exist some scattered amorphous carbon islands. In the HAADF image (Supplementary Fig. 1b and c), we can easily find the broken holes (because of electron irradiation) around the amorphous carbon. The change of image contrast at the broken holes, monolayer graphene and amorphous carbon can help us estimate the thickness of amorphous carbon contamination[3]. By analyzing the line profile of HADDF image (Supplementary Fig. 1 c and d), we can conclude that the contrast between amorphous carbon and the monolayer graphene is about 4 times of that between monolayer graphene and background. Since the graphene layers is roughly proportional to the relative intensity of HADDF contrast[3], the thickness of amorphous carbon is about 4 layers.

In the TEM mode, we also find that the amorphous carbon can move around at acceleration voltage of 80 kV and beam current of 3 nA (Supplementary Fig. 2 and Supplementary Video 1), which indicate that the bonding between amorphous carbon and graphene surface is weak enough to be removed (Supplementary Fig. 3).

Supplementary Note 2: Adhesion removal mechanism of activated carbon-coating lint roller.

Activated carbon is porous with low degree of graphitization. According to our BET measurement, the specific surface area is about 797.5510 m^2/g, and the average pore width is about 28.4064 Å. Raman spectroscopy characterization in Supplementary Fig. 3a shows obvious D peak and G peak, but no clear 2D peak, which indicate its low degree graphitization. The disturbances in the microcrystalline structure plays important role on the arrangement of electron clouds and this influences the adsorption properties of activated carbon. In addition, surface functional groups modify the surface properties of activated carbon and influence the surface characteristics. X-ray photoelectron spectroscopy (XPS) has been employed to examine the surface structures of activated carbon (Supplementary Fig. 3b). Semi-quantitative analysis of XPS data[4,5] indicate that the main form of carbon is sp^2 bonded (~42.5%) and sp^3 bonded (~27.9%), and there are some oxygen function groups such as hydroxyl group (-OH, ~2.9%), Carbonyl group (C=O, ~12.1%), and carboxyl group (COOH, ~14.6%).

Owing to the surface structures of activated carbon and defective amorphous carbon, the interaction between activated carbon and amorphous carbon is stronger than that between amorphous carbon and perfect graphene. To verify the hypothesis, adhesion force measurement was conducted by atomic force microscopy. Dirty graphene was grown on copper microspheres under the same CVD system, and then glued to an AFM cantilever. The adhesion force between amorphous carbon and graphene is measured as 93.1 $\pm$ 10.9 nN, which is about a quarter of adhesion force between activated carbon and amorphous carbon (Supplementary Fig. 6). Note that, the distribution of adhesion force between activated carbon and amorphous carbon is wide due to the surface morphology of activated carbon compound.

Supplementary Note 3: Visualizing the cleanness of graphene via TiO₂ selectively deposition on the contamination.

To visualize the amorphous carbon on graphene by optical microscopy and naked eyes, graphene samples on Cu foil were brought into the $TiCl_4$ vapor. Due to the reaction (1), TiO_2 particles were formed and deposited on the amorphous carbon preferentially in humid air.

$$TiCl_4 + 2H_2O = TiO_2 + 4HCl \qquad (1)$$
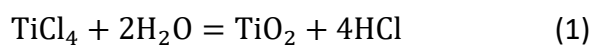
Photographs of graphene/Cu foil by TiO_2 visualized are shown in Supplementary Fig. 7a-c, where the unclean regions exhibit multi-colored and the as-treated super-clean regions exhibit uniform color. In dark-field optical microscopy, the contaminated region and super-clean region display the different ability of absorbing TiO_2 particles (Supplementary Fig. 7d and e). TEM image (Supplementary Fig. 7f) and corresponding HAADF image with EDS maps (Supplementary Fig.7 g-k) were conducted to confirm the TiO_2 selectively absorption on amorphous carbon. The Ti and O element distribution is very similar to the amorphous carbon.

Supplementary Note 4: Dry transferring graphene and fabricating hBN-encapsulated heterostructure using hot pick-up method.

The as prepared clean graphene was assembled into hBN-encapsulated heterostructure via hot pick-up transfer technique according to the literature. The polypropylene carbonate (PPC)/polydimethylsiloxane (PDMS) stack on a glass slide attached to a micromanipulator was used to pick up hBN flake at 110 ^{o}C. Then the graphene was picked up from the native oxidized copper substrate onto the PDMS/PPC/hBN stack at 110 ^{o}C due to the relatively strong Van der Waals forces between hBN and graphene. The stack was brought into contact with another flake of hBN on the SiO_2/Si substrate and then release the the hBN/graphene under 40 ^{o}C, resulting in hBN/graphene/hBN heterostructure.

Supplementary Table 1. Post growth treatments to remove the surface contamination on graphene.

Group	Method	Size	challenges	Ref
Adrian Bachtold et. al.	Current Joule heating	1 μm	Danger of burning devices	6
Po-Wen Chiu et, al.	Thermal annealing in air and Ar/H_2	-	Unavoidable to introducing defects	7
Georg S. Duesberg et, al.	Plasma treatment	-	Unavoidable to introducing	8

			defects	
Hans-Werner Fink et, al.	Platinum-metal catalysis	10 mm	complicated process	9
Jeong-O Lee et, al.	Electrostatic force cleaning	10 mm	Unavoidable broken	10
Chia-Seng Chang et, al.	Thermal annealing in H_2	3 mm	Ultra high vacuum and high temperature treatment	11
O. Renault et, al.	H_2 and H_2-N_2 plasma treatment	-	Unavoidable to introducing defects	12
Toma Susi	Radiative heating treatment	3 mm	Ultra high vacuum complicated process	13

Supplementary Figures

d

57,891.3 ± 1531.3

14,833.2 ± 1499.5

4,427.0 ± 733.8
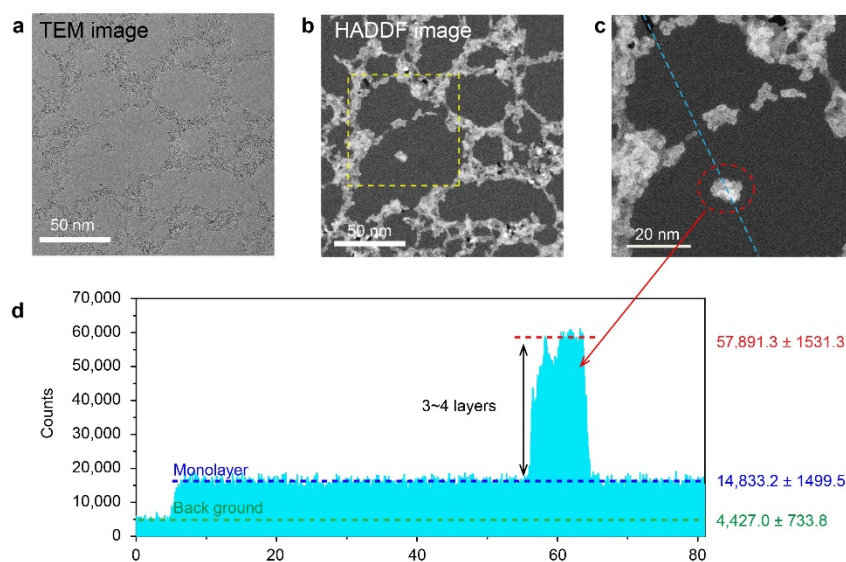
Supplementary Figure 1: structure of the amorphous carbon on graphene surface. a, TEM image of unclean graphene with amorphous carbon. **b**, HAADF image of unclean graphene corresponding to the same region of (a). **c**, magnification of the box in (b). d, line profile along the dashed blue line across the monolayer graphene, amorphous carbon and a broken hole. Form the line profile of HAADF intensity, the layer thickness of amorphous carbon could be roughly identified.
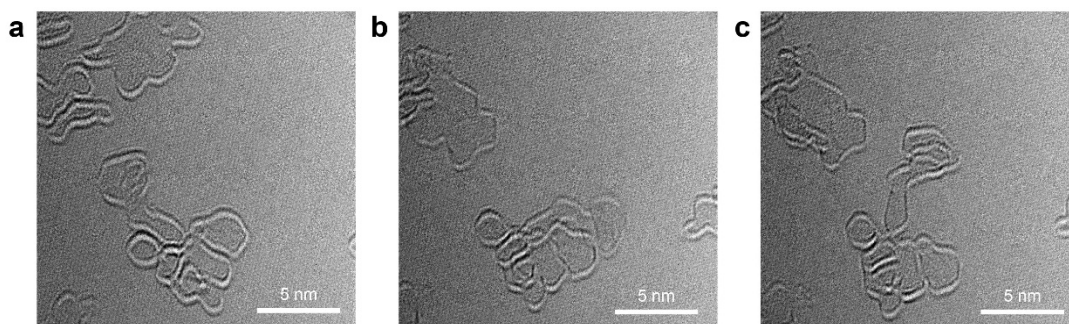
Supplementary Figure 2: weak bonding between amorphous carbon and graphene. The amorphous carbon is moving around on graphene surface under accelerated voltage of 80 kV and beam current of 3 nA.
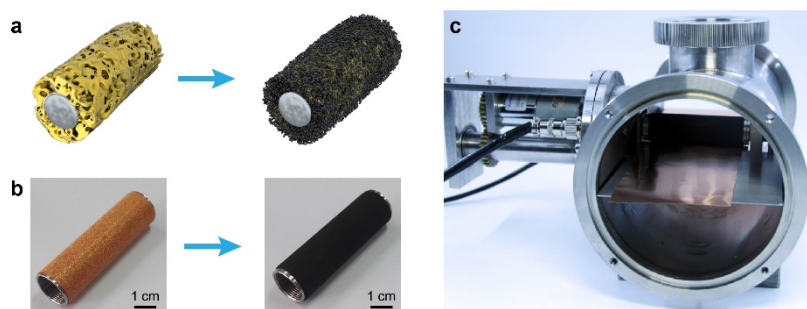
Supplementary Figure 3: Fabrication of activated-carbon-containing lint roller. a, schematic of the fabricating process of activated-carbon-containing lint roller by loading the powder of $C_{activated}$ on the Cu foam using binder. **b,** photographs of the roller which made of Cu foam and activated-carbon-containing lint roller **c,** The equipment where large area of graphene on Cu foil could be treated by activated-carbon-containing lint roller at vacuum and 170 °C.
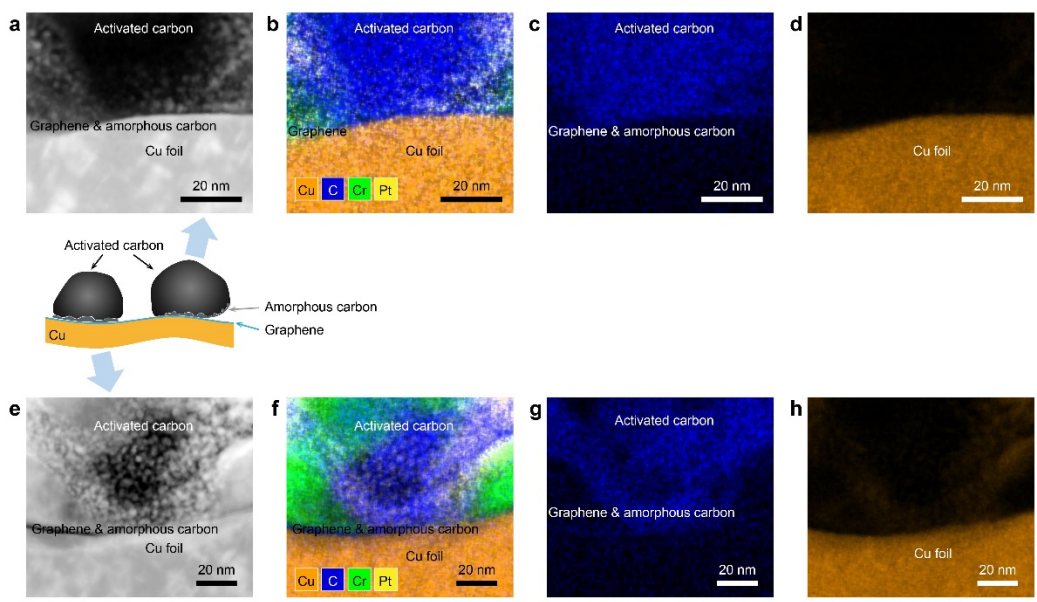
Supplementary Figure 4: microscopy of the contact between activated carbon and amorphous carbon/graphene surface. HAADF image (a,e) and energy-dispersive spectroscopy (EDS) mapping of contact area(b-d,f-h).
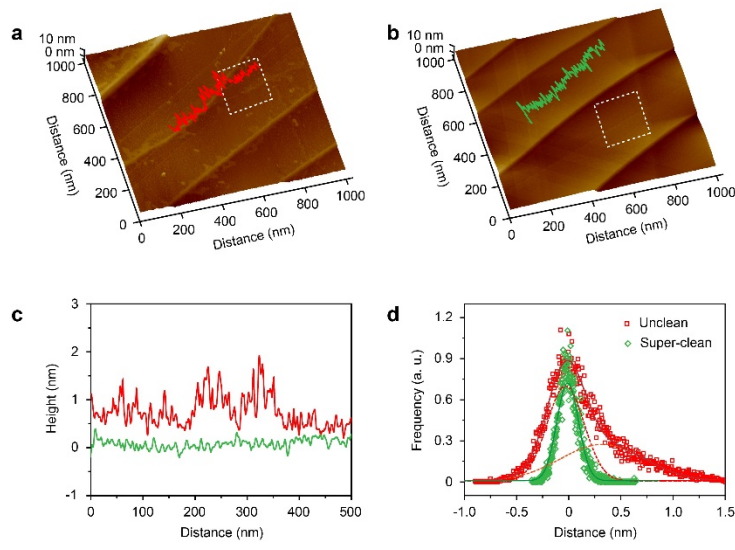
Supplementary Figure 5: AFM image and analysis of surface morphology of unclean and super-clean graphene on Cu surface. a,b, unclean graphene and as-cleaned graphene on Cu foil. **c,** Line profile across the unclean (red line) and clean graphene (green line). The height of the contamination is about 1.2 nm. **d**, Height distribution of unclean graphene and super-clean graphene corresponding to the

dashed box in (**a**) (red) and (**b**) (green).
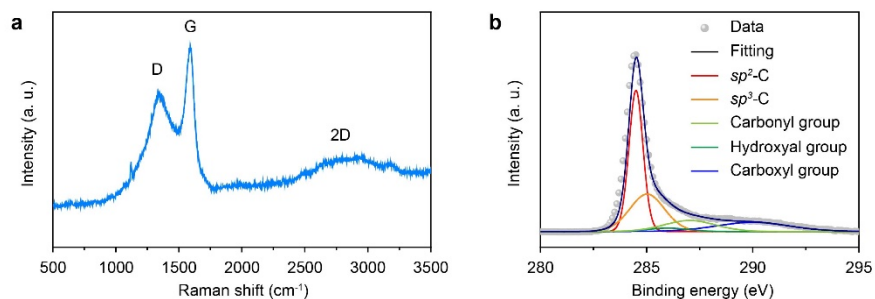
Supplementary Figure 6: Raman and XPS characterization of activated carbon. a, Raman spectrum of activated carbon, which shows strong D peak and G peak and very weak 2D peak. **b**, XPS peaks of activated carbon indicate that there is amount of functional groups on the surface of activated carbon.
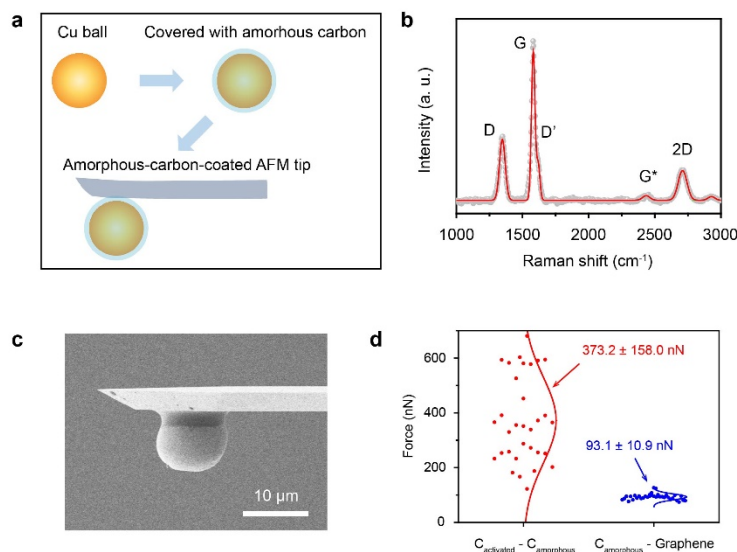
Supplementary Figure 7: Adhesion force measurement of $C_{amorphous}$ - $C_{activated}$ and $C_{amorphous}$ - Graphene. Micro-Cu ball was covered by amorphous carbon by growing dirty graphene, and then glued onto an AFM cantilever. Adhesion force of $C_{amorphous}$ - $C_{activated}$ and $C_{amorphous}$ - Graphene are shown with red dots and blue dots, respectively.
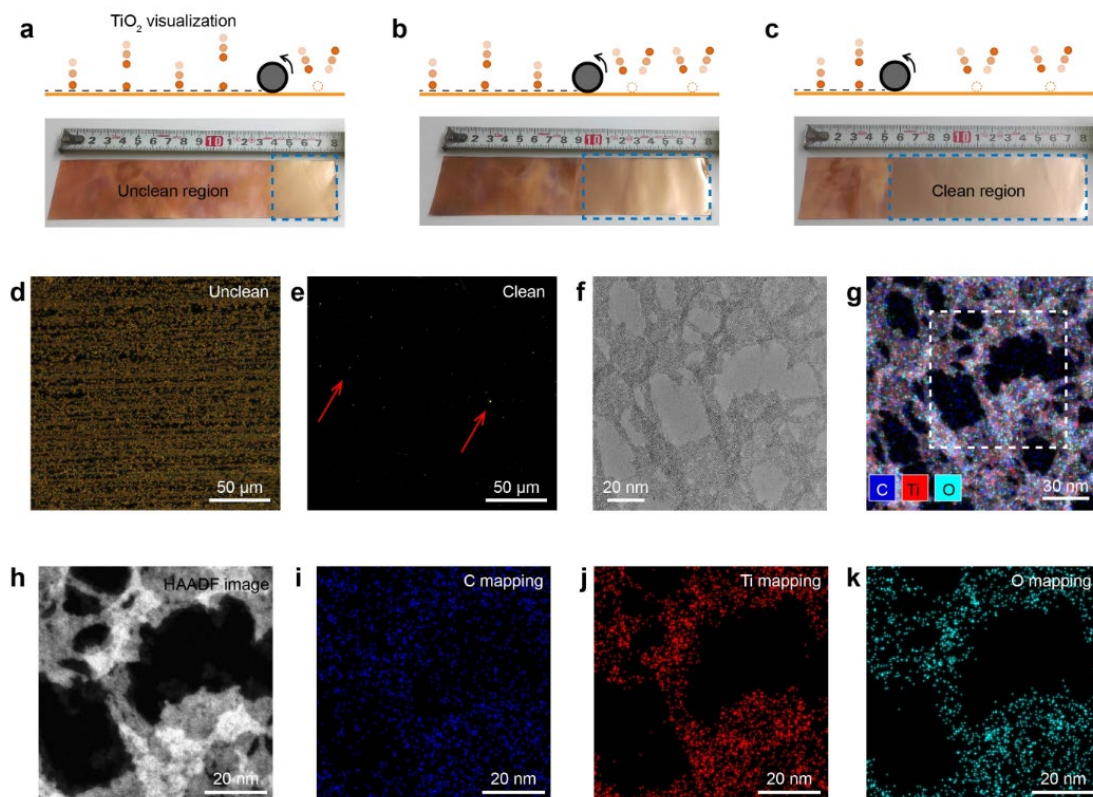
Supplementary Figure 8: Activated-carbon-containing lint roller cleaning the graphene surface on Cu foil and visualization of cleanness via TiO₂ selectively deposition on contamination. a-c, Demonstration of different cleaning regions of graphene on Cu foil, visualized by TiO₂ selectively deposition. The graphene on Cu foil Cleaning process by activated-carbon-containing lint roller
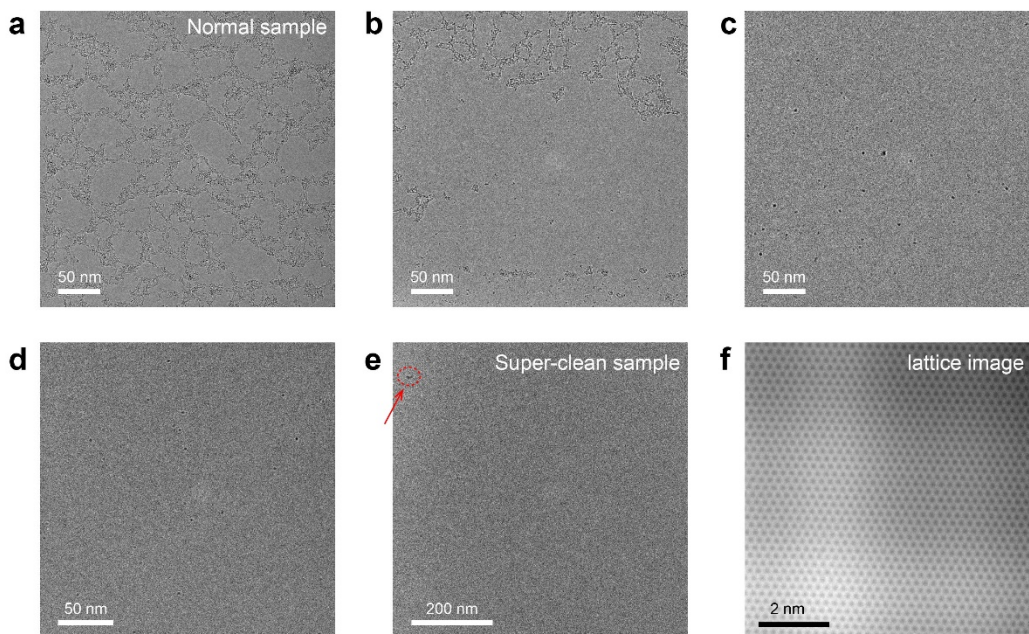
**Supplementary Figure 9: TEM images of normal and super clean graphene. a,** Normal graphene sample transferred onto TEM grid with cleanness of 30~50%. **b-e,** as cleaned graphene samples with high cleanness. **f,** lattice image taken from super-clean graphene.
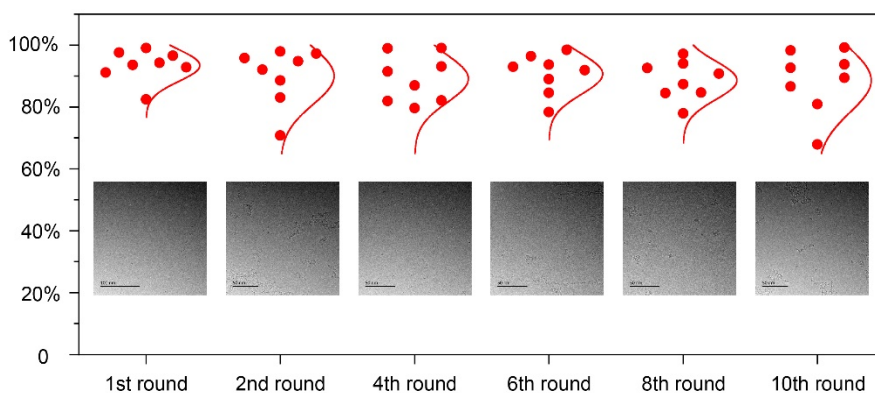

Supplementary Figure 10: Cleanness investigation for the as-cleaned graphene sample. Inset: TEM images of graphene under which the lint-roller has been used in cleaning graphene for different rounds. The comparable cleanness of graphene under 10 rounds with that under 1 round indicates the sustainable cleaning effects of lint-roller.
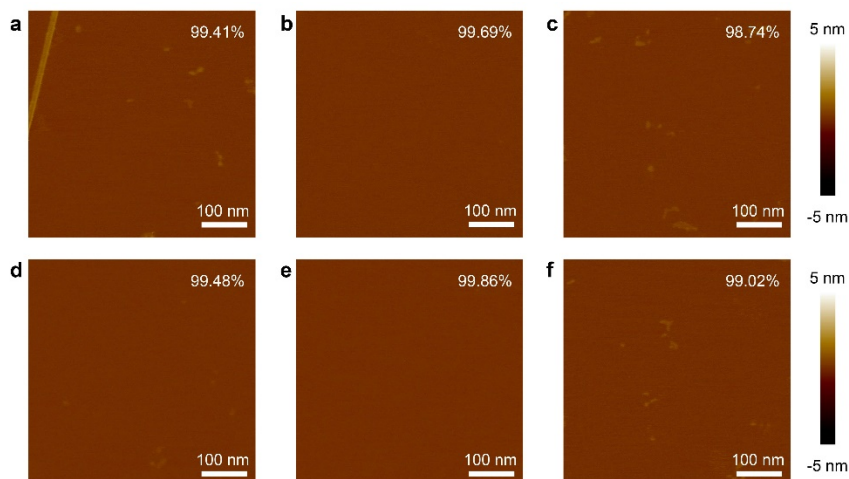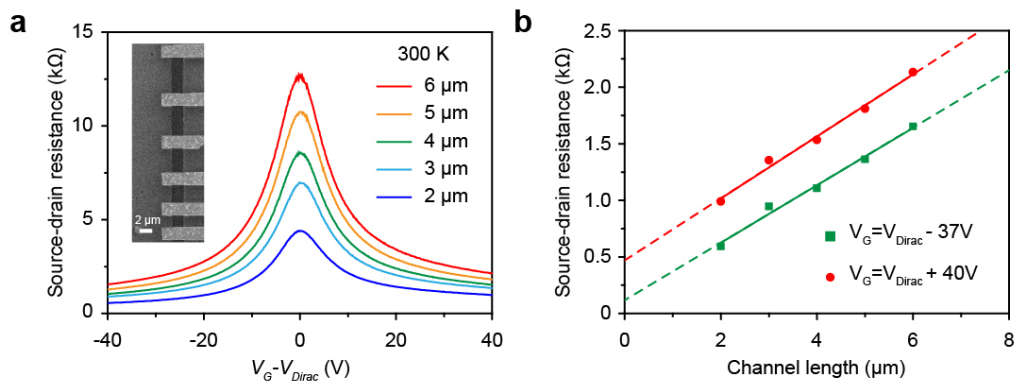
Supplementary Figure 11: AFM images of super-clean graphene transferred onto 4 inch sized mica. The cleanness statistics are carried out by calculating the percentage of pixels at clean region to the whole pixel number. Note that, the wrinkles region are deducted when calculate the cleanness.
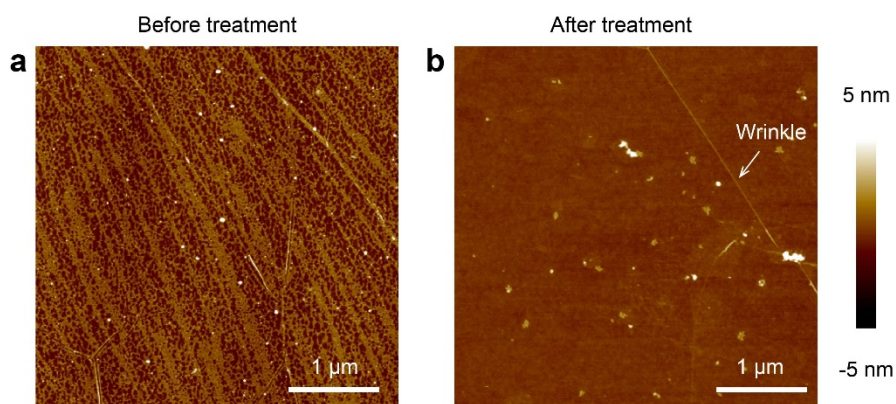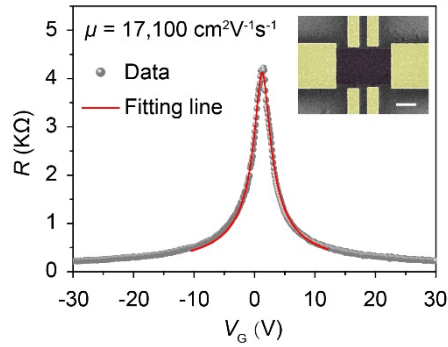

Supplementary figure 12. Clean graphene surface after transferred onto SiO₂/Si substrate. a, AFM image of graphene surface with PMMA residues. **b,** AFM image of graphene surface after cleaned by activated carbon-coating lint roller.
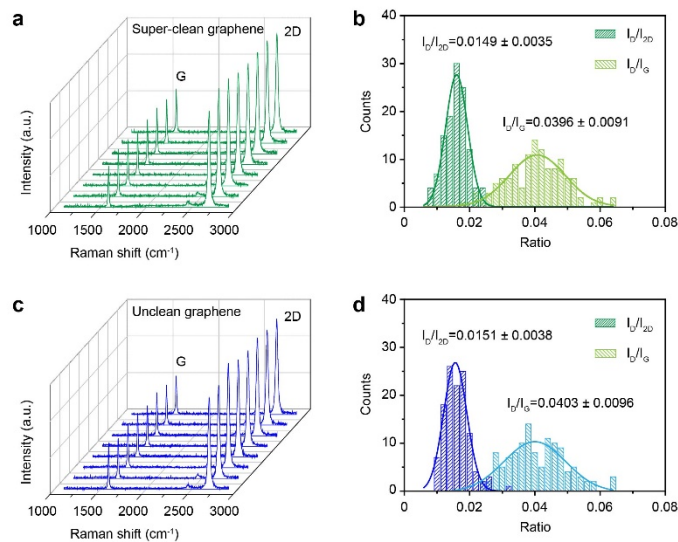
Supplementary Figure 13: Raman spectroscopy measurement of super-clean graphene and unclean graphene. (a,c). Raman spectra carried out randomly at the super-clean graphene (a) and normal graphene (c) transferred on the SiO_2/Si substrate. (b,d) I_D/I_G and I_D/I_{2D} statistics of super-clean graphene (b) and normal graphene (d) film according to our randomly sampling spectra. I_D almost comes from the background noise of Raman instrument, and the Ratio of I_{2D}/I_G is larger than 2.


Supplementary Figure 14: Contact resistance extracted by a graphene transistor array. (a). Source drain resistivity of as-received super-clean graphene as functions of gate bias (V_G - V_{Dirac}, V_{Dirac} = 15V). Inset: SEM image of the TLM-measured graphene transistor array, where the channel lengths vary from 2 to 6 μm; scale bar: 2 μm. (b). Source drain resistance as functions of channel length at gate bias of $V_G = V_{Dirac} - 37$ V (green) and $V_G = V_{Dirac} + 40$ V (red).

Supplementary Figure 15: Carrier mobility of super-clean graphene on SiO₂ substrate. Resistivity of super-clean graphene as a function of back-gate voltage at T= 1.9 K, and the nonlinear fitting of mobility is 17,100 $cm^2V^{-1}s^{-1}$.
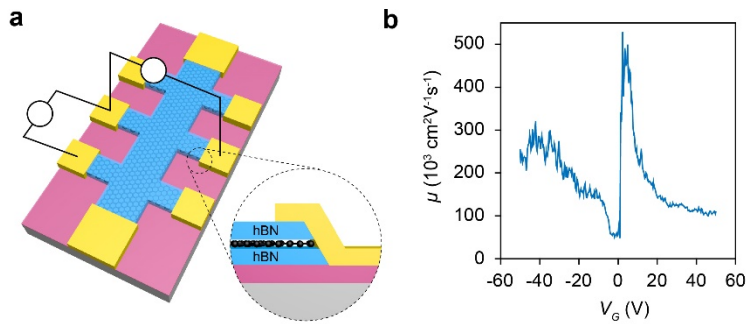
Supplementary Figure 16: Hall mobility extracted from hBN-encapsulated graphene Hall bar device with edge contact. (a). Schematic diagram of hBN-encapsulated graphene Hall bar, which was fabricated by using hot pick-up technique. (b). The Hall mobility as a function of back gate voltage (V_G), where, the carrier mobility near the Dirac point can exceed 500,000 $cm^2\,V^{-1}\,s^{-1}$.

Graphene film transferred onto PET substrate
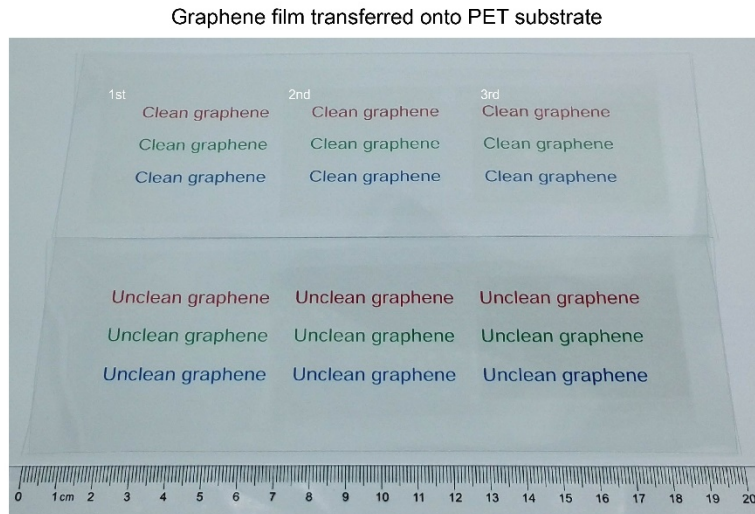
Supplementary Figure 17: Large scale of unclean and super-clean graphene transferred onto PET substrate. There is almost no difference between unclean and super-clean monolayer graphene under naked eyes. By stacking graphene layers, the unclean graphene become darker than super-clean graphene.

Reference:

1. Yan, Z., Peng, Z. W. & Tour, J. M. Chemical Vapor Deposition of Graphene Single Crystals. *Acc. Chem. Res.* **47**, 1327-1337 (2014).

2. Zhang, J. *et al.* Clean Transfer of Large Graphene Single Crystals for High-Intactness Suspended Membranes and Liquid Cells. *Adv. Mater.* **29** (2017).

3. Gass, M. H. *et al.* Free-standing graphene at atomic resolution. *Nat. Nanotechnol.* **3**, 676-681 (2008).

4. Jackson, S. T. & Nuzzo, R. G. Determining Hybridization Differences for Amorphous-Carbon from the Xps C-1s Envelope. *Appl. Surf. Sci.* **90**, 195-203 (1995).

5. Bansal, R. C. & Goyal, M. *Activated carbon adsorption*. (CRC Press, 2005).

6. Moser, J., Barreiro, A. & Bachtold, A. Current-induced cleaning of graphene. *Appl. Phys. Lett.* **91**, 163513 (2007).

7. Lin, Y. C. *et al.* Graphene annealing: how clean can it be? *Nano Lett* **12**, 414-419 (2012).

8. Peltekis, N. *et al.* The effect of downstream plasma treatments on graphene surfaces. *Carbon* **50**, 395-403 (2012).

9. Longchamp, J.-N., Escher, C. & Fink, H.-W. Ultraclean freestanding graphene by platinum-metal catalysis. *Journal of Vacuum Science & Technology B, Nanotechnology and Microelectronics: Materials, Processing, Measurement, and Phenomena* **31**, 020605 (2013).

10. Choi, W. J. *et al.* A simple method for cleaning graphene surfaces with an electrostatic force. *Adv Mater* **26**, 637-644 (2014).

11. Huang, L.-W. *et al.* Characterization of the cleaning process on a transferred graphene. *Journal of Vacuum Science & Technology A: Vacuum, Surfaces, and Films* **32**, 050601 (2014).

12. Cunge, G. *et al.* Dry efficient cleaning of poly-methyl-methacrylate residues from graphene with high-density H2 and H2-N2 plasmas. *J. Appl. Phys.* **118**, 123302 (2015).

13. Tripathi, M. *et al.* Cleaning graphene: Comparing heat treatments in air and in vacuum. *Phys. Status. Solidi-R.* **11** (2017).

Paper 5 (accepted by Nature Communication, Contributed equally)

My contribution: Performed the transport measurement for the twisted CVD graphene and gave feedback to the fabrication side for any quality improvement.

Ex situ nucleation for growing twisted bilayer graphene with a wide range of twist angles

Luzhao Sun, Zihao Wang, Yuechen Wang, Liang Zhao, Yanglizhi Li, Buhang Chen, Shishu Zhang, Wendong Wang, Shan Zhong, Haiyang Liu, Lianming Tong, Mark H. Rümmeli, Konstantin S. Novoselov, Hailin Peng*, Li Lin*, and Zhongfan Liu*

L.Z. Sun,[#] Y. C. Wang,[#] Y.L.Z. Li, S.S. Zhang, S. Zhong, H.Y. Liu, Prof. L.M. Tong, Prof. H.L. Peng* and Prof. Z.F. Liu*
Center for Nanochemistry, Beijing Science and Engineering Center for Nanocarbons, Beijing National Laboratory for Molecular Sciences, College of Chemistry and Molecular Engineering, Peking University, Beijing 100871, P. R. China

L.Z. Sun,[#] Y. C. Wang,[#] and Y.L.Z. Li
Academy for Advanced Interdisciplinary Studies, Peking University, Beijing 100871, P. R. China

Z.H. Wang[#], W. D. Wang, Prof. K.S. Novoselov, and Dr. L. Lin*
School of Physics and Astronomy, University of Manchester, Manchester M13 9PL, UK

Dr. L. Zhao and Prof. M.H. Rümmeli
Soochow Institute for Energy and Materials Innovation, Soochow University, Suzhou 215006, P. R. China

B.H. Chen, Prof. H.L. Peng* and Prof. Z.F. Liu*

Beijing Graphene Institute, Beijing 100095, P. R. China

*E-mail: zfliu@pku.edu.cn, li.lin-2@manchester.ac.uk, hlpeng@pku.edu.cn

Abstract

Twisted bilayer graphene (tBLG) has recently attracted growing interest due to its unique twist-angle-dependent electronic properties. Fundamental investigations and applications of tBLG rely heavily on the availability of large-area tBLG with a broad range of twist angles. However, current fabrication methods are hindered by the small twisted region size or the large portions of non-twisted bilayer graphene, i.e., AB-stacked bilayer graphene. Here, we demonstrate a chemical vapor deposition (CVD) approach for growing high-quality tBLG using an *ex situ* nucleation strategy, which enables the nucleation of the second layer at a different site from that of the first layer. The portion of tBLGs with twist angles ranging from 0° to 30° were found to be improved to 86%, which is significantly higher than those reported previously. The *ex situ* nucleation behavior was carefully investigated using an isotope-labelling technique. Furthermore, the clear Moiré patterns and ultrahigh room-temperature carrier mobility of 68,000 cm^2 V^{-1} s^{-1} confirmed the high crystalline quality of our tBLG. Our study opens a new avenue for the controllable growth of tBLGs for both fundamental research and practical applications.

Recently, twisted bilayer graphene (tBLG), which is composed of two graphene layers with an interlayer twist angle (θ),[1] has emerged as an exciting material for both fundamental studies and practical applications because of its unique θ-dependent properties.[2, 3] Specifically, the presence of twist angle causes van Hove singularities (VHSs) to emerge in the electronic density of states, resulting in an enhanced optical absorption[4] and photocurrent generation at certain wavelengths.[5, 6] Furthermore, the realization of a correlated Mott-insulator and super-conductivity, at the magic angle (tBLG with θ of 1.1°), has attracted worldwide interest.[7, 8] Consequently, an approach for producing large-area, high-

quality tBLG, with a full range of θ from 0° to 30° would significantly improve the ability to investigate its unique physical properties and applications. To achieve this, SiC-epitaxial[9] and artificial-stacking[6, 10] methods have been reported, though these are hindered by tedious transfer processes and unavoidable contamination, respectively.

Direct growth of tBLG on transition metal substrates such as Cu[11-19] or Cu-Ni alloy[20, 21] *via* chemical vapor deposition (CVD) is currently considered one of the most promising methods, due to the high scalability and the excellent quality of CVD graphene.[22, 23] However, during the high-temperature CVD growth, the energetically favorable bilayer graphene structure is the non-twisted one, i.e., AB-stacked bilayer graphene (AB-BLG), whereas any rotation between the two layers would need to overcome a high energy barrier.[24, 25] Thus, compared to AB-BLG, the proportions of tBLG were limited to less than 50% in previous reports.[12, 15, 17, 26] Thus, an efficient approach for growing tBLGs, especially in high proportions of twisted graphene and with a full range of twist angles, is still highly desirable.

In CVD approach, since the microscopic environment surrounding the nucleation site determines the orientation of graphene, two layers in bilayer graphene sharing the same nucleation center would preferentially grow with either the same orientation or solely with a twist angle of 30°. Therefore, in this study, an *ex situ* nucleation strategy, where the two graphene layers nucleate at different sites, is developed to significantly enhance the proportion of tBLGs to 86%, with the range of θ from 0° to 30°. As proven by using a carbon isotope labeling technique, the gas-flow turbulence was capable of controllably initiating this *ex situ* nucleation. The high crystalline quality of the as-grown tBLGs was confirmed by the clear Moiré patterns in high-resolution (HR)-transmission electron microscopy (TEM), and by the ultrahigh carrier mobility of 68,000 cm^2 V^{-1} s^{-1} at room temperature.

Without the introduction of the gas-flow turbulence, both graphene layers would share the same nucleation site and grow simultaneously.[14] In this case, the same surrounding microscopic environment, including Cu steps and particles, would results in the same crystalline orientation of the two layers, thus AB-BLG with no interlayer rotation is preferentially formed (Figure S1a, Supporting Information). In contrast, in our *ex situ* nucleation strategy, after nucleation of the first graphene layer, the subsequent nucleation of the second graphene layer is initiated by introducing a gas-flow turbulence to ensure that the nucleation of the second layer occurs at a distinct site, i.e., *ex situ* nucleation (**Figure 1**a). Therefore,

the new layer would have an orientation that is determined by a different local environment, enabling the presence of interlayer twist angle and the formation of tBLGs. Note that the sudden carbon source supply enhancement was used as gas-flow turbulence, which is previously reported to be capable of initiating new nucleation (Figure S1b, Supporting Information).[27, 28] Optical microscopy (OM) was used to measure the resulting θ of the tBLG, based on the sharp edges of the hexagonal tBLG domains (Figure 1b), which clearly indicates that tBLGs with a wide range of twist angles were grown successfully. Since the centers of hexagonal graphene domains are typically the original nucleation sites of the layers,[17] the nonconcentric structure of the tBLG domains observed in Figure 1b clearly confirm the *ex situ* nucleation behavior of the second layer graphene.

Raman spectra were acquired to characterize their crystalline quality and interlayer coupling of the as-grown tBLGs, which exhibit strong θ-dependent vibrational modes (Figure 1c and Figure S2, Supporting Information). At a low twist angle (<10°), an R' band is clearly observed, while the 2D band intensity is relatively weak compared to that of monolayer graphene (MLG), consistent with the reported results of tBLGs.[29] In addition, The G band is strongly enhanced at a twist angle of ~12°, because the incident laser energy (λ = 532 nm, E_{ex} = 2.33 eV) matches the energy between VHSs of the tBLG.[30]

Carbon isotope labeling experiments in conjunction with Raman spectroscopy were performed to investigate the *ex situ* nucleation growth mechanism. Here, ^{12}C-labeled and ^{13}C-labeled methane ($^{12}CH_4$/$^{13}CH_4$) were sequentially introduced to the CVD chamber in alternating 5 min periods over a total of four cycles. To confirm its contribution to the *ex situ* nucleation behavior, the flow turbulence was introduced, by increasing the flow rates of H_2 and CH_4, after either 5 or 10 min (**Figure 2**a, b). The nucleation centers of each layer can be inferred from the hexagonal domain shapes observed in the OM images (Figure 2c, d). When flow turbulence was introduced at 5 min, a small shift in the nucleation center of the new layer, from the original, is observed (Figure 2c). This shift increases when turbulence was introduced after a longer duration of 10 min (Figure 2b, d). Furthermore, because the first and second layers both follow a surface-mediated growth mechanism, the spatial distribution of ^{12}C and ^{13}C in each layer can be visualized by Raman mapping, based on the different modes of ^{12}C-graphene and ^{13}C-graphene (Figure S3, Supporting Information).[18, 31] In the Raman 2D^{13}-intensity maps of the as-

grown tBLGs, the nucleation center shifts in the second layer can be clearly visualized by the isotope distribution (Figure 2e,f and Figure S4, Supporting Information). In general, the first graphene layer displays four cycles of alternating $^{12}CH_4$ and $^{13}CH_4$, indicating the growth duration of 20 min. In contrast when turbulence was introduced at 5 or 10 min, the second graphene layer exhibits three or two cycles, confirming the growth duration for second layer is 15 min or 10 min, and their domain centers are located right at the ^{12}C-^{13}C boundary of the first layer. These results confirm that the second layer nucleation occurs at either 5 or 10 min, exactly when turbulence was introduced. In addition, plotting the time evolution of the two graphene layers (Figure 2g) can also reveal the nucleation time for the second layer, which can be obtained by the intersection of the fitted growth line and the time axis (Figure S4b, d, Supporting Information).[28] Thus, we can safely conclude that the *ex situ* nucleation of the second layer was controllably induced by the introduction of turbulence. In addition, a nucleation time (t_0) is required for the first layer, after dosing of $^{13}CH_4$ or $^{12}CH_4$, because it must overcome an energy barrier to form a stable nucleus.[28] Note that, the twist angles in Figure 2c,d are ~30° and ~9°, respectively, which are remarkably different from the ^{12}C-^{13}C-labeled AB-BLG grown without flow turbulence, confirming the importance of *ex situ* nucleation for growing tBLGs (Figure S5, Supporting Information).

Generally, the turbulence would produce an over-saturated supply of active carbon species for initiating the new nucleation of the second layer. If the second layer shares the same nucleation center with first layer, the as-decomposed active carbon species need migrate across the growth frontier of the first layer and move underneath the first layer subsequently to fuel the nucleation of the second layer. Because the distance between the nucleation center and the growth frontier increases as the first layer grows, the active carbon species must move a longer distance, as time increases, to enable new nucleation. Therefore, when turbulence is introduced, the second layer preferentially nucleates near the growth frontier of the first layer, rather than at the original nucleation center. Thus, the nucleation site of the second layer can be controlled by the timing of the flow turbulence introduction, which agrees with the results in Figure 2g.

To achieve *ex situ* nucleation for tBLG growth, three key conditions are required: 1) no second layer can form during the nucleation stage of the first layer; 2) the second *ex situ* nucleation must be triggered by

a turbulence; and 3) carbon source must be sufficient for the growth of second layer. A series of experiments were conducted to improve the growth controllability with respect to the three conditions. **Figure 3**a shows the ratio of MLG domains (second-layer-free domains) as functions of the H_2 and CH_4 (carbon-source supply) flow rates. This reveals a clear gap between the parameter regions that are suitable for growing either second-layer-free or second-layer-rich bilayer domains with high ratio. Overall, H_2 and CH_4 flow rates below 400 sccm and 0.5 sccm, respectively (red region, Figure 3a) are suitable for growing second-layer-free graphene during the first nucleation step, while H_2 and CH_4 flow rates over 800 sccm and 0.8 sccm, respectively (blue region, Figure 3a) enable the formation of second layer (Figure S6a and b, Supporting Information).

The ratios of bilayer graphene domains to all graphene domains as a function of the ratio of H_2 flow in *ex situ* nucleation step to that in first nucleation step is displayed in Figure 3b. Clearly, an increased H_2 flow rate ratio in the flow turbulence is important for enhancing the bilayer graphene proportion. High H_2 partial pressures enables H-termination of the graphene edge, which allows additional active carbon species to diffuse beneath the first layer of graphene to fuel the growth of the second layer graphene.[32] Considering that an excess partial pressure of H_2 or CH_4 (over 1200 and 1.5 sccm for H_2 and CH_4, respectively) would induce undesirable few-layer graphene (FLG) formation, the CH_4 flow ratio must be carefully controlled in the *ex situ* nucleation step (Figure S6c, d, Supporting Information). Without *ex situ* nucleation, the twisted proportion in all the bilayer domains is only 16% (Figure 3c and Figure S7, Supporting Information), while it is 86% when *ex situ* nucleation was employed. This remarkable increase highlights the importance of our *ex situ* nucleation strategy for growing tBLG (Figure 3c and Figure S8, Supporting Information). Furthermore, a wide distribution of twist angles were observed, by measuring the sharp edges of the hexagonal tBLG domains in OM images, with a relatively higher proportions of bilayers with twist angles around 0° and 30° (Figure 3d).[15]

The twist angles of the as-grown tBLGs were further characterized by TEM and selective-area electron diffraction (SAED). Note that, for a vivid evaluation, SAED was conducted on suspended graphene with more than 600 holes (Figure S9, Supporting Information). **Figure 4**a shows a representative tBLG SAED pattern, exhibiting two groups of hexagonal points with a relative rotation of 9°, which reflects the twist angle between the two layers. Because of the relatively weak interactions between the two layers, the

corresponding intensity ratio of the diffraction points (I_{2100}/I_{1100}), is lower than unity (Figure 4b), which is consistent with previous tBLG results.[15] The proportion of tBLG within all bilayer domains, and the corresponding distribution of twist angles, were obtained by analyzing all of the obtained diffraction patterns (Figure 4c, Figure S10, and S11, Supporting Information). Interestingly, the portion of tBLG was calculated to be as high as 88%, which represents a striking increase over the results obtained without the *ex situ* nucleation strategy.[15] Note that tBLG, with very small twist angles (less than 3°), is difficult to grow because of the relatively higher stability of AB-BLG. The portion of twist angles near 30° is significantly higher than the other tBLGs.

Figure 4d-g shows HR-TEM images of representative tBLGs with twist angles of 2.8°, 9.4°, 18.3°, and 30°, respectively, all of which show clear tBLG super-lattices that confirm the high crystalline quality. In addition, the corresponding Moiré patterns, with a Moiré period of 4.8 nm, are clearly observed for the 2.8° tBLG. The signature 12-fold rotational symmetry is also clearly visible in the as-grown 30° tBLG, indicating that a high-quality quasi-crystalline system was formed (Figure S12, Supporting Information).

A hexagonal boron nitride (hBN)-encapsulated tBLG hall bar device, with a one-dimensional edge contact, was fabricated to investigate the electronic quality of as-grown tBLGs (**Figure 5**a). Notably, it is difficult to pick CVD-grown tBLG directly up from the Cu substrate,[33, 34] because of the relatively weak interlayer interactions. Thus, the as-grown tBLGs were first transferred onto a SiO_2/Si substrate with the assistance of poly(methyl methacrylate) (PMMA). The selected tBLG domain was then picked up from the SiO_2 using an hBN flake, denoted as top hBN or t-hBN, and subsequently dropped down onto another hBN flake, denoted as bottom hBN or b-hBN, on SiO_2, to form an hBN/tBLG/hBN sandwich structure (Figure S13, Supporting Information).[38] Annealing was then conducted to help clean the interfaces in the hBN/tBLG/hBN structure, yielding blister-free regions for device fabrication (Figure S14, Supporting Information).[35, 36]

Raman spectroscopy is sensitive to global environmental factors such as doping, strain, and flatness. For the tBLG sample on SiO_2 (blue curve in Figure 5b), the G peak position (ω_G) is ~1587 cm^{-1}, with a full width at half-maximum (FWHM) of the G peak (Γ_G) of 11 cm^{-1}, while the 2D peak position (ω_{2D}) is ~2700 cm^{-1}, with the FWHM (Γ_{2D}) of 34 cm^{-1}. The high I_G/I_{2D} peak ratio of ~20, together with the R peak at 1493

cm^{-1}, indicate an interlayer twist angle of ~12°. For the tBLG encapsulated in hBN (red curve in Figure 5b), the I_G/I_{2D} peak ratio decreased to ~7; the ω_G and ω_{2D} showed clear red shifts to ~1580 cm^{-1} and ~2689 cm^{-1}, respectively; and the Γ_{2D} decreased to ~27 cm^{-1}, all of which can be attributed to the fine encapsulation (Figure 5b,c).[36, 37] Electrical transport measurements were conducted to probe the quality of the tBLG with a twist angle of 12°. Figure 5d shows the resistivity as a function of gate voltage V_G at room temperature. By plotting the conductivity as a function of the carrier density (*n*) and performing a linear fit near the charge neutrality point, we obtain the room-temperature carrier mobility of 67,000 and 68,000 cm^2 V^{-1} s^{-1} for electrons and holes, respectively, which confirm the high quality of the as-grown tBLG (Figure S15b, Supporting Information).[38]

Conclusion

This work describes an *ex situ* nucleation strategy for successfully growing the tBLG with the proportion of tBLG higher than 86%, and a wide range of twist angle from 0° to 30°. The *ex situ* nucleation mechanism was investigated by isotope labeling in conjunction with micro-Raman spectroscopy, confirming that the nucleation of the second layer is controllable, simply by the introduction of flow turbulence. The high quality of the as-grown tBLG was corroborated by clear Moiré patterns in the HR-TEM and carrier mobility exceeding 68,000 cm^2 V^{-1} s^{-1} at room-temperature. Our work would certainly provide a new synthesis strategy for growing twisted graphene and other two-dimensional materials by the intentional design of nucleation sites.

Experimental Section

tBLG growth: tBLGs were grown on commercially available 50-μm-thick Cu foil (Kunshan Luzhifa Electron Technology Co., Ltd. China) in a low pressure CVD system. Cu-foil pieces were placed in a quartz-tube furnace and sequentially heated to 800 °C for 30 min (500 sccm Ar), annealed for 10 min at 800 °C (500 sccm Ar), heated to 1020 °C for 10 min (500 sccm H$_2$), and annealed for 30 min at 1020 °C (500 sccm H$_2$). Graphene growth proceeded by introducing ^{12}CH$_4$ or ^{13}CH$_4$ (99% purity, Sigma-Aldrich) after the flow of H$_2$ was stable at the appropriate value (parameters are shown in Figure 2 and Figure 3, as well as Figure S5 and S6, Supporting Information). Note that, the relationship between partial pressure (Pa) and flow rate (sccm) of H$_2$ in our CVD system can be approximately described by the formula: $P = 0.91\,f$, where

P is the partial pressure, and f is the flow rate.

Graphene transfer: tBLGs were transferred onto SiO_2 with the assistance of PMMA. The tBLG/Cu sample was spin-coated with PMMA (2000 rpm) and baked at 170 °C (3 min), followed by the removal of the Cu foil by etching in 1 M $Na_2S_2O_8$ solution. After being washed with deionized water, the PMMA/graphene was subsequently placed onto SiO_2 and the PMMA was dissolved with acetone. The graphene was transferred onto a TEM grid using a non-polymer-assisted method, as reported previously. [38]

Characterizing the tBLG samples: OM images of tBLGs on SiO_2/Si substrates (SiO_2 thickness: 90 nm or 285 nm) were obtained by optical microscopy (Nikon LV100ND equipped with DS-Ri2 camera). Raman spectra and maps were obtained using a Horiba HR800 instrument with a 532-nm laser or a Witech Alpha RSA300+ instrument with a 488-nm laser. SAED patterns and Moiré pattern images were collected using an aberration-corrected transmission electron microscope (FEI Titan Cubed Themis G2 300; under 80 kV). SEM images were acquired on a Hitachi S-4800 (under 2 kV) instrument.

hBN-encapsulated tBLG Device fabrication: An hBN flake was picked up at 55 °C by a PPC/ PDMS stack on a glass slide, which was attached to a micromanipulator. The as-formed hBN/PPC/PDMS stack was then used to pick up the tBLG from the SiO_2/Si at 55 °C, because the van der Waals forces between hBN and the tBLG are relatively stronger than those between SiO_2 and the tBLG. Consequently, the tBLG/hBN/PPC/PDMS stack was brought into contact with another hBN flake, after which the tBLG/hBN was released from the PPC at 70 °C, yielding an hBN/tBLG/hBN heterostructure. Annealing (350 °C in air) was necessary following the construction of hBN/tBLG/hBN, which helped to clean the interfaces between hBN and tBLG.[35, 36, 38] The Hall bar device was fabricated with alignments marks. To pattern graphene into a Hall bar geometry, e-beam lithography and reactive ion etching (RIE) were employed. Cr/Au (3/50 nm) electrodes were deposited by electron-beam evaporation.

Supporting Information

Supporting Information is available from the Wiley Online Library or from the author.

Acknowledgements

References

[1] J. M. B. L. dos Santos, N. M. R. Peres, A. H. Castro, *Phys. Rev. Lett.* **2007**, 99.

[2] G. Li, A. Luican, J. M. B. Lopes dos Santos, A. H. Castro Neto, A. Reina, J. Kong, E. Y. Andrei, *Nat. Phys.* **2009**, 6, 109.

[3] G. T. de Laissardiere, D. Mayou, L. Magaud, *Nano Lett.* **2010**, 10, 804.

[4] P. Moon, M. Koshino, *Phys. Rev. B* **2013**, 87.

[5] J. B. Yin, H. Wang, H. Peng, Z. J. Tan, L. Liao, L. Lin, X. Sun, A. L. Koh, Y. L. Chen, H. L. Peng, Z. F. Liu, *Nat. Commun.* **2016**, 7.

[6] Z. Tan, J. Yin, C. Chen, H. Wang, L. Lin, L. Sun, J. Wu, X. Sun, H. Yang, Y. Chen, H. Peng, Z. Liu, *ACS Nano* **2016**, 10, 6725.

[7] Y. Cao, V. Fatemi, S. Fang, K. Watanabe, T. Taniguchi, E. Kaxiras, P. Jarillo-Herrero, *Nature* **2018**, 556, 43.

[8] Y. Cao, V. Fatemi, A. Demir, S. Fang, S. L. Tomarken, J. Y. Luo, J. D. Sanchez-Yamagishi, K. Watanabe, T. Taniguchi, E. Kaxiras, R. C. Ashoori, P. Jarillo-Herrero, *Nature* **2018**, 556, 80.

[9] M. Sprinkle, J. Hicks, A. Tejeda, A. Taleb-Ibrahimi, P. Le Fèvre, F. Bertran, H. Tinkey, M. C. Clark, P. Soukiassian, D. Martinotti, J. Hass, E. H. Conrad, *J. Phys. D: Appl. Phys.* **2010**, 43, 374006.

[10]   V. L. Nguyen, D. J. Perello, S. Lee, C. T. Nai, B. G. Shin, J.-G. Kim, H. Y. Park, H. Y. Jeong, J. Zhao, Q. A. Vu, S. H. Lee, K. P. Loh, S.-Y. Jeong, Y. H. Lee, *Adv. Mater.* **2016**.

[11] K. Yan, H. L. Peng, Y. Zhou, H. Li, Z. F. Liu, *Nano Lett.* **2011**, 11, 1106.

[12] L. X. Liu, H. L. Zhou, R. Cheng, W. J. Yu, Y. Liu, Y. Chen, J. Shaw, X. Zhong, Y. Huang, X. F. Duan, *ACS Nano* **2012**, 6, 8241.

[13] Z. Z. Sun, A. R. O. Raji, Y. Zhu, C. S. Xiang, Z. Yan, C. Kittrel, E. L. G. Samuel, J. M. Tour, *ACS Nano* **2012**, 6, 9790.

[14] Q. Y. Li, H. Chou, J. H. Zhong, J. Y. Liu, A. Dolocan, J. Y. Zhang, Y. H. Zhou, R. S. Ruoff, S. S. Chen, W. W. Cai, *Nano Lett.* **2013**, 13, 486.

[15] C. C. Lu, Y. C. Lin, Z. Liu, C. H. Yeh, K. Suenaga, P. W. Chiu, *Acs Nano* **2013**, 7, 2587.

[16] W. J. Fang, A. L. Hsu, Y. Song, A. G. Birdwell, M. Amani, M. Dubey, M. S. Dresselhaus, T. Palacios, J. Kong, *ACS Nano* **2014**, 8, 6491.

[17] Z. Yan, Y. Liu, L. Ju, Z. Peng, J. Lin, G. Wang, H. Zhou, C. Xiang, E. L. Samuel, C. Kittrell, V. I. Artyukhov, F. Wang, B. I. Yakobson, J. M. Tour, *Angew. Chem. Int. Ed. Engl.* **2014**, 53, 1565.

[18] Y. F. Hao, L. Wang, Y. Y. Liu, H. Chen, X. H. Wang, C. Tan, S. Nie, J. W. Suk, T. F. Jiang, T. F. Liang, J. F. Xiao, W. J. Ye, C. R. Dean, B. I. Yakobson, K. F. McCarty, P. Kim, J. Hone, L. Colombo, R. S. Ruoff, *Nat. Nanotechnol.* **2016**, 11, 426.

[19] H. Q. Ta, D. J. Perello, D. L. Duong, G. H. Han, S. Gorantla, V. L. Nguyen, A. Bachmatiuk, S. V. Rotkin, Y. H. Lee, M. H. Rummeli, *Nano Lett.* **2016**.

[20] W. Liu, S. Kraemer, D. Sarkar, H. Li, P. M. Ajayan, K. Banerjee, *Chem. Mater.* **2013**, 26, 907.

[21] M. Huang, P. V. Bakharev, Z. J. Wang, M. Biswal, Z. Yang, S. Jin, B. Wang, H. J. Park, Y. Li, D. Qu, Y. Kwon, X. Chen, S. H. Lee, M. G. Willinger, W. J. Yoo, Z. Lee, R. S. Ruoff, *Nat. Nanotechnol.* **2020**.

[22] L. Lin, H. Peng, Z. Liu, *Nat. Mater.* **2019**, 18, 520.

[23] L. Lin, B. Deng, J. Sun, H. Peng, Z. Liu, *Chem Rev* **2018**, 118, 9281.

[24] L. Brown, R. Hovden, P. Huang, M. Wojcik, D. A. Muller, J. Park, *Nano Lett.* **2012**, 12, 1609.

[25] Y. Shibuta, J. A. Elliott, *Chemical Physics Letters* **2011**, 512, 146.

[26] B. Deng, B. Wang, N. Li, R. Li, Y. Wang, J. Tang, Q. Fu, Z. Tian, P. Gao, J. Xue, H. Peng, *ACS Nano* **2020**.

[27] L. Lin, L. Z. Sun, J. C. Zhang, J. Y. Sun, A. L. Koh, H. L. Peng, Z. F. Liu, *Adv. Mater.* **2016**, 28, 4671.

[28] L. Sun, L. Lin, J. Zhang, H. Wang, H. Peng, Z. Liu, *Nano Res.* **2016**, 10, 355.

[29] C.-H. Yeh, Y.-C. Lin, P. K. Nayak, C.-C. Lu, Z. Liu, K. Suenaga, P.-W. Chiu, *J. Raman Spectrosc.* **2014**, 45, 912.

[30] R. W. Havener, H. Zhuang, L. Brown, R. G. Hennig, J. Park, *Nano Lett* **2012**, 12, 3162.

[31] W. Fang, A. L. Hsu, R. Caudillo, Y. Song, A. G. Birdwell, E. Zakar, M. Kalbac, M. Dubey, T. Palacios, M. S. Dresselhaus, P. T. Araujo, J. Kong, *Nano Lett.* **2013**, 13, 1541.

[32] X. Y. Zhang, L. Wang, J. Xin, B. I. Yakobson, F. Ding, *J. Am. Chem. Soc.* **2014**, 136, 3040.

[33] L. Banszerus, M. Schmitz, S. Engels, J. Dauber, M. Oellers, F. Haupt, K. Watanabe, T. Taniguchi, B. Beschoten, C. Stampfer, *Sci. Adv.* **2015**, 1, e1500222.

[34] L. Sun, L. Lin, Z. Wang, D. Rui, Z. Yu, J. Zhang, Y. Li, X. Liu, K. Jia, K. Wang, L. Zheng, B. Deng, T. Ma, N. Kang, H. Xu, K. S. Novoselov, H. Peng, Z. Liu, *Adv. Mater.* **2019**, e1902978.

[35] F. Pizzocchero, L. Gammelgaard, B. S. Jessen, J. M. Caridad, L. Wang, J. Hone, P. Boggild, T. J. Booth, *Nat. Commun.* **2016**, 7, 11894.

[36] D. G. Purdie, N. M. Pugno, T. Taniguchi, K. Watanabe, A. C. Ferrari, A. Lombardo, *Nat. Commun.* **2018**, 9, 5387.

[37] J. E. Lee, G. Ahn, J. Shim, Y. S. Lee, S. Ryu, *Nat. Commun.* **2012**, 3, 1024.

[38] D. De Fazio, D. G. Purdie, A. K. Ott, P. Braeuninger-Weimer, T. Khodkov, S. Goossens, T. Taniguchi, K. Watanabe, P. Livreri, F. H. L. Koppens, S. Hofmann, I. Goykhman, A. C. Ferrari, A. Lombardo, *ACS Nano* **2019**, 13, 8926.
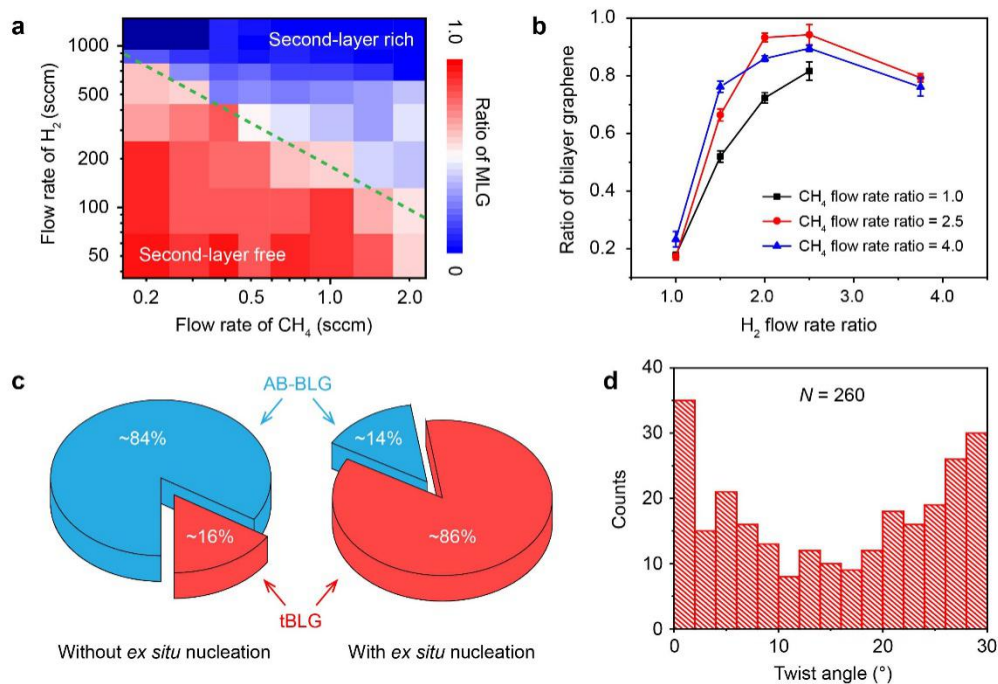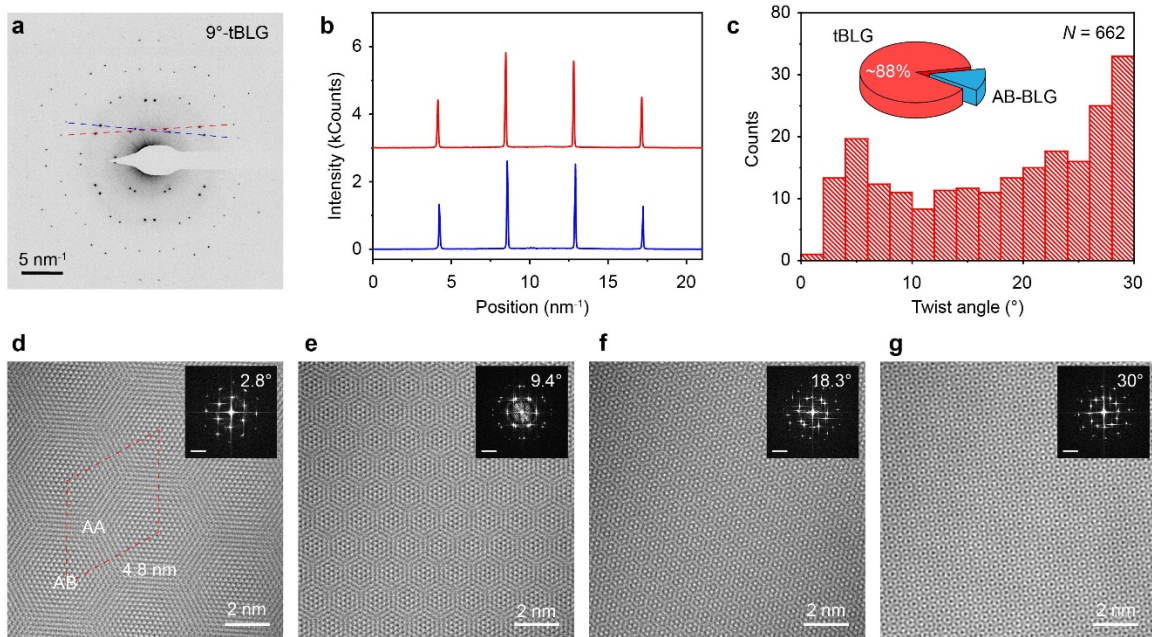
Figures
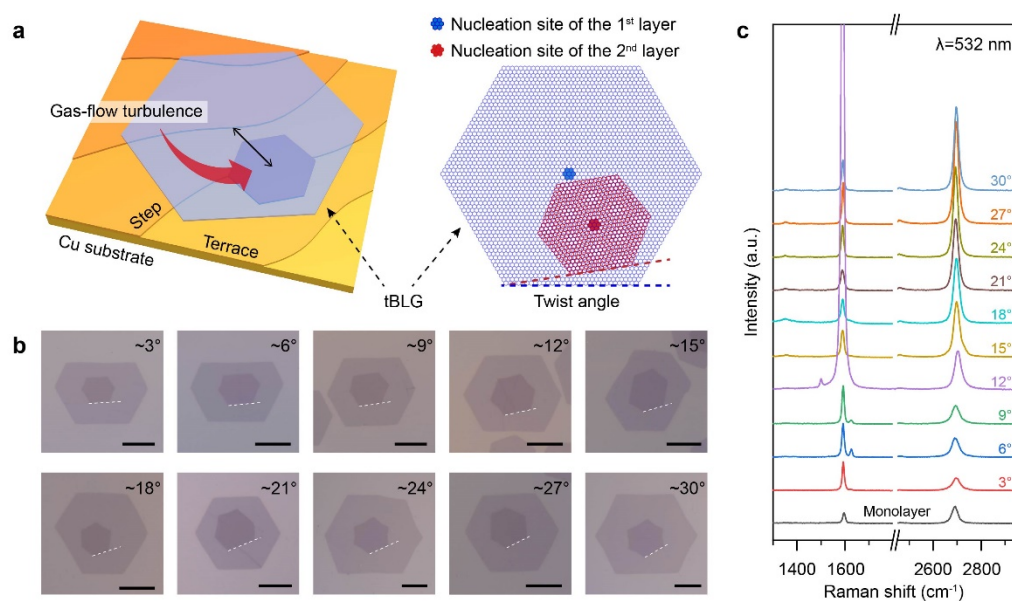
Figure 1. *Ex situ* nucleation strategy for growing tBLG. a) Schematic of the *ex situ* nucleation for growing tBLG on a Cu substrate, where the nucleation site of second layer graphene (red) is different from that of first layer (blue). Note that the nucleation behavior of graphene is usually determined by microscopic environment surrounding the nucleation site, such as Cu steps. b) OM images of as-grown tBLGs with twist angles of ~3°, ~6°, ~9°, ~12°, ~15°, ~18°, ~21°, ~24°, ~27°, and ~30°; scale bars: 10 μm. c) Raman spectra of corresponding tBLGs samples in panel (b).
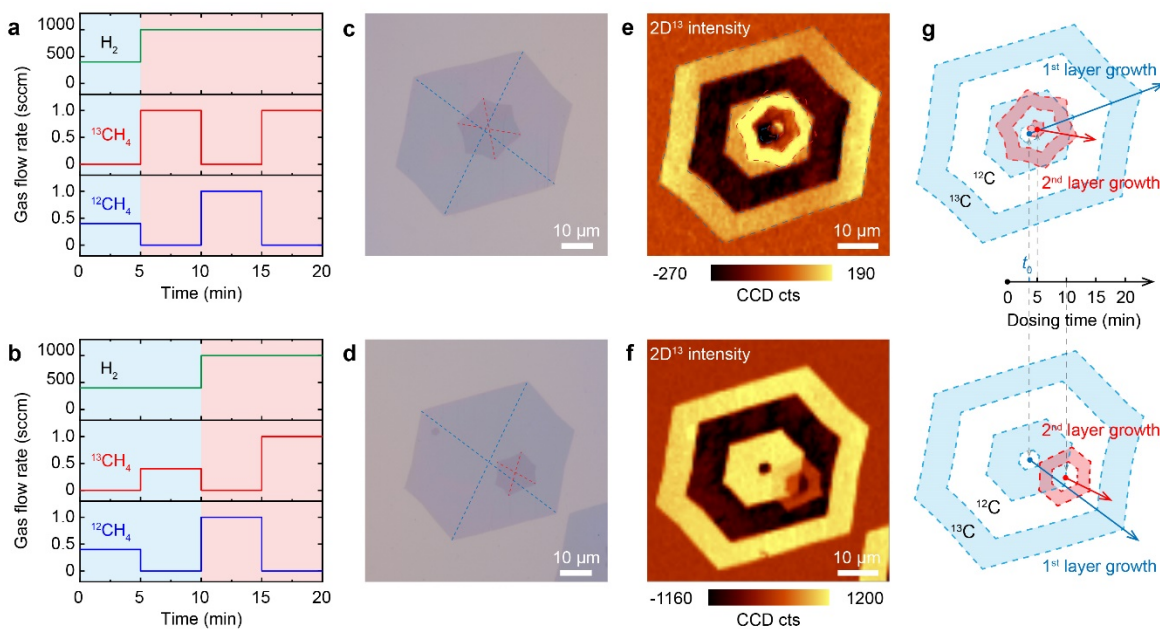
Figure 2. *Ex situ* nucleation and the growth process of tBLGs visualized by isotopic labeling in conjunction with micro-Raman spectroscopy. a,b) Feedstock feeding process for growth of isotope-labeled tBLG using the *ex situ* nucleation strategy, where gas flow turbulence is introduced at (a) 5 min and (b) 10 min, respectively. c,d) Resulting OM images of transferred tBLGs. The dashed lines guide the eye to the nucleation sites of the first and second graphene layers, represented by the intersections of blue and red lines, respectively. e,f) Raman $2D^{13}$-intensity maps (integrated from 2560 cm^{-1} to 2620 cm^{-1}) of areas corresponding to (c) and (d), respectively. g) Schematics of the isotopic distribution and corresponding growth processes of the tBLGs corresponding to (e, top) and (f, bottom). The blue and red rings represent the first and the second graphene layers, respectively. The time axis shows the nucleation times of the second layers, which can be controlled by the introduction of gas-flow turbulence.

Figure 3. Growth parameters for tBLGs. a) Ratio of second-layer-free domain to all graphene domains as a function of the gas flow of H_2 and CH_4, respectively. The red and blue blocks denote the second-layer-free and second-layer-rich regions, respectively. The horizontal and vertical coordinates are logarithmic, while the color varies linearly with the ratio of second-layer-free domain to all graphene domains. b) Ratios of bilayer graphene domains as functions of the ratio of H_2 flow in *ex situ* nucleation step to that in first nucleation step. c) Pie charts of stacking order (AB-BLG or tBLG) for graphene growth without (left) and with (right) *ex situ* nucleation, respectively. d) Distribution of the twist angles in as-grown tBLGs obtained by measuring the sharp edges of hexagonal graphene domains using the OM results.

Figure 4. TEM characterization of as-grown tBLG. a) Typical SAED pattern of tBLG with a twist angle of ~9°. b) Intensity profiles, along the axes marked in (a) with red and blue dashed lines. c) Histogram of twist angles, determined from the SAED tBLG patterns. Inset: Pie charts of stacking order (AB stacking or non-AB stacking) based on all SAED patterns obtained from transferred samples. d-g) HR-TEM images of tBLG with clear Moiré patterns. Insets: Fast Fourier Transforms (FFTs) of the corresponding HR-TEM images; scale bars: 5 nm^{-1}.
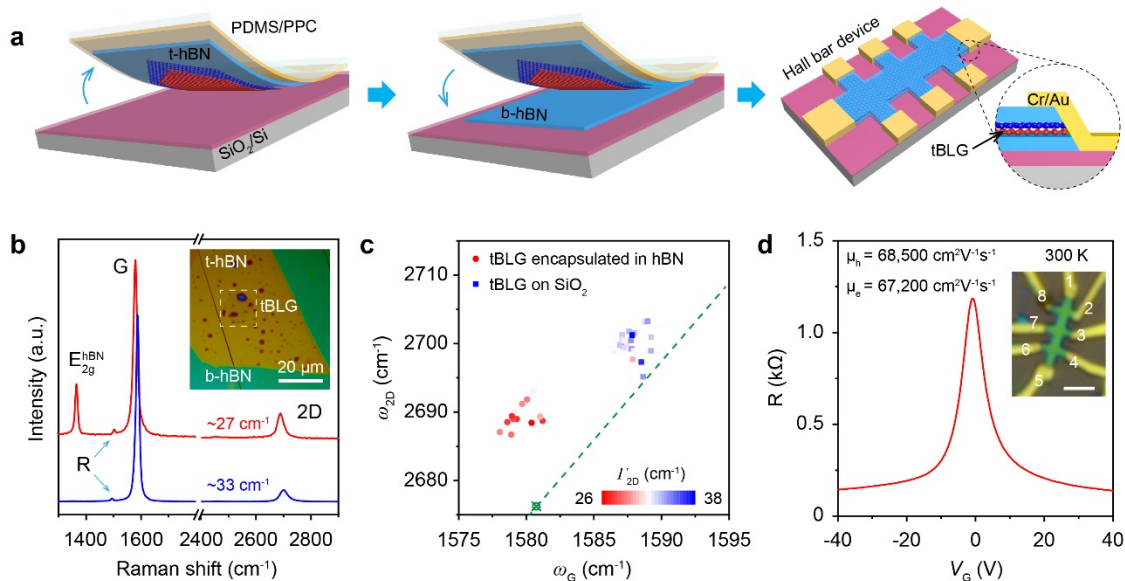
Figure 5. Ultrahigh carrier mobility of as-grown tBLG. a) Schematic of the fabrication process of hBN-

encapsulated Hall bar devices with edge-contact between tBLG and Cr/Au electrodes. b) Raman spectra of ~12° tBLG encapsulated in hBN (red curve), and on SiO_2 (blue curve). Inset: enhanced OM image of ~12° tBLG encapsulated in hBN. c) Correlation plot of 2D peak position (ω_{2D}) as a function of G peak position (ω_G). The circles and squares represent the data taken from tBLG encapsulated in hBN and on SiO_2, respectively. The colors of all the data points represent the full width at half-maximum (FWHM) of the 2D peak, Γ_{2D}, according to the color scale bar included in the figure. d) Four-terminal resistance as a function of gate voltage (V_G) at room temperature ($T = 300$ K). Inset: OM image of the encapsulated tBLG Hall bar device, scale bar: 2 μm.

Table of Contents

A new approach for growing twisted bilayer graphene with a wide variety of twist angles, achieved via *ex situ* nucleation strategy, is reported and confirmed by isotope labeling techniques. The as-grown tBLGs, with twist angles distributed between 0–30°, are of high crystalline quality, show clear Moiré patterns in HR-TEM images, and achieve a high room-temperature carrier mobility exceeding 68,000 cm^2 V^{-1} s^{-1}.

ToC figure
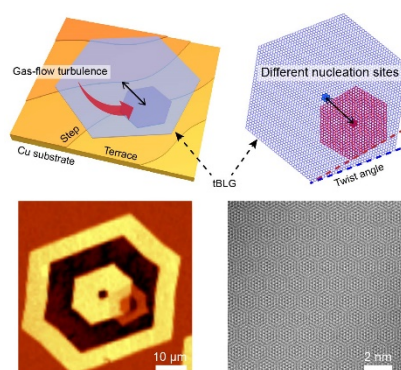
Supporting Information

Ex-situ nucleation for growing twisted bilayer graphene with rich twist angles

Luzhao Sun, Zihao Wang, Yuechen Wang, Liang Zhao, Yanglizhi Li, Buhang Chen, Shishu Zhang, Wendong Wang, Shan Zhong, Haiyang Liu, Lianming Tong, Mark H. Rümmeli, Konstantin S. Novoselov, Hailin Peng*, Li Lin*, and Zhongfan Liu*

*E-mail: zfliu@pku.edu.cn, li.lin-2@manchester.ac.uk, hlpeng@pku.edu.cn

Supporting Information Note 1: Growth modes of bilayer graphene and the factors that influence stacking order

The growth of bilayer graphene or few-layer graphene (FLG) follow one of two modes, namely the Stranski-Krastanov (SK) mode or the Volmer-Weber (VW) mode.[1] In SK mode, especially when carbon-source supply is extremely high, the secondary-layer islands with an irregular morphology will be formed after the full coverage of the first layer. In VW mode, secondary-layer islands grow beneath the first layer, which is catalyzed by the Cu substrate. Since the as-recived graphene domains exhibits a regular hexagonal shape, VW mode is mainly discussed in this article,

The twist angle is determined by the orientations of the two layers according to the VW mode. If the two graphene layers are formed simultaneously, they will prefer to choose the same orientation, as AB stacking without any interlayer rotation provides the most stable configuration. If the second layer is formed after the nucleation of first layer, the orientation of the second layer is mainly influenced by the underlying Cu substrate. Especially edge interactions between graphene and Cu atoms dominate the orientation of the graphene lattice at the nucleation stage,[2, 3] and interactions between the graphene edge and Cu atoms are more important than those between graphene layers.[4] Therefore, the

orientations of the second layers are determined mainly by the microscopic environment of Cu substrate near their nucleation sites in our *ex situ* nucleation strategy, which are clearly different from those of the first layer.

Supporting Information Note 2: Raman spectra of tBLGs

Raman spectra were acquired in tBLGs samples with the twist angles in the full range from 0° to 30°, confirming interlayer rotation in as-received tBLGs. An excitation wavelength of 532 nm (corresponding to an energy of 2.33 eV) was used, which can produce the rotation-related R' peak for BLGs with small twist angles (<10°) due to intravalley double-resonance. R' peak is nondispersive, whose maximum intensity occurs at the critical angle where the excited phonons match the laser energy.[5, 6] Figure S2a shows the R' peaks of tBLG with twist angle of 3° (3°-tBLG), 6° (6°-tBLG), and 9° (9°-tBLG). The intensity of R' peak of 6°-tBLG is higher than those of 3°-tBLG and 9°-tBLG, which agrees well with the reported literature.[5-7] Figures 1c and S2a also show typical spectra of 12°-tBLG, in which the G band is strongly enhanced and a new twist-related R peak is clearly observed. The enhancement of G band is ascribed to the energy matching between the VHS and exciting laser (2.33 eV).[8] The G band intensity of as-grown 12°-tBLG is around 45 times higher than that of monolayer graphene (MLG), and is 20 times higher than that of 2D peak of 12°-tBLG. The R peak, originating from the intervalley processes, is also nondispersive. The R peak of 12°-tBLG is centered at ~1500 cm^{-1}, and the peak position decreases with increasing twist angle.[5] For large twist angles, a D-like peak (centered at ~1350 cm^{-1}) and an R peak (centered in the 1370–1400 cm^{-1} range) can be observed (Figures 1c and S2b, c). Note that the D-like peak of tBLG is caused by the rotated interlayer stacking of the two layers, where one of the graphene layers would weakly perturb the other, rather than caused by in-plane disorder (point defects or grain boundaries).[5, 9, 10] Nevertheless, to confirm this, Raman spectra were acquired in the monolayer region of the same domain of 27°-tBLG, which clearly shows the lack of the D band (Figure S2b).

Supporting Information Note 3: Isotope-labelled growth of tBLGs for exploring the mechanism of *ex situ* nucleation

To confirm the mechanism of our *ex situ* nucleation strategy and capability of flow turbulence to initiate the nucleation of second layer, the $^{12}CH_4$ and $^{13}CH_4$ were switched every 5 min during the experiments.

In detail, for the 30°-tBLG shown in Figures 2c, the *ex situ* nucleation began at the time point of 5 min by increasing the flow rates of H_2 (from 400 sccm to 1000 sccm) and CH_4 (from 0.4 sccm for $^{12}CH_4$ to 1.0 sccm for $^{13}CH_4$) (Figure 2a). For the ~9°-tBLG shown in Figures 2d, the second layer was initiated at the time point of 10 min, when the carbon source was changed from $^{13}CH_4$ to $^{12}CH_4$ (Figure 2b). In contrast, the isotope-labelled growth of bilayer graphene without flow turbulence was carried out according to the sequence shown in Figure S5, which resulted in AB-stacked BLG (AB-BLG). These experiments confirmed as follows: 1) the nucleation of second graphene layer can be initiated by increasing H_2 and CH_4, irrespective of the $^{12}CH_4$ to $^{13}CH_4$ or $^{13}CH_4$ to $^{12}CH_4$ switching; 2) the nucleation site of the second layer can be controlled by the gas flow, which further highlights the importance of the *ex situ* nucleation strategy.

Supporting Information Note 4: Parameters for growing tBLGs

To determine the appropriate parameters for growing second-layer-free graphene (for first nucleation of the first layer) and second-layer-rich graphene (for *ex situ* nucleation), gas flow windows (Figure 3a and Figure S6) were plotted by conducting series of growth experiments without turbulence. After annealing at 1020 °C under 500 sccm of H_2 for 30 min, growth proceeded under a flow of H_2 and CH_4, as shown in Figures 3a and S6a,b. Clear gaps exists between the monolayer region and the bilayer region in Figures 3a and S6a, and a clear gap is observed between the bilayer region and the few-layer region in Figure S6b, which indicates that a higher partial pressure of H_2 produces thicker graphene. Therefore, we selected flow rates of 400 sccm and 0.4 sccm for H_2 and CH_4, respectively, for 5 min during the first nucleation step, after which the flow rate of H_2 was tuned from 400 sccm to 1500 sccm during the *ex situ* nucleation step. To increase the probability of secondary nucleation at the edges of the first-layer islands, and to increase the carbon source supply for bilayer growth, we also increased the flow rate of CH_4 to 1.0 sccm and 1.6 sccm, respectively (0.4 sccm of CH_4 in the second step is the control group). Figures 3b and S6c,d suggest that appropriate H_2 flow ratio and CH_4 flow ratio are important. In this regard, values of the gas-flow parameters, namely $H_2 : CH_4$ = 400 sccm : 0.4 sccm during the first nucleation step, $H_2 : CH_4$ = 1000 sccm : 1 sccm during the *ex situ* nucleation step, were selected for tBLG growth. Typical OM images of tBLGs are shown in Figures 1b.

For calculating the proportions of tBLG domains to all as-formed bilayer graphene domains, OM images

and corresponding Raman maps are analyzed. From the OM images (Figure S7a and Figure S8a) and Raman G-intensity (I_G) maps (Figure S7b and Figure S8b), the bilayer graphene can be easily observed, since I_G increases as the number of layers. The intensity of the 2D band (I_{2D}) and full width at half-maximum (FWHM) of the 2D band (Γ_{2D}) are used to check the stacking orders of the bilayer graphene. The bright regions in I_{2D} maps (Figure S7c and Figure S8c) indicate the t-BLG domains, and AB-BLG domains show larger Γ_{2D} (50-60 cm^{-1}) (Figure S7d and Figure S8d). The I_{2D} for tBLG with small twist angle (<10°) is weaker than that for MLG (Figure S8d). The R peak and R' peak are also characteristics for identifying tBLG domains (Figure 8e).

Supporting Information Note 5: Characterizing graphene by TEM

Graphene samples were transferred onto commercially available TEM grids (Quantifoil) using a non-polymer-assisted method.[11] The structure of the TEM grid is shown in Figure S9, which consists of metal mesh and porous carbon film. We collected the diffraction patterns over all of the intact graphene holes (suspended graphene on the carbon-film holes) for investigating the stacking order of BLG. We can obtain the proportions of tBLG and AB-BLG over all of the bilayer graphene by analyzing the SAED patterns. Figure S10 shows the representative SAED patterns of MLG and AB-BLG. The intensity ratio of the diffraction points, I_{2100}/I_{1100} in AB-BLG is clearly higher than that in MLG, which help us to distinguish AB-BLG from MLG by using the SAED patterns, despite each showing single groups of hexagonal points.[7, 12] Therefore, the proportion of tBLG within BLG domains can be obtained by counting the numbers of tBLG and AB-BLG. Figure S11 shows the library of SAED patterns of tBLG with the twist angle in the full range from 0° to 30°.
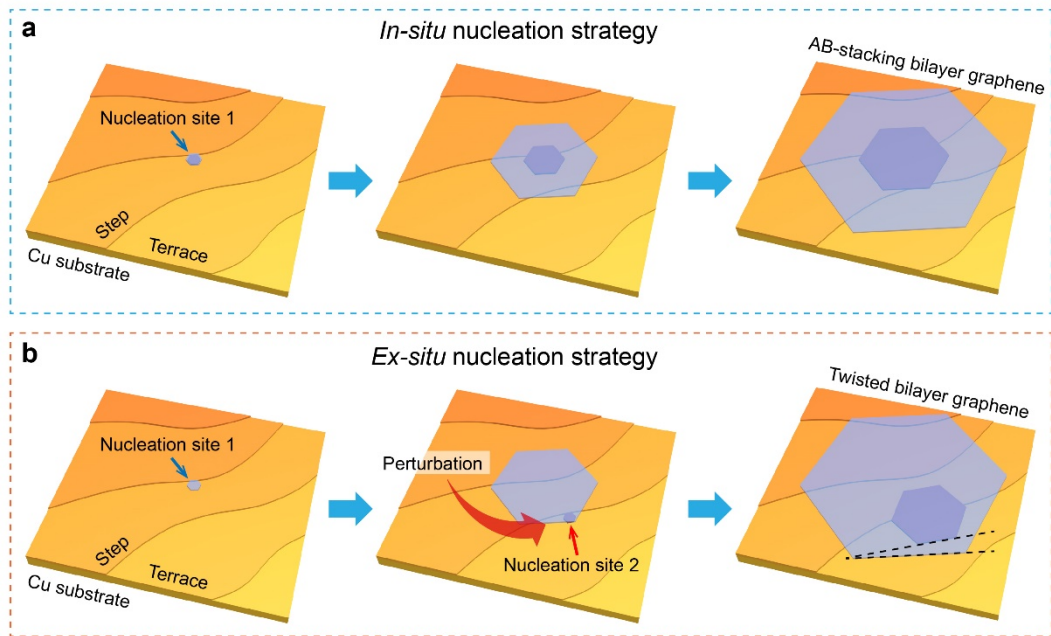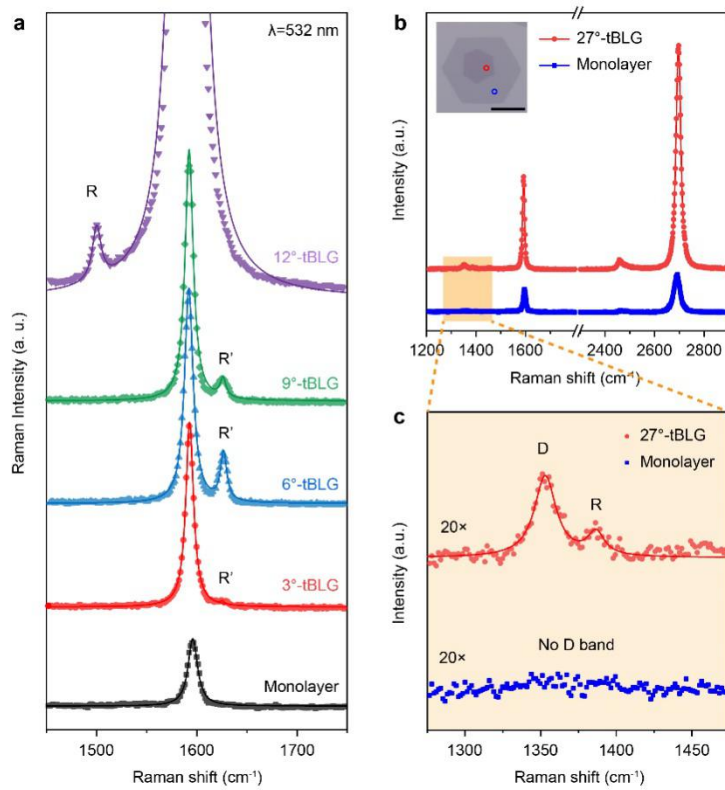
Supplementary Figures:

Figure S1. Schematic diagrams of *in situ* nucleation and *ex situ* nucleation strategies for growing (a) AB-BLG and (b) tBLG.
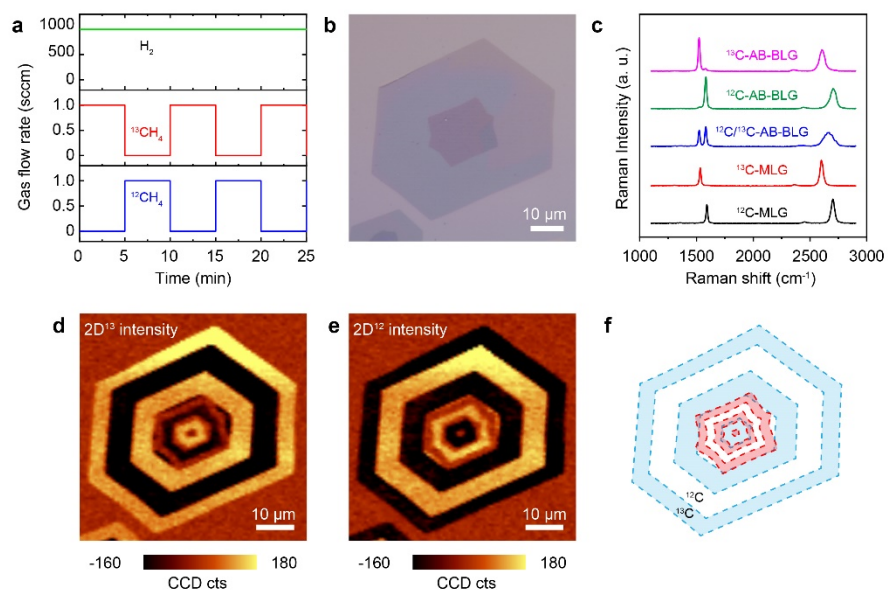
Figure S2. Raman spectra of tBLG. a) Raman spectra of 3°-tBLG, 6°-tBLG, 9°-tBLG and 12°-tBLG in the frequency range from 1450 to 1750 cm^{-1}. b) Raman spectra of the monolayer graphene and 27°-tBLG regions in the same domain. Inset: OM image of 27°-tBLG; scale bar: 10 μm. c) Enlarged Raman spectra in panel (b) in the frequency range from 1275 to 1475 cm^{-1}.
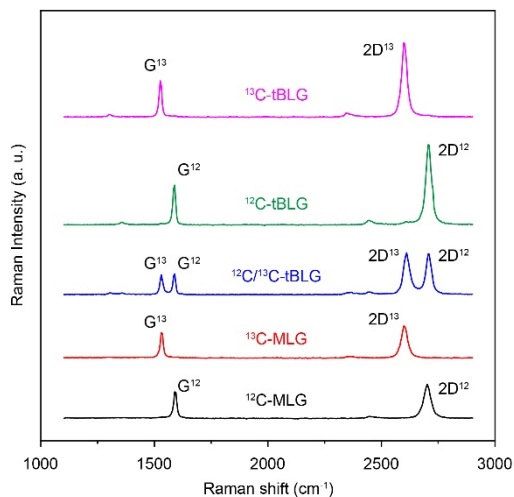

Figure S3. Raman spectra of ^{12}C monolayer graphene (^{12}C-MLG, black), ^{13}C monolayer graphene (^{13}C-MLG, red), ^{12}C/^{13}C twisted bilayer graphene (^{12}C/^{13}C-tBLG, blue), ^{12}C twisted bilayer graphene (^{12}C-tBLG, green), and ^{13}C twisted bilayer graphene (^{13}C-tBLG, purple). Note that the twist angle is about 30°.
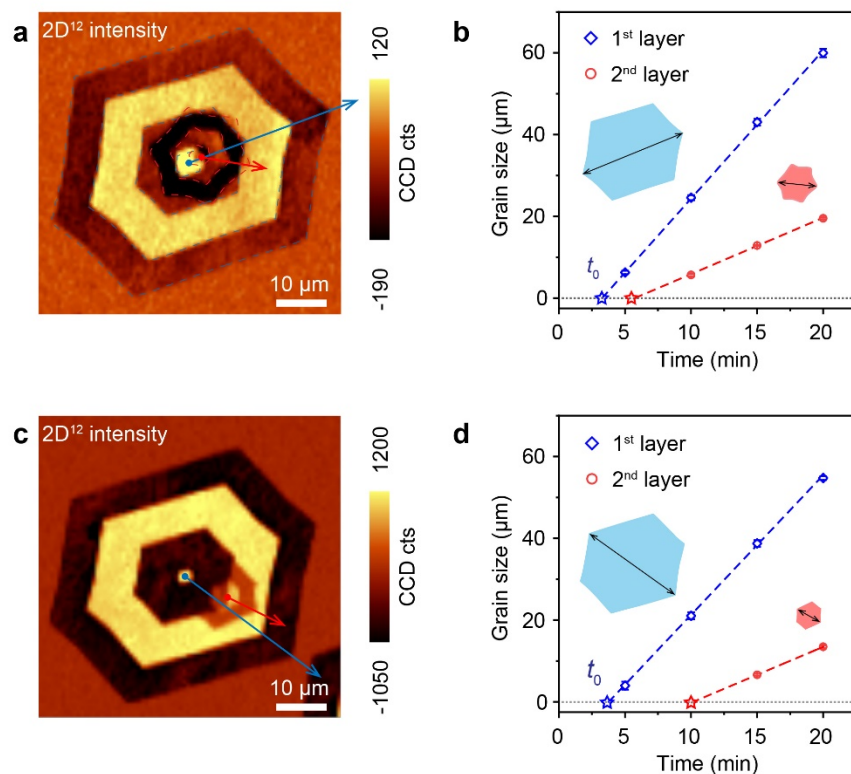
Figure S4. Raman 2D^{12}-intensity maps and corresponding schematic diagrams depicting the growth of isotope-labelled tBLGs. a,c) Raman 2D^{12}-intensity maps (integrated from 2660 cm^{-1} to 2720 cm^{-1}), which complement the 2D^{13}-intensity maps (integrated from 2560 cm^{-1} to 2620 cm^{-1}) shown in Figure 3e and 3f of the main text. b,d) The grain sizes (diagonal) of the 1st-layer (blue) and the 2nd-layer (red) graphene as functions of growth time corresponding to (a) and (c), respectively.

Figure S5. Isotope-labelled growth of AB-BLG using the normal one-step method. a) Feedstock feeding process for AB-BLG-growth. b) OM image of as-grown AB-BLG on a SiO$_2$/Si substrate. c) Raman spectra of ^{13}C-AB-BLG (purple), ^{12}C-AB-BLG (green), ^{12}C/^{13}C-AB-BLG (blue), ^{13}C monolayer graphene (red), and ^{12}C monolayer graphene (black). d) Raman 2D^{12}-intensity (integrated from 2660 cm^{-1} to 2720 cm^{-1}) and 2D^{13}-intensity (integrated from 2560 cm^{-1} to 2620 cm^{-1}) maps of the AB-BLG corresponding to panel (b). f) Schematic diagram of the AB-BLG growth process corresponding to panels (a-e). Scale bars: 10 μm.
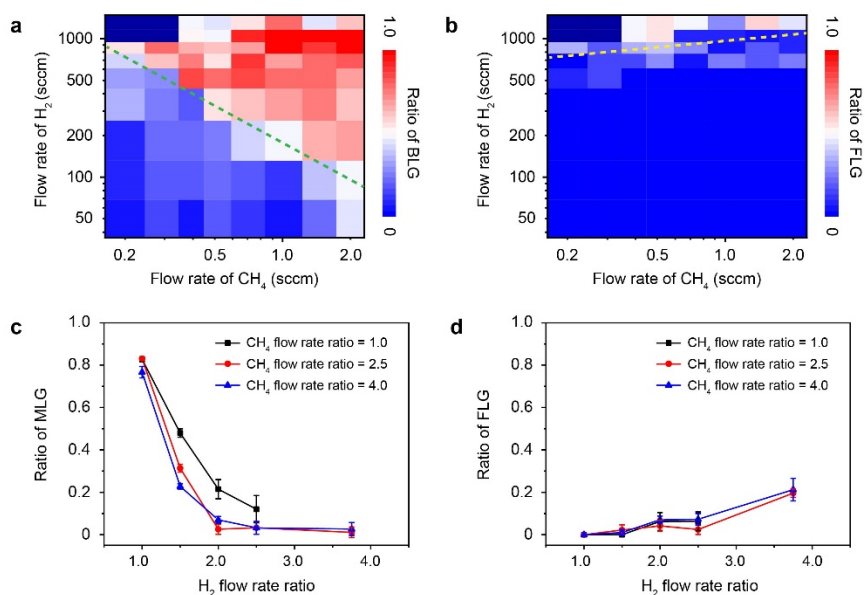
Figure S6. Gas flow parameters for growing bilayer and few-layer graphene with and without using *ex situ* nucleation strategy. a,b) Ratios of (a) bilayer graphene and (b) few-layer graphene (FLG) domains as functions of H_2 and CH_4 flow rates. c,d) Ratio of (c) monolayer graphene (MLG) and (d) FLG domains as functions of the ratio between the H_2 flow rate during *ex situ* nucleation step and that during the first nucleation step. Black, red and blue curves indicate that the ratio between the flow rate of CH_4 during *ex situ* nucleation step and that during the first nucleation step are 1.0, 2.5, and 4.0, respectively.
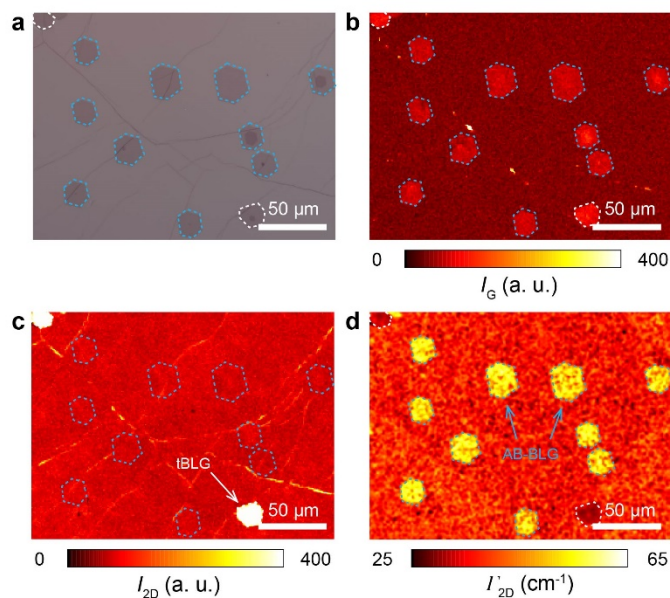

Figure S7. Typical OM image and Raman mapping of bilayer graphene without *ex situ* nucleation. a) OM image of BLGs. The dashed lines help to confirm AB-BLGs (blue) and tBLGs (white). b-d) Raman mapping showing intensity of G band (b), intensity of 2D band (c), and width of 2D band (d), for the selected area in (a).
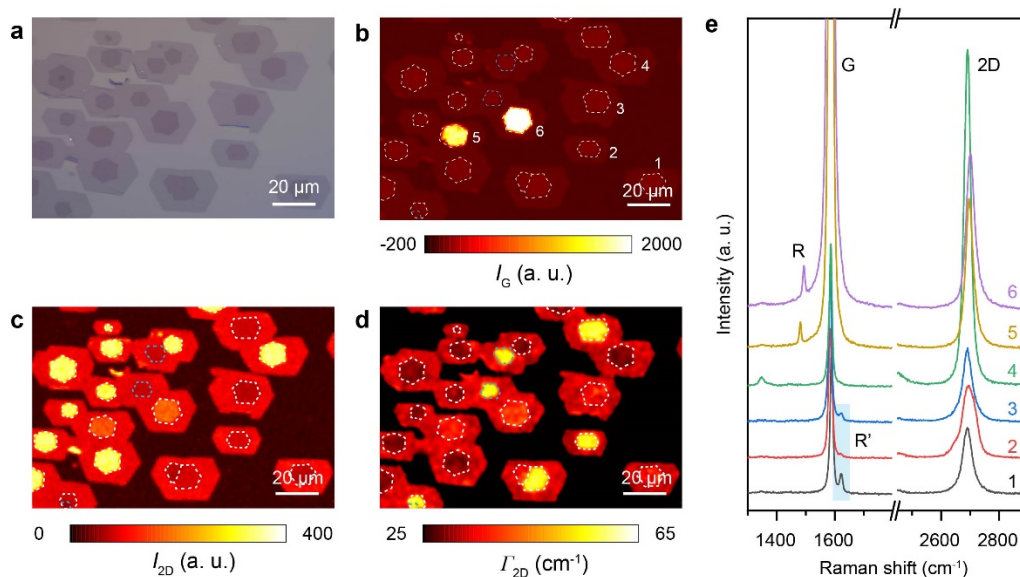
Figure S8. Typical OM image and Raman mapping of bilayer graphene with *ex situ* nucleation. a) Optical microscopy image of BLGs. b-d) Raman mapping showing intensity of G band (b), intensity of 2D band (c), and width of 2D band (d), for the selected area in (a). The dashed lines help to confirm BLG domains. e) Raman spectra of tBLGs corresponding to the samples marked in panel (b).
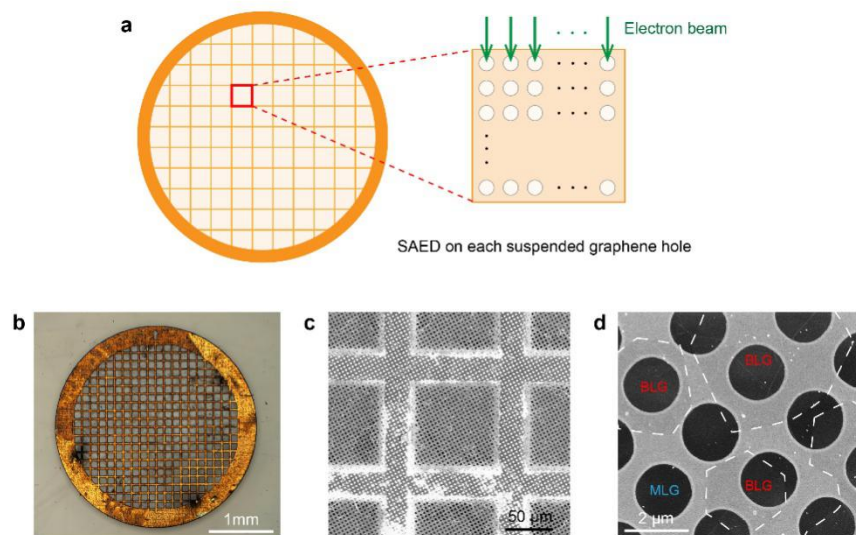
Figure S9. Preparing a sample of as-grown tBLGs for TEM. a) Schematic of the TEM grid and the process for collecting SAED results . b) OM image of the TEM grid covered by the tBLG sample. c,d) SEM images of the as-transferred tBLG sample on the TEM grid. MLG and tBLG are distinguishable by contrast.
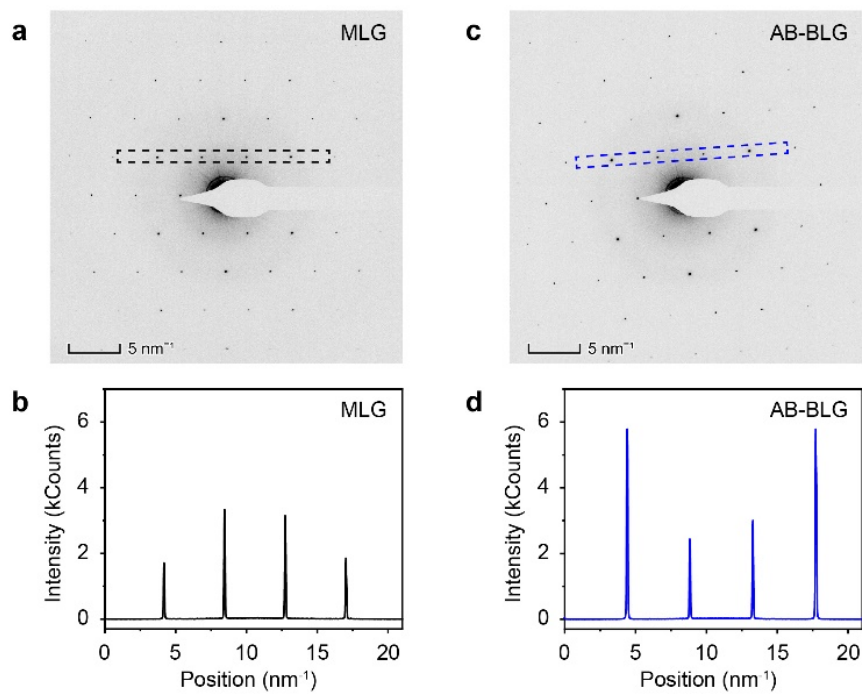
Figure S10. Typical diffraction patterns of MLG and AB-BLG (a,c) and corresponding spot intensity profiles (b,d).
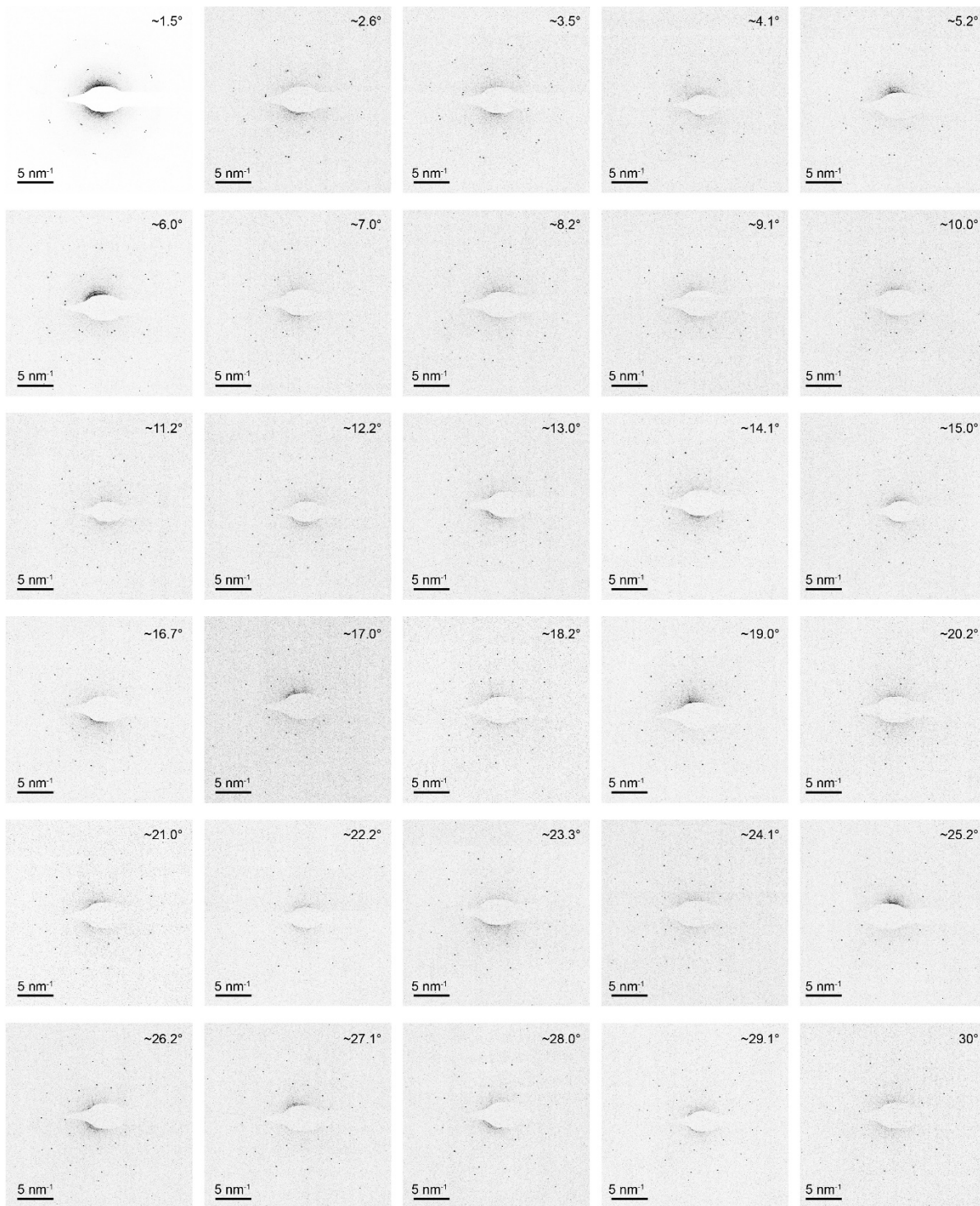
Figure S11. Library of SAED patterns in the full 0–30° range of interlayer twist angles.
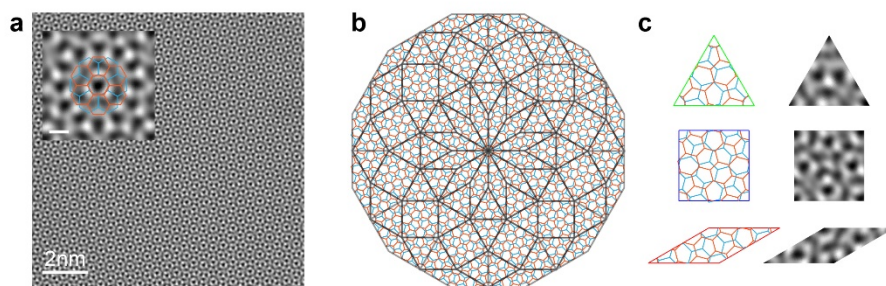
Figure S12. HR-TEM image and crystal structure of 30°-tBLG quasicrystal. a) HR-TEM image of 30°-tBLG. Inset: enlarged lattice image with corresponding crystal structure; Scale bar: 0.2 nm. b) dodecagonal quasicrystal structure of 30°-tBLG. c) Structrue units of dodecagonal quasicrystal and corresponding HR-TEM images.
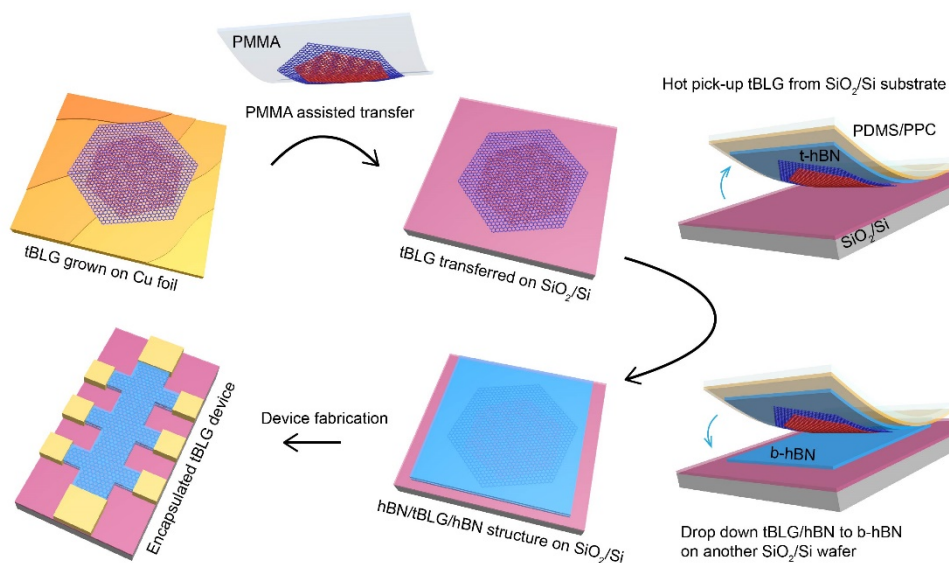
Figure S13. Schematic for the fabrication of the hBN-encapsulated tBLG Hall bar device with one-dimensional edge contact.
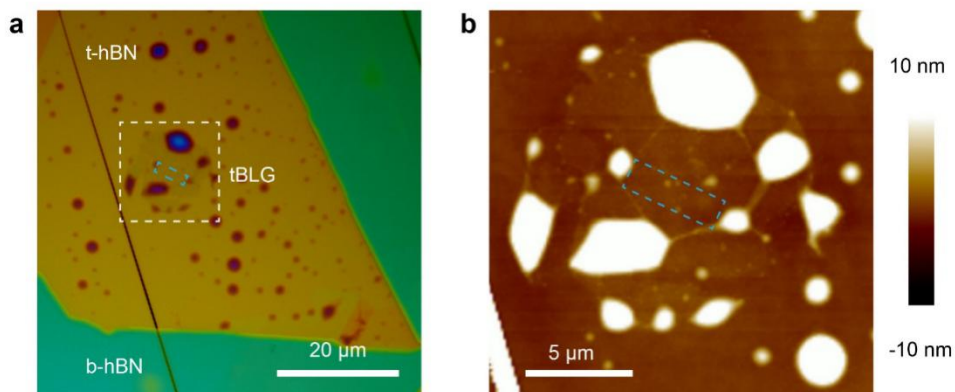
Figure S14. a) Enhanced OM image of as-fabricated hBN/tBLG/hBN structure. b) AFM image corresponding to the region in the dashed white box in (a). The region enclosed in the dashed green rectangular was selected to fabricate the Hall bar device.
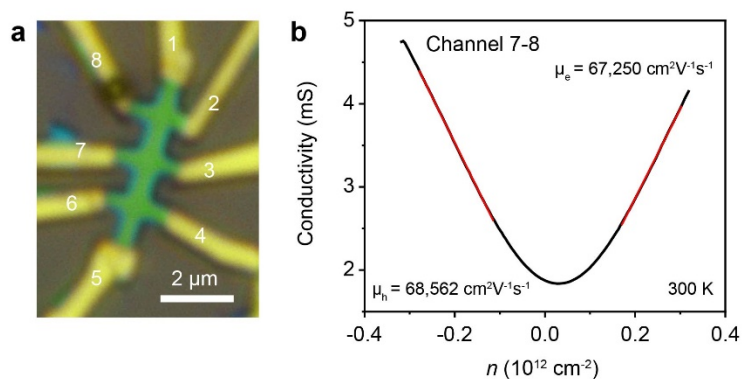
Figure S15. Carrier mobility of as-grown tBLG. a) OM image of the Hall bar device of encapsulated tBLG. b) Linear fit of the conductivity σ (channel 7-8) as a function of the charge-carrier density *n*.

Reference

[1]   H. Q. Ta, D. J. Perello, D. L. Duong, G. H. Han, S. Gorantla, V. L. Nguyen, A. Bachmatiuk, S. V. Rotkin, Y. H. Lee, M. H. Rummeli, *Nano Lett* **2016**.

[2]   X. Y. Zhang, Z. W. Xu, L. Hui, J. Xin, F. Ding, *J. Phys. Chem. Lett.* **2012**, 3, 2822.

[3]   Q. H. Yuan, B. I. Yakobson, F. Ding, *J Phys Chem Lett* **2014**, 5, 3093.

[4]   Z. Yan, Y. Liu, L. Ju, Z. Peng, J. Lin, G. Wang, H. Zhou, C. Xiang, E. L. Samuel, C. Kittrell, V. I. Artyukhov, F. Wang, B. I. Yakobson, J. M. Tour, *Angewandte Chemie* **2014**, 53, 1565.

[5]   V. Carozo, C. M. Almeida, E. H. Ferreira, L. G. Cancado, C. A. Achete, A. Jorio, *Nano Lett* **2011**, 11, 4527.

[6]   C.-H. Yeh, Y.-C. Lin, P. K. Nayak, C.-C. Lu, Z. Liu, K. Suenaga, P.-W. Chiu, *J. Raman Spectrosc.* **2014**, 45, 912.

[7]   C. C. Lu, Y. C. Lin, Z. Liu, C. H. Yeh, K. Suenaga, P. W. Chiu, *Acs Nano* **2013**, 7, 2587.

[8]   K. Kim, S. Coh, L. Z. Tan, W. Regan, J. M. Yuk, E. Chatterjee, M. F. Crommie, M. L. Cohen, S. G. Louie, A. Zettl, *Physical Review Letters* **2012**, 108.

[9]   A. K. Gupta, Y. Tang, V. H. Crespi, P. C. Eklund, *Physical Review B* **2010**, 82.

[10]   Y. Chen, L. Meng, W. Zhao, Z. Liang, X. Wu, H. Nan, Z. Wu, S. Huang, L. Sun, J. Wang, Z. Ni, *Phys Chem Chem Phys* **2014**, 16, 21682.

[11]   J. Zhang, L. Lin, L. Sun, Y. Huang, A. L. Koh, W. Dang, J. Yin, M. Wang, C. Tan, T. Li, Z. Tan, Z. Liu, H. Peng, *Adv. Mater.* **2017**, 29, 1700639.

[12]   J. C. Meyer, A. K. Geim, M. I. Katsnelson, K. S. Novoselov, T. J. Booth, S. Roth, *Nature* **2007**, 446, 60.

4.Closing remarks

Van der Waals heterostructures, as vertical stacks assembled by different 2D crystals, are widely used to produce predetermined functionalities that are independent from their constituents. Apart from the selection and sequence of 2D crystals, controlling the twist angle between stacking layers enabled an additional degree of freedom. Furthermore, alignment between two crystals with similar lattice mismatch results in a moiré pattern.

Graphene was the first 2D material to be discovered, and subsequently gained a vast amount of attention compared with other 2D crystals. Due to their exceptional quality and mature fabrication process, graphene-based heterostructures have been the centre of attention for many years. As an ideal substrate for graphene devices, hBN also has a similar hexagonal lattice structure, with a mismatch of only 1.8% to graphene. The single aligned hBn-graphene-hBn heterostructures have been researched for an extensive amount of time. The key feature of the graphene–hBN superlattice, in terms of electrical transport, is that its superlattice Brillouin zone is much smaller than the original Brillouin zone of a pristine graphene lattice. This is valuable because several interesting phenomena related to the Brillouin zone edge occur within the experimental range, such as secondary Dirac points and BZ oscillations. Since the magnetic length of the superlattice period is also within the range of our experimental fields, their commensuration results in the Hofstadter butterfly. Section 3.2 details the transport results of the temperature dependence of $R_{xx}(n)$, proving the existence of UEE scattering.

Unlike the single aligned heterostructures comprising one moiré pattern, Section 3.3 reported a doubly aligned structure whereby fully encapsulated graphene simultaneously aligned to the top and bottom of hBNs. As a result of the moiré pattern, two periodic potentials are applied to graphene concurrently, which can be evidenced by two secondary Dirac points in the transport measurement, as well as two sets of hexagonal patterns in the Fourier transformation of AFM images. Moreover, the differential creates another set of supermoirés; in this situation, the supermoiré with the largest period can be independent of the difference in the lattice constants between two crystals, and can subsequently overcome the restrictions of this lattice mismatch to achieve a period greater than the maximal 14 nm. This is significant as it would make it possible to design graphene band reconstruction at arbitrarily low

Fermi energies. The Brillouin zone in the reciprocal lattice can be controlled to be as large as possible.

Regarding the superlattices of other 2D materials, there is an increasing number of papers being published focusing on TMD superconductors. Research concerning twisted NbSe$_2$ layers has been explored in Section 3.4, which also includes moiré-related phenomena in magnetic field measurements.

CVD is an important method to manufacture graphene in industrial applications. Section 3.5 discusses progression in the improvement of CVD graphene quality and highlights our attempts to create twisted bilayer graphene directly using the CVD method.

References

1. Novoselov, K. S., Mishchenko, A., Carvalho, A. & Neto, A. H. C. 2D materials and van der Waals heterostructures. *Science* **353**, aac9439 (2016).

2. Dean, C. R. *et al.* Boron nitride substrates for high-quality graphene electronics. *Nature Nanotech* **5**, 722–726 (2010).

3. Kretinin, A. V. *et al.* Electronic Properties of Graphene Encapsulated with Different Two-Dimensional Atomic Crystals. *Nano Lett.* **14**, 3270–3276 (2014).

4. Yang, W. *et al.* Epitaxial growth of single-domain graphene on hexagonal boron nitride. *Nature Materials* **12**, 792–797 (2013).

5. Yankowitz, M. *et al.* Emergence of superlattice Dirac points in graphene on hexagonal boron nitride. *Nature Physics* **8**, 382–386 (2012).

6. Ponomarenko, L. A. *et al.* Cloning of Dirac fermions in graphene superlattices. *Nature* **497**, 594–597 (2013).

7. Dean, C. R. *et al.* Hofstadter's butterfly and the fractal quantum Hall effect in moiré superlattices. *Nature* **497**, 598–602 (2013).

8. Hunt, B. *et al.* Massive Dirac Fermions and Hofstadter Butterfly in a van der Waals Heterostructure. *Science* 1237240 (2013)

9. Kumar, R. K. *et al.* High-temperature quantum oscillations caused by recurring Bloch states in graphene superlattices. *Science* **357**, 181–184 (2017).

10. Krishna Kumar, R. *et al.* High-order fractal states in graphene superlattices. *Proc Natl Acad Sci USA* **115**, 5135 (2018).

11. Woods, C. R. *et al.* Commensurate–incommensurate transition in graphene on hexagonal boron nitride. *Nature Physics* **10**, 451–456 (2014).

12. Misra, R., McCarthy, M. & Hebard, A. F. Electric field gating with ionic liquids. *Appl. Phys. Lett.* **90**, 052905 (2007).

13. Datta, S. *Electronic Transport in Mesoscopic Systems*. (Cambridge University Press, 1995).

14. Bandurin, D. A. *et al.* Negative local resistance caused by viscous electron backflow in graphene. *Science* **351**, 1055–1058 (2016).

15. Sólyom, J. *Fundamentals of the Physics of Solids: Volume II: Electronic Properties*. (Springer-Verlag, 2009).

16. Luryi, S. Quantum capacitance devices. *Applied Physics Letters* **52**, 501–503 (1988).

17. Xia, J., Chen, F., Li, J. & Tao, N. Measurement of the quantum capacitance of graphene. *Nature Nanotechnology* **4**, 505–509 (2009).

18. Zibrov, A. A. *et al.* Tunable interacting composite fermion phases in a half-filled bilayer-graphene Landau level. *Nature* **549**, 360–364 (2017).

19. Lee, K. *et al.* Chemical potential and quantum Hall ferromagnetism in bilayer graphene. *Science* **345**, 58–61 (2014).

20. Maher, P. *et al.* Tunable fractional quantum Hall phases in bilayer graphene. *Science* **345**, 61–64 (2014).

21. Lv, H. Y. *et al.* Perfect charge compensation in WTe_2 for the extraordinary magnetoresistance: From bulk to monolayer. *EPL* **110**, 37004 (2015).

22. Kwan, Y. H. *et al.* Quantum oscillations probe the Fermi surface topology of the nodal-line semimetal CaAgAs. *Phys. Rev. Research* **2**, 012055 (2020).

23. Kumaravadivel, P. *et al.* Strong magnetophonon oscillations in extra-large graphene. *Nature Communications* **10**, 3334 (2019).

24. Chiu, H.-Y., Perebeinos, V., Lin, Y.-M. & Avouris, P. Controllable p-n Junction Formation in Monolayer Graphene Using Electrostatic Substrate Engineering. *Nano Lett.* **10**, 4634–4639 (2010).

25. Williams, J. R., DiCarlo, L. & Marcus, C. M. Quantum Hall Effect in a Gate-Controlled p-n Junction of Graphene. *Science* **317**, 638–641 (2007).

26. Hoffman, J. E. *et al.* Imaging Quasiparticle Interference in $Bi_2Sr_2CaCu_2O_{8+\delta}$. *Science* **297**, 1148–1151 (2002).

27. Cao, Y. *et al.* Correlated insulator behaviour at half-filling in magic-angle graphene superlattices. *Nature* **556**, 80–84 (2018).

28. Cao, Y. *et al.* Unconventional superconductivity in magic-angle graphene superlattices. *Nature* **556**, 43–50 (2018).

29. Ghazaryan, D. *et al.* Magnon-assisted tunnelling in van der Waals heterostructures based on $CrBr_3$. *Nature Electronics* **1**, 344–349 (2018).

30. Li, M. *et al.* Theory of electron–phonon–dislon interacting system—toward a quantized theory of dislocations. *New J. Phys.* **20**, 023010 (2018).

31. Goldman, V. J. A game of five halves. *Nature Physics* **3**, 517–518 (2007).

32. Banerjee, A. *et al.* Proximate Kitaev quantum spin liquid behaviour in a honeycomb magnet. *Nature Mater* **15**, 733–740 (2016).

33. Shaginyan, V. R., Msezane, A. Z., Popov, K. G., Japaridze, G. S. & Stephanovich, V. A. Identification of strongly correlated spin liquid in herbertsmithite. *EPL* **97**, 56001 (2012).

34. Xu, S.-Y. *et al.* Discovery of Lorentz-violating type II Weyl fermions in LaAlGe. *Science Advances* **3**, e1603266 (2017).

35. Soluyanov, A. A. *et al.* Type-II Weyl semimetals. *Nature* **527**, 495–498 (2015).

36. Modesti, S., Valle, F. D., Rosei, R., Tosatti, E. & Glazer, J. Ferromagnetic Stoner excitations detected by electron-energy-loss spectroscopy. *Phys. Rev. B* **31**, 5471–5473 (1985).

37. Hopster, H. Direct observation of Stoner excitations in itinerant ferromagnets by spin-polarized inelastic electron scattering (invited; abstract). *Journal of Applied Physics* **57**, 3017–3017 (1985).

38. Cao, Y. *et al.* Mapping the orbital wavefunction of the surface states in three-dimensional topological

insulators. *Nature Physics* **9**, 499–504 (2013).

39. Shoenberg, D. The de Haas-Van Alphen Effect. in *Low Temperature Physics LT9* (eds. Daunt, J. G., Edwards, D. O., Milford, F. J. & Yaqub, M.) 665–676 (Springer US, 1965).

40. Holstein, T., Norton, R. E. & Pincus, P. de Haas-van Alphen Effect and the Specific Heat of an Electron Gas. *Phys. Rev. B* **8**, 2649–2656 (1973).

41. Pauw, L. A METHOD OF MEASURING SPECIFIC RESISTIVITY AND HALL EFFECT OF DISCS OF ARBITRARY SHAPE. Semiconductor Devices: Pioneering Papers, pp. 174-182 (1991).

42. Koon, D. W. & Knickerbocker, C. J. What do you measure when you measure resistivity? *Review of Scientific Instruments* **63**, 207 (1998).

43. Chwang, R., Smith, B. J. & Crowell, C. R. Contact size effects on the van der Pauw method for resistivity and Hall coefficient measurement. *Solid-State Electronics* **17**, 1217–1227 (1974).

44. Zeng, Y. *et al.* High-Quality Magnetotransport in Graphene Using the Edge-Free Corbino Geometry. *Phys. Rev. Lett.* **122**, 137701 (2019)

45. Peters, E. C., Giesbers, A. J. M., Burghard, M. & Kern, K. Scaling in the quantum Hall regime of graphene Corbino devices. *Appl. Phys. Lett.* **104**, 203109 (2014).

46. Panchal, V. *et al.* Visualisation of edge effects in side-gated graphene nanodevices. *Scientific Reports* **4**, 5881 (2014).

47. Britnell, L. *et al.* Field-Effect Tunneling Transistor Based on Vertical Graphene Heterostructures. *Science* **335**, 947–950 (2012).

48. Simmons, J. G. Generalized Formula for the Electric Tunnel Effect between Similar Electrodes Separated by a Thin Insulating Film. *Journal of Applied Physics* **34**, 1793–1803 (1963).

49. Zhu, M. *et al.* Stacking transition in bilayer graphene caused by thermally activated rotation. *2D Mater.* **4**, 011013 (2016).

50. Amet, F. *et al.* Tunneling spectroscopy of graphene-boron-nitride heterostructures. *Phys. Rev. B* **85**, 073405 (2012).

51. Chandni, U., Watanabe, K., Taniguchi, T. & Eisenstein, J. P. Signatures of Phonon and Defect-Assisted

Tunneling in Planar Metal–Hexagonal Boron Nitride–Graphene Junctions. *Nano Lett.* **16**, 7982–7987 (2016).

52. Vdovin, E. E. *et al.* Phonon-Assisted Resonant Tunneling of Electrons in Graphene--Boron Nitride Transistors. *Phys. Rev. Lett.* **116**, 186603 (2016).

53. Yu, G. L. *et al.* Hierarchy of Hofstadter states and replica quantum Hall ferromagnetism in graphene superlattices. *Nature Physics* **10**, 525–529 (2014).

54. Yu, G. L. *et al.* Interaction phenomena in graphene seen through quantum capacitance. *PNAS* **110**, 3282–3286 (2013).

55. Novoselov, K. S. *et al.* Electric Field Effect in Atomically Thin Carbon Films. *Science* **306**, 666–669 (2004).

56. Novoselov, K. S. *et al.* Two-dimensional atomic crystals. *PNAS* **102**, 10451–10453 (2005).

57. Novoselov, K. S. *et al.* A roadmap for graphene. *Nature* **490**, 192–200 (2012).

58. Castro Neto, A. H., Guinea, F., Peres, N. M. R., Novoselov, K. S. & Geim, A. K. The electronic properties of graphene. *Rev. Mod. Phys.* **81**, 109–162 (2009).

59. Katsnelson, M. I., Novoselov, K. S. & Geim, A. K. Chiral tunnelling and the Klein paradox in graphene. *Nature Physics* **2**, 620–625 (2006).

60. Wallace, P. R. The Band Theory of Graphite. *Phys. Rev.* **71**, 622–634 (1947).

61. Wang, E. *et al.* Gaps induced by inversion symmetry breaking and second-generation Dirac cones in graphene/hexagonal boron nitride. *Nature Physics* **12**, 1111–1115 (2016).

62. Diez, M., Dahlhaus, J. P., Wimmer, M. & Beenakker, C. W. J. Emergence of Massless Dirac Fermions in Graphene's Hofstadter Butterfly at Switches of the Quantum Hall Phase Connectivity. *Phys. Rev. Lett.* **112**, 196602 (2014).

63. Zak, J. Magnetic Translation Group. *Phys. Rev.* **134**, A1602–A1606 (1964).

64. Hofstadter, D. R. Energy levels and wave functions of Bloch electrons in rational and irrational magnetic fields. *Phys. Rev. B* **14**, 2239–2249 (1976).